

Important Notice

This copy may be used only for the purposes of research and private study, and any use of the copy for a purpose other than research or private study may require the authorization of the copyright owner of the work in question. Responsibility regarding questions of copyright that may arise in the use of this copy is assumed by the recipient.

UNIVERSITY OF CALGARY

Seismic Detection and Characterization of a CO₂ Flood in Ardley Coals, Alberta, Canada

by

Michael Jason McCrank

A THESIS

SUBMITTED TO THE FACULTY OF GRADUATE STUDIES
IN PARTIAL FULFILMENT OF THE REQUIREMENTS FOR THE
DEGREE OF MASTER OF SCIENCE

DEPARTMENT OF GEOSCIENCE

CALGARY, ALBERTA

JANUARY, 2009

© M. Jason McCrank 2009

UNIVERSITY OF CALGARY
FACULTY OF GRADUATE STUDIES

The undersigned certify that they have read, and recommend to the Faculty of Graduate Studies for acceptance, a thesis entitled "Seismic Detection and Characterization of a CO₂ Flood in Ardley Coals, Alberta, Canada" submitted by Michael Jason McCrank in partial fulfilment of the requirements of the degree of Master of Science.

*Supervisor, Dr. D. C. Lawton
Department of Geoscience*

*Dr. G. F. Margrave
Department of Geoscience*

*Dr. L. R. Lines
Department of Geoscience*

*Dr. E. C. Fear
Department of Electrical and Computer Engineering*

Date

Abstract

At the Alder Flats pilot project, 180 tonnes of gaseous CO₂ was injected into the Ardley Coals at a depth of 0.4 km to test enhanced coalbed methane production, as well as carbon sequestration in coals. This thesis discusses the seismic monitoring program which was executed to image the CO₂ flood. Prior to commencement of CO₂ injection, two preliminary 2D surveys were conducted in order to assist in designing a third 3D survey which was acquired after CO₂ injection. Poststack inversion of the 3D vertical component data showed a low acoustic impedance anomaly up-dip and along strike of the preferential fluid pathway in the target coal zone. The size and location of the anomaly concurs with the expected imprint of the injected CO₂ and it has been interpreted as the CO₂ flood. The magnitude of the acoustic impedance anomaly suggests that a reduction in the elastic stiffness of the coal matrix frame may have been detected.

Acknowledgements

Firstly, I would like to thank my thesis supervisor, Dr. Don Lawton, for connecting the University of Calgary to the Alder Flats CO₂ pilot project and allowing me to take part. I also thank him for his advice, support and proof reading of various abstracts and submissions. Without his eagle eyes this thesis might have discussed how the petrophysical effect of a CO₂ flood in coals is subtle and may be at the limit of delectability.

I would like to thank the staff of CREWES and the University of Calgary, especially Kevin Hall, Han-xing Lu, Malcolm Bertrand, Eric Gallant, Dave Henley and Henry Bland, for their varied assistance in acquisition, processing and making sense of the seismic data. And the chats and good humour too.

Over the course of my M.Sc. degree I have had the pleasure to learn from many people, but especially those who have taken the time to put together courses: Dr.'s Lawton, Krebs, Spila, Stewart, Margrave, Lines, Bancroft, Spratt and Cook.

Then there are the students. I have learned from and been inspired by many. To name just a few: Chad Hogan, Kelley Classen, Joanna Cooper, Maria Quijada, Mike Wahmsteiker, Brett Miles, Gareth Johnson, Katrina Chueng, Tyler Beaty, Chris Coueslan and Sarah Cutten.

I am grateful for the advice and assistance of Brian Russell, John Pendrel, Cheran Mangat, and Dave Secord.

My family is a continual source of encouragement and, lastly, but most importantly, I am eternally grateful for the unwavering support and patience of Heather.

Table of Contents

Approval Page.....	ii
Abstract.....	iii
Acknowledgements.....	iv
Table of Contents.....	v
List of Tables.....	viii
List of Figures and Illustrations.....	x
List of Symbols, Abbreviations and Nomenclature.....	xx
CHAPTER ONE: INTRODUCTION.....	1
1.1 Coal and Coalbed Methane.....	1
1.2 Enhanced Coalbed Methane Production.....	3
1.3 Carbon Storage.....	4
1.4 Monitoring, Measuring and Verification of Carbon Storage.....	5
1.5 The Use of Reflection Seismic Data to Characterize Coals.....	6
1.6 The Alder Flats ECBM Pilot Project.....	7
1.7 Thesis Objectives.....	10
1.8 Thesis Outline.....	11
1.9 Software.....	12
CHAPTER TWO: GEOLOGY AND PETROPHYSICS.....	13
2.1 Regional and Local Geology of the Alder Flats Location.....	13
2.1.1 Regional Stratigraphy.....	13
2.1.2 Geological Cross-sections.....	16
2.2 Well Data.....	21
2.2.1 Injection Well Petrophysical Logs.....	21
2.3 The Physical Properties of Coals.....	25
2.3.1 An Introduction to Coal.....	25
2.3.2 Characterizing Coals.....	26
2.3.3 Porosity and Permeability.....	27
2.3.4 Fluid Distribution in Coals and Gas Sorption.....	28
2.4 Ardley Coal Reservoir Characterization.....	30
2.5 Rock Physics of Injecting CO ₂ into Coal.....	31
2.5.1 Physical Properties of CO ₂ at Reservoir Conditions.....	31
2.5.2 Gassmann Fluid Substitution Modelling.....	32
2.5.3 The Effect of CO ₂ on the Elastic Properties of Coals.....	34
2.5.4 Dissolution of CO ₂ in the Formation Water.....	36
2.6 Conclusions.....	36
CHAPTER THREE: 2D SEISMIC SURVEYS.....	38
3.1 Introduction.....	38
3.2 Survey Design: Offset and Bandwidth Requirements.....	38
3.3 Stratigraphic Seismic Modelling.....	42
3.4 June 2006 2D Survey.....	43
3.4.1 Acquisition.....	43
3.4.2 Data Processing.....	45

3.4.3 Wavelet Estimation	48
3.4.4 Extending the 102/7-28 Well Logs.....	49
3.4.5 Interpretation	50
3.4.6 Conclusions from the June 2006 2D Survey	52
3.5 March 2007 2D Survey.....	52
3.5.1 Acquisition	52
3.5.2 Data Processing	56
3.5.3 Wavelet Estimation	78
3.5.4 Conclusions from the March 2007 Survey.....	81
CHAPTER FOUR: 3D – ACQUISITION, PROCESSING AND INTERPRETATION..	83
4.1 Introduction.....	83
4.2 Survey Design.....	83
4.3 Acquisition.....	86
4.4 Data Processing.....	92
4.5 Interpretation Vertical Component Post Stack	95
4.5.1 Base Map.....	95
4.5.2 Wavelet Estimation	97
4.5.3 Interpreted Seismic Events.....	101
4.5.4 Ardley Coal Time Structure and Amplitude Maps.....	103
4.6 Pre-stack Data Interpretation	108
4.7 Conclusions.....	115
CHAPTER FIVE: 3D CONVERTED-WAVE DATA.....	116
5.1 Introduction.....	116
5.2 Converted-wave Data	116
5.3 Converted-wave Data at Alder Flats.....	117
5.3.1 Survey Design and Acquisition.....	117
5.3.2 Converted-wave Processing.....	118
5.3.3 Interpretation of the 3D Data.....	119
5.3.4 Interpretation of the 2D Stack	121
5.4 Conclusions.....	123
CHAPTER SIX: ACOUSTIC IMPEDANCE INVERSION.....	124
6.1 Introduction.....	124
6.1.1 The Utility of Acoustic Impedance Inversion	124
6.2 Methods of Inversion.....	125
6.2.1 Band-limited Inversion.....	125
6.2.2 Model-based Inversion.....	126
6.2.3 Sparse Spike Inversion.....	128
6.2.4 Mixed-norm Inversion.....	129
6.3 Acoustic Impedance of the Ardley Coals	130
6.3.1 Petrophysics at Well Log Resolution.....	130
6.3.2 Petrophysics at Seismic Resolution.....	133
6.4 Model Based Inversion of the Alder Flats 3D Data.....	135
6.4.1 Low Frequency Initial Guess Model	136
6.4.2 Inversion Parameter Testing.....	138

6.4.3 Inversion and Wavelet Scaling	141
6.4.4 Interpretation	143
6.5 Mixed-norm Constrained Sparse Spike Inversion of the Alder Flats 3D Data	147
6.5.1 Wavelet Estimation	148
6.5.2 Setting the Inversion Parameters	150
6.5.3 Inversion QCs	152
6.5.4 Interpretation	157
6.6 Short-period Multiples	161
6.7 Deconvolving the Multiple Train	164
6.7.1 Zero-phase deconvolution	164
6.7.2 Minimum phase deconvolution	167
6.7.3 Acoustic impedance estimates after deconvolution	169
6.8 Petrophysical Interpretation of the Anomaly	171
6.9 Discussion and Conclusions	175
 CHAPTER SEVEN: CONCLUSIONS	 177
7.1 Discussion	177
7.2 Recommendations for Continued Research	178
 REFERENCES	 180

List of Tables

Table 2-1: Table of average densities, velocities, and Vp/Vs ratio for major lithologic units of the 102/7-28 well.	23
Table 2-2: Average elastic properties for coals, sandstones and shales from the well logs of 102/7-28.	23
Table 2-3: The petrophysical log values that identify coal sub-lithologies (AGS, 2004)	25
Table 2-4: Characteristics of the Mynheer coal seam at Alder Flats (Mavor and Faltinson, 2008)	30
Table 3-1: A comparison of Ardley Coal Zone bed time-thicknesses and the tuning thickness (T/4) of wavelets with different periods. Light grey cells indicate that the bed is below the tuning thickness and dark grey indicates the bed is within 1ms of the tuning thickness for the wavelet.....	41
Table 3-2: A comparison of Ardley Coal Zone bed time-thicknesses and the limit of resolution thickness (T/8) of wavelets with different periods. Light grey cells indicate that the bed is below the limit of resolution.	41
Table 3-3: The acquisition parameters for the June 2006 2D survey	44
Table 3-4: The standard processing flow used by CREWES for the June 2006 survey... ..	45
Table 3-5: Acquisition parameters for the March 2007 survey	54
Table 3-6: The processing flow applied to the vertical component of the March 2007 data.....	56
Table 4-1: Acquisition parameters for the June 2007 3D vertical component survey.....	86
Table 4-2: The processing flow for the vertical component data.	93
Table 6-1: Parameters used in the model-based impedance inversion	139
Table 6-2: The impedance error and synthetic-seismic correlation after impedance inversion at the 102/7-28 well location using the parameters from Table 6-1 (100-600 ms).....	140
Table 6-3: Parameters for the spiking deconvolution	165
Table 6-4: Parameters for the Gabor deconvolutions	165
Table 6-5: The average elastic properties of the Mynheer coals used to model the substitution of water for gaseous CO ₂ using the Gassmann method.	174

List of Figures and Illustrations

Figure 1-1: Stratigraphic intervals containing coal zones with CBM potential (ERCB, 2008).	2
Figure 1-2: The typical trend of fluid production from a CBM reservoir (from Morad et al., 2008).	3
Figure 1-3: A map of the Alder Flats site showing wells, roads and the locations of the 2D and 3D seismic surveys conducted.	8
Figure 1-4: Petrophysical logs and stratigraphic column of the Ardley Coals in the 102/7-28 well.	9
Figure 2-1: Statigraphy of the Pembina Field area (Alberta Geological Survey, 2004). The purple colour indicates major coal zones.....	14
Figure 2-2: Typical lithological profile of the Scollard Formation in the Pembina Field showing the sub-zones of the Ardley Coal Zone (from Pana, 2007).....	15
Figure 2-3: Map of cross section location (Alberta Geological Survey, 2004).	16
Figure 2-4: Regional east-west cross-section showing the sub-zones of the Ardley Coal Zone (dark orange) and the channel sandstones of the Scollard and Paskapoo Formations (dotted yellow) and the regional aquitard Battle Formation (light blue). The left log track is the gamma log and the right track is the density log (Alberta Geological Survey, 2004).	17
Figure 2-5: Map of cross section locations.	18
Figure 2-6: Local north-south cross section showing the sub-zones of the Ardley Coal Zone and the channel sandstones of the Scollard and Paskapoo formations. The datum is sea level (courtesy IHS Energy Accumap).	19
Figure 2-7: Local east-west cross section showing the sub-zones of the Ardley Coal Zone and the channel sandstones of the Scollard and Paskapoo Formations. The datum is sea level (courtesy IHS Energy Accumap).	20
Figure 2-8: Full length petrophysical logs from 102/7-28.....	22
Figure 2-9: Petrophysical logs from 102/7-28 in the vicinity of the Ardley Coal Zone... ..	25
Figure 2-10: Single component isotherms for Tiffany Coals at 55°C (after Gasem et al., 2002).	29
Figure 2-11: Total dissolved solids versus depth for the Tertiary-Upper Cretaceous strata in the Pembina Field area (Pana, 2007).....	31
Figure 2-12: CO ₂ Phase Diagram	32

Figure 3-1: PP synthetic seismogram using a 5-10-60-70 Hz Ormsby zero-phase wavelet.	39
Figure 3-2: (a) A 5-10-60-70 Hz Ormsby zero-phase wavelet and (b) its amplitude spectrum.	40
Figure 3-3: Three synthetic geological models and the related synthetic seismograms. All models use a 5-10-50-60 Hz Ormsby wavelet. (a) show varying P-wave velocity in the Mynheer coals. (b) shows varying the thickness of the thin shale in the Lower Ardley Coal Zone. (c) shows varying the thickness of the shale between the Upper and Lower Ardley Coal Zone.	43
Figure 3-4: Field layout for the June 2006 survey.	44
Figure 3-5: The raw field data gathered from a common receiver immediately west of the 102/7-28 well. A 300 ms AGC has been applied. The Ardley reflections occur at approximately 300-350 ms. The red box shows the window for amplitude spectrum calculation.	46
Figure 3-6: The amplitude spectrum calculated in a 180 ms window over the Ardley Coal reflections.	47
Figure 3-7: The migrated N-S line from the June 2006 survey.	47
Figure 3-8: The migrated E-W line from the June 2006 survey.	48
Figure 3-9: The wavelet extracted from the June 2006 north-south migrated section using the autocorrelation of CDP# 3300 – 3400 from 200 – 800 ms. (a) amplitude and phase spectrum, (b) the time domain wavelet.	49
Figure 3-10: The fabricated 102/7-28 well logs generated by splicing data onto the bottom of the actual 102/7-28 logs. The synthetic seismogram is generated with a 5-10-50-60 Hz Ormsby wavelet.	50
Figure 3-11: A portion of the north-south seismic line from the June 2006 survey with the synthetic tie and the Lower (purple) and Upper (blue) Ardley Coal horizon picks.	51
Figure 3-12: A short time window examination of the synthetic-seismic tie at the Ardley Coal Zone for the June 2006 2D data.	52
Figure 3-13: Field layout for the March 2007 survey.	54
Figure 3-14: A raw receiver gather for the geophone immediately west of the 102/7-28 well showing every second source location. Automatic gain control with a 300 ms window was applied. The red box shows the window for the amplitude spectrum calculation.	55

Figure 3-15: The amplitude spectrum calculated over a 180 ms window that included the Ardley Coal reflections.	55
Figure 3-16: Fold for the March 2007 survey.....	57
Figure 3-17: A shot gather before (a) and after (b) correcting the amplitudes for spherical divergence effects.....	58
Figure 3-18: First break picks: (a) auto picked and (b) edited.....	59
Figure 3-19: First break picks in the near offset range: (a) auto picked and (b) edited....	59
Figure 3-20: The first break data (coloured points) and the approximated velocity picks (lines) for the initial model used in the near surface model GLI inversion.....	61
Figure 3-21: The initial guess model of the thickness of the two layers (blue and red) of the near surface used in the GLI inversion. Each is assumed to have a velocity that varies laterally but is constant in depth at each lateral location.....	61
Figure 3-22: The near surface model that resulted from the GLI inversion. (a) shows the layer thicknesses and (b) shows the layer velocities.....	62
Figure 3-23: The receiver and shot statics required at each location along the 2D survey line.....	62
Figure 3-24: A shot gather shown before (a) and after (b) applying the required static correction.	63
Figure 3-25: Illustration of how data is transformed from the XT domain to the RT domain (from Henley, 1999). (a) the XT domain, (b) the RT domain.	64
Figure 3-26: A shot record (a) before and (b) after applying radial trace filtering.....	65
Figure 3-27: A shot gather before deconvolution.....	67
Figure 3-28: The shot gather after application of Gabor deconvolution.....	68
Figure 3-29: A shot gather with different band pass filtering. Note the subtle signal present in (b) but not in (c).	69
Figure 3-30: A shot gather after 5-10-100-110 Hz bandpass noise filtering.....	69
Figure 3-31: Collecting traces from multiple source/receiver pairs into a common mid-point (CMP) that is directly over the common depth point (CDP).	70
Figure 3-32: A typical CMP gather from the middle of the line.....	71
Figure 3-33: Stacking velocity picks with semblance and velocity-stack panels.....	73

Figure 3-34: Initial stacking velocity model established from velocity picking.	73
Figure 3-35: The smoothed model of stacking velocities.	74
Figure 3-36: A CMP gather (a) before and (b) after NMO removal and application of the offset-dependant mute function.....	74
Figure 3-37: The complete seismic section after CMP stacking. The Ardley Coals are the prominent set of reflections around 300 ms.....	76
Figure 3-38: Stacked section after applying F-x deconvolution which reduces the incoherent lateral noise.	77
Figure 3-39: Section after post-stack Kirchhoff time migration.....	77
Figure 3-40: (a) The zero-phase wavelet extracted from the March 2007 migrated section using a window from 200 – 800 ms and the 50 CMPs nearest the 102/7-28 well, and (b) the amplitude and phase spectra.	78
Figure 3-41: (a) The matching filter wavelet and its amplitude and phase spectra extracted by matching the 102/7-28 well to the migrated data in a window from 150 – 370 ms, and (b) the amplitude and phase spectra.	79
Figure 3-42: The migrated seismic section showing the seismic-synthetic tie and the interpretation of the Upper and Lower Ardley Coal events.....	80
Figure 3-43: The synthetic-seismic tie and well tie in the Ardley Coal Zone using the matching filter wavelet.	81
Figure 4-1: (a) The survey design for the vertical component survey, and (b) the associated fold map. Source lines (red) run north-south and receiver lines (blue) run east-west. The black circles show the locations of the 102/7-28 and 100/7-28 wells.	84
Figure 4-2: Maps of the offset attributes for the survey design. The black circles show the location of the 102/7-28 and 100/7-28 wells.	85
Figure 4-3: Maps of the offset and azimuth distribution quality for the survey design. The black circles show the locations of the 102/7-28 and 100/7-28 wells.	85
Figure 4-4: The survey layout in the field. Source lines run north-south and receiver lines run east-west.....	87
Figure 4-5: The actual layout for the vertical component survey. The coloured circles show the locations of sources or receivers for the gather in the following figures...	87
Figure 4-6: A complete source gather with no data enhancement. The source is on receiver line #3.....	88

Figure 4-7: A complete source gather with a 200 ms window automatic gain control. The source is on receiver line #3.	89
Figure 4-8: A raw receiver gather from the June 2007 3D survey. The gather is for the receiver beside the north-south road nearest the 102/7-28 well and the sources are those along the north-south road.	90
Figure 4-9: The amplitude spectrum for data in a 180 ms window around the Ardley Coal events in Figure 4-8.	90
Figure 4-10: A raw receiver gather from the June 2007 3D survey. The gather is for a receiver in the grassy field with all sources in a north-south line in the grassy field.	91
Figure 4-11: The amplitude spectrum for data in a 180 ms window around the Ardley Coal events in Figure 4-10.	91
Figure 4-12: The fold attained in the vertical component data.	92
Figure 4-13: The migrated 3D PP data volume showing a chair display with a time slice at the level of the Ardley Coals.	95
Figure 4-14: A time slice at (a) 250 ms and (b) 300 ms through the seismic volume. Inline #71 and crossline #40 intersect the 102/7-28 well and are often referred to in this thesis.	96
Figure 4-15: Cross section from the 3D volume showing Inline #71. The Ardley Coal events are between 300-350 ms.	96
Figure 4-16: Cross section from the 3D volume showing Crossline #40. The Ardley Coal events are between 300-350 ms.	97
Figure 4-17: The tie between the synthetic seismogram and seismic data achieved with the wavelet extracted using the autocorrelation of the traces over a window from 180 – 800 ms. (a) The blue traces are synthetic seismograms, the red traces are a single composite of the black trace actual data. (b) the wavelet and (c) the amplitude and phase spectra.	98
Figure 4-18: The amplitude spectrum of each trace in crossline #40 section that intersects the 102/7-28 well.	99
Figure 4-19: The tie between the synthetic seismogram and seismic data achieved with the wavelet extracted as a matching filter between the 102/7-28 well reflectivity log to the seismic data over a window from 180 – 380 ms. (a) The blue traces are synthetic seismograms, the red traces are a single composite of the black trace actual data. (b) the wavelet and (c) the amplitude and phase spectra.	100

Figure 4-20: The tie between the synthetic seismogram and seismic data with a comparison to the P-impedance well log in the Ardley Coal Zone. Events are picked for the Upper Ardley Coals, the top of the Lower Ardley Coals, and the base of the Lower Ardley Coals.....	101
Figure 4-21: The east-west section that intersects the 102/7-28 well and the tie to the well data and synthetic seismogram.	102
Figure 4-22: The north-south section that intersects the 102/7-28 well and the tie to the well data and synthetic seismogram.....	103
Figure 4-23: The time structure of the top of the Upper Ardley Coal horizon.....	104
Figure 4-24: The time structure of the top of the Lower Ardley Coal horizon.	104
Figure 4-25: The time structure of the base of the Lower Ardley Coal event.....	105
Figure 4-26: The isochron between the Upper and Lower Ardley Coal horizons. Smoothing has been applied to the map.	106
Figure 4-27: The isochron between the top and base of the Lower Ardley Coal events. No smoothing has been applied to the map in order to preserve fidelity of the data.....	106
Figure 4-28: The minimum amplitude of the Upper Ardley Coal seismic trough event.	107
Figure 4-29: The minimum amplitude of the Lower Ardley Coal seismic trough event.....	107
Figure 4-30: Three CDP gathers near the 102/7-28 well. The Upper Ardley (UA) and Lower Ardley (LA) Coal events are highlighted and the log is the acoustic impedance.	110
Figure 4-31: Super gathers showing traces that are binned from neighbouring CDP locations into stacks with common offsets. All gather are from inline #71. (a) shows gathers near the 102/7-28 well (crossline # 39-43) and (b) shows gathers from further east at crossline # 62-64. The Upper Ardley (UA) and Lower Ardley (LA) Coal events are highlighted and the log is the acoustic impedance...	111
Figure 4-32: The angle gathers showing traces that are binned from neighbouring CDP locations into stacks with equal angles of incidence. All gather are from inline #71. (a) shows gathers near the 102/7-28 well (crossline # 39-43) and (b) shows gathers from further east at crossline # 62-64. The Upper Ardley (UA) and Lower Ardley (LA) Coal events are highlighted and the log is the acoustic impedance.	112
Figure 4-33: The best fit line matching the amplitude variation with incidence angle for data from three CDP locations on inline #71. The red line shows the	

amplitudes picked from the base of the Lower Ardley peak event (positive amplitudes) and the blue line shows the amplitudes picked from the top of the Lower Ardley trough event (negative amplitudes).	113
Figure 4-34: The AVA gradient mapped for the Lower Ardley seismic event using only angles of incidence from $15^{\circ} - 45^{\circ}$	114
Figure 4-35: The AVA intercept mapped for the Lower Ardley seismic event using only angles of incidence from $15^{\circ} - 45^{\circ}$	114
Figure 5-1: A PS reflection at its conversion point (CP) and the PP reflection at its mid-point (MP). The CP is closer to the receiver than the source. (From Stewart et al., 2002).	117
Figure 5-2: (a) The design for the converted-wave survey. Source lines run north-south (red) and the single receiver line runs east-west (blue). (b) The associated fold map.	118
Figure 5-3: The location of the CCP moves away from the receiver location with increasing depth but at the limit of depth approaches an asymptotic conversion point (ACP). From Stewart et al. (2002).....	119
Figure 5-4: An offset gather synthetic seismogram of the radial component converted-wave using a 25 Hz Ricker wavelet. The 3 traces on the left are the stack, repeated 3 times.	120
Figure 5-5: A west-east inline (#10) section from the 3D PS data volume showing the picks of the Upper and Lower Ardley Coals. The data are displayed in PS time... ..	120
Figure 5-6: The 2D stack of the PS data. The trace is displayed in PS time. The Upper and Lower Ardley horizons are picked.	121
Figure 5-7: The correlation between the PP data and the PS data. The real data are post-stack whereas the synthetic data are pre-stack offset gathers. Each synthetic seismogram was created with a zero-phase wavelet extracted from the respective data sets. The data are displayed in PP time (i.e. the PS arrivals have been time-compressed to match the PP data events).	122
Figure 5-8: Vp/Vs ratio between the Upper and Lower Ardley Coals calculated by registering similar seismic events in the PP and the PS data. The zones above and below the Ardley Coal horizons were assigned constant Vp/Vs. The traces are the PP data displayed in PP time.	123
Figure 6-1: A cross-plot of impedance and Vp/Vs with gamma values in colour for 102/7-28 from 300 - 475 m (KB). Lithologies are blocked into coals, sandstones and shales in cross-plot space.	131

Figure 6-2: The lithology log from in the vicinity of the Ardley Coal Zone for 102/7-28.....	131
Figure 6-3: Cross-plot of impedance and gamma log response from 300 – 475 m (KB) for 102/7-28.	132
Figure 6-4: Lithology log showing the sub-lithologies of coal in the vicinity of the Ardley Coal Zone for 102/7-28.....	133
Figure 6-5: A cross-plot of impedance and Vp/Vs for 102/7-28 from 300 - 475 m (KB) at 1 ms sampling with a 60 – 70 Hz high cut filter.....	134
Figure 6-6: (a) The impedance log at logging resolution and with a 60 – 70 Hz high cut filter and the corresponding lithology logs: (b) at logging resolution and (c) after high cut filtering.	135
Figure 6-7: (a) The match filter wavelet used for the model-based inversion and (b) the amplitude and phase spectra.....	136
Figure 6-8: The initial guess impedance model at log resolution (inline 71).	137
Figure 6-9: The initial guess impedance model after low pass filtering 10-15 Hz (inline 71).	138
Figure 6-10: Analysis of the inverted impedance estimation at the 102/7-28 well location. In the left track, the blue curve is the log impedance, the black curve is the initial guess impedance, and the red trace is the inverted impedance. The middle track black curve is the error in the impedance estimate. On the right, the red seismogram is the synthetic generated from the impedance inversion and the black seismogram is the actual seismic data and the traces on the far right is the difference between the red and black seismogram.	140
Figure 6-11: The RMS of the trace amplitudes in the 3D data in a window from 150 ms above the Upper Ardley Coal horizon to 500 ms below the Upper Ardley Coal horizon.....	142
Figure 6-12: The inverted impedance (inline 71) with the impedance log from 102/7-28 superimposed.	143
Figure 6-13: The inverted impedance (crossline 40) with the impedance log from 102/7-28 superimposed. The horizons are those picked from the seismic.	144
Figure 6-14: A map of the mean impedance in a 10 ms window through the Lower Ardley impedance zone.....	145
Figure 6-15: The residual difference between the seismic traces and the synthetic seismogram created from the impedance estimation (crossline 40).	146

Figure 6-16: Cross plot of the impedance inversion estimate values and the 102/7-28 well log impedance values after high cut filtering (60-70 Hz).	147
Figure 6-17: (a) The wavelet estimated using the CSS inversion, (b) the amplitude spectrum and (c) the phase spectrum.	149
Figure 6-18: The amplitude spectrum of the wavelet and the seismic data.....	149
Figure 6-19: The amplitude spectrum of the reflectivity series from the 102/7-28 well logs generated from a 512 ms time series with 1 ms sampling and an 80-100 Hz high-cut filter.	150
Figure 6-20: Testing the λ value. (a) the seismic (black) and the residual (red) in the time domain and (b) the inverted impedance (black) compared to the well log impedance (blue).....	151
Figure 6-21: The inverted impedance (crossline 40).	153
Figure 6-22: (a) The inverted impedance (crossline 40) and (b) the original seismic. Lower and Upper Ardley Coal horizon picked on seismic (black) and on the impedance data 6.0×10^6 kg/m ³ *m/s cut-off (blue).....	153
Figure 6-23: Inverted synthetic seismogram cross-correlation with the seismic data.	154
Figure 6-24: The seismic data (black) and the residual error (red) plotted at the same amplitude scale (crossline 40).....	155
Figure 6-25: The inverted impedance and the 102/7-28 well log impedance with a 60-70 Hz high cut filter.	156
Figure 6-26: The cross-plot of the inverted impedance and the well log impedance after high cut filtering (60-70 Hz).....	156
Figure 6-27: (a) The inverted impedance with the well log impedance after 60-70 Hz high cut filtering, (b) the original seismic, (c) the inverted reflectivity, and (d) the inverted synthetic seismogram (a portion of crossline #40).	157
Figure 6-28: 1 ms steps through the inverted impedance of the Lower Ardley Coal Zone from 3 - 14 ms below the Lower Ardley Coal seismic pick horizon.....	158
Figure 6-29: Examination of a horizon slice through the middle of the Lower Ardley Coal low impedance zone. (a) crossline #40 showing the slice location and (b) the slice. Crossline #40 is the black dotted line in (b).	159
Figure 6-30: The mean impedance in a 10 ms window below the Lower Ardley horizon picked from the impedance volume.	160

Figure 6-31: 3D rendering of the clusters of area where the impedance is less than $5.0 \times 10^6 \text{ kg/m}^3 \cdot \text{m/s}$. Note the Upper Ardley Coal forms the large cluster in red, while a sole cluster exists in the Lower Ardley Coal Zone (green).....	160
Figure 6-32: An example that illustrates how the initial pulse at time zero can be dominated by delayed arrivals of short-path multiple pulses after the wave transmits through a series of coal seams (after Schoenberger and Levin, 1974)....	162
Figure 6-33: Synthetic seismograms showing the effect of short-path multiples and mode conversions by comparing gathers and stacks with and without including multiples in the model. All models were created with a zero-phase 5-10-50-60 Hz Ormsby wavelet. The dotted lines are constant time lines for comparing the phase of the different models.....	163
Figure 6-34: Traces produced by stacking offset synthetic data to evaluate the effectiveness of several methods of deconvolution	166
Figure 6-35: (a) A synthetic offset gather created with (b) a minimum phase 5-10-50-60 Hz Ormsby wavelet and including all multiples.....	168
Figure 6-36: A comparison of deconvolving minimum phase synthetic seismograms. The brown traces are stacks of model data created with a zero-phase wavelet and the black traces are stacks of minimum phase synthetic data that has been deconvolved.....	169
Figure 6-37: Comparison of the post-stack acoustic impedance inversion of various traces. Inversion a) and b) are based on the traces produced with a zero-phase wavelet. Inversions c), d), and e) are based on the deconvolved minimum phase data. The blue curve is the real log impedance, the black curve is the initial guess model for the inversion (10 Hz high cut), and the red curve is the inversion result. The error value is the residual difference between the log curve and the inverted curve between 200-450 ms.	171
Figure 6-38: The original impedance log from the 102/7-28 well (red) and the log adjusted by a 10% reduction in impedance in the Mynheer coal zone (blue). The curves are at log resolution on the left and with a 60-70 Hz high cut filter on the right.....	172

List of Symbols, Abbreviations and Nomenclature

<u>Symbol</u>	<u>Definition</u>
AI	Acoustic Impedance
AGC	Automatic Gain Control
AVA	Amplitude Variation with Angle
AVO	Amplitude Variation with Offset
CCP	Common Conversion Point
CDP	Common Depth Point
CMP	Common Mid Point
CSEMP	Carbon Sequestration and Enhanced Methane Project
FFT	Fast Fourier Transform
Gr	Gamma ray log
HRS	Hampson Russell Software
JGW	Jason Geoscience Workbench
KB	Kelly Bushing (~4m above grade)
ms	millisecond
QC	Quality Control
Rho	ρ = density
RMS	Root Mean Square
TVD	True Vertical Depth
TWT	Two Way Time
Vp	P-wave velocity (compressional)
Vs	S-wave velocity (shear)
Zp or Z	Acoustic impedance

Chapter One: Introduction

1.1 Coal and Coalbed Methane

Coal, a sedimentary rock composed mainly of organic material, has been mined extensively for the energy contained in its solid matrix. In addition to the chemical energy of coal's macro-molecular matrix, *in situ* coals usually contain methane gas which is referred to as coalbed methane (CBM). Coals are a micro-porous material and have an enormous surface area for gas storage via various chemo-physical sorption processes (Bustin, 2001). Sorbed gases (discussed in greater detail in Chapter 2) have a density that is believed to approach that of a liquid state, and as such coal seams can hold a large amount of methane.

When a coal seam is de-pressured, sorbed methane can gasify and escape from the coal beds. While this gas is a safety concern for coal mines, it is a potential resource in coals that are buried too deeply to be mined. The resource has been exploited through CBM production, a process that involves drilling into coal seams, reducing the pressure, and producing formation fluids including methane (Schraufnagel, 1993). Currently, CBM production accounts for approximately 10 % of the USA gas production (Morad et al., 2008). In Alberta, CBM gas-in-place from all of stratigraphic intervals with sizeable coal deposits (Figure 1-1) is estimated to be as high as $1.42 \times 10^{13} \text{ m}^3$ (Beaton, 2003). The Ardley Coal Zone, the interval of interest in this thesis, is estimated to contain a total of $323 \times 10^9 \text{ m}^3$ gas-in-place (Pana, 2007).

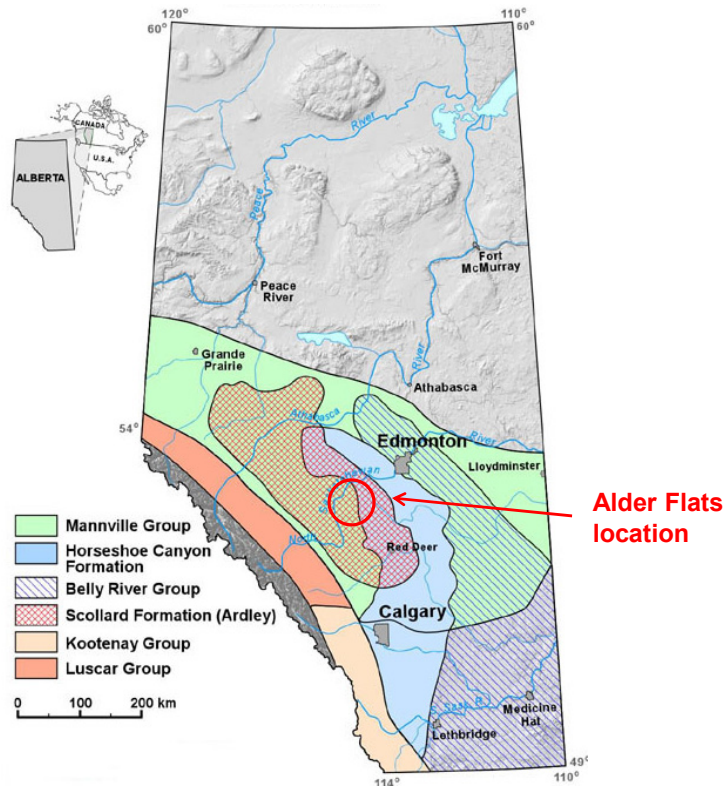


Figure 1-1: Stratigraphic intervals containing coal zones with CBM potential (ERCB, 2008).

CBM development is considered to be unconventional because the coal forms both the petroleum source rock and the reservoir rock, and because coal is typified by exceptionally low permeability (Bustin, 2001). What permeability coals do have is dominated by natural fractures called cleats. Because of coal's low permeability, CBM wells can take a very long time to produce significant amounts of gas; but because of the quantity of the resource in the rock, wells can produce at a steady, albeit slow, rate for a very long time (Thomas, 2002). Therefore, two critical factors in CBM development are the coal's gas storage capacity and saturation, and the coal's permeability. Additionally, many coals have a high degree of water saturation. This water must be produced in order to reduce the reservoir pressure to the point that methane will de-sorb, as well as to increase the relative permeability of gas to water in the cleat system (Mazumder et al., 2003). Figure 1-2 shows the typical production history of a CBM well. Because coals with high water saturation must undergo prolonged water production before economic

quantities of methane can be produced, water saturation is a third critical consideration in CBM production.

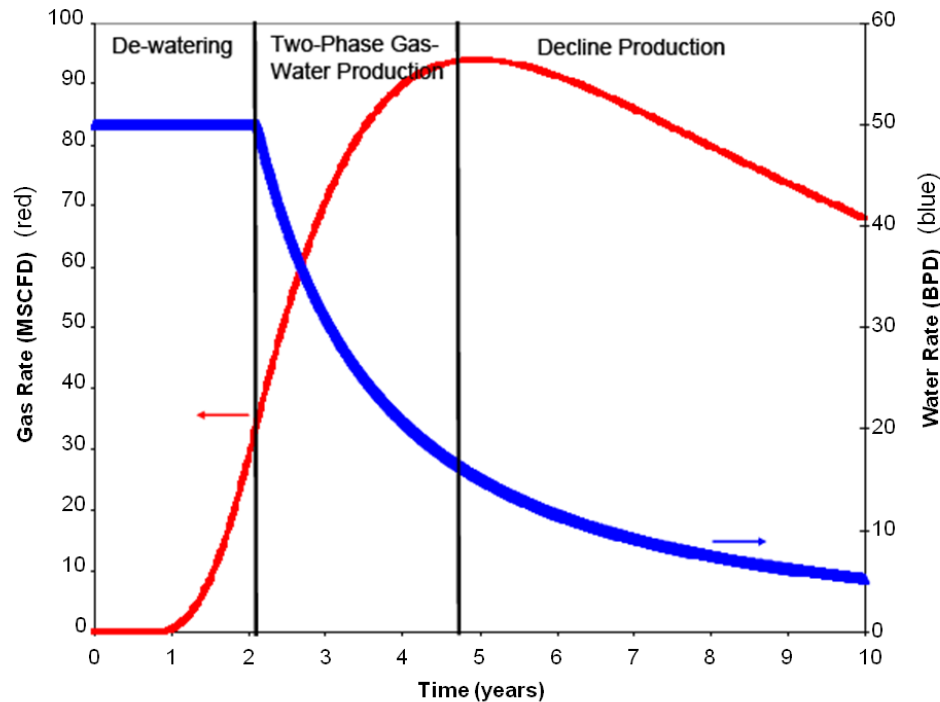


Figure 1-2: The typical trend of fluid production from a CBM reservoir (from Morad et al., 2008).

1.2 Enhanced Coalbed Methane Production

Interest in enhanced coalbed methane (ECBM) processes has been spurred by numerous factors including prolonged dewatering phases, protracted periods of low gas production rates even after dewatering and ultimate recovery rates totaling only ~50% of the original gas-in-place (Thomas, 2002). ECBM involves injecting fluids into the reservoir to encourage methane desorption. Two fluids that have been used for ECBM are carbon dioxide (CO₂) and nitrogen (N₂) (Zhu et al., 2003).

The driving mechanism in CO₂-ECBM is the phenomena that coals have a stronger affinity to sorb CO₂ rather than methane. Through competitive sorption, methane can be replaced by CO₂ in the sorbed state; freeing methane for production. However, a critical challenge for CO₂-ECBM is that coals volumetrically swell as they sorb CO₂ and the

swelling can diminish the already limited permeability of the natural fracture system (Bustin et al., 2008).

In N₂-ECBM, the injected gas creates a partial pressure difference between the cleat system and the coal matrix for both N₂ and methane; resulting in gas exchange (Shimada et al., 2005). Coals preferentially sorb methane over N₂ which thus avoids issues related to coal swelling. Additionally, because N₂ is relatively inert in coals, the injected N₂ may act to increase or stabilize fluid pressure in the cleat system, which would otherwise be decreasing as a result of fluid production. The increased fluid pressure can act to maintain fracture aperture size and fracture permeability. However, pure N₂-ECBM is ultimately limited due to the lower affinity for coals to sorb N₂ relative to methane. A concept of continued investigation is that of injecting a combination of CO₂ and N₂ (Bustin et al., 2008).

1.3 Carbon Storage

An additional advantage of CO₂-ECBM is that with competitive sorption, CO₂ replaces methane in the sorbed state and may be permanently stored in the coal matrix. Geological storage of CO₂ is being considered as a method of reducing the emissions of the gas into the atmosphere (White et al., 2005). Worldwide CO₂-ECBM has the potential to store up to 150 Gt of this greenhouse gas with limited risk of leakage (Gale and Freund, 2001). Therefore, understanding the technology of storing CO₂ in coalbeds is of significant importance.

Worldwide, only a few CO₂-ECBM pilot-projects have been reported:

- Burlington Resources operated an ECBM project in the San Juan Basin of New Mexico that injected CO₂ into a thick coal zone for 6 years from 1995 to 2001 (Reeves et al., 2003). The goal of the Burlington project was enhanced methane production and was not designed as a carbon sequestration exercise.
- A micro-pilot project in Alberta, Canada at Fenn-Big Valley was reported on by Gunter et al. (2004) who found that CO₂ injection into very low permeability coals was possible and that injectivity was actually increased through an alternating injection and shut-in sequence.

- The European Commission undertook a demonstration project in Kaniów, Poland called RECOPOL that attempted to conduct a multi-well CO₂-ECBM program. The project also intended to monitor the project with time-lapse seismic analysis. However, lack of permeability in the reservoir resulted in a truncated injection program and no time-lapse seismic data were collected (Benedictus et al., 2008).
- A consortium of Canadian institutions lead by the Canadian International Development Agency (CIDA), in conjunction with the Chinese Ministry of Commerce, conducted a micro-pilot CO₂ injection test in Qinshui, China that is reported on by the Alberta Research Council (2007). The study found that enhanced methane production and carbon sequestration was achieved on a micro-pilot scale.

Although not associated with a specific test project, Hughes et al. (1999) conducted a regional analysis of the potential for CO₂-ECBM in the Ardley Coal Zone of Alberta, Canada.

1.4 Monitoring, Measuring and Verification of Carbon Storage

Leakage of injected CO₂ into zones other than the target reservoir or into overburden formations is a potential risk associated with any CO₂ geological storage process (International Panel on Climate Change, 2005). A means of reducing the potential impact of a leak is to monitor the injection process in order that a leakage scenario would be identified quickly and rectification measures taken promptly. Such monitoring, measuring and verifying (MMV) techniques would not only reduce the risks associated with carbon storage, but would serve to reassure the public that the risks are being managed responsibly and comprehensively (Wilson et al., 2003).

Benson (2005) discusses various methods to monitor the geological storage of CO₂. Techniques that can monitor time-lapse evolution of the subsurface include (Arts and Winthagen, 2005):

Down hole (well bore) techniques

- passive seismic monitoring
- pressure-temperature monitoring

- time-lapse wire-line well logging
- geochemical fluid sampling

Surface monitoring techniques

- surface seismic surveys (time-lapse 4D)
- gravity surveys
- tilt-meter monitoring
- soil and atmospheric sampling

Key advantages of the surface seismic method are that it provides high resolution, full volume coverage of the subsurface relative to the other methods. In time-lapse 4D seismic monitoring, 3D surveys are repeated identically at different times during the injection program. Ideally, differences between the surveys would show where reservoir changes have occurred, or in the unplanned case of leakage, where the leaked CO₂ has moved to. 4D time-lapse seismic monitoring can provide full volume coverage of the subsurface and can reasonably be expected to remotely detect a leak long before the fluid is detected in the near surface or in monitoring wells located stochastically throughout a storage field. However, a key knowledge gap is a comprehensive understanding of the minimum volume of CO₂ that can be detected using time-lapse seismology when CO₂ imbibes into various rock or formation types.

1.5 The Use of Reflection Seismic Data to Characterize Coals

Monitoring CO₂ injection into a formation requires seismic characterization of the reservoir. However, characterization of subsurface coals using seismic data presents some unique challenges. Coals occur in stratigraphic beds with thicknesses that are often less than the seismic wavelet wavelength which results in tuning effects when the reflection from the top and bottom of a bed interfere constructively or destructively. Such tuning make coalbed dimensions difficult to resolve with seismic data (Gochioco, 1991). This is further complicated by the fact that coals typically have a very low density and low seismic wave velocity relative to the encasing sediments, resulting in high reflection coefficients and low transmission coefficients for incident seismic waves (Gochioco,

1989; Knapp, 1990). As pointed out by Schoenberger and Levin (1974, 1978), seismic wave transmission through a stacked series of highly reflective beds such as coals may result in a significant energy build-up in a train of short-period inter- and intra- bed multiples that further complicates the imaging of coals.

Despite the challenges, a number of techniques of seismic reflection imaging and characterization of CBM reservoirs have been attempted (Gochioco, 2002). Amplitude variation with offset techniques has been used to identify zones of higher fracture density (Peng et al., 2006; Ramos and Davis, 1997). Marroquin and Hart (2004) used seismic attributes to characterize thinly-bedded CBM reservoir thicknesses, subtle bedding structures and their relationship to zones of enhanced permeability. Converted wave seismic data (generated when compressional-mode waves convert to shear-mode waves upon reflection in an elastic medium) can be used to find interval V_p/V_s ratios (the ratio of compressional wave velocity to shear wave velocity) and in some instances converted wave data have resolution comparable to conventional compressional wave seismic data (Hendrick, 2006). Although challenging because of issues related to tuning, interference and multiples, Fogg (2001) gives recommendations for interpreting acoustic impedance estimates in stacks of coal isotherms in the UK Staffordshire field.

1.6 The Alder Flats ECBM Pilot Project

The Alder Flats location is in the Pembina Field of the west-central Alberta plains (Figure 1-1). The pilot project was originally intended to be a multi-well program where CO_2 would be injected into the coals through an injection well and production would occur from a second nearby well. At the time that this thesis was written, the project had seen several stages of formation testing and short-term fluid injection but continuous CO_2 injection had been curtailed due to unforeseen problems with the injection well.

The layout of the site is illustrated in Figure 1-3. The injector well is 102/7-28-46-7 W5M (here after referred to as 102/7-28) and the producer well is 100/7-28-46-7 W5M (100/7-28). The locations of other wells discussed in this thesis, as well as the location of the various seismic surveys that were conducted at the site are also illustrated in Figure 1-3.

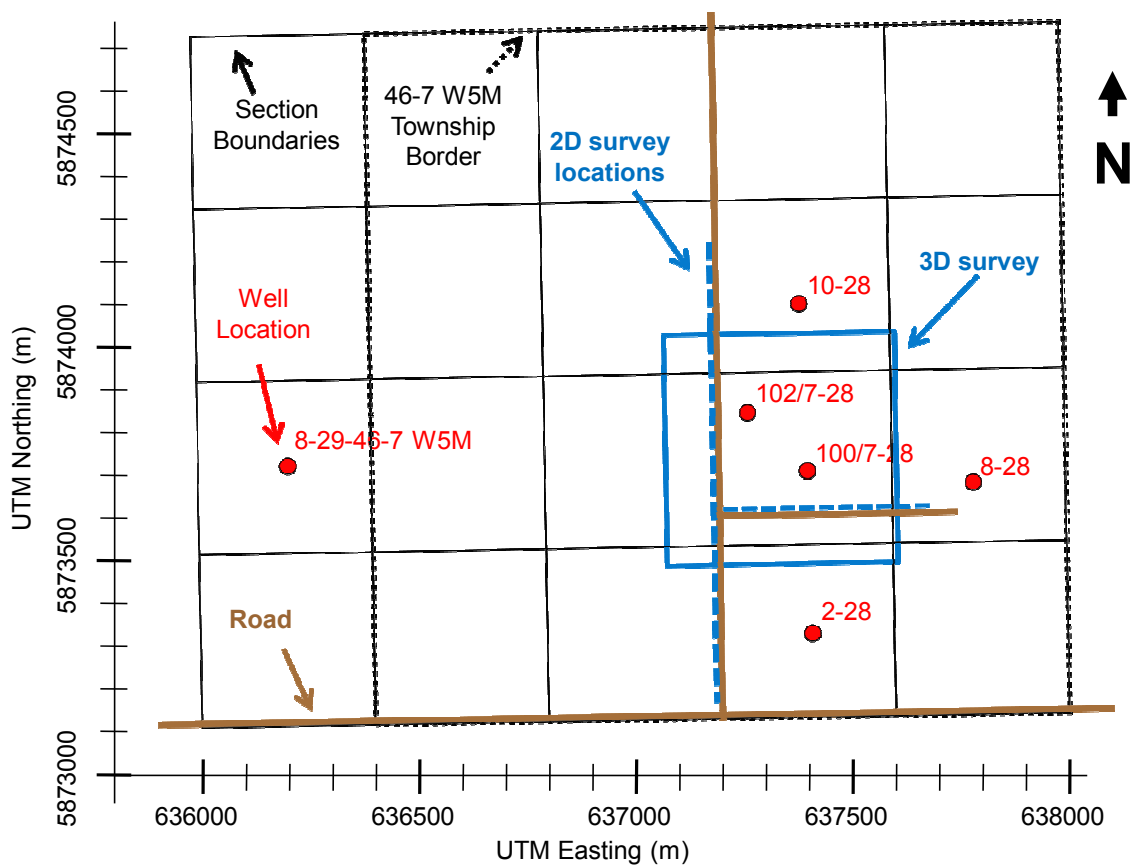


Figure 1-3: A map of the Alder Flats site showing wells, roads and the locations of the 2D and 3D seismic surveys conducted.

The Ardley Coal Zone has several sub-zones that are shown in the stratigraphic column of Figure 1-4. The stratigraphy of the project site is discussed in greater detail in Chapter 2.

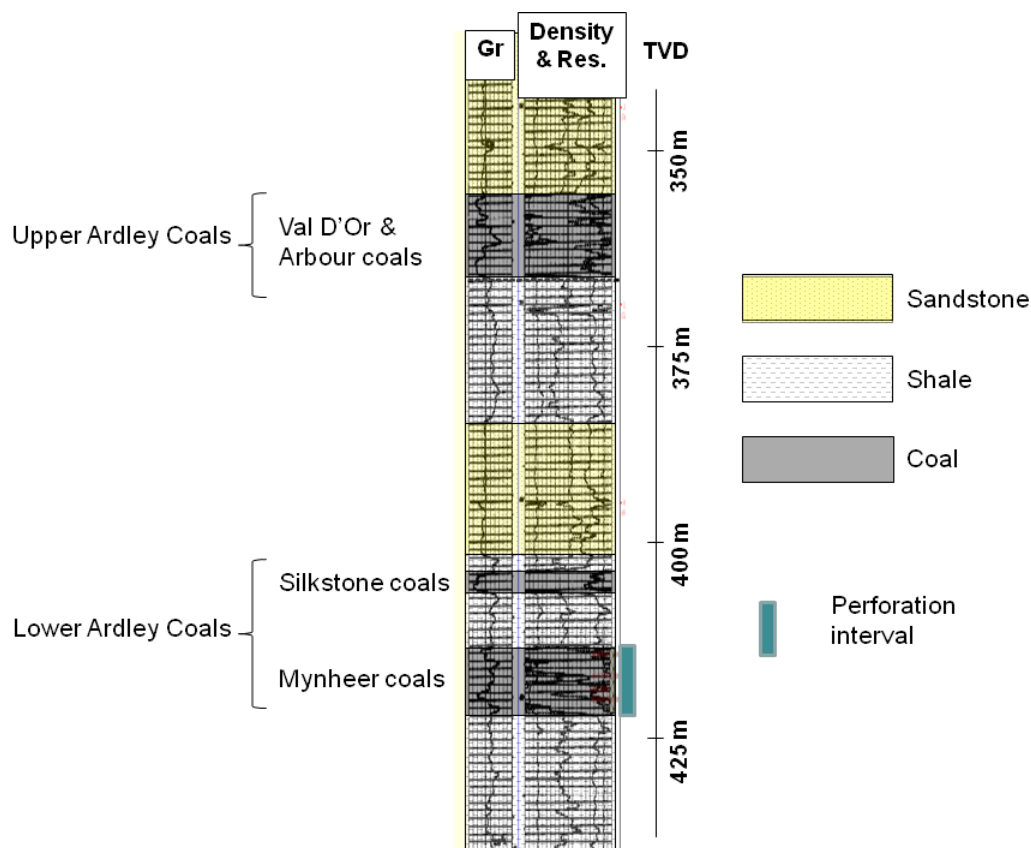


Figure 1-4: Petrophysical logs and stratigraphic column of the Ardley Coals in the 102/7-28 well.

To test the reservoir properties, as well as to prepare for the injection program, the 102/7-28 well went through several processes that included hydraulic fracture stimulation and a short-term CO₂ injection test (described in the Alberta Research Council, ARC, project report by Mavor and Faltinson, 2008). The short-term CO₂ injection test occurred in September of 2006. In total 180 tonnes of CO₂ was injected through well perforations in the Mynheer coal zone (Figure 1-4). At the temperature and pressure conditions of these coals (discussed in Chapter 2), the CO₂ would have been in a gaseous state. The ARC report states that if the CO₂ entered the full thickness of the Lower Ardley Coal Zone, the area of the region contacted by CO₂ would be 1,495 m² and that if the region were circular around the injection well (102/7-28) the equivalent radius would be 21.8 m. However, the report also notes that, based on surface tilt-meter data, the hydraulically stimulated fracture, which was created before the CO₂ injection, was believed to extend

to the southwest and to the northeast of 102/7-28. This orientation was expected based on the regional stress field (Bell, 2006) that shows the maximum principle horizontal stress in a southwest-to-northeast direction. Therefore, the preferential permeability pathway near the well bore would also be in line with the stimulated fracture and would trend southwest-northeast.

The Alder Flats project had several research goals including the collection of data through various MMV technologies:

1. Down hole pressure monitoring
2. Production well fluid sampling
3. Surface tiltmeter monitoring
4. Surface seismic monitoring

This thesis focuses on the data that was collected as a part of the surface seismic monitoring program. Three separate seismic surveys were conducted. The first two, in June 2006 and March 2007, were 2D surveys and were acquired with the intent to test data acquisition and processing parameters. A 3D survey was acquired in June 2007 and was intended to form the baseline survey for future time-lapse analysis. However, because continuous injection of CO₂ has not been achieved, no monitor survey has been acquired. Therefore this thesis focuses on analysis of the two 2D data sets and the single 3D data set. Significantly, the June 2007 survey was acquired after the 180 tonne CO₂ flood had soaked in the coal reservoir for approximately 9 months.

1.7 Thesis Objectives

The principal goal of this thesis was to quantitatively interpret the seismic data collected at the Alder Flats site to determine if the 180 tonnes of injected CO₂ can be detected and its location characterized. This goal was achieved through two objectives.

The first objective was to gain an *a priori* understanding of the site stratigraphy, the petrophysics of the coals and encasing strata, the physical properties of the coals, and the ability of seismic techniques to characterize the rocks and fluids. The research methods included a literature review of the regional geology and the physical properties of coals, analysis of the petrophysical data from local wells, and synthetic seismic modelling.

The second objective was to acquire, process and interpret seismic data for mapping coals and fluids. The research methods involved synthetic modelling to optimize the acquisition design, actual field acquisition, and testing and execution of data processing procedures. Particular attention was paid to understanding the data in the context of the local geology, the high reflectivity of coal beds, the phenomena of thin-bed tuning, and the complications of inter- and intra-bed multiple reflections. Analysis included an inversion of the seismic data to estimate acoustic impedance.

1.8 Thesis Outline

Chapter 2 consists of an introduction to the site geology. Relevant literature is reviewed and well correlation cross-sections are constructed. The physical properties of the Ardley Coals and characterization of coals in general are reviewed. Finally, literature about the effect of injecting CO₂ on the elastic properties of coals is reviewed.

Chapter 3 discusses the acquisition, processing and interpretation of the two 2D seismic surveys that were collected at the Alder Flats location. The different acquisition parameters and processing flows tested on each data set are compared. The data quality is analyzed; and how the results were used to design the subsequent 3D survey is discussed. Synthetic modelling is used to understand thin-bed tuning phenomena and non-uniqueness in possible data interpretations.

Chapter 4 discusses the acquisition, processing and interpretation of the 3D seismic data set. Acquisition parameters and processing flow are documented. Horizon time-structure and reflection amplitude analysis is described and the character of the pre-stack seismic data is investigated.

Chapter 5 discusses the interpretation of the converted wave data collected in the June 2007 3D survey. The data were generated in a sparse, low-fold 3D survey that was stacked into a higher fold 2D data set. The Ardley Coal Zone V_p/V_s ratio is assessed with these data.

Chapter 6 discusses inversion of the post-stack data to estimate acoustic impedance. The theory of two inversion methods is reviewed. The quantitative details of the results are analyzed and compared to the acoustic impedance measurements from the

petrophysical well log data. The results are interpreted in terms of the likely detectability of the injected CO₂. Also, the results of synthetic modelling are reviewed in order to assess the effect of short-path multiples on the Alder Flats data.

Chapter 7 contains conclusions and recommendations for future research.

1.9 Software

The following software was utilized to conduct the analysis in this thesis:

- Promax2D from Landmark
- Hampson Russell Software: eLog, AVO, Strata, ProMC
- Fugro-Jason Jason Geoscience Workbench: InverTrace
- KingdomSuite
- Matlab
- IHS Accumap
- Vista
- CREWES Syngram and QUADDES

Chapter Two: Geology and Petrophysics

2.1 Regional and Local Geology of the Alder Flats Location

2.1.1 Regional Stratigraphy

Figure 2-1 illustrates the stratigraphy of the west-central Alberta Plains and the major coal zones. The Ardley Coals are a zone of the Scollard Formation, a Late Cretaceous and Early Tertiary aged succession of fluvial deposits that has no marine deposition in the Pembina Field area (Gibson, 1977). The Scollard Formation is informally divided into the Upper and Lower Members, with the Lower Member made up of siltstone and mudstone with discontinuous thin, clean channel sandstones, whereas the Upper Member is characterized by a mixture of interbedded mudstone, siltstone, sandstone, and coals (Langenberg, 2007). The boundary of the Upper and Lower Scollard Formation, that divides the Cretaceous from the Tertiary rocks, is marked by the initiation of coal deposition. The Upper Scollard Formation is bounded by coals at its base and at its top, forming a sequence of coals called the Ardley Coal Zone.

Overlying the Scollard Formation (and the Ardley Coal Zone) is the Paskapoo Formation which is typified by channelized sandstone and siltstone (Langenberg et al., 2002). Regionally, stacked channel sandstones overlie and are in direct contact with the uppermost coals of the Ardley Coal Zone.

Underlying the Scollard Formation is the Battle Formation, a package of interbedded tonstein (a kaolinitic mudstone) and other mudstone layers that average 10 m in thickness (Pana, 2007). The Battle Formation, easily identified on petrophysical logs by its high gamma ray signature, forms a regional aquitard that separates the underlying aquifer system of the Wapiti Group and the overlying aquifer system of the Scollard-Paskapoo Formations (Jerzykiewicz, 1997).

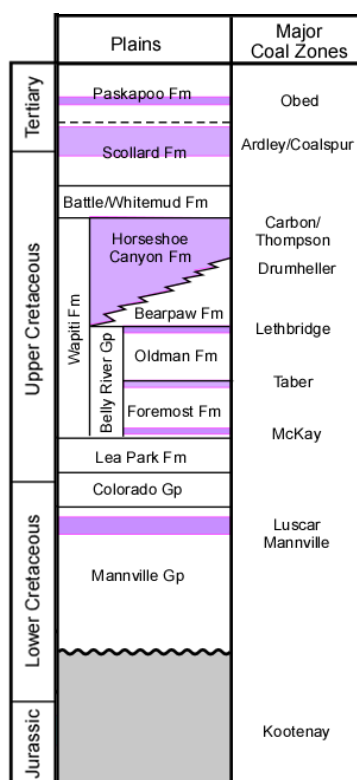


Figure 2-1: Stratigraphy of the Pembina Field area (Alberta Geological Survey, 2004). The purple colour indicates major coal zones.

The Upper Scollard Formation includes 4 distinct cycles of coal deposition which form four coal sub-zones. These are named from base to top: the Mynheer, the Silkstone, the Arbour, and the Val D'Or coal zones (Dawson et al., 2000). Figure 2-2 illustrates the typical stratigraphy and lithological make up of the Scollard Formation with emphasis on the coals of the Ardley Coal Zone. The figure illustrates that each sub-zone often contains layers of pure coal as well as layers of coaly shale, shaley coal, and tonstein. The Silkstone, Arbour, and Val D'Or zones have been documented to be laterally consistent stratigraphic sequences, whereas the Mynheer zone is more irregular and has less lateral continuity in well-to-well correlations (Pana, 2007).

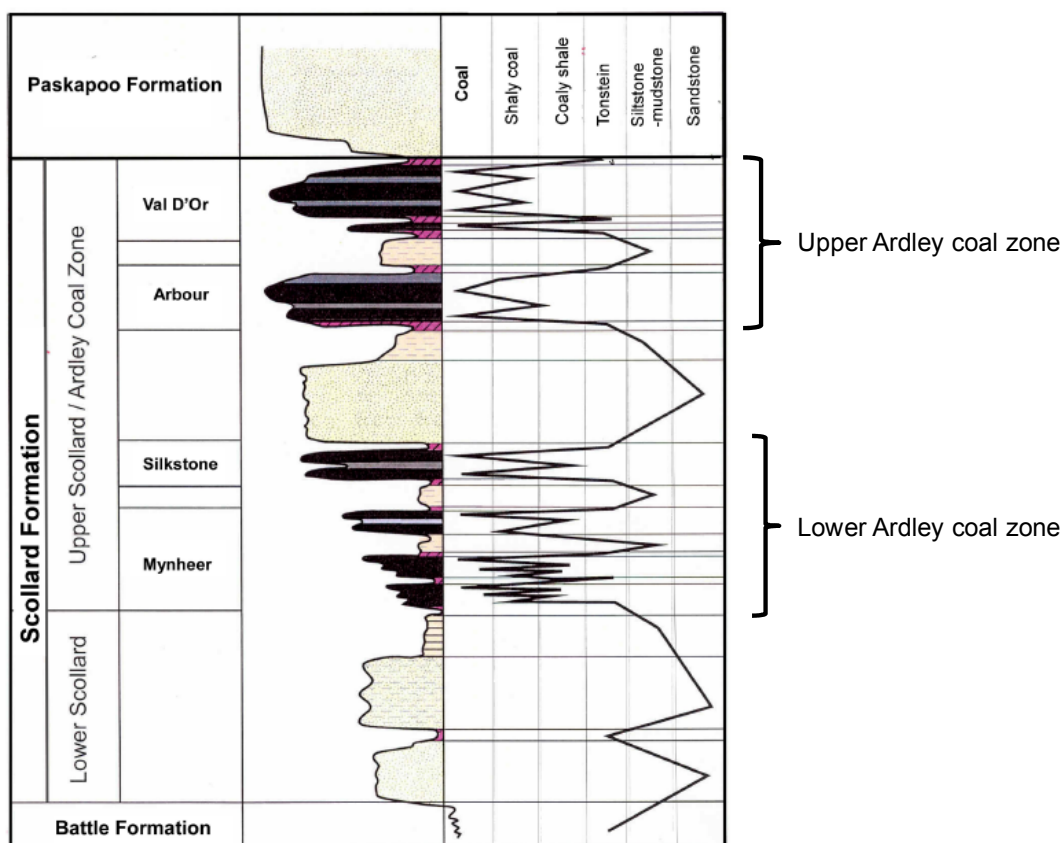


Figure 2-2: Typical lithological profile of the Scollard Formation in the Pembina Field showing the sub-zones of the Ardley Coal Zone (from Pana, 2007).

Regionally, the four sub-zones are typically separated by shales and channel sandstone packages ranging in thickness from metres to tens of metres (Beaton, 2002). The thickest package of non-coal sediments occurs between the Silkstone and the Arbour sub-zones. Because this clastic package leaves the lower two zones vertically separated from the upper two zones, the more basal Mynheer and Silkstone sub-zones are often referred to as the Lower Ardley Coal Zone, while the Arbour and Val D'Or sub-zones are referred to as the Upper Ardley Coal Zone. In this thesis the nomenclature of the Upper and Lower Ardley Coal Zones will be used for convenience when it is not necessary to refer to each sub-zone specifically.

2.1.2 Geological Cross-sections

Figure 2-3 and Figure 2-4 show a regional ~10 km long stratigraphic cross-section of the Ardley Coal Zone that includes 100/7-28 (producer well). The figure illustrates the lateral continuity of the coal sub-zones and the interbedded shale and sandstone units. A channel sandstone package called the Arbour-Silkstone channel sandstone overlies the Silkstone coal in the study area. Regionally this sandstone package ranges in thickness from 10 to 20 m. Overlying the Arbour-Silkstone channel sandstone and underlying the Upper Ardley Coals is a 10 to 20 m thickness of shale strata. The Arbour and Val D'Or coals are very closely spaced and, as illustrated in Figure 2-6 and Figure 2-7, are difficult to separate using petrophysical logs. The Upper Ardley Coals are overlain by channel sandstones of the Paskapoo Formation. These trends also remain consistent in a north-south cross-section (Alberta Geological Survey, 2004).

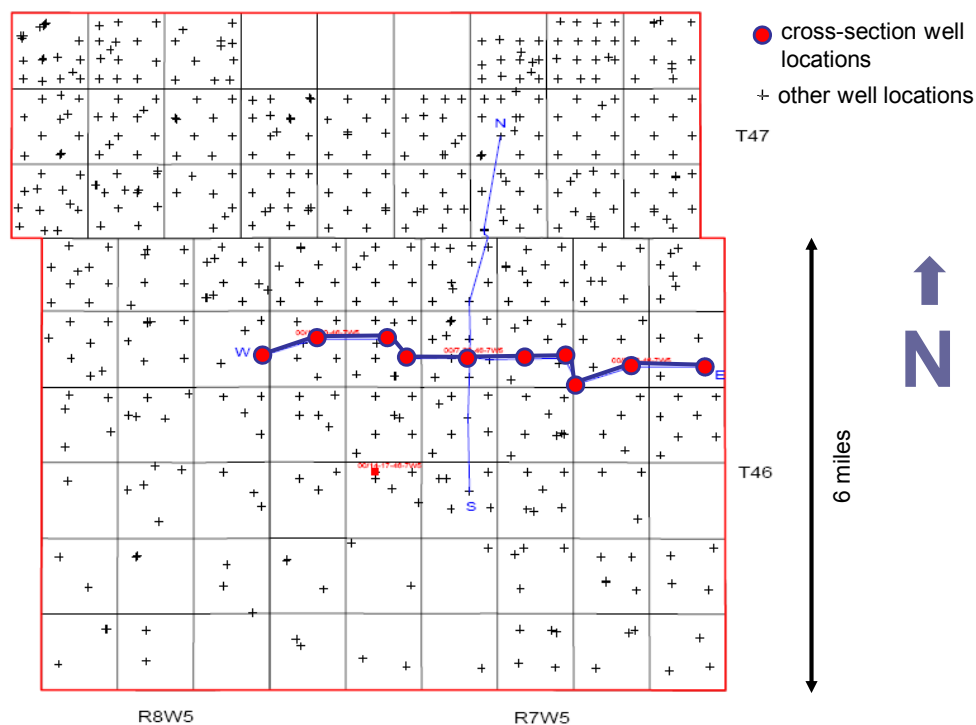


Figure 2-3: Map of cross section location (Alberta Geological Survey, 2004).

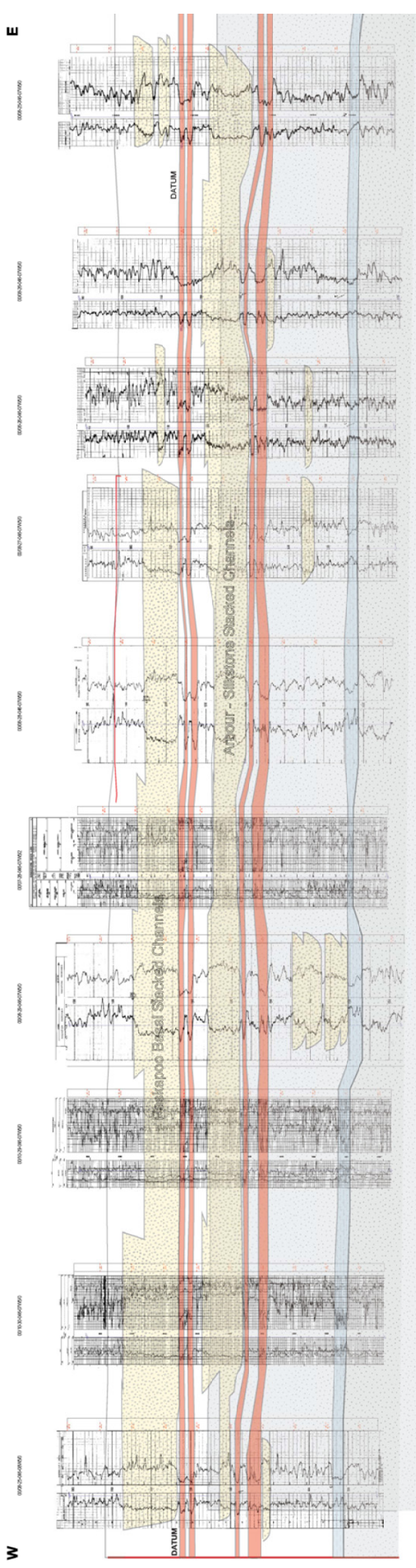


Figure 2-4: Regional east-west cross-section showing the sub-zones of the Ardley Coal Zone (dark orange) and the channel sandstones of the Scollard and Paskapoo Formations (dotted yellow) and the regional aquitard Battle Formation (light blue). The left log track is the gamma log and the right track is the density log (Alberta Geological Survey, 2004).

Figure 2-6 and Figure 2-7 show an ~1 km north-south and a ~1.8 km east-west log correlation cross-section that connects 102/7-28 and 100/7-28 to the closest wells to the east, west, north, and south of injector-producer pair that had interpretable petrophysical logs. The density log was used to classify the coal lithology (very low density) and the sandstone/shale delineation was based on the gamma log. Again, the lateral continuity of the coal sub-zones and the interbedded sandstones and shales is illustrated. The Upper Ardley Coal is encountered at a depth of approximately 350 – 365 m (all depths are measured in true vertical depth, TVD, below the Kelly Bushing, KB) and the Lower Ardley Coals are encountered at a depth of approximately 395 – 420 m. The east-west section shows the expected slight structural dip to the west, whereas the north-south section shows a subtle syncline structure.

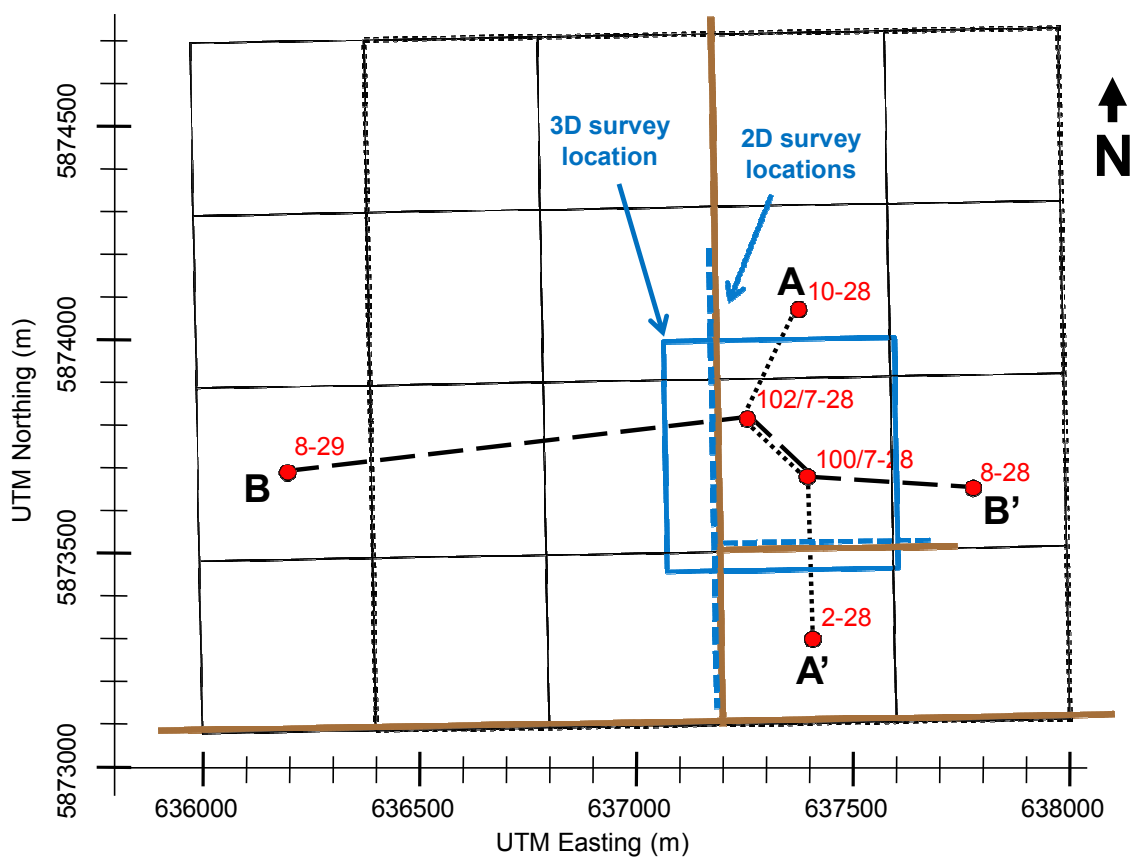


Figure 2-5: Map of cross section locations.

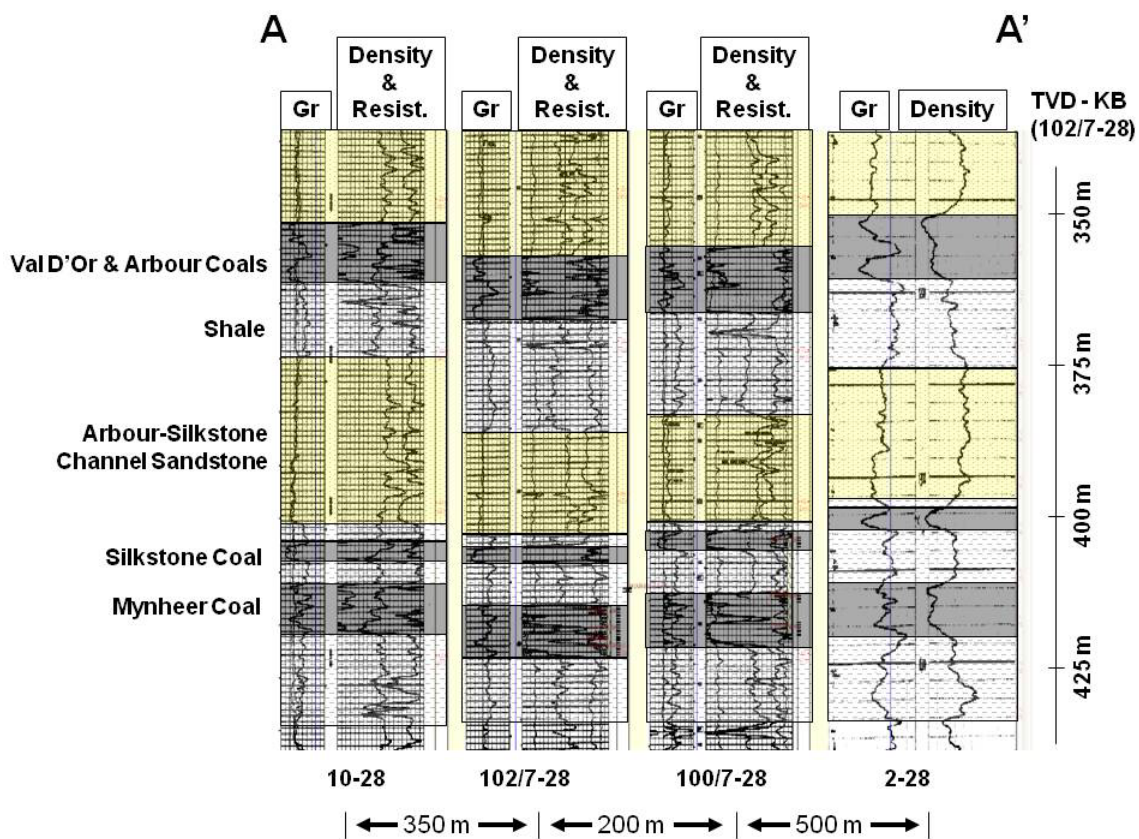


Figure 2-6: Local north-south cross section showing the sub-zones of the Ardley Coal Zone and the channel sandstones of the Scollard and Paskapoo formations. The datum is sea level (courtesy IHS Energy Accumap).

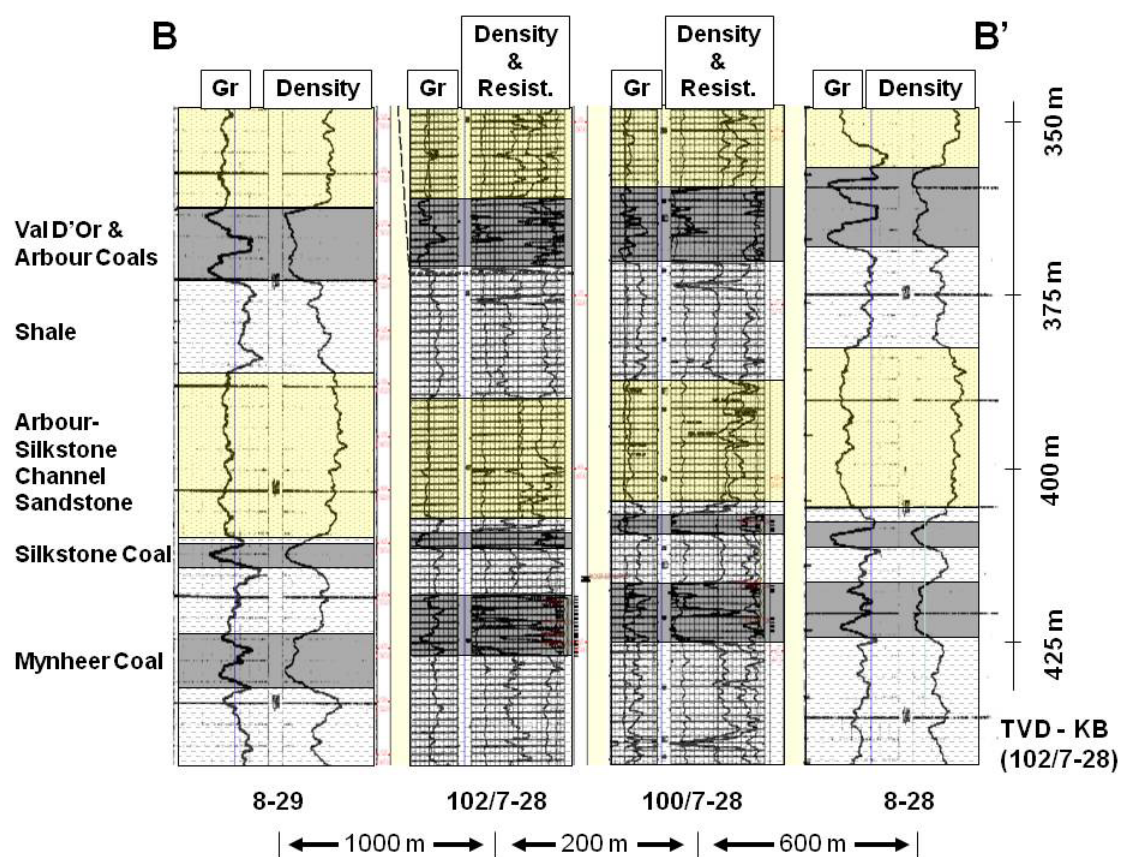


Figure 2-7: Local east-west cross section showing the sub-zones of the Ardley Coal Zone and the channel sandstones of the Scollard and Paskapoo Formations. The datum is sea level (courtesy IHS Energy Accumap).

The sections in Figure 2-6 and Figure 2-7 show a fairly uniform isopach of each of the coal sub-zones. However, the Arbour-Silkstone sandstone shows variability in thickness between 10 to 20 m, and the overlying shale varies between 10 to 15 m in thickness. The shale unit separating the Mynheer and the Silkstone coals also shows variability in thickness from 4 to 6 m.

2.2 Well Data

2.2.1 Injection Well Petrophysical Logs

A suite of wire-line petrophysical logs from well 102/7-28, over a depth range from 87.6 – 512.0 m KB, is illustrated in Figure 2-8. Ardley Coals were intersected between 350 – 425 m. The gamma and density log together can be used separate the stratigraphy into a number of lithologic units. These units, their depth below surface, and their arithmetic average elastic properties are listed in Table 2-1. Table 2-2 captures the average elastic properties of the coals, sandstones and shales from the 102/7-28 well logs. The densities and velocities of the coals are much lower than those of the siliciclastic rocks, and coal's V_p/V_s of 2.39 and Poisson's Ratio of 0.39 are higher than for either sandstone or shale.

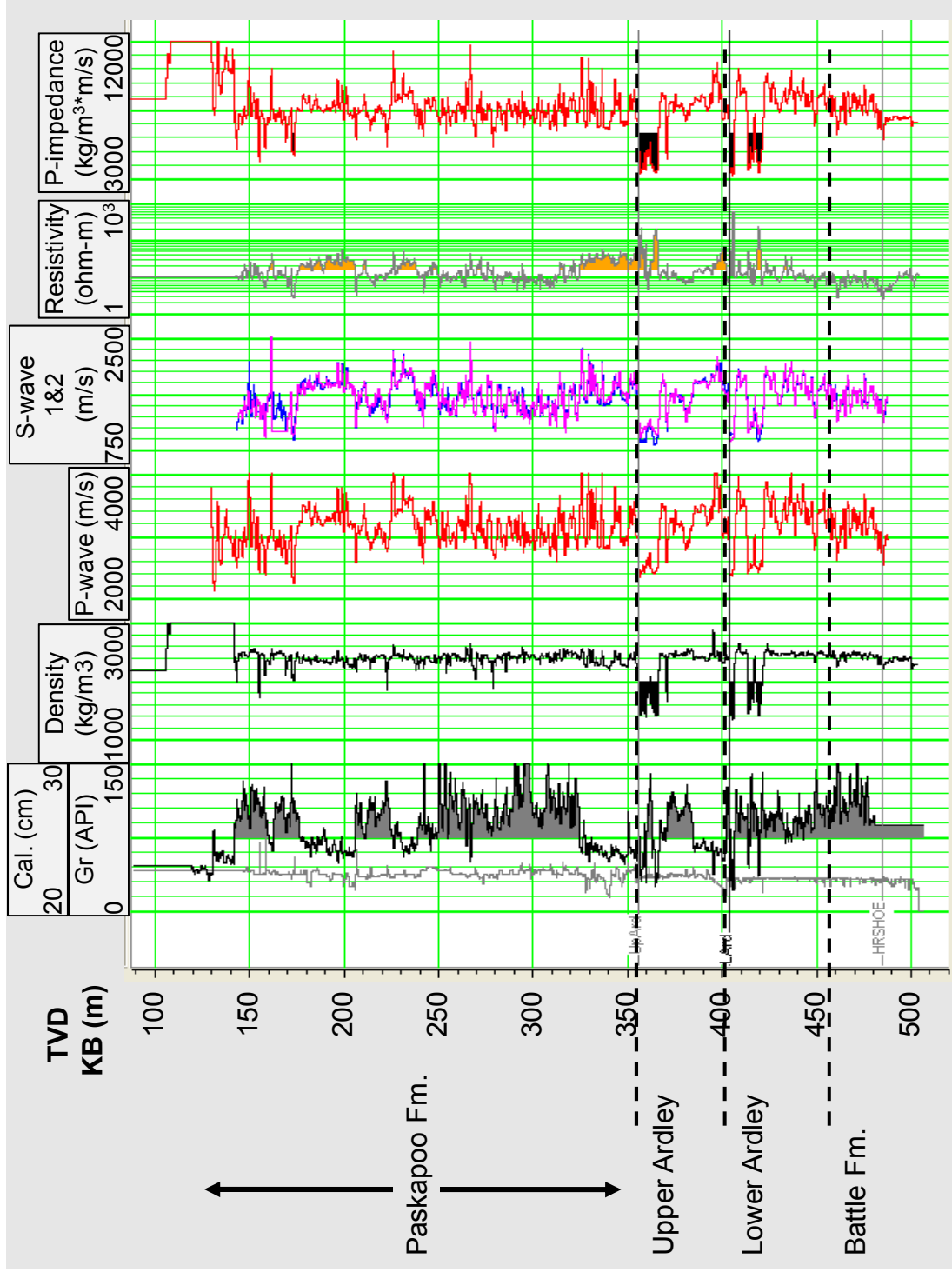


Figure 2-8: Full length petrophysical logs from 102/7-28.

Table 2-1: Table of average densities, velocities, and Vp/Vs ratio for major lithologic units of the 102/7-28 well.

Lithologic unit	Depth below surface (m)	Thickness (m)	Density (kg/m ³)	P-wave velocity (m/s)	S-wave velocity** (m/s)	Vp/Vs
Overburden	0.0	131.2	2205	1600*	800	2.00
Paskapoo shale	131.2	46.2	2391	2910	1376	2.11
Paskapoo sandstone	177.4	29.4	2340	3309	1780	1.86
Paskapoo shale	206.8	18.8	2360	3012	1471	2.05
Paskapoo sandstone	225.6	13.4	2414	3506	1872	1.87
Paskapoo shale	239.0	86.6	2394	3086	1500	2.06
Paskapoo sandstone	325.6	31.3	2350	3196	1682	1.90
<i>Val D'Or/Arbour coal</i>	<i>356.9</i>	<i>10.2</i>	<i>1609</i>	<i>2491</i>	<i>964</i>	<i>2.58</i>
Scollard shale	367.1	18.5	2427	3135	1523	2.06
Scollard sandstone	385.6	18.9	2407	3429	1837	1.87
<i>Silkstone coal</i>	<i>404.5</i>	<i>2.7</i>	<i>1619</i>	<i>2498</i>	<i>1104</i>	<i>2.26</i>
Scollard shale	407.2	7.2	2496	3451	1760	1.96
<i>Mynheer coal</i>	<i>414.4</i>	<i>8.0</i>	<i>1797</i>	<i>2567</i>	<i>1097</i>	<i>2.34</i>
Scollard shale	422.4		2419	3250	1632	1.99

* assumed to have a linear gradient of 6.92 m/s per m from surface to the top of the log measurements.

** based on one of the two shear sonic logs only.

Table 2-2: Average elastic properties for coals, sandstones and shales from the well logs of 102/7-28.

Lithology	Average density (kg/m ³)	Average P-wave velocity (m/s)	Acoustic impedance (kg/m ³ *m/s)	Average S-wave velocity (m/s)	Vp/Vs	Poisson's Ratio
coals	1675	2519	4.2E+06	1055	2.39	0.39
sandstone	2378	3360	8.0E+06	1793	1.88	0.30
shale	2415	3141	7.6E+06	1544	2.04	0.34

Figure 2-9 illustrates details of the petrophysical logs in the Ardley Coal Zone. It can be seen that within the coal zones the gamma log ranges from a low of 25 API to over 140 API and that lower gamma readings generally correspond to higher readings on the deep induction log. As noted in section 2.1.1, the Ardley Coal Zone contains stacked

sequences of pure coal, shaley coal, and coaly shale. The Alberta Geological Survey (2004) makes the distinction based the criteria listed in Table 2-3. As noted previously, these sub-lithotypes in the coal zones form sequences that are generally laterally consistent for the Silkstone, Arbour, and Val D'Or members, but are laterally more variable in the Mynheer coals. However, a 0.5 m shale (tonstein) bed, evident within the Mynheer coals, is continuous in the local wells as shown in Figure 2-6 and Figure 2-7. Also, only a thin shale bed separates the Arbour and Val D'Or coals which together form approximately 10 m of gross coal zone thickness; as discussed previously these are lumped together as the Upper Ardley Coal Zone.

Figure 2-9 also show the calliper log from 102/7-28 and little deterioration of the borehole condition through the coal zones is seen. For this reason, no editing of the log data was conducted.

The cross-dipole shear sonic log run in 102/7-28 is also illustrated in Figure 2-9. The tool measures the shear wave velocity in a vertically propagating direction but with two perpendicular polarization orientations. The two shear sonic responses in the coal zones diverge as seen in Figure 2-9 which indicates some azimuthal anisotropy in the coals. The two shear sonic logs show very similar response in the sandstone and shales, indicating that these lithologies are more azimuthally isotropic. Ramos and Davies (1995) and Al Duhailan (2008) also showed that coals exhibit azimuthal anisotropy that can be detected with analysis of the azimuthal variation of coal reflectivity.

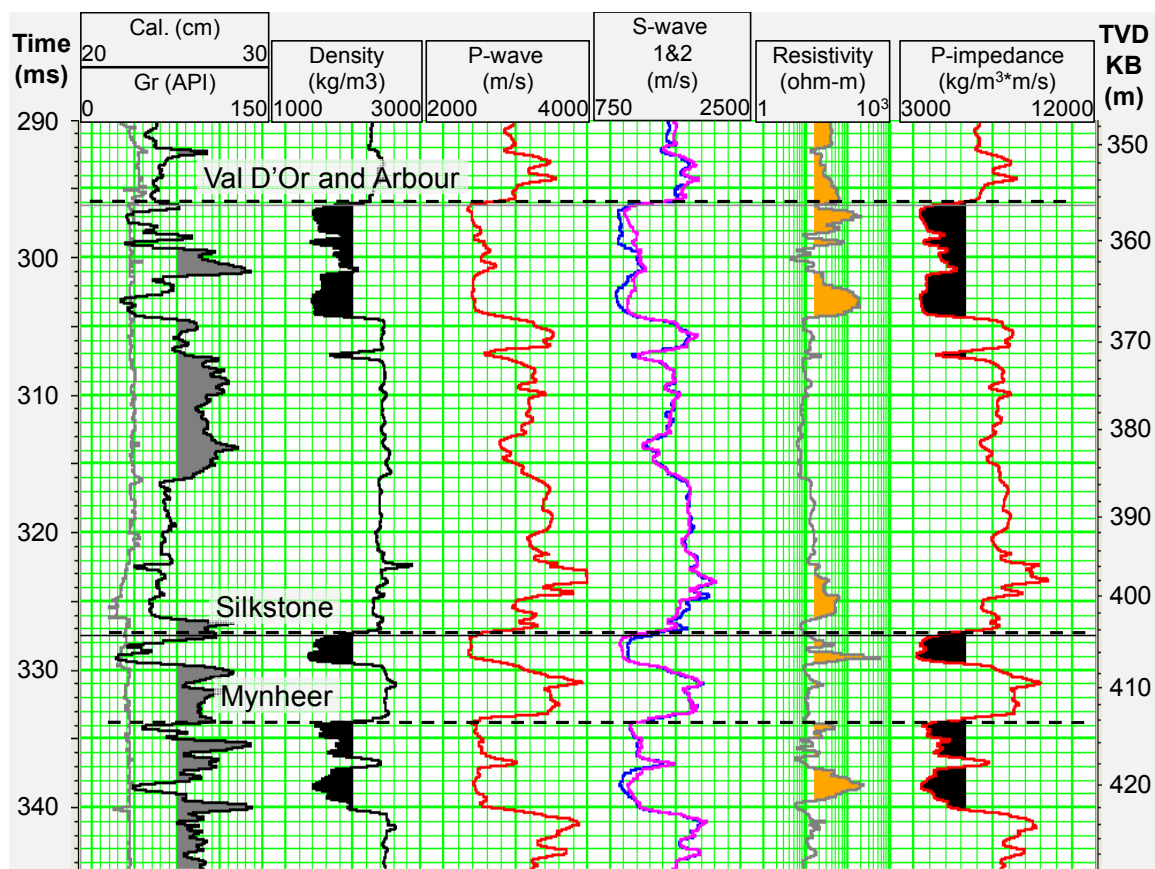


Figure 2-9: Petrophysical logs from 102/7-28 in the vicinity of the Ardley Coal Zone.

Table 2-3: The petrophysical log values that identify coal sub-lithologies (AGS, 2004)

Sub-lithology	Gamma ray (API)	Density (kg/m ³)	Conductivity (ohm-m)
Clean coal	< 30	< 1.7	0
Shaley coal	30 – 45	1.7 – 1.9	10
Coaly shale	55 – 60	1.9 – 2.1	> 10

2.3 The Physical Properties of Coals

2.3.1 An Introduction to Coal

Coal is composed principally of organic material organized into a matrix with porosity on multiple scales (Thomas, 2002). Fluids can exist in multiple states in the coal porosity with the main fluids being methane, water, carbon dioxide and nitrogen (Yee et al., 1993). In large pore spaces, gasses exist in a free state, while in small or tiny pore

spaces the same fluids are adsorbed to the walls of the pore space and exist in a non-free adsorbed state. An understanding of the physical properties of coals is required in order to estimate the possible fate of the fluids that were injected into the Ardley Coals at Alder Flats.

2.3.2 Characterizing Coals

Coal is derived mainly from organic material deposited during a period of protracted planty-material build-up in an anoxic environment such as a swamp or bog (Flores, 1993). When buried, such material turns into peat in the first stage of a diagenetic process called coalification (Taylor et al, 1998). With deeper burial, increased temperature and pressure cause further coalification as the rock progressively loses volatile constituents. Increasing stages of coalification are referred to as the coal's rank which are (in order): peat, lignite, subbituminous, high-, medium-, low- volatile bituminous coal, semi-anthracite and anthracite.

The constituents of coal are a mixture of organic and non-organic matter. One method of characterizing a coal sample is to quantify its components. In proximate analysis, a sample is dried, heated, and finally combusted in order to quantify the relative abundance of moisture, ash, volatiles, and fixed carbon in coals (Bustin, 2001). Characterization of the constituents of coal is important in order to quantify gas storage capacity. Both the ash and water content of coal affect its capacity to store gasses in the coal matrix since ash typically does not sorb gasses and water competes for adsorption sites with gasses and can block access to micro-pores.

Macroscopically, coals can be characterized by identifiable lamina called lithotypes that are mainly differentiated by the visual "brightness" of the beds. Mechanical properties vary with lithotype which can be used to predict cleating and permeability. For example, brighter lithotypes tend to have more cleating than duller lithotypes (Bustin, 2001).

Microscopically, coals are made up of recognizable units called macerals (analogous to mineral assemblages in non-organic rocks) that are defined by their visual appearance or method of genesis (Taylor et al., 1998). There are three main maceral

groups: vitrinite which comes from the cellulose and lignin of higher plants, liptinite which comes from lipid rich parts of plants such as spores and pollens, and inertinite which is fire charred plant matter. Macerals types have different chemical and physical properties such as microscopic porosity and adsorption capacity. For example, inertinite maceral group has been shown to be mainly meso- to macro-scale porosity (defined in section 2.3.3 below) while vitrinite is mainly micro- to meso-scale porosity (Harris and Yust, 1976). Gas adsorption capacity has also been shown to increase with increasing vitrinite content (Lamberson and Bustin, 1993). With increasing coal rank, the luminous reflectivity of vitrinite macerals increases; thus vitrinite reflectance is used to measure a coal's rank.

2.3.3 Porosity and Permeability

Porosity in coal exists at multiple scales. The International Union of Pure and Applied Chemistry (IUPAC) classifies porosity in coals as micro-pores (< 2 nm), meso-pores (2 – 50 nm), and macro-pores (> 50 nm). Micro-porosity is a controlling factor in gas storage capacity by adsorption and meso-porosity controls the transmissibility of gases between the micro- to macro-pores (Gamson et al., 1996). Macro-porosity is represented mainly by cleat or fracture porosity. In coal there are usually two sets of fractures called cleats that are perpendicular to bedding and to each other. The dominant fracture set, called face cleats, are long and continuous, whereas butt cleats truncate at the intersection with face cleats. Cleats can terminate vertically at lithotype boundaries or cross-cut lithotype boundaries.

Fluid flow in coals is believed to be described by a dual porosity model. In the macro-porosity or cleats, flow is described by Darcy's law while movement between the macro-porosity and the micro-porosity of the coal matrix is described by Fick's law of diffusion. CBM reservoir permeability comes from macro-porosity fractures, whereas gas storage comes from the matrix (Harpalani and Schraufnagel, 1990). Notably, because the cleat system is anisotropic, so is the permeability in coals (Li et al., 2004).

Because coals are relatively weak mechanically, an increase in effective stress (the difference between the confining stress and pore pressure) can have a significant effect

on cleat aperture and consequently, absolute permeability (Gentzis, 2006). Decreasing pore pressure, for example during CBM production, can have the effect of decreasing reservoir permeability. Studies show an exponential decrease in permeability with increasing effective stress (Bustin, 1997; Gentzis, 2006). A relationship between permeability (k), cleat spacing (a) and cleat aperture width (b) has been described (Bustin et al., 2008) which shows how sensitive permeability is on aperture width:

$$k = \frac{b^3}{12a} \quad 2.1$$

While reducing the pore pressure in the cleat system during CBM production causes an increase in effective stress and a consequent decrease in cleat permeability, decreasing the pore pressure has the effect of creating a pressure and gas concentration imbalance between the micro-porosity of the matrix and the macro-porosity of the cleat system. Gases will desorb from the matrix and through diffusion, enter the cleat system. The movement of mass out of the matrix causes the matrix to shrink and consequently the aperture of cleats to increase. Also, with the removal of formation water from the cleat system, the relative permeability of gas to water changes. The competing effects of matrix shrinkage, pore pressure changes, and absolute and relative permeability changes are complex and not yet fully understood (Bustin, 2001 and 2008).

2.3.4 Fluid Distribution in Coals and Gas Sorption

Fluids are stored in coals in the micro-, meso-, and macro-porosity. In the larger pore spaces, CH₄, CO₂, and N₂ exist in a free gaseous state (assuming modest pressures) and water exists in a liquid state which can dissolve the gaseous phases. These species are held in the small pores in the coal matrix by various sorption mechanisms (Yee et al., 1993). Sorption, defined to include surface adsorption, absorption, and capillary condensation, holds gasses in coals physically or chemically. In the case of methane, the main sorption mechanism in coals is believed be physical adsorption that holds the molecules to the pore space walls by van der Waals forces. Because the sorbed states are much denser than the gaseous state, the bulk of the CH₄, CO₂, and N₂ stored in coals is in the sorbed states.

The most commonly used model to describe gas sorption capacity is the Langmuir isotherm model which tracks the amount of a given molecular species that a coal sample can adsorb at constant temperature but varying pressures (Morad et al., 2008). The model shows a steep increase in adsorption with increasing pressure at low pressures and a flattened plateau adsorption trend with increasing pressure at higher pressures (for example see Figure 2-10). The plateau is assumed to coincide with the completion of a mono-layer of adsorbed gas on the pore walls (Gregg and Sing, 1982). The “Langmuir volume” is defined as the maximum amount of gas that can be adsorbed as the pressure goes to infinity and the “Langmuir pressure” is defined as the pressure at which the adsorbed gas volume is half of the maximum value. A higher Langmuir volume for a given coal samples coincides with a higher gas storage capacity. In general, higher rank coals have higher gas storage capacity.

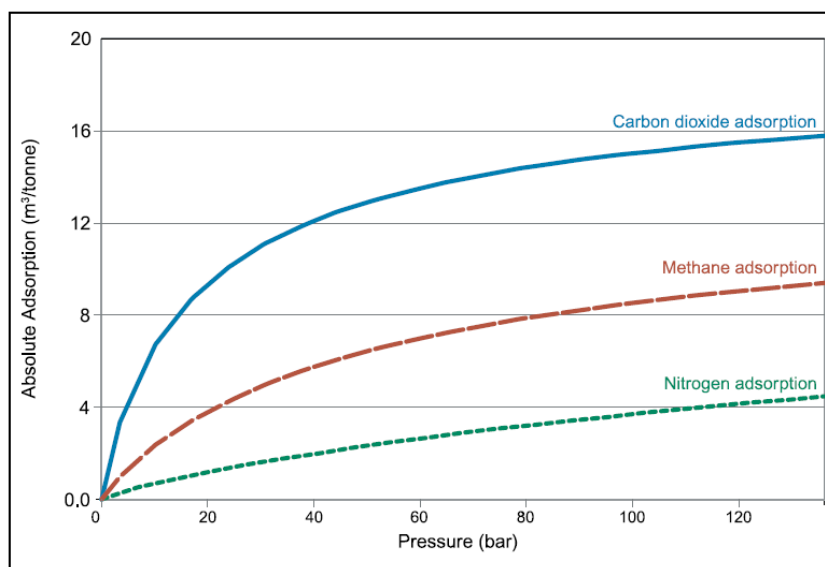


Figure 2-10: Single component isotherms for Tiffany Coals at 55°C (after Gasem et al., 2002).

The most common molecules that compete for adsorption sites in coal are methane, CO₂, nitrogen, and water (Bustin, 2001). The Langmuir volume for CO₂ has been shown to be 2 to 10 times that of methane in coals (Levy, 1997). The Langmuir volume for methane is in turn greater than that of nitrogen, as illustrated in the example in Figure

2-10. However, why one molecule has a higher sorption rate and Langmuir volume than another is not explained by the Langmuir isotherm model which assumes that all adsorption sites can be equally accessed by different molecular species (Gregg and Sing, 1982). In part, the greater sorption capacity for CO₂ is likely related to the more polar nature of CO₂ molecules compared to the other species (Levy et al., 1997). Also, N₂ and CH₄ have slightly larger kinetic diameters than CO₂ (Shimada et al., 2005) and so may be unable to access the smallest pores.

In addition to adsorption of CO₂, modern studies have shown that CO₂ may be absorbed by a coal's organic molecular structure. This absorption may account for the preferential sorption characteristics of CO₂ and also accounts for some of the effects on the mechanical/elastic properties of coal caused by exposure to CO₂ (discussed below).

2.4 Ardley Coal Reservoir Characterization

The coals of the Mynheer coal zone have been characterized and the data reported in the Alberta Research Council project summary (Mavor and Faltinson, 2008), summarized in Table 2-4.

Table 2-4: Characteristics of the Mynheer coal seam at Alder Flats (Mavor and Faltinson, 2008)

Rank	high volatile B bituminous
Maceral content	vitritinite 34-53%, inertinite 17-43%, liptinitite 3-5%.
Air dry ash content	Average about 35%
Fracture porosity	Maximum of 1%
Initial Silkstone coal pressure	1.60 MPa
Initial Silkstone coal temperature	16.4 °C
Initial Mynheer coal pressure	1.73 MPa
Initial Mynheer coal temperature	16.6 °C

The confining pressure is estimated by integrating the density log and assuming $g = 9.81 \text{ m/s}^2$. Integrating the density log from 130 m to 400 m, the overburden pressure

was calculated to be 6.24 MPa at 400 m depth. Assuming an average density of 2300 kg/m³ from surface to 130 m, the total overburden pressure at 400 m depth would be approximately 9.17 MPa.

Regionally the Scollard Formation is typified as under pressured and contains waters with low salinity (Michael and Bachu, 2001). Figure 2-11 shows the total dissolved solids trend with depth for the Tertiary to Upper Cretaceous strata in the Pembina Field area and shows that at a depth of 400 m the estimated total dissolved solids is approximately 1500 mg/L (Pana, 2007) which corresponds to approximately 450 ppm. The Alberta Research Council report (Mavor and Faltinson, 2008) lists the total dissolved solids in the formation water as 1931 ppm.

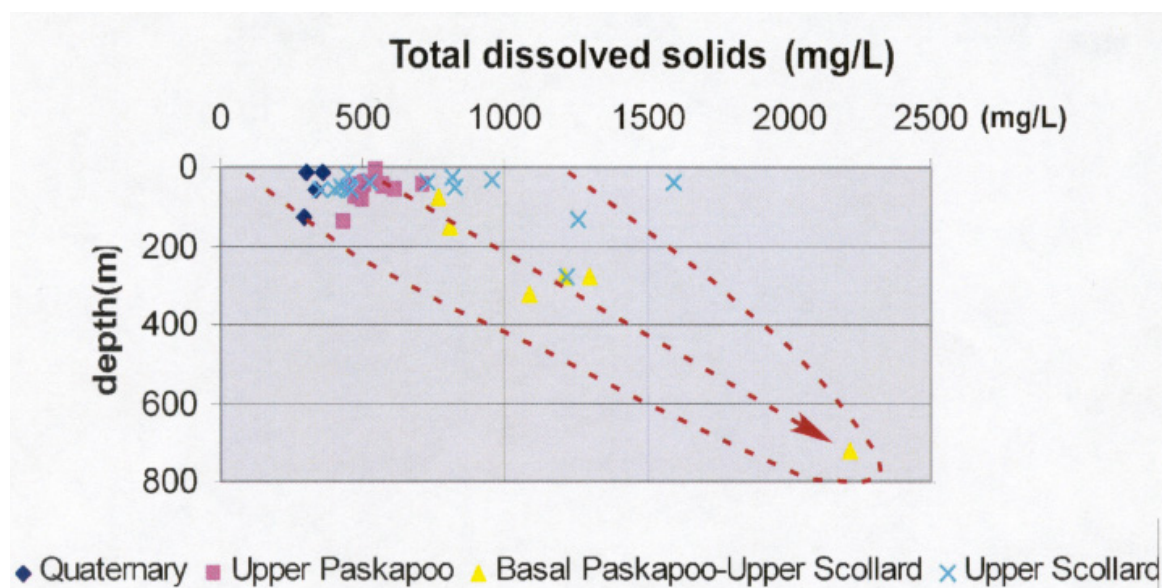


Figure 2-11: Total dissolved solids versus depth for the Tertiary-Upper Cretaceous strata in the Pembina Field area (Pana, 2007).

2.5 Rock Physics of Injecting CO₂ into Coal

2.5.1 Physical Properties of CO₂ at Reservoir Conditions

Depending on the pressure and temperature, CO₂ can exist as a gas, liquid, solid, or super critical fluid. Figure 2-12 illustrates the phases of CO₂ as a function of temperature

and pressure. At the reservoir conditions of the Mynheer coal zone, CO₂ would be gaseous.

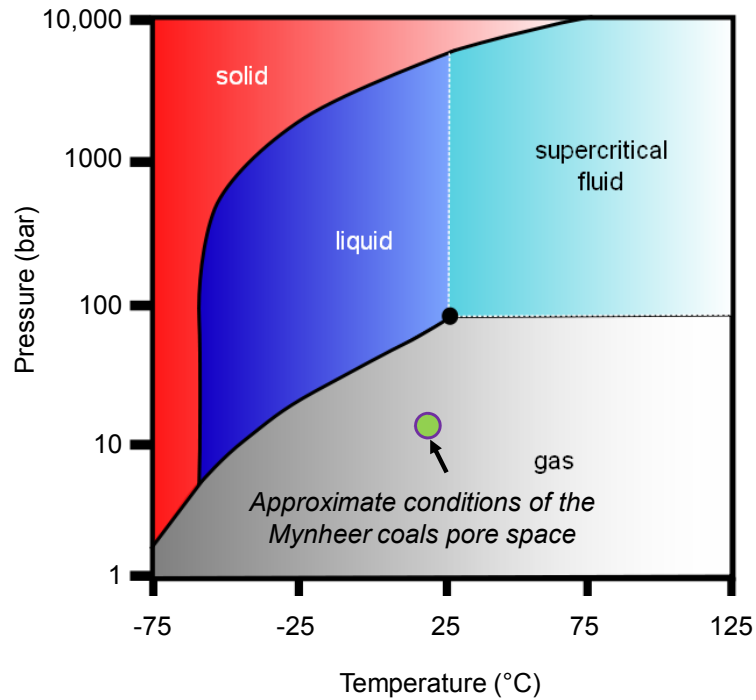


Figure 2-12: CO₂ Phase Diagram

2.5.2 Gassmann Fluid Substitution Modelling

For an isotropic, homogenous medium, the P-wave and S-wave velocities are given by:

$$v_p = \sqrt{\frac{K + (4/3)\mu}{\rho}} \quad 2.2$$

$$v_s = \sqrt{\frac{\mu}{\rho}} \quad 2.3$$

where K is the bulk modulus, μ is the shear modulus, and ρ is the density. In a rock with a porosity of ϕ that is filled with a fluid, the density of the saturated rock can be calculated:

$$\rho = \phi\rho_f + (1 - \phi)\rho_{fr} \quad 2.4$$

where ρ_f is the fluid density and ρ_{fr} is the density of the rock frame.

With some assumptions, the bulk modulus of the fluid saturated rock can be modelled with the common Gassmann method (Wang, 2001). The method is captured by the following equation:

$$\frac{K_{sat}}{K_0 - K_{sat}} = \frac{K_{fr}}{K_0 - K_{fr}} + \frac{K_f}{\phi(K_0 - K_f)} \quad 2.5$$

where K_{sat} is the bulk modulus of the fluid saturated rock, K_{fr} is the bulk modulus of the dry rock frame, K_0 is the bulk modulus of the rock mineral, and K_f is the bulk modulus of the fluid. The bulk modulus of a fluid saturated rock can be calculated when the fluid is replaced by another fluid. It is assumed that since fluids do not support a shear stress that the shear modulus of a rock is unchanged with a change of saturating fluid; giving:

$$\mu_{sat} = \mu_{dry} \quad 2.6$$

where μ_{sat} and μ_{dry} are the shear moduli of the fluid saturated and dry rock, respectively. Using equations 2.5 to 2.9, the change in density, velocities, and impedances can be calculated when substituting one fluid with another in a porous rock.

While the Gassmann fluid substitution model has successfully predicted the bulk modulus of some porous rocks, several assumptions are important (Wang, 2001):

1. The rock is macroscopically homogeneous,
2. All pores are interconnected and communicating,
3. The pores are filled with a frictionless fluid, and
4. The fluids that are exchanged do not interact with the matrix in any way that would soften or harden the frame.

Replacement of water in the cleat system of coals with gaseous CO₂ may be accurately modeled by the Gassmann fluid substitution method. However, with the replacement of water by CO₂ in the cleats, CO₂ will diffuse into the micro pores of the coal matrix. Having a stronger affinity for CO₂ than methane, the coal will sorb the CO₂

and desorb methane. With fluid replacement on this level there are expected to be a number of effects that will contravene the fourth assumption above. This may render the Gassmann model inadequate for predicting the effect on the elastic properties of coals when CO₂ is introduced to a coal system.

2.5.3 The Effect of CO₂ on the Elastic Properties of Coals

In addition to the effects of fluid substitution discussed in section 2.5.2, when CO₂ is introduced into a coal there are expected to be a number of reactions that will affect the elastic properties of coals as a result of the sorption characteristics of coals.

A dominant effect of a CO₂ flood is the swelling of coals that has been well documented (Skawinski, 1999). As a gas is de-sorbed from coals, the coal matrix shrinks in volume, and as a gas is sorbed by coals, the matrix swells (Bustin, 2001). Some authors relate this change in volume to the surface energy of the pore walls with different adsorbants. Pan and Connell (2007) suggest that different molecular species have different specific surface energies when they adsorb to the coal micro-porosity wall and the size of the pore dilates/contracts in order to change its surface area in response to adsorbant replacement. The competing effects of matrix shrinking and swelling make the enhancement of methane production by competitive CO₂ sorption challenging, since coals, having a greater affinity to sorb CO₂ than methane, exhibit a net swelling with CO₂-ECBM production. With swelling, cleat aperture may be reduced and fracture permeability may be diminished. On the other hand, as noted in section 2.3.3, the permeability of coals can be positively correlated with pore pressure, and the increased pressure that results from the injection of CO₂ may increase permeability (Bustin, 2008). Evidence from pilot projects suggests that the net effect is coal swelling and a reduction in permeability (Benedictus et al., 2008). What effect this swelling and reduction of fracture aperture have on the elastic properties of coals has not been documented in the literature. Furthermore, any attempt to model the effective media of the coal-cleat system must include other known and suspect effects as discussed below.

In addition to matrix swelling due to the inclusion of mass via adsorption into the micro-porosity of the coal, there is evidence that CO₂ dissolves into the molecules of the

coal matrix causing a structural change in the coal and resulting in additional swelling. Larson (2004) claims that the modification of the physical structure of the coal is associated with a relaxation and rearrangement of the macromolecular structure of the coal. The structure is initially in a strained, cross-linked arrangement which is not its lowest energy state. As evidence he points to an experimental study by Hsieh and Duba (1987) that showed that coals swell mostly in a direction perpendicular to bedding upon first exposure to CO₂, but swell isotropically upon a second exposure to CO₂ if the gas is desorbed between exposures. The initial anisotropic swelling is taken as evidence that the molecular structure of the coals is in a different state perpendicular to bedding as a result of the conditions under which coalification occurred (Karacan, 2007). However, after initial relaxation in an unstressed laboratory state, the molecular structure is isotropic and subsequent relaxation and swelling is isotropic. Swelling has been shown to result in linear strain of up to 1-2 % when measured under confining pressure (Day et al., 2007). Larson (2004) also notes that after initial sorption of CO₂ by coal and consequent swelling, some of the CO₂ is then desorbed from the re-structured coal. It has been reported that vitrinite swells the most, while inertinite does not swell, but in fact may be compressed in response to swelling of other coal macerals (Karacan, 2007).

Under some pressure and temperature conditions CO₂ acts as an organic solvent in coal and can have the effect of lowering the temperature at which coals change from a glassy material with brittle properties to a rubbery material (Karacan, 2007; Larson 2004). The latter paper references work by Kahn and Jenkins (1985) that shows that the softening temperature of coal drops dramatically from over 673 K to less than 373 K as gas pressure is elevated from 3 MPa to over 5 MPa.

Additionally, Viete and Ranjith (2006) showed laboratory results where the mechanical strength and elastic modulus of coal samples was reduced after exposure to CO₂ at pressures of 2.0 MPa. They attributed the change in the mechanical strength of coal to replacement of the molecular species adsorbant in the micro-porosity and a consequent change in the surface energy of the pore walls. Their laboratory results showed a 26 % decrease in the static elastic modulus of CO₂-saturated coals under uni-axial stress when compared to air-saturated coals; however, under tri-axial stress with

internal gas pressures of 2.0 MPa and confining pressure of 10 MPa, analogous coal samples showed no decrease in mechanical strength. They were not able to offer an explanation for the lack of coal weakening under tri-axial stress conditions but in a subsequent paper (Viète and Ranjith, 2007) suggest that there is no reason to believe that coal weakening under *in situ* conditions is not a reality when coals are exposed to CO₂; although mechanical failure may not be of primary concern.

Other evidence is conflicting. Day et al. (2007) demonstrated an experiment where coal did not plasticize during CO₂ adsorption at temperatures and pressures where the CO₂ was supercritical. Meanwhile, Shimada et al. (2005) claim that the hypothesis that CO₂ dissolves into the coal matrix remains unverified. Furthermore, models to describe the surface energy of adsorbant species in coal micro-porosity remain theoretical (Pan and Connell, 2007). It is evident that investigation into the dissolution of CO₂ into the macro-molecular structure of coal, changes in pore surface energy and the net effects on the elastic properties (both static and dynamic) of coal warrants further experimental and theoretical research.

2.5.4 Dissolution of CO₂ in the Formation Water

It is likely that some of the CO₂ injected into the coals would dissolve into the formation water that is presumed to initially saturate the cleats of the coals. Quantifying the amount of dissolution that would have occurred is challenging. While solubility of CO₂ in aqueous solutions can be modeled, dissolution rates are difficult to calculate since they depend upon surface contact areas, diffusion rates, and convection rates which are not trivially estimated or modelled. The quantity of CO₂ that would have dissolved into the formation water in the coal is not estimated here.

2.6 Conclusions

At the Alder Flats site, the Arley Coal Zone can be divided into several sub-zones. The Upper Ardley Coal Zone has two sub-zones but at Alder Flats is essentially a single zone with ~10 m in gross thickness. The Lower Ardley Coal Zone can be sub-divided into two smaller zones: the Mynheer Coal Zone and the Silkstone Coal Zone. The

Mynheer Coals are the deepest sub-zone representing ~8 m in gross thickness while the shallower Silkstone Coals are ~3 m in gross thickness. Based on the petrophysical logs, the coals show very low density and low wave velocity, and have an average acoustic impedance of $4.2 \times 10^6 \text{ kg/m}^3 \cdot \text{m/s}$ and a mean V_p/V_s of 2.39.

While the physical properties of coals have been studied and documented in the literature, the effect that injected CO_2 will have on the properties of coals is not well understood or documented. Coals, which have enormous micro-porosity surface area for adsorption of gasses, have been shown to swell in volume with the competitive adsorption of CO_2 in place of methane. This swelling is known to potentially decrease absolute permeability in the fractured cleat system. Additionally, there is evidence from laboratory studies that the matrix of coal weakens with CO_2 adsorption and/or absorption. However, the net effect in terms of the elastic properties of the rocks on a formation scale is not fully understood.

Chapter Three: 2D Seismic Surveys

3.1 Introduction

2D seismic surveys were acquired at Alder Flats in June 2006 and March 2007. The surveys were conducted to test acquisition parameters, reflection character from the Ardley Coals, seasonal variations in data quality, and data processing flows. This chapter discusses the investigation of these aspects of the two surveys. The June 2006 data were processed by the CREWES project team, whereas the March 2007 data were processed by the author, as discussed in this chapter in detail.

3.2 Survey Design: Offset and Bandwidth Requirements

Prior to the field work, seismic modeling was conducted to gauge the arrival time of reflections from the Ardley Coals, to gauge the angle of incidence for reflections from the coals as a function of source-to-receiver offset, and to understand the resolution that could be expected from surface seismic data. Initially, the petrophysical logs from 102/7-28 were used to generate offset synthetic seismograms. Figure 3-1 shows a normal moveout corrected convolutional synthetic seismogram generated using a 5-10-60-70 Hz Ormsby wavelet. The Ardley Coal reflection events occur between approximately 260 – 310 ms two-way-time (TWT) in the model. Figure 3-1 also illustrates the angles of incidence for reflections from the coals that would be recorded by receivers at various offsets. At an offset of 600 m the angle of incidence at the top of the Upper Ardley Coals is approximately 40 degrees and at the base of the Lower Ardley Coals is approximately 37 degrees.

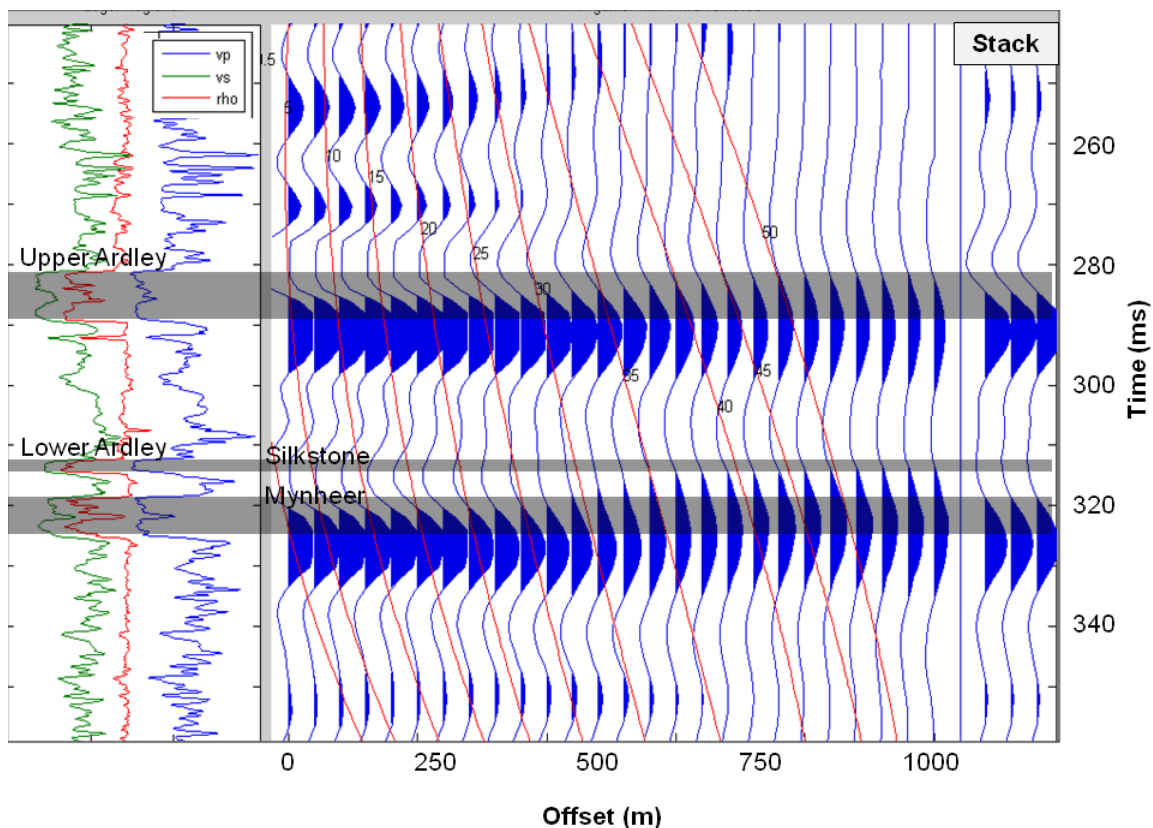


Figure 3-1: PP synthetic seismogram using a 5-10-60-70 Hz Ormsby zero-phase wavelet.

Figure 3-1 shows the resolution provided by a 5-10-60-70 Hz Ormsby wavelet that has the approximate bandwidth expected from a surface seismic survey. The wavelet itself, shown in Figure 3-2, has a dominant period of about 24 ms. This bandwidth resolves the top and bottom of the Upper Ardley Coal Zone as a distinct trough-peak pair, however, neither the Mynheer and Silkstone coal zones nor the Lower Ardley Coal Zone as a whole can be resolved as distinct seismic events.

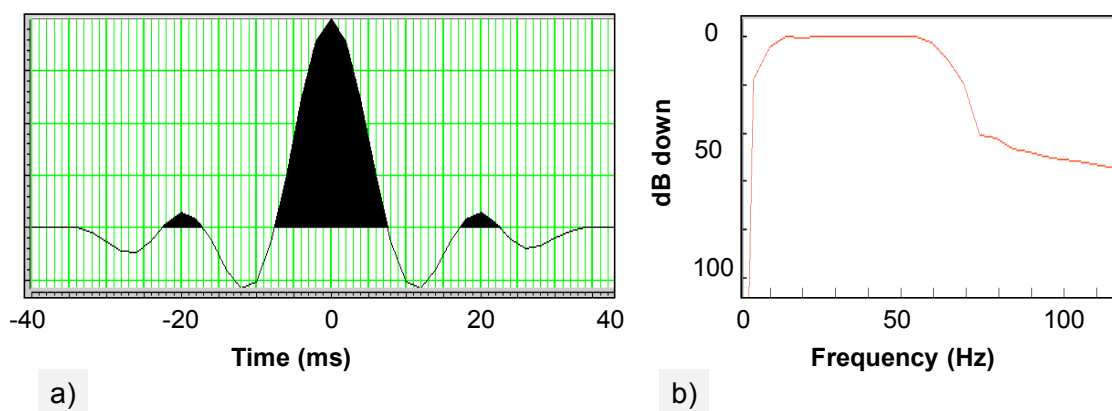


Figure 3-2: (a) A 5-10-60-70 Hz Ormsby zero-phase wavelet and (b) its amplitude spectrum.

Widess (1973) showed that when the time thickness of a bed is equal to $\frac{1}{4}$ of a wavelet's dominant wavelength (λ), the bed will be “tuned”; reflections from the top and bottom of a bed will achieve maximum constructive interference resulting in a high amplitude event that will tie in time to the top and bottom of the bed.¹ When the bed thickness is less than $\frac{1}{8}$ th of the wavelet's dominant wavelength then the interference between the two reflections will diminish the net amplitude of each of the reflections and the time separation of the maximum peak/trough will no longer tie to the top/bottom of the bed, but will have a time separation approximately equal to that of a bed with thickness equal to $\frac{1}{8}$ th of the wavelet's dominant wavelength. Widess (1973) defined $\lambda/8$ as the limit of resolution. If the dominant period ($T = \text{dominant wavelength}/\text{wave velocity}$) of a wavelet is known then the tuning thickness $T/4$ (in time) and the limit of resolution $T/8$ can be found.

Table 3-1 lists the time thickness of each of the beds of the Ardley Coal Zone and compares them to $T/4$ for wavelets with different dominant periods. The table shows when the beds are equal to or less than the tuning thickness for each wavelet. Similarly, Table 3-2 compares the time thicknesses of the beds to the limit of resolution ($T/8$) for different wavelets. The data shows that all of the Ardley Coal Zone beds would be equal to or thinner than the tuning thickness ($T/4$) if the wavelet's dominant period is 25 ms or

¹ Widess (1973) assumes a wavelet that is a single frequency and ignores multiples and transmission losses.

longer. For the Silkstone coal zone and the shale bed between the Mynheer and Silkstone coal zones $T/8$ will be greater than the bed thickness for wavelets with dominant periods of 20 ms or longer. This helps to explain the phenomena seen in Figure 3-1 where no distinct events are resolved for the zones of the Lower Ardley Coals. The data in Table 3-1 shows that even a wavelet with a dominant period of 10 ms will be tuned by some of the Ardley Coal Zone reflections.

Table 3-1: A comparison of Ardley Coal Zone bed time-thicknesses and the tuning thickness ($T/4$) of wavelets with different periods. Light grey cells indicate that the bed is below the tuning thickness and dark grey indicates the bed is within 1ms of the tuning thickness for the wavelet.

Lithologic unit	Thickness (m)	Mean P-vel. (m/s)	Time Thickness (ms)	Wavelet dominant period (ms)						
				10	15	20	25	30	35	
				<i>Grey if the bed is below the tuning thickness</i>						
Val D'Or/Arbour coal	10.2	2491	4.09							
Scollard shale	18.5	3135	5.90							
Scollard sandstone	18.9	3429	5.51							
Silkstone coal	2.7	2498	1.08							
Scollard shale	7.2	3451	2.09							
Mynheer coal	8.0	2567	3.12							

Table 3-2: A comparison of Ardley Coal Zone bed time-thicknesses and the limit of resolution thickness ($T/8$) of wavelets with different periods. Light grey cells indicate that the bed is below the limit of resolution.

Lithologic unit	Thickness (m)	Mean P-vel. (m/s)	Time Thickness (ms)	Wavelet dominant period (ms)						
				10	15	20	25	30	35	
				<i>Grey if the bed is below the limit of resolution</i>						
Val D'Or/Arbour coal	10.2	2491	4.09							
Scollard shale	18.5	3135	5.90							
Scollard sandstone	18.9	3429	5.51							
Silkstone coal	2.7	2498	1.08							
Scollard shale	7.2	3451	2.09							
Mynheer coal	8.0	2567	3.12							

In his paper, Widess (1973) discusses the tuning of a single thin bed that is isolated from other reflectors. In the Ardley Coal Zone there are a series of closely spaced thin beds, many of which are expected to be close to or below the tuning thickness and even possibly beyond the resolution limit. The net effect of the reflections from each of these beds can only be predicted by constructing synthetic seismograms to model the full tuning response.

3.3 Stratigraphic Seismic Modelling

Synthetic seismic modelling was undertaken to understand how variability in the stratigraphy and rock properties might manifest itself in the seismic trace waveform. Figure 3-3 illustrates three separate geological models and the related zero-offset synthetic seismograms. The geological models are shown as synthetic sonic logs where each model varies one aspect of the Ardley Coal Zone:

- a) varies the P-wave velocity of the Mynheer coals from 90 to 110 % of their actual logged values.
- b) varies the thickness of the shale package between the Mynheer and Silkstone coals from 3.5 to 8.5 m. The actual thickness is 7.2 m in the 102/7-28 well.
- c) varies the thickness of the clastic package between the Lower and Upper Ardley Coal seam from 30 to 40 m. The actual thickness is 37.4 m in the 102/7-28 well.

Inspection of the synthetic seismograms shows that it would be difficult to interpret the variability of each model uniquely. While each model shows subtle variability in the trace amplitude and the time from peak-to-peak of the Ardley Coal events, the effects on the waveform are similar. Lack of resolution and tuning effects make interpretation of amplitudes and time structure between seismic events difficult to interpret uniquely.

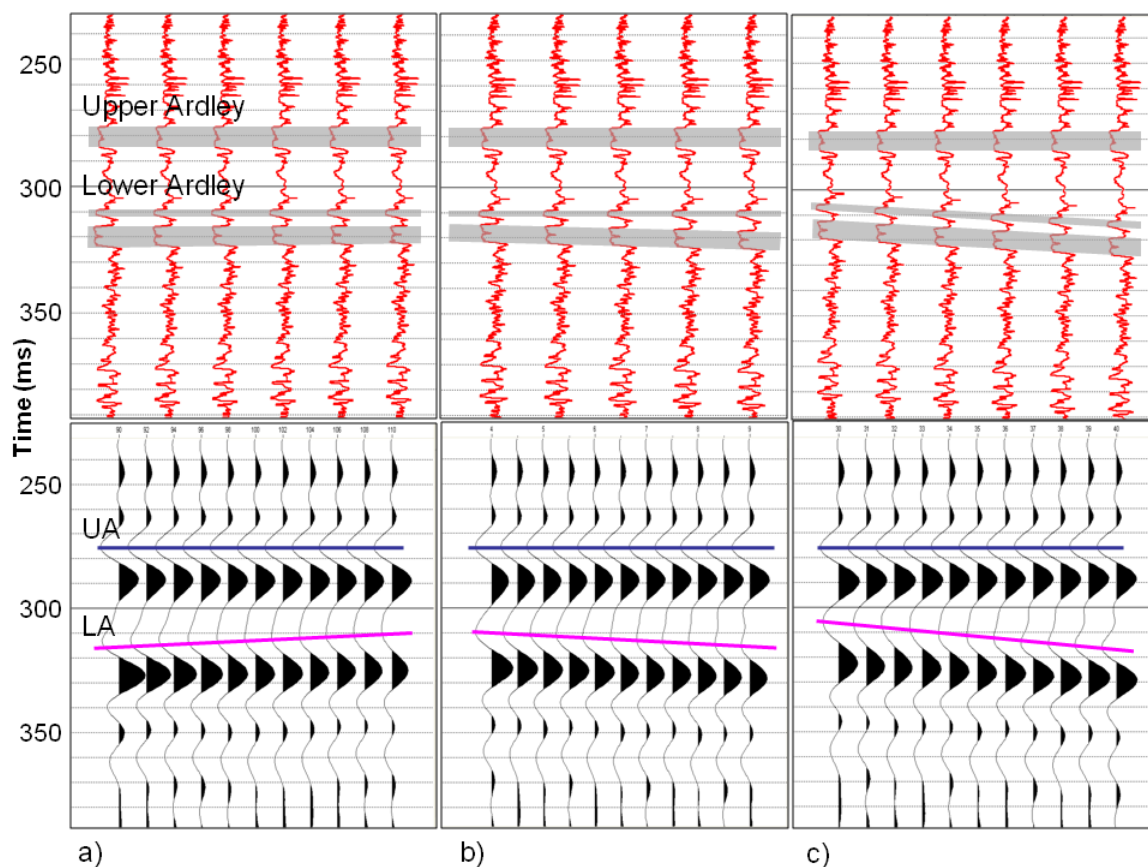


Figure 3-3: Three synthetic geological models and the related synthetic seismograms. All models use a 5-10-50-60 Hz Ormsby wavelet. (a) show varying P-wave velocity in the Mynheer coals. (b) shows varying the thickness of the thin shale in the Lower Ardley Coal Zone. (c) shows varying the thickness of the shale between the Upper and Lower Ardley Coal Zone.

3.4 June 2006 2D Survey

3.4.1 Acquisition

The first seismic survey conducted at the Alder Flats site was acquired on June 10-11, 2006. The survey tested the useful offsets and the recoverable bandwidth that would image the Ardley Coals in a field study with summer conditions. Table 3-3 lists the acquisition parameters for the survey and Figure 3-4 shows the layout for a 995 m north-south 2D line and a 470 m east-west 2D line each acquired along the local roads. The source interval was 10 m on the north-south line whereas the source interval was 30 m on the east-west line.

Table 3-3: The acquisition parameters for the June 2006 2D survey

Source	EnviroVibe 10-200 Hz – 4 sweep diversity stack
Source interval	10 m for N-S line, 30 m for E-W line
Receivers	1C IO SM-24 Marsh phone (10 Hz dominant)
Receiver interval	5 m for N-S and E-W lines
Sweep length	8 sec
Listen time	9 sec
Maximum offset	995 m NS line, 465 m EW line
Field sample rate	1000 Hz
Ground conditions	Very wet, summer

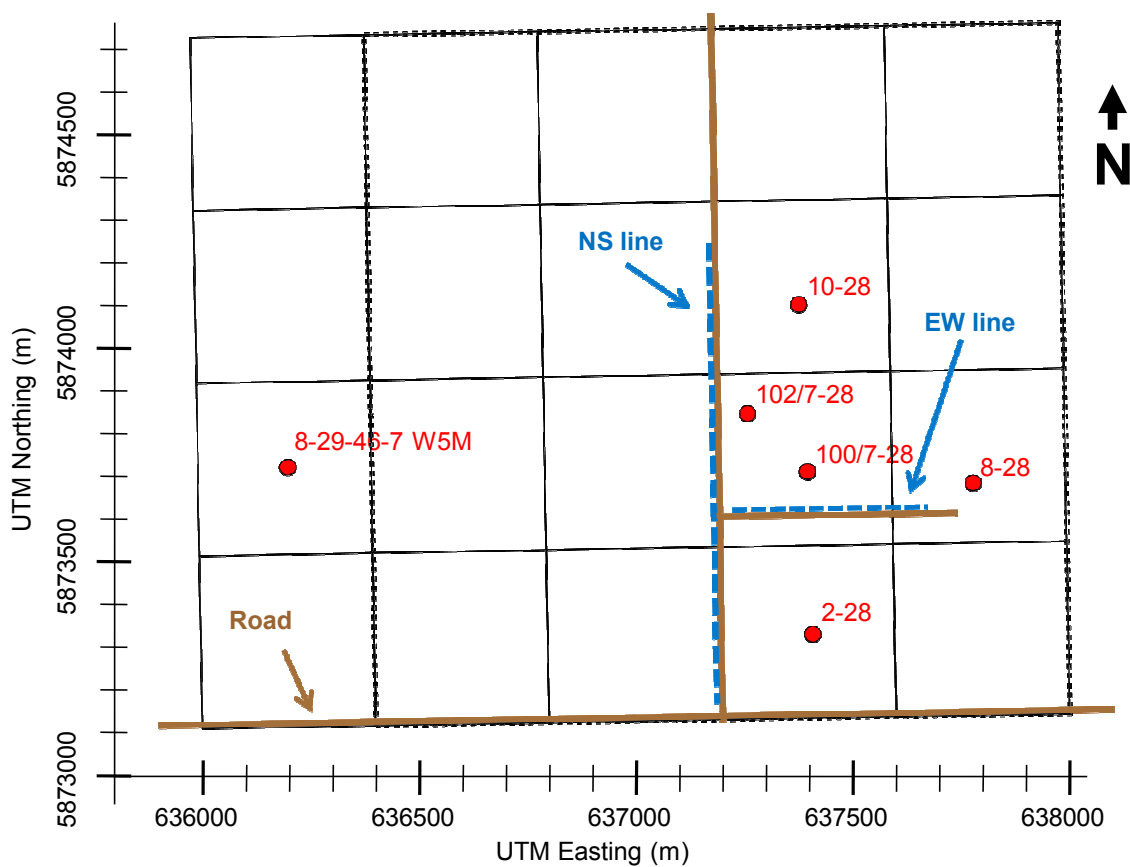


Figure 3-4: Field layout for the June 2006 survey

3.4.2 Data Processing

An example of the raw data with a 300 ms automatic gain control (AGC) is illustrated in Figure 3-5. The figure shows a gather of all data recorded by a single receiver (i.e. traces collected from multiple source records). The reflections from the Ardley Coals occur at approximately 300-350 ms two-way time (TWT). The figure also shows that ground roll and air blast contaminates the Ardley Coal reflections at offsets less than 60 m while reverberations of refracted energy contaminates the Ardley Coal reflections at offsets greater than 400 – 500 m. The amplitude spectrum in the 180 ms window depicted as boxes in Figure 3-5 is illustrated in Figure 3-6. It shows a peak frequency at approximately 25 Hz and is approximately 15 dB down at 50 Hz.

In order to exclude the noise in the near offset data, traces with an offset of less than 60 m were excluded from the stack which resulted in an acceptable migrated section (McCrank et al., 2006). The migrated sections for the two lines are illustrated in Figure 3-7 and Figure 3-8. The processing flow used for this data set is listed in Table 3-4. The common midpoint bin spacing for the June 2006 survey was 2.5 m.

Table 3-4: The standard processing flow used by CREWES for the June 2006 survey.

Standard flow
Set up geometry
Trace edit
True amplitude recovery
Surface consistent amplitude recovery
Time varying spectral whitening
Elevation and refraction statics corrections
Velocity analysis
Residual surface consistent statics
NMO correction

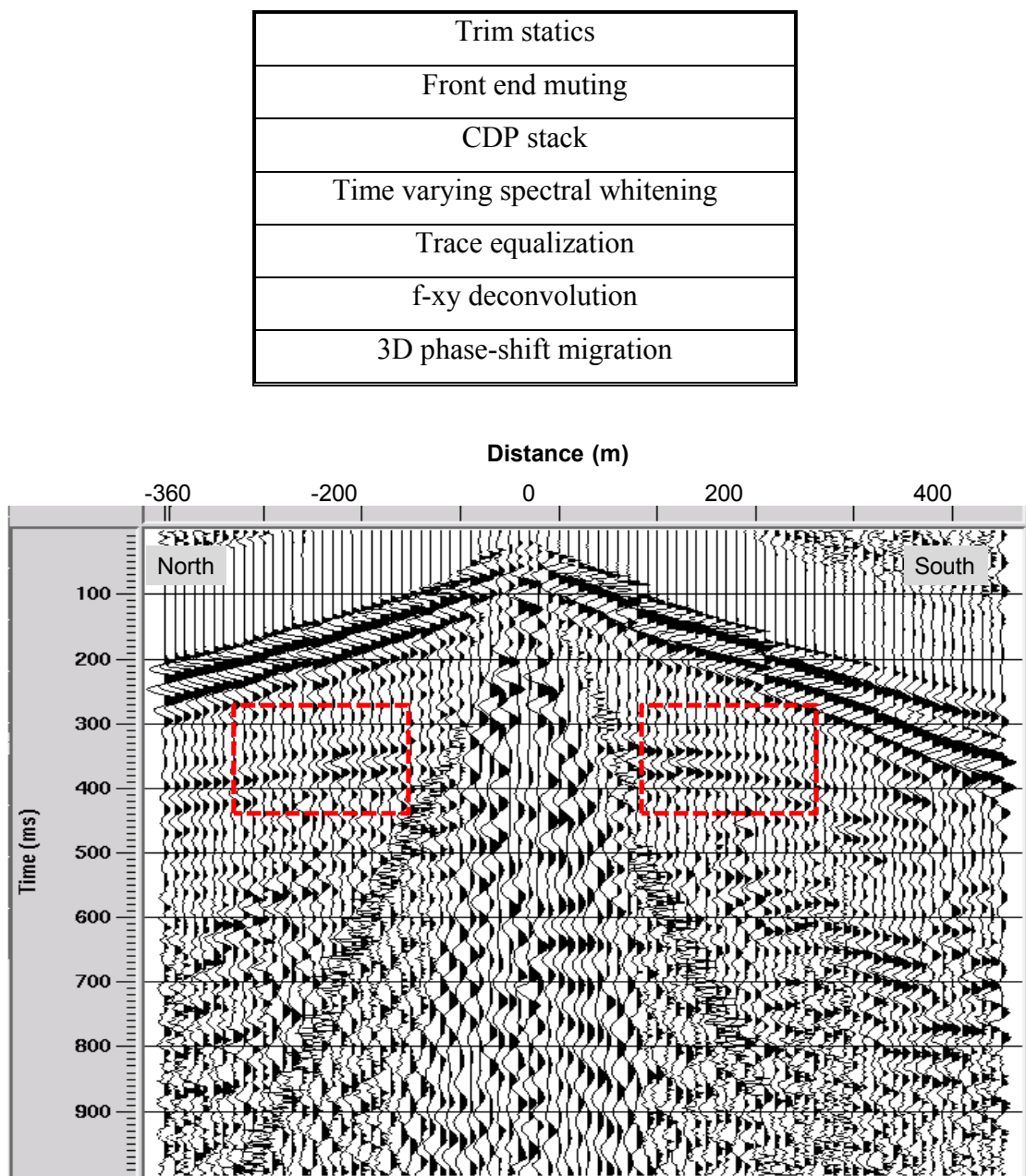


Figure 3-5: The raw field data gathered from a common receiver immediately west of the 102/7-28 well. A 300 ms AGC has been applied. The Ardley reflections occur at approximately 300-350 ms. The red box shows the window for amplitude spectrum calculation.

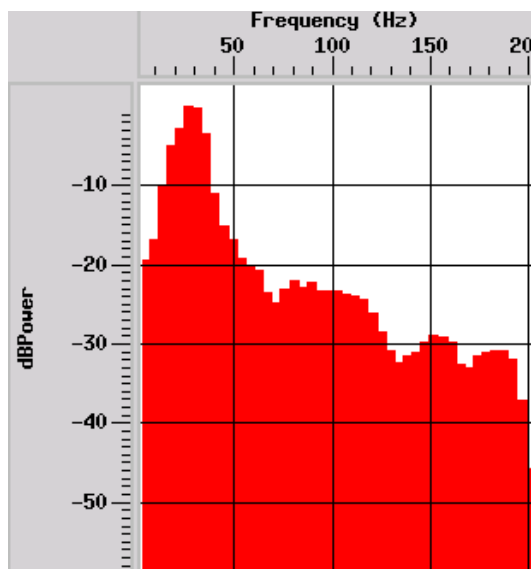


Figure 3-6: The amplitude spectrum calculated in a 180 ms window over the Ardley Coal reflections.

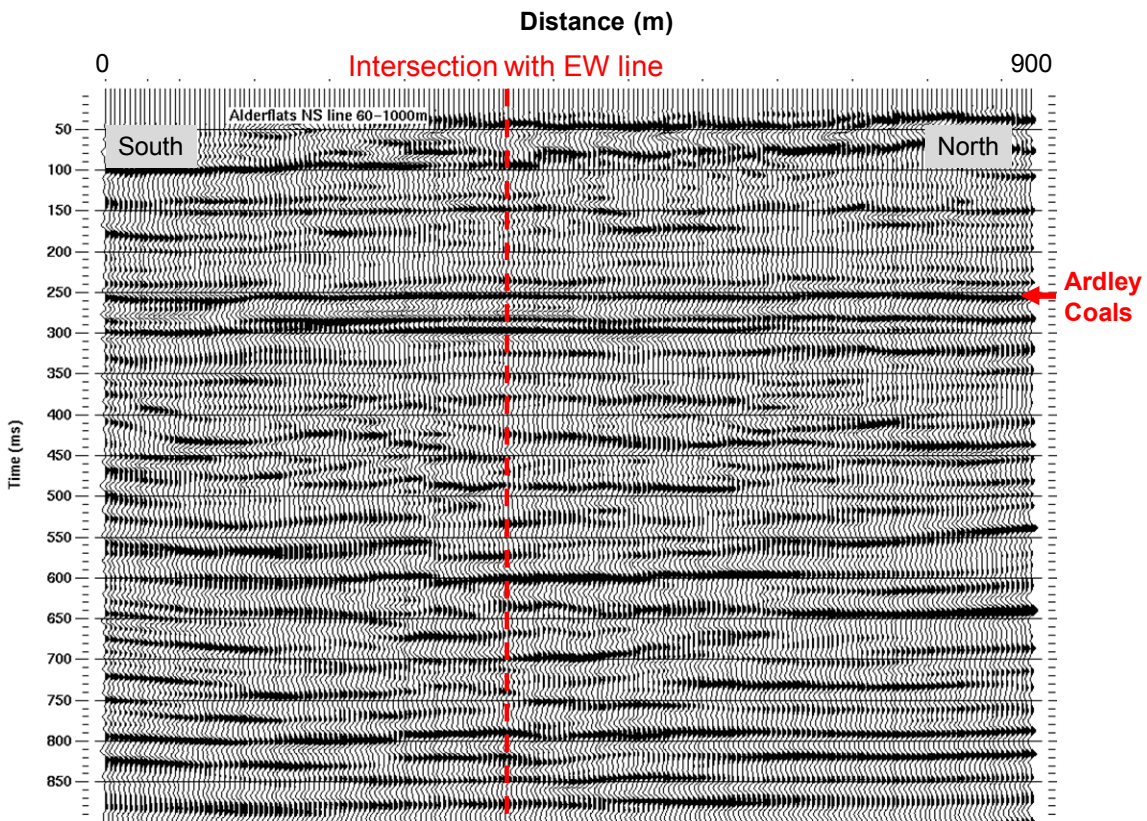


Figure 3-7: The migrated N-S line from the June 2006 survey.

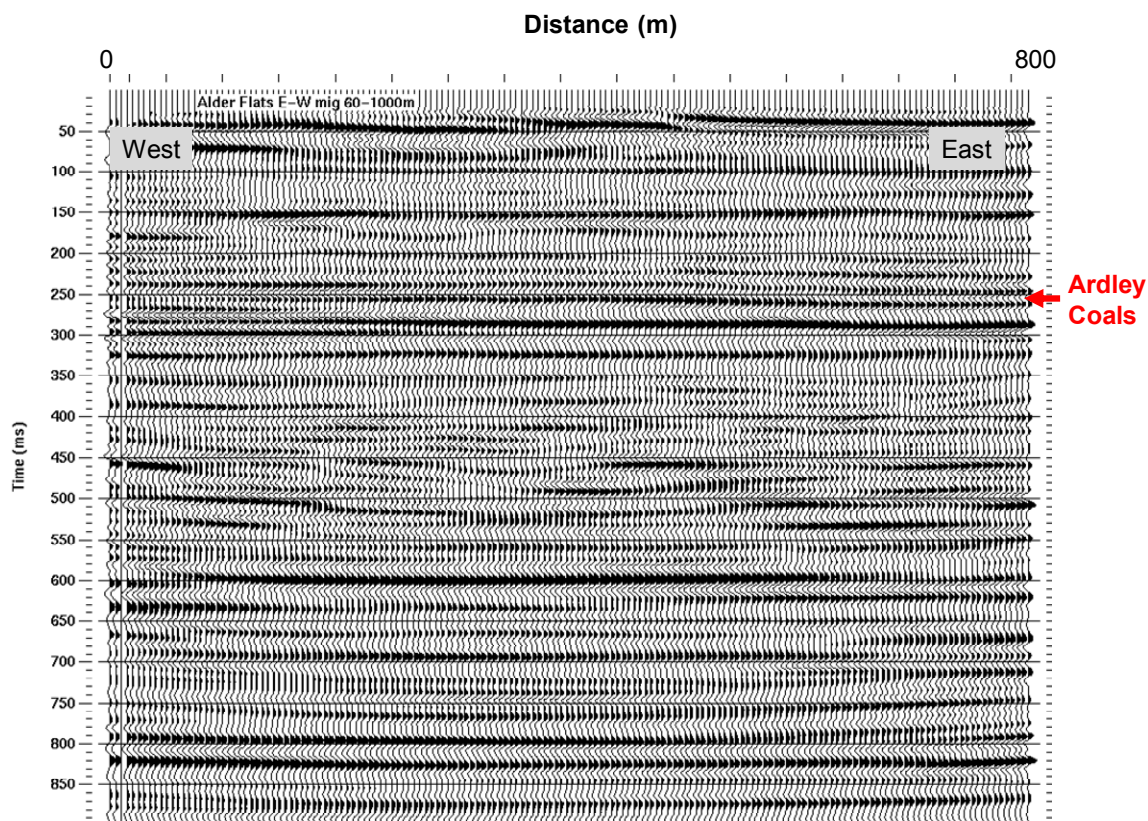


Figure 3-8: The migrated E-W line from the June 2006 survey.

3.4.3 Wavelet Estimation

Hampson Russell Software was used to estimate the amplitude spectrum of the processed data. The method employed first finds the autocorrelation of a set of traces; each of which is then truncated to 64 positive and 64 negative lags giving a 128 ms time series which is tapered at its ends using a cosine taper (Hampson Russell Software manual, 2007, ver. 5.2). The amplitude spectrum of the Fourier transform of this autocorrelation is calculated and the square root of the autocorrelation spectrum approximates the wavelet amplitude spectrum. The inverse Fourier transform of this spectrum gives the zero-phase wavelet. When several traces are used in the wavelet estimation, the estimations are averaged to yield the final wavelet. However, the phase remains unknown. In the case of the June 2006 2D survey, to estimate the wavelet phase,

the wavelet was then convolved with the reflectivity series derived from the 102/7-28 well logs to create a synthetic seismogram which was compared to the seismic data. After numerous tests with increasing wavelet phase, an excellent synthetic-seismic tie was achieved by rotating the phase of the wavelet by +90 degrees, yielding the wavelet illustrated in Figure 3-9. The wavelet shows energy up to ~90 Hz but also demonstrates a notched amplitude spectrum. The dominant period of the wavelet is approximately 17 ms which will demonstrate tuning effects as discussed in Section 3.2.

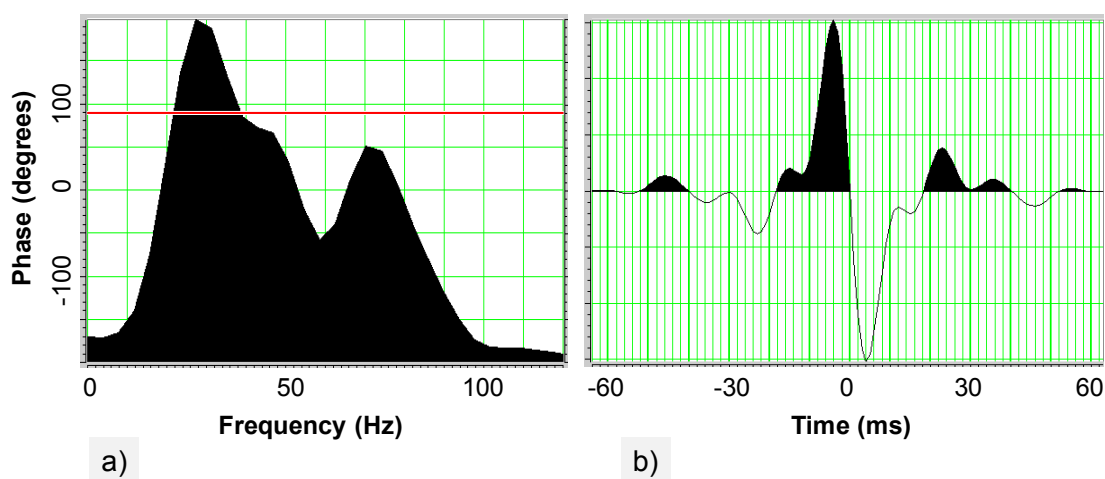


Figure 3-9: The wavelet extracted from the June 2006 north-south migrated section using the autocorrelation of CDP# 3300 – 3400 from 200 – 800 ms. (a) amplitude and phase spectrum, (b) the time domain wavelet.

3.4.4 Extending the 102/7-28 Well Logs

The 102/7-28 well log extends to the bottom of the well at 485 m TVD which correlates to ~390 ms. For the purpose of tying the well to seismic data it is desirable to have a sonic and density log that extends beyond the bottom of the actual 102/7-28 logged data. Log extension can be achieved by splicing data donated from another well onto the bottom of the 102/7-28 well logs. The nearest well with both a P-wave sonic and a density log is the 100/05-31-046-07 W5M well that is approximately 4.5 km from the 102/7-28 well. Synthetic well logs were created for the 102/7-28 well by finding the lowest coal of the Ardley Coal Zone in the donor well and aligning the depths of this geological marker between both of the wells. An extension was then spliced onto the

102/7-28 logs by adding the data from the donor well onto the bottom of the 102/7-28 well while retaining as much of the 102/7-28 log data as possible. The donated spliced data logs start at 485 m (TVD KB). Figure 3-10 illustrates the full length fabricated well logs for the 102/7-28 well with data donated from 100/05-31-04607W5. Also shown in Figure 3-10 is the fabricated addition to the top of the 102/7-28 logs. The fabrication assumes a linear gradient in the P-wave velocity of 6.92 m/s per m from surface to the top of the log measurements. The P-wave velocity is assumed to be 2000 m/s at surface.

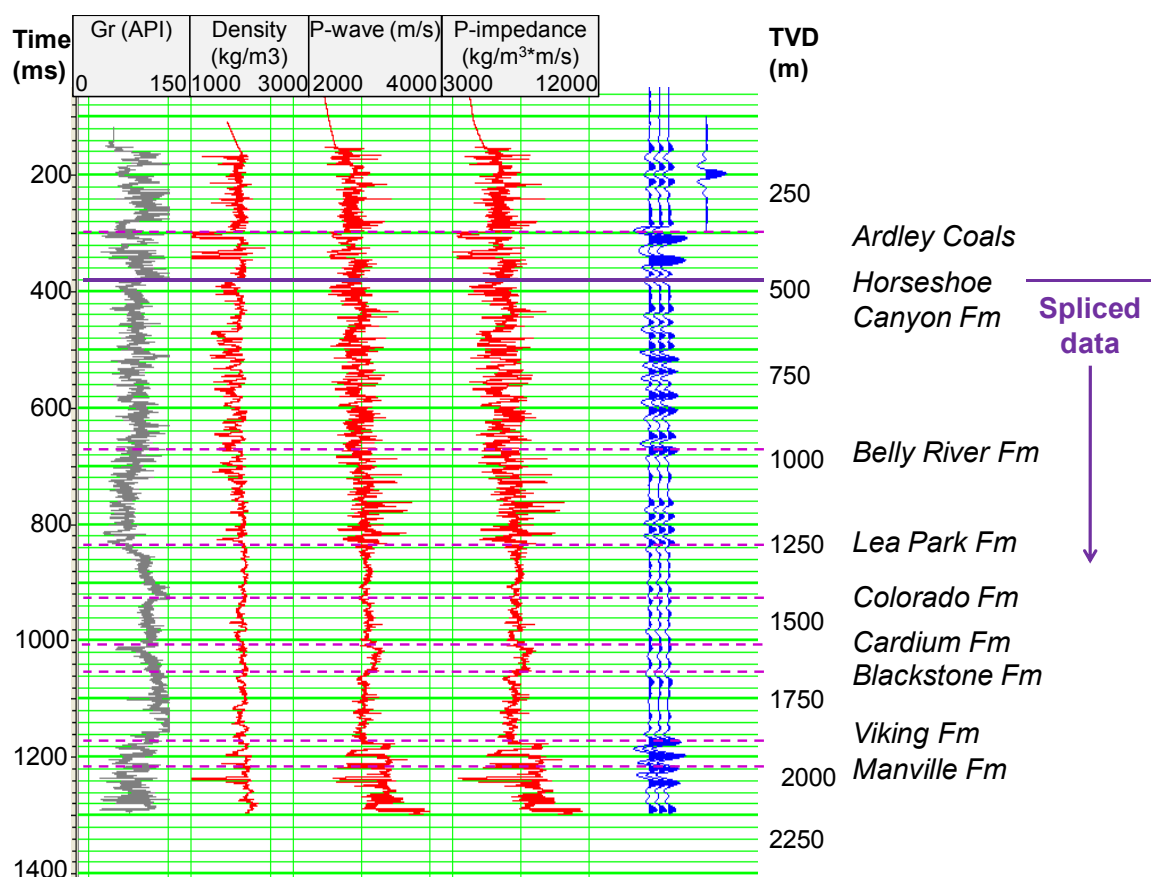


Figure 3-10: The fabricated 102/7-28 well logs generated by splicing data onto the bottom of the actual 102/7-28 logs. The synthetic seismogram is generated with a 5-10-50-60 Hz Ormsby wavelet.

3.4.5 Interpretation

The optimum synthetic-seismic tie is illustrated in Figure 3-11 and a close inspection of the Ardley Coal reflection events is shown in Figure 3-12. The Lower and

Upper Ardley Coal Zones can be correlated with distinct reflections, although the top and base of the zones are not clearly resolved. Figure 3-11 shows the interpretation of the Lower and Upper Ardley Coal events.

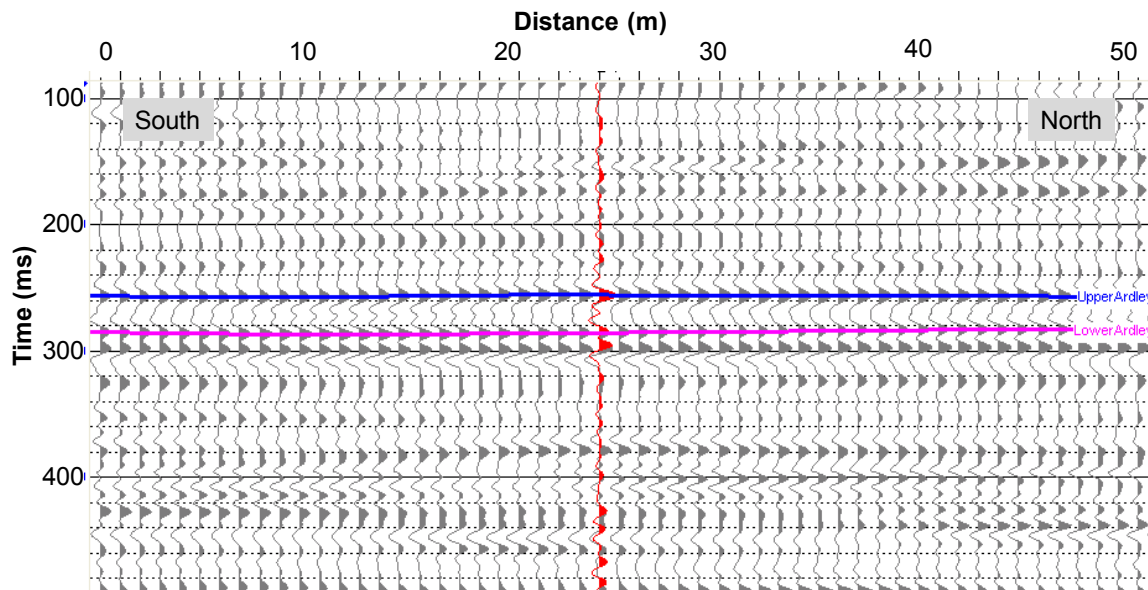


Figure 3-11: A portion of the north-south seismic line from the June 2006 survey with the synthetic tie and the Lower (purple) and Upper (blue) Ardley Coal horizon picks.

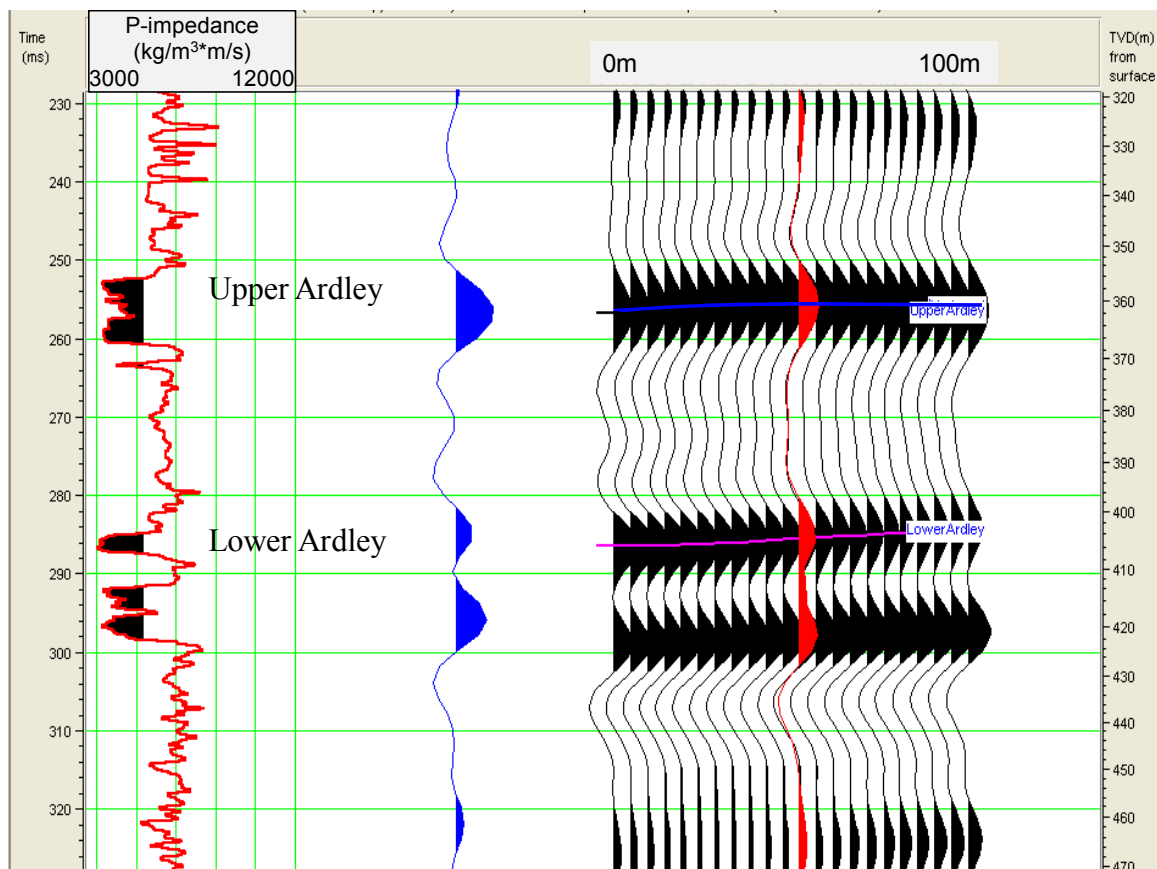


Figure 3-12: A short time window examination of the synthetic-seismic tie at the Ardley Coal Zone for the June 2006 2D data.

3.4.6 Conclusions from the June 2006 2D Survey

The results of the survey show that reflections from the Ardley Coals showed useful energy in the frequency band from 10 – 90 Hz with the processing flow used. The data also show that reflections from the coals are uncontaminated by direct source noise and refracted energy for source-receiver offsets between 60 – 500 m.

3.5 March 2007 2D Survey

3.5.1 Acquisition

In order to test seasonal variation in data quality and to test the utility of multi-component acquisition, a second seismic survey was conducted at the Alder Flats site in March 6-7, 2007. During the acquisition the ground was frozen at the surface with air

temperatures of about -5°C . Although the survey geometry was similar to the north-south line of the June 2006 survey, exact source and receiver station locations were not repeated. The geophones were placed in pre-drilled holes and at the time of acquisition were partially frozen into the ground due to the sub-zero temperature conditions.

The field layout is illustrated in Figure 3-13 and the acquisition parameters are listed in Table 3-5. 144 receivers were placed at 5 m intervals in a ditch beside the north-south road. The receiver line was entirely live and unchanged during the survey. The centre of the receiver line (receiver #72) was directly west of the 102/7-28 wellhead. Source points were on the road approximately 3 m to the east of the ditch. An attempt was made to place a source location beside each receiver location; however, source points over pipelines were skipped. In addition, 8 source points, spaced 40 m apart were recorded off the south end of the line.

Figure 3-14 shows a receiver gather of the raw data from the survey. Again the Ardley Coal reflections are centered around 300 ms. The amplitude spectrum from the windows depicted as red boxes in Figure 3-14 is illustrated in Figure 3-15 which shows a peak amplitude between 25 – 50 Hz. This shows higher frequency content than that from the June 2006 survey (Figure 3-6) which may be attributed to reduced attenuation in the near surface in the frozen winter conditions, and superior source and receiver coupling on and along the frozen road.

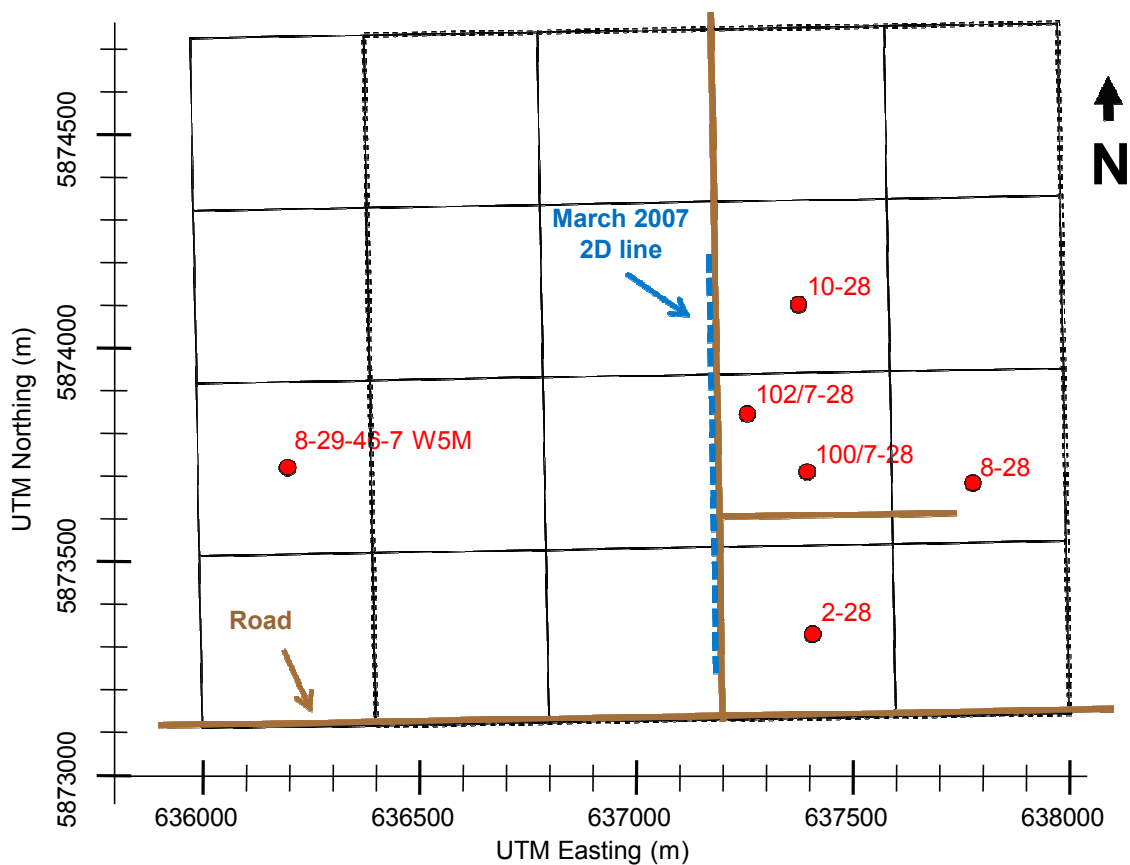


Figure 3-13: Field layout for the March 2007 survey

Table 3-5: Acquisition parameters for the March 2007 survey

Source	EnviroVibe 10-250 Hz – 4 sweep diversity stack
Source interval	5 m
Receivers	I/O sensor SM-24 3C geophones
Receiver interval	5 m
Sweep length	12 seconds
Listen time	14 seconds
Maximum offset	1040 m
Field sample rate	1000 Hz
Ground conditions	Frozen, snow and ice covered.

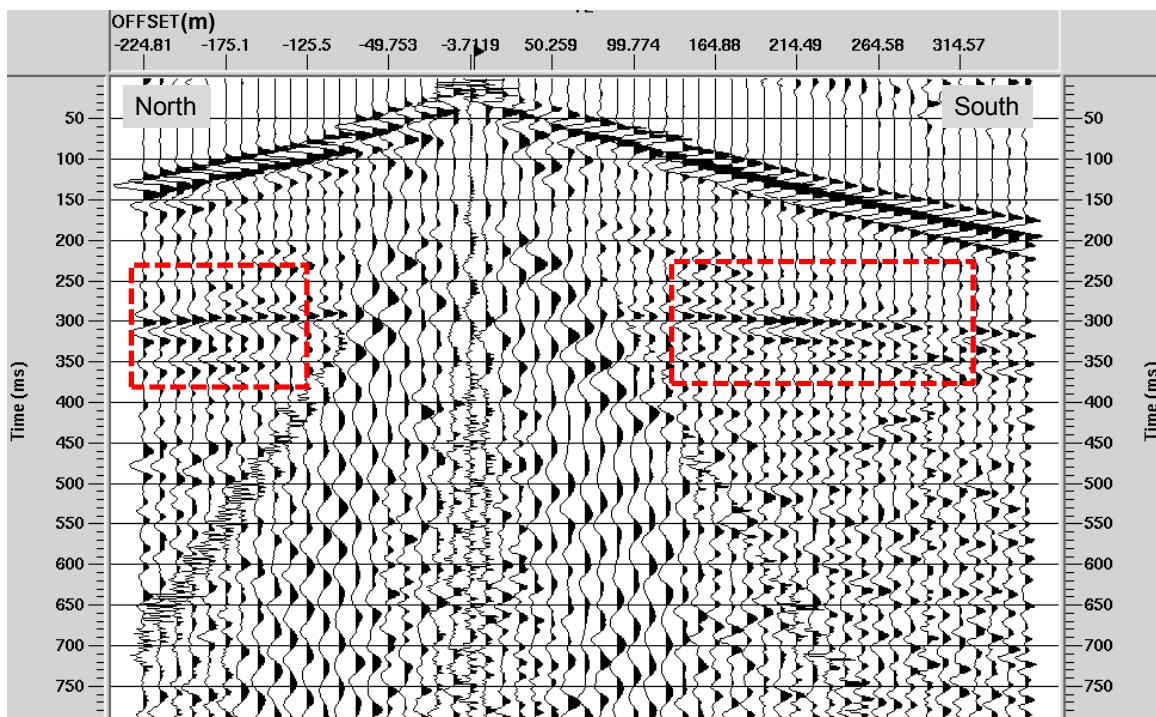


Figure 3-14: A raw receiver gather for the geophone immediately west of the 102/7-28 well showing every second source location. Automatic gain control with a 300 ms window was applied. The red box shows the window for the amplitude spectrum calculation.

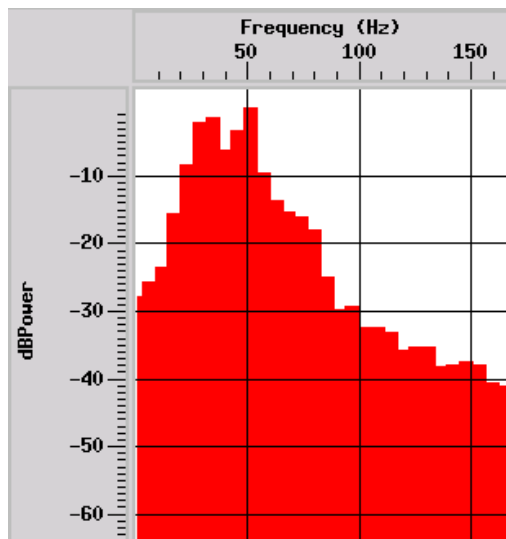


Figure 3-15: The amplitude spectrum calculated over a 180 ms window that included the Ardley Coal reflections.

3.5.2 Data Processing

The vertical component data processing followed a standard flow (summarized in Table 3-6) that paid particular attention to minimizing the impact of coherent source noise and to maintain true amplitudes using processing techniques recommended by Resnick (1993). Differences between this flow and the flow from the June 2006 processing mostly reflect differences in the individual preferences of the data processor.

Table 3-6: The processing flow applied to the vertical component of the March 2007 data.

Process	Parameters
Set up geometry	2.5m CDP spacing
Isolate the vertical component data	
Trace edit	
Amplitude correction for geometric spreading	$\frac{1}{v_{rms}^2 \cdot t}$ correction only
First break picks	
Refraction statics calculated with HR GLI	3 layers
Application of elevation and refraction statics	Datum elevation = 897 m Replacement velocity = 2000 m/s
Radial trace filter – 3 passes	Fan filter - max. vel. +/-2500 m/s Dip filter +/- 2500 m/s Dip filter +/- 175 m/s
Gabor deconvolution	Gaussian window width = 0.4 s Window increment = 0.05 s Stabilization factor = 0.1 %
Band pass filter	5-10-90-100 Hz
Outside mute	
Velocity analysis and NMO removal	
Surface consistent amplitude scaling	Source and receiver only
CMP Stack	

fx deconvolution	Horizontal window length = 100 traces Prewhitening = 1%
Kirchhoff time migration	45 degree dip limit 100 % stacking velocities
Trace equalization	Based on RMS of the whole trace

Processing started with the definition of the geometry. Both the nominal source and receiver spacing were 5 m, so the geometry was set to 2.5 m common midpoint bins resulting in the fold distribution illustrated in Figure 3-16. Common midpoint # 544 was directly west of the 102/7-28 well head. Bad traces were then edited from the data set.

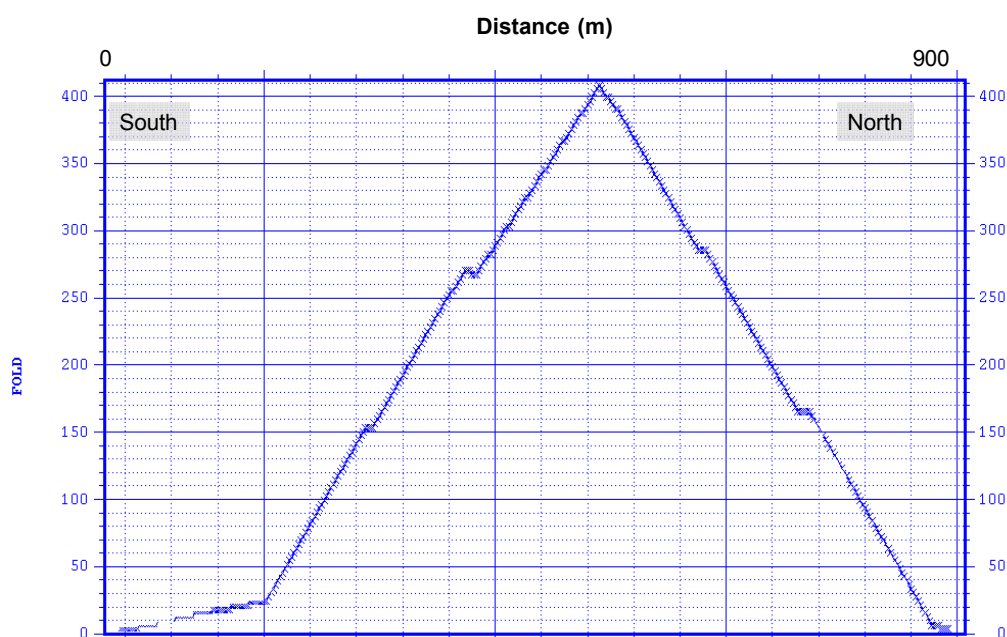


Figure 3-16: Fold for the March 2007 survey.

Next, the amplitudes were corrected for losses resulting from geometric spreading of the source energy over the surface of the propagating wavefront. The loss of amplitude can be corrected if the velocity field is known using a correction factor of (Margrave, 2006):

$$\frac{1}{v_{rms}^2 \cdot t}$$

3.1

where v_{rms} is the RMS velocity from the velocity model and t is time. Since the velocity field needs to be known in advance to accurately estimate the spherical loss, this step is applied during a second pass through the processing flow, after a velocity model has been estimated in the first pass. The velocities utilized were the stacking velocities discussed later in this section. Figure 3-17 illustrates the effect of this amplitude correction.

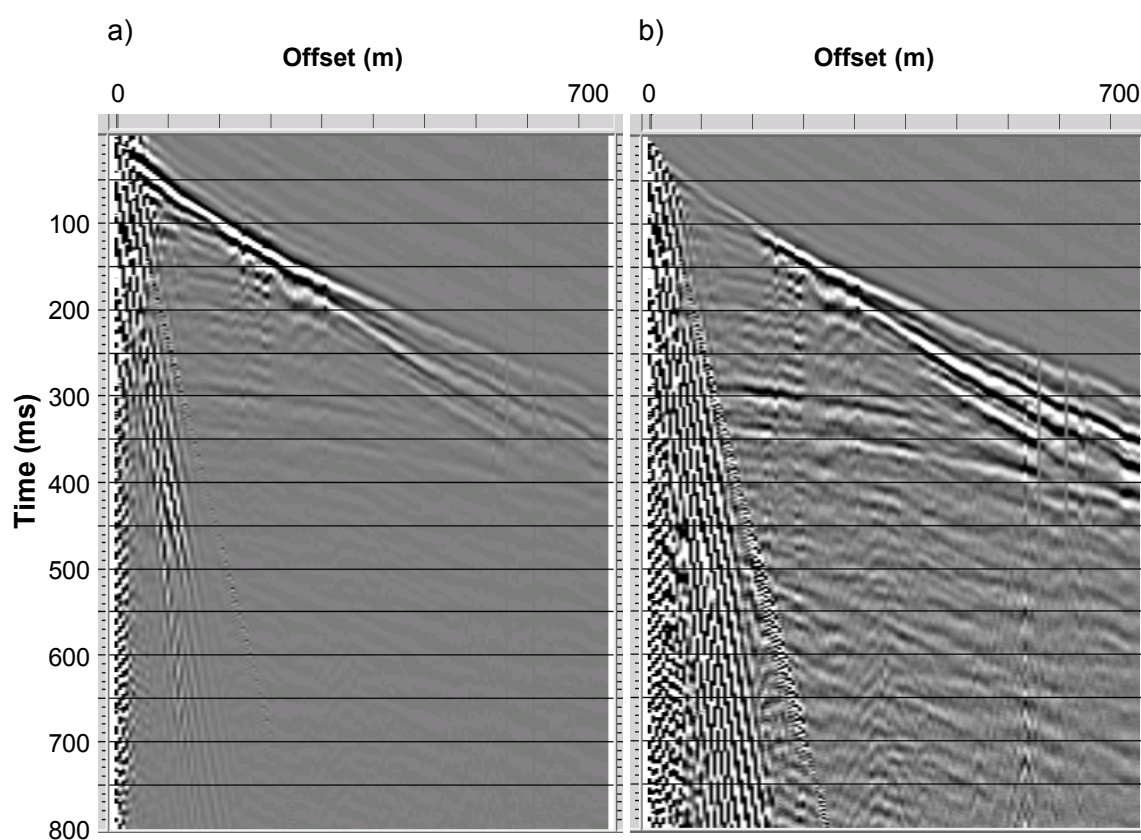


Figure 3-17: A shot gather before (a) and after (b) correcting the amplitudes for spherical divergence effects.

The next step was first break picking. In many cases, auto picking of the first breaks was unsuccessful, and the picks were edited by hand. Figure 3-18 and Figure 3-19 illustrate the editing. At the near offsets, shown in Figure 3-19, the first break was

impossible to identify so a straight line was interpolated between the source location and the first discernable first break at approximately 35 m.

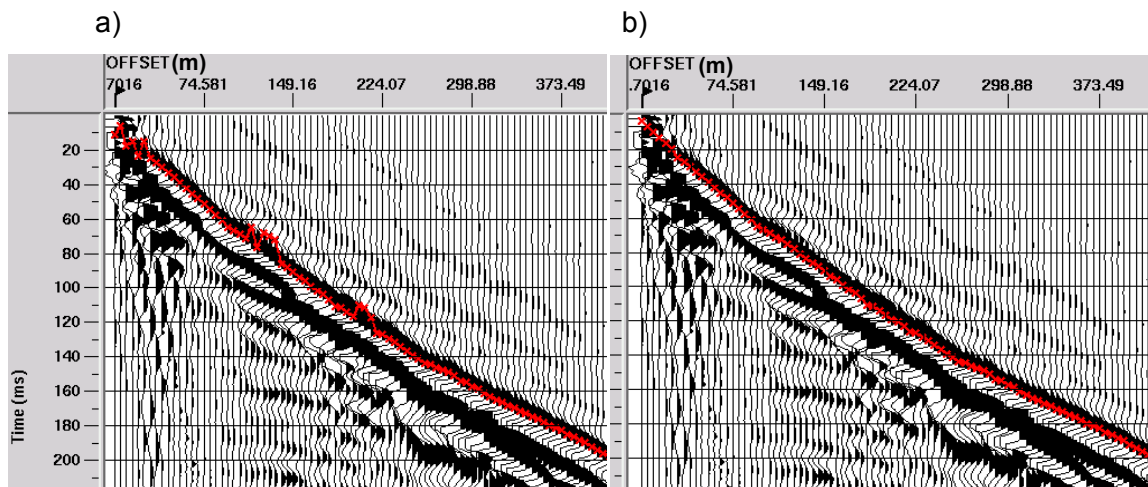


Figure 3-18: First break picks: (a) auto picked and (b) edited.

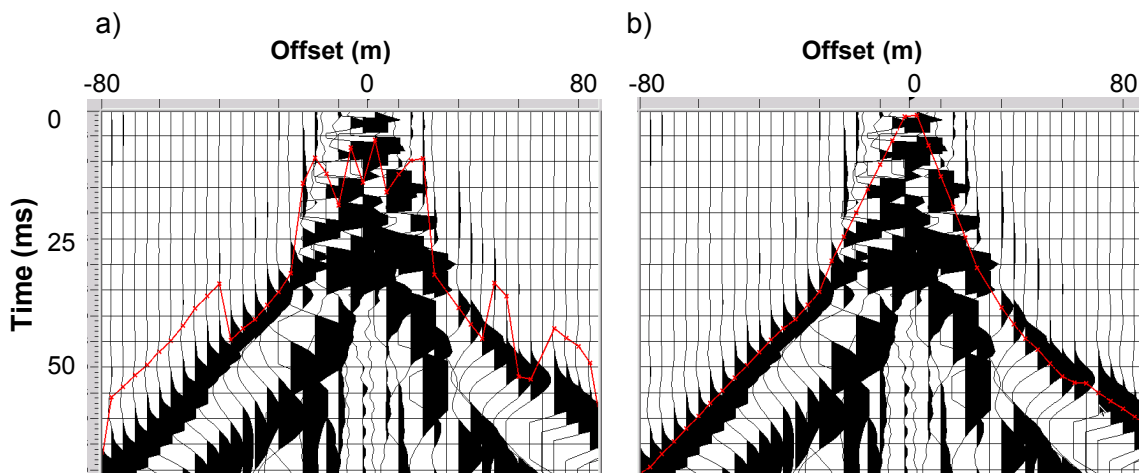


Figure 3-19: First break picks in the near offset range: (a) auto picked and (b) edited.

The next step was to correct for the variable static time shift that each trace required as a result of variable thickness and velocity in the weathering layer below each source and receiver location as well as small surface elevation changes. A time shift was applied to each trace to compensate for the variable near surface conditions and to set the

reflection arrival times to the time that would have been observed if all measurements had been acquired on a flat plane with a uniform velocity near surface layer.

The Hampson Russell GLI near surface inversion program was used to solve for a model of the near surface. An initial guess model of layer thicknesses and velocities was manually identified from the first break picks. The software perturbs the initial model to minimize the discrepancy between the precise first break times and those predicted by the model. The first break data indicated that a three layer model was required and Figure 3-20 illustrates the first break picks and the initial velocity picks for the three layers. Manual estimation of the near surface model at 11 locations along the survey line resulted in the initial guess model depicted in Figure 3-21. The inverted solution model is depicted in Figure 3-22 which shows that the top layer is on average about 5 m thick. The velocity of this first layer was identified before the inversion to be 600 m/s. The layer below is approximately 62 m thick and has a velocity of approximately 2000 m/s. The static correction for each source and each receiver, illustrated in Figure 3-23, was applied to each trace to remove the travel time through the two near surface layers at the source side and at the receiver side. Finally the static shift is added to each trace to account for the travel time through a replacement layer that would exist between the seismic datum (897 m) and the top of the deepest layer in the model. The velocity of this replacement layer was set to be 2000 m/s.

Figure 3-24 illustrates a shot gather before and after the application of static corrections. The effect can be seen in the slight smoothing of the hyperbolic shape and a small decrease in the arrival time of the reflection at approximately 300 ms.

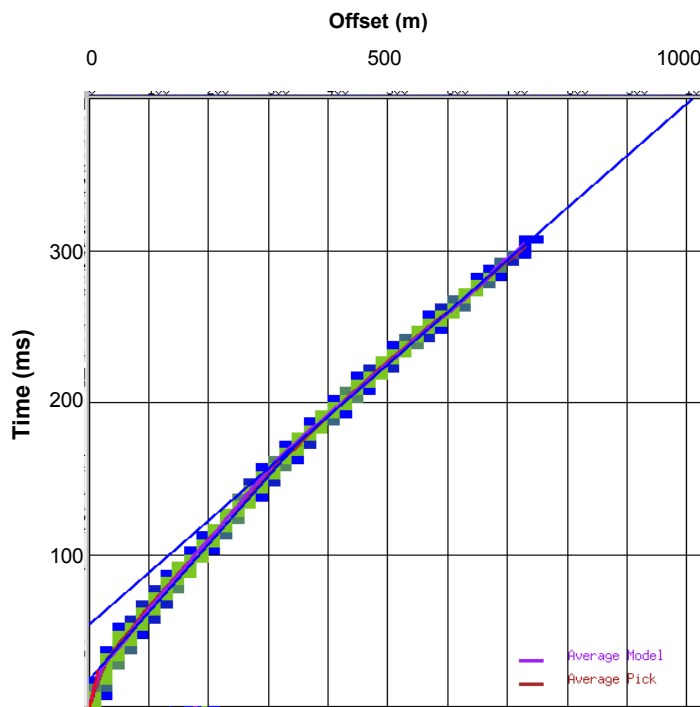


Figure 3-20: The first break data (coloured points) and the approximated velocity picks (lines) for the initial model used in the near surface model GLI inversion.

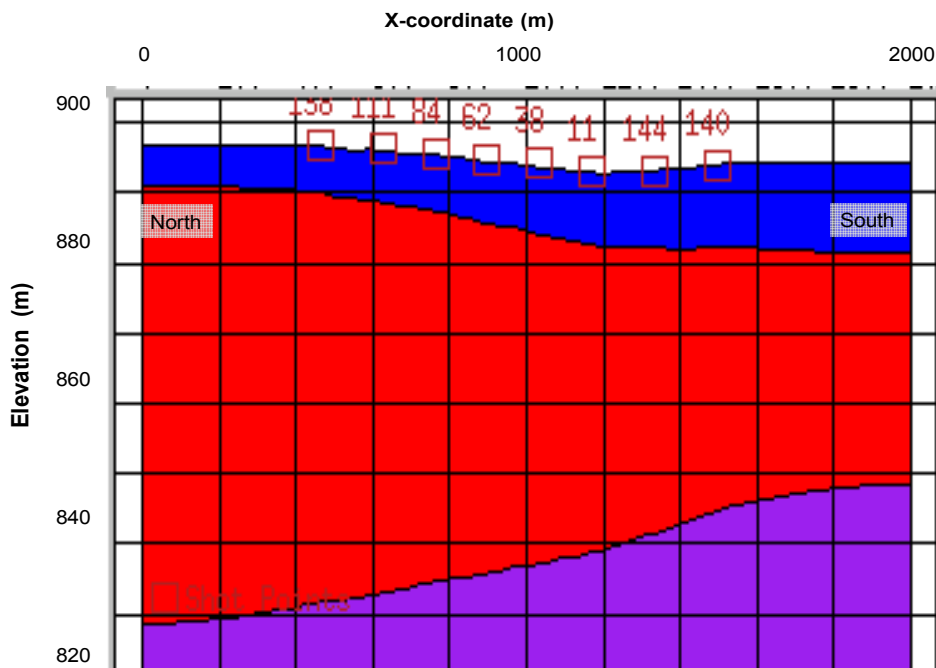


Figure 3-21: The initial guess model of the thickness of the two layers (blue and red) of the near surface used in the GLI inversion. Each is assumed to have a velocity that varies laterally but is constant in depth at each lateral location.

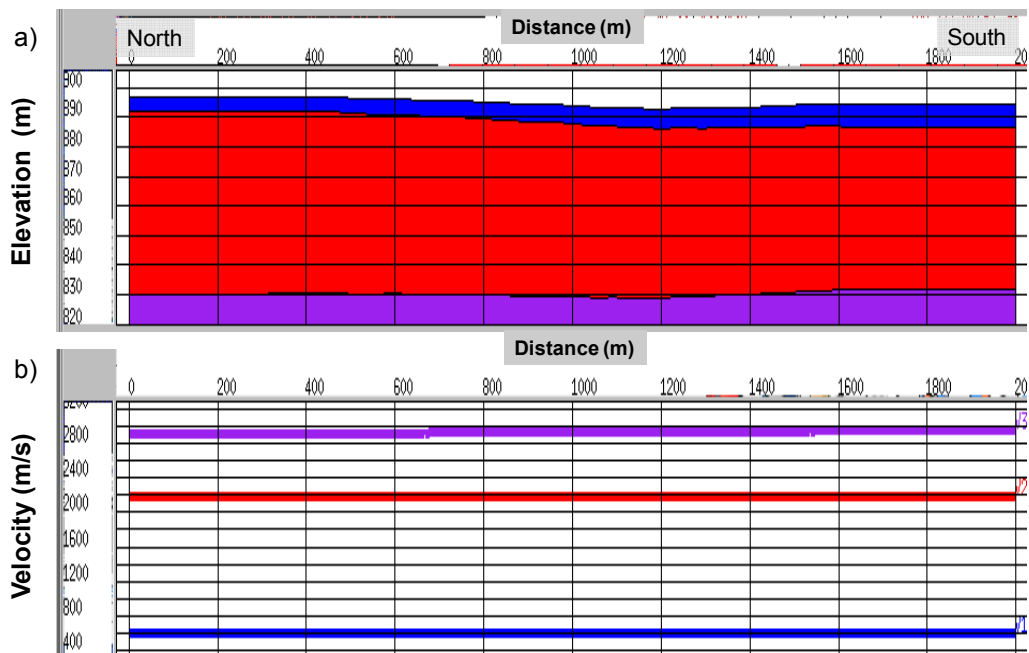


Figure 3-22: The near surface model that resulted from the GLI inversion. (a) shows the layer thicknesses and (b) shows the layer velocities.

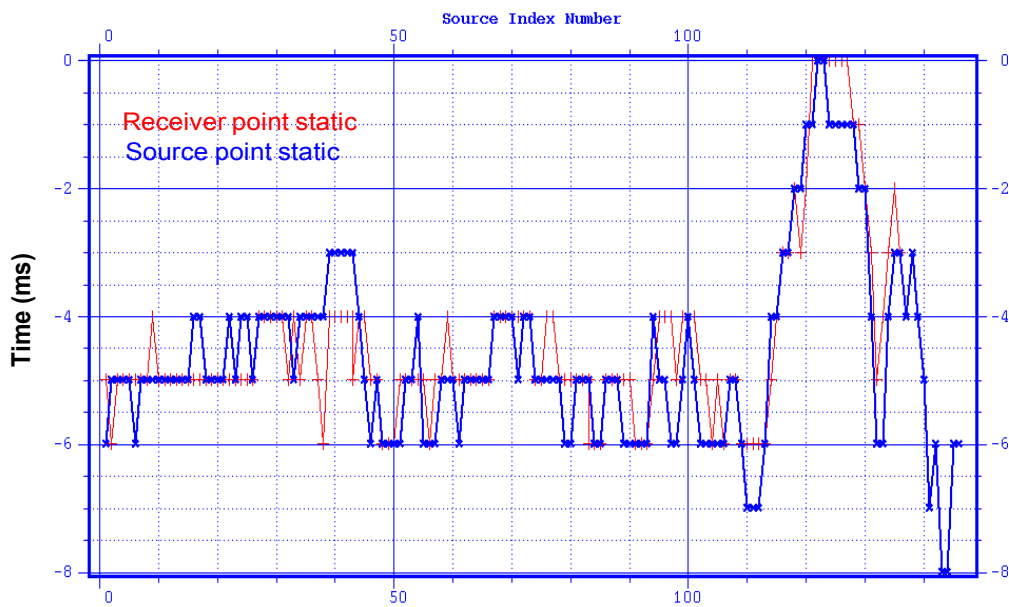


Figure 3-23: The receiver and shot statics required at each location along the 2D survey line.

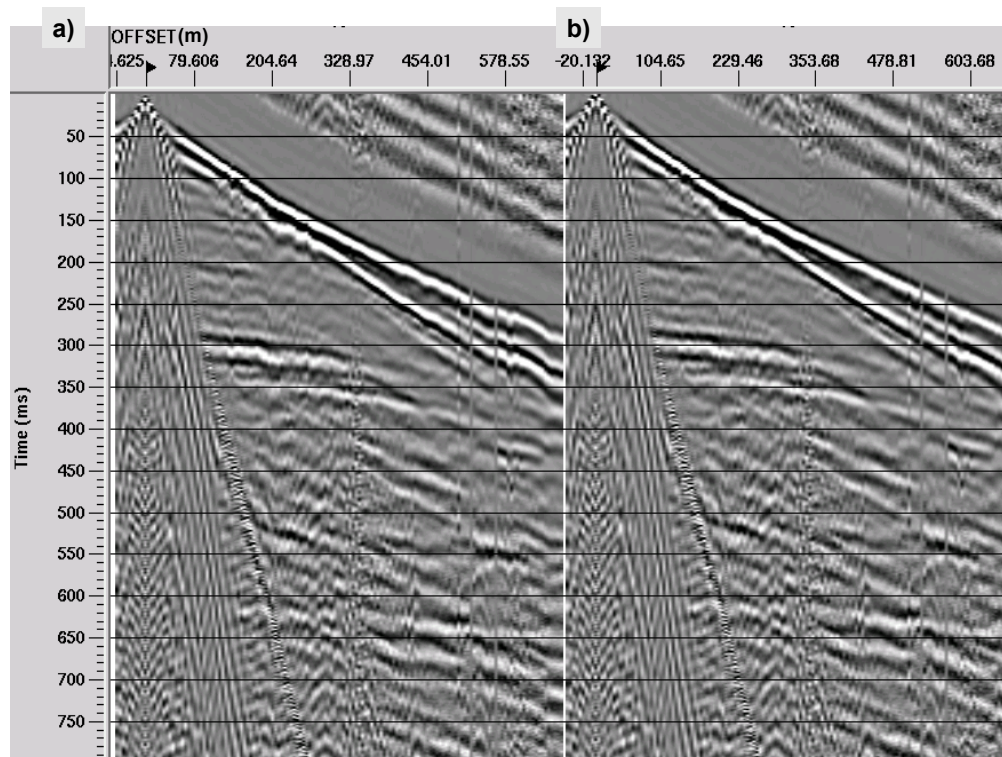


Figure 3-24: A shot gather shown before (a) and after (b) applying the required static correction.

The shot record in Figure 3-24 also shows contamination due to several forms of coherent noise: surface waves and air blast, the reverberating first breaks, and an unidentified linear noise seen often at times greater than 400 ms and at offsets greater than 100 m. The amplitudes of these noise trains dominate many of the reflection amplitudes. Radial trace (RT) filtering, as implemented by CREWES (Henley, 1999), was used to attenuate some of these coherent noise events.

In RT filtering, data from the horizontal distance and travel time domain (XT) is transformed to the domain of apparent velocity and travel time, called the RT domain. The transform maps data from the XT domain that occurs along a linear trajectory with a specific origin and with a specific take-off angle (radial trace), to a domain where each trace represents the line (take off origin and angle). A series of radial traces is mapped from the XT to the RT domain. Figure 3-25 illustrates the transform and how different events in the XT domain map into the RT domain. Both domains share the same time scale. Where radial trajectories cross time lines between traces in the XT domain,

amplitudes are interpolated along constant time lines. A fan of radial trajectories can be set to have an origin at the source origin or any other point in the XT domain. Also, effective dip filtering can be achieved by setting the origin of the trajectories to be a certain distance from the origin in the XT domain and specifying a narrow range of apparent velocities for the radial trajectories. Aliasing at far offsets and long travel times is avoided by specifying more radial traces than there are traces in the XT domain.

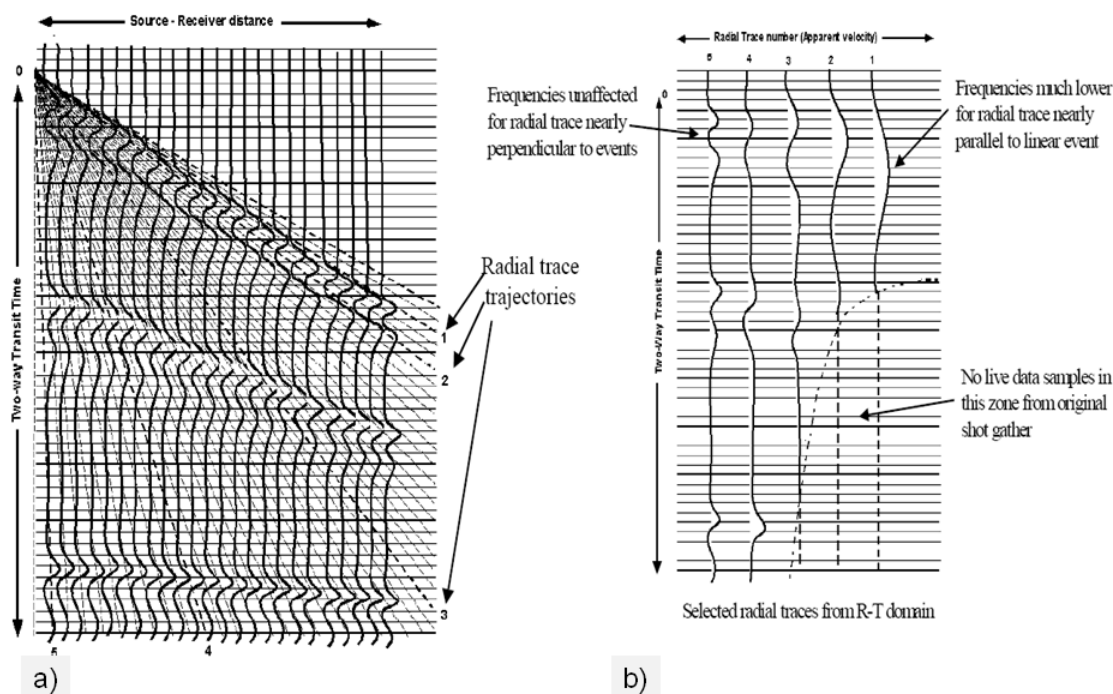


Figure 3-25: Illustration of how data is transformed from the XT domain to the RT domain (from Henley, 1999). (a) the XT domain, (b) the RT domain.

A consequence of the transform is that the time duration of an event can be lengthened or shortened in the RT domain, depending upon its angle in XT space relative to the radial trace trajectory. An event in the XT domain that is close to parallel to a radial trajectory will have a lengthened duration in the RT domain; thus lowering its apparent frequency. This fact can be used to filter linear events in the XT domain by removing this low frequency data in the RT domain and then inverse radial transforming the result. An advantage of the RT filter method over fk filter tools is that RT filtering

can be used to target specific noise events while fk filtering methods attenuate or enhance all events with similar frequency and wavenumber.

One pass of fan radial trace filtering and two passes of dip radial trace filtering greatly reduced the linear noise, as illustrated in Figure 3-26. Improvement is seen in the reflection event amplitude at 300 ms as well as at the event at 600 ms, each of which can be detected at near offsets inside the cone formerly dominated by ground roll and at far offsets where refracted energy dominated. Although quite effective at reducing coherent noise, the RT filter can add spurious “dipping” noise seen especially in the upper right of Figure 3-26b.

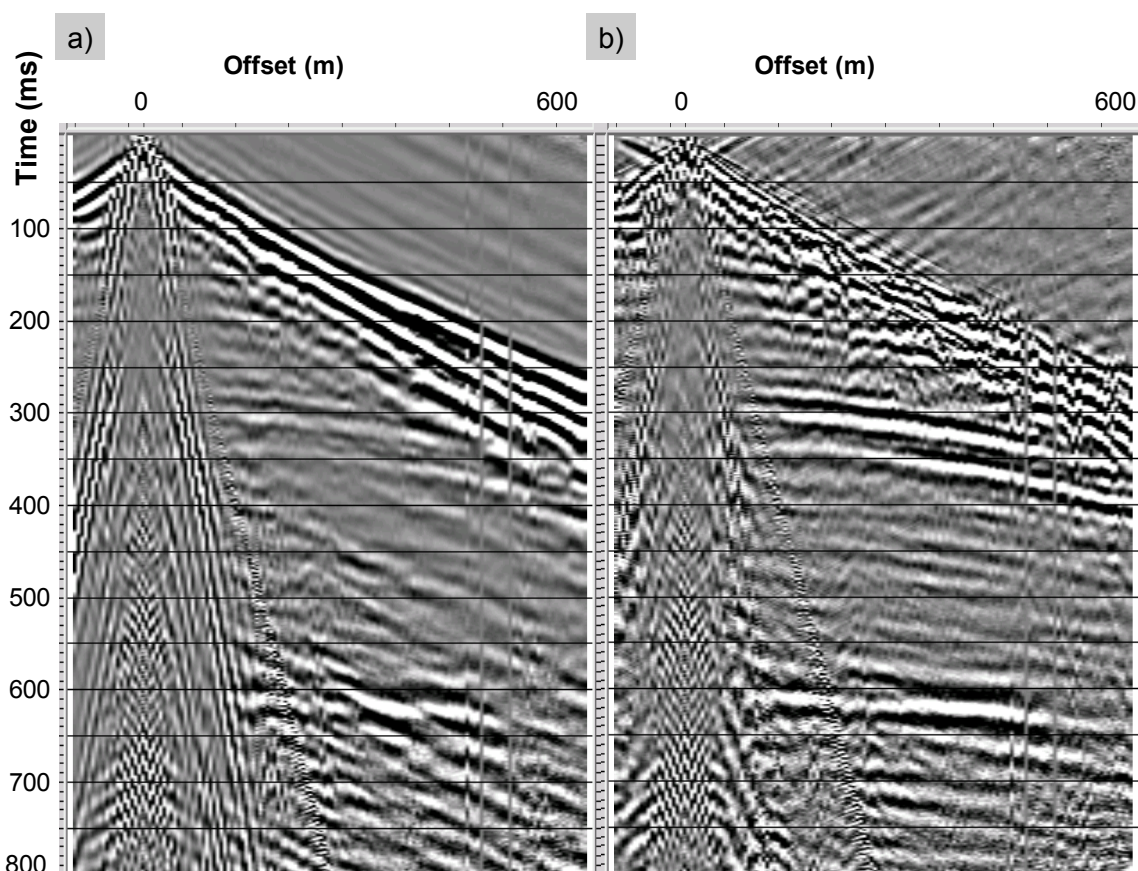


Figure 3-26: A shot record (a) before and (b) after applying radial trace filtering.

The next processing step was a deconvolution which attempts to remove the effective wavelet from the seismic trace to recover the reflectivity time series. The assumed (stationary) convolution model for the seismic trace time series is:

$$s = w_e \otimes r + noise \quad 3.2$$

where

s = seismic trace

r = the earth reflectivity

$$w_e = w_s \otimes n_s \otimes m = \text{effective wavelet} \quad 3.3$$

w_s = source wavelet

n_s = near surface effect

m = multiples.

Deconvolution attempts to remove the effective wavelet, w_e , from the seismic trace. Since the convolutional model makes the assumption that seismic trace is a filtered version of the reflectivity series (plus some noise), deconvolution attempts to find an inverse filter that, when applied to the trace, removes the amplitude and phase effect of the effective wavelet. The resulting trace should have a more balanced amplitude spectrum and a phase spectrum that has been adjusted to be more easily interpretable (i.e. ideally closer to zero-phase).

A common method of deconvolution is spiking deconvolution. Although used successfully in many examples, spiking deconvolution makes the assumption that the effective wavelet is time-invariant. This assumption is known to be invalid since attenuation in anelastic rocks and attenuation due to short path multiples results in a wavelet that evolves with propagation through the earth. An attempt to correct for this effect is incorporated in the Gabor deconvolution method as developed by Margrave and Lamoureux (2006). The Gabor deconvolution develops a time-varying deconvolution operator by analyzing the seismic trace in time-limited windowed segments. The result is a deconvolution that removes the time varying wavelet and so attempts to account for attenuation. The Gabor deconvolution algorithm uses a Gaussian windowing technique to sample the seismic trace before transforming to the Gabor-Fourier domain where the operator is designed.

The CREWES Gabor algorithm was used to deconvolve the Alder Flats data. A shot gather before and after application of minimum-phase Gabor deconvolution is

illustrated in Figure 3-27 and Figure 3-28. The window length was 400 ms and the time increment for the Gaussian windows was 50 ms. The effect on the amplitude spectrum is apparent as the boost in the higher frequencies is easily apparent in the deconvolved data.

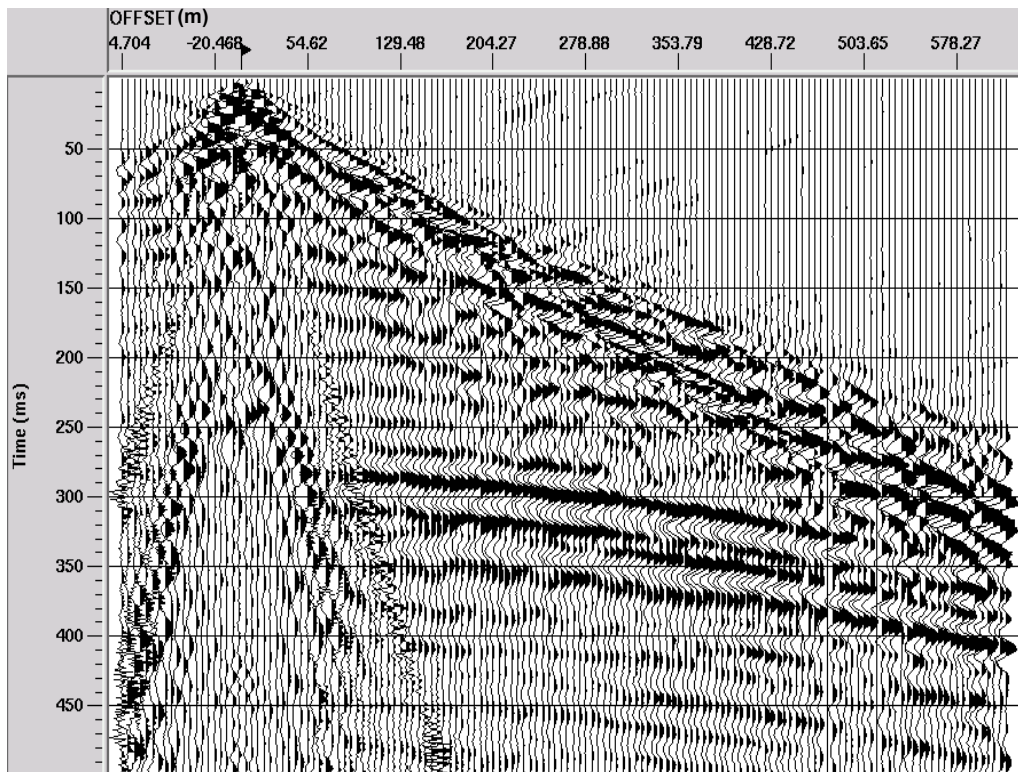


Figure 3-27: A shot gather before deconvolution.

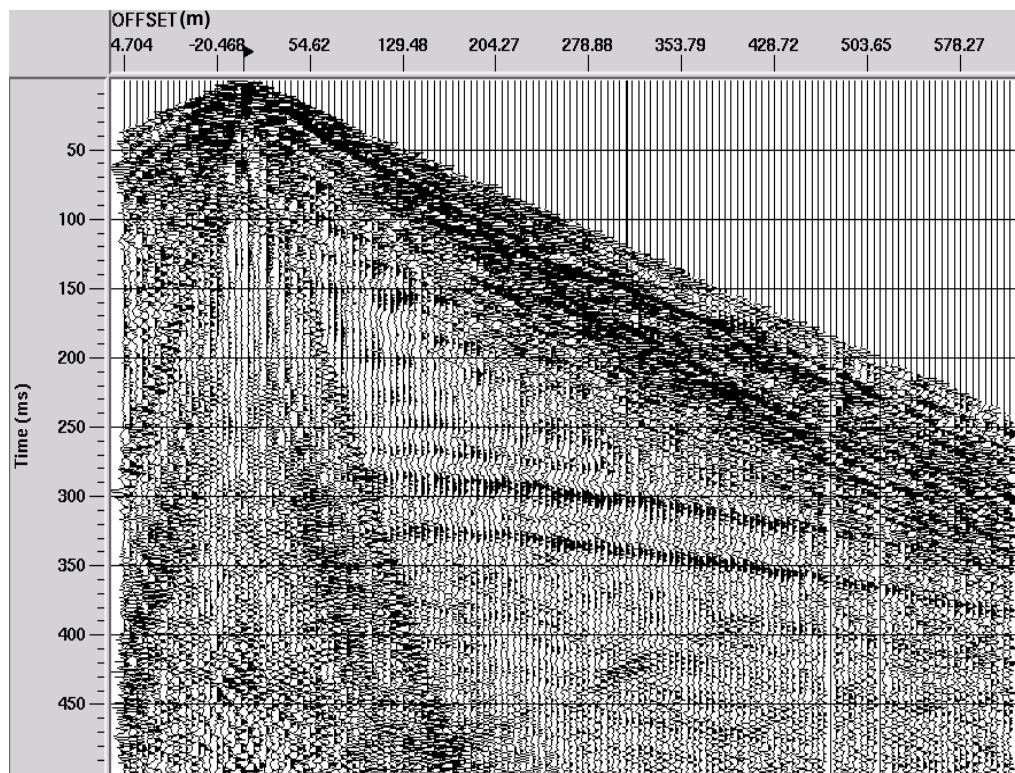


Figure 3-28: The shot gather after application of Gabor deconvolution.

After deconvolution, the data was analyzed to assess the upper frequency band in which the signal was definitely greater than the noise. Filter panels were designed to visually assess the upper frequency bandwidth at which the signal disappeared. Figure 3-29 shows that the reflector at about 300 ms was detectable in the 80-90-100-110 Hz window but not in the 90-100-110-120 Hz window. Therefore, a 5-10-100-110 Hz bandpass filter was applied to the data to eliminate noise. The result, after applying this filter is shown in Figure 3-30.

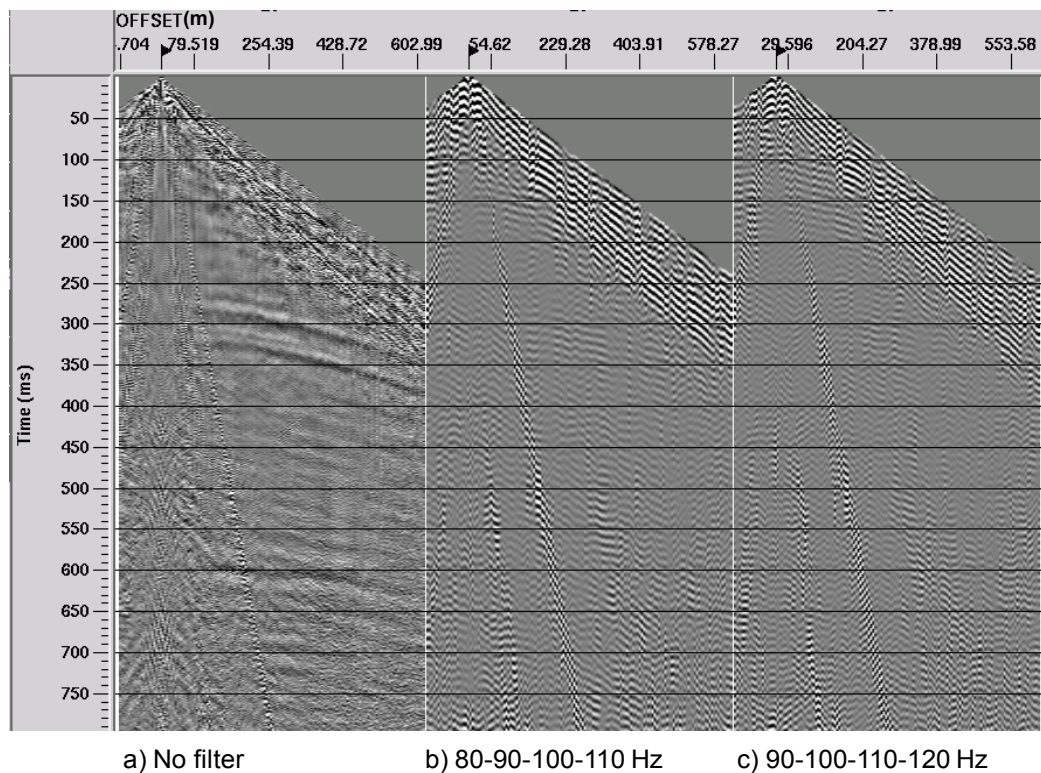


Figure 3-29: A shot gather with different band pass filtering. Note the subtle signal present in (b) but not in (c).

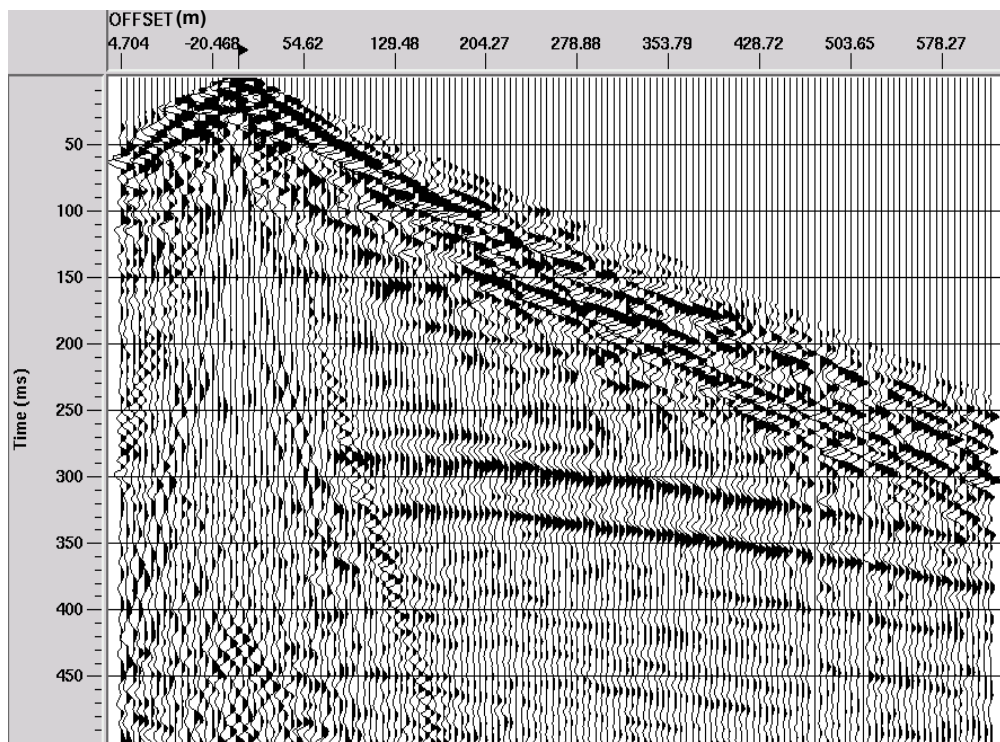


Figure 3-30: A shot gather after 5-10-100-110 Hz bandpass noise filtering.

Next, the traces are distributed into common mid-point (CMP) bins. The concept of CMP binning is illustrated in Figure 3-31 where all pairs of traces that have the same mid-point between source and receiver locations are collected together. As illustrated in the figure, if the reflectors are horizontal and the ray trajectory is symmetric before and after reflection, the common mid-point is directly above the common depth point (CDP) that corresponds to the point of all the reflections in the CMP gather. A CMP gather is illustrated in Figure 3-32.

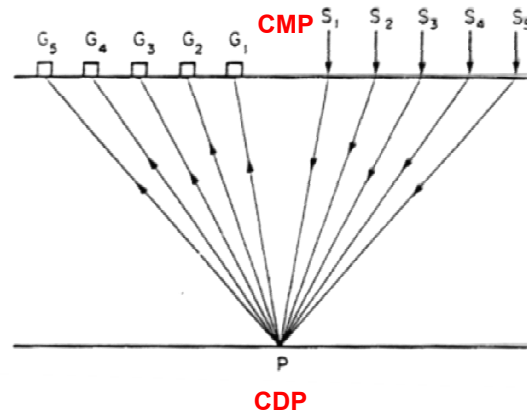


Figure 3-31: Collecting traces from multiple source/receiver pairs into a common mid-point (CMP) that is directly over the common depth point (CDP).

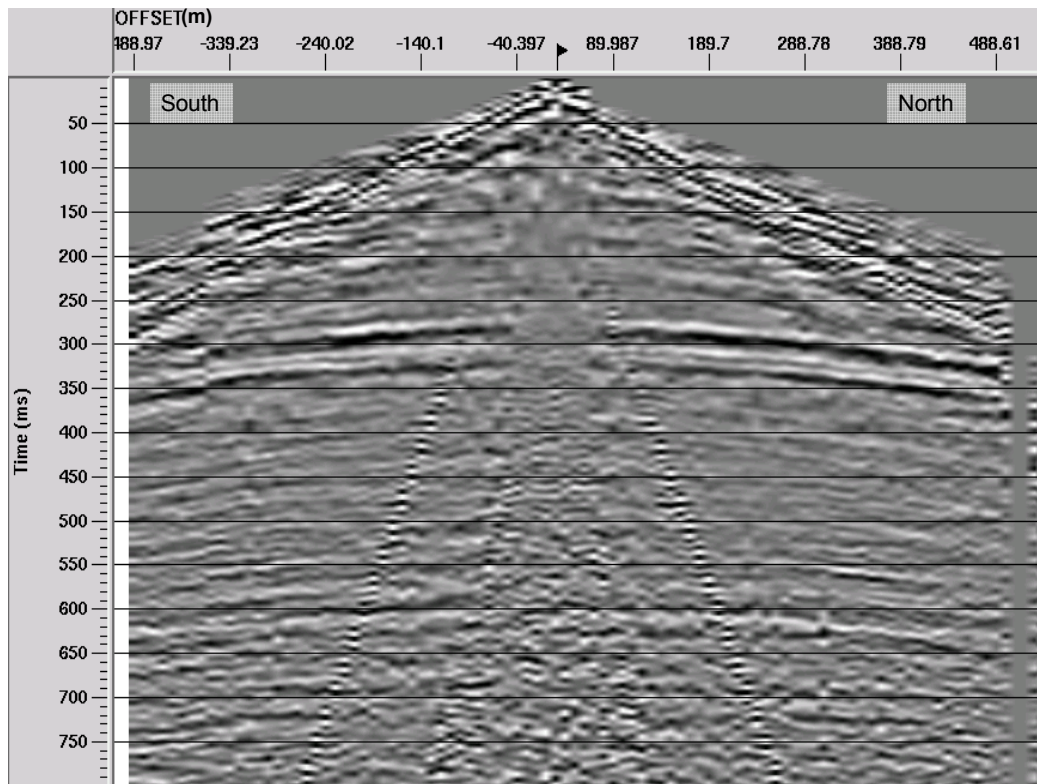


Figure 3-32: A typical CMP gather from the middle of the line.

Because energy in the refracted data was likely to overwhelm early reflection events for velocity analysis and stacking, these first arrival were removed with an offset-dependant mute function (Figure 3-36).

The arrival times of a reflection event on a trace that is at non-zero source/receiver offset will be delayed in time relative the same reflection arrival time at zero-offset according to approximation (valid for short offsets and a laterally uniform layered medium):

$$t^2 = t_o^2 + \frac{x^2}{v_{rms}^2} \quad 3.4$$

where t is the event arrival time at offset x , t_o is the event arrival time at zero-offset and v_{rms} is the RMS velocity of the layered medium. The delay in time relative to the zero-offset arrival time, the normal moveout (NMO), can be removed if the RMS velocity is known. Velocity analysis attempts to find the “stacking” velocities that will remove NMO and align reflection events at identical times for all offsets in a CMP gather. All

traces in a CMP gather can then be stacked (summed) into a single trace; thus improving the signal-to-noise of the stack by cancelling random noise. To pick the most appropriate velocities, a plot is constructed of the stack that would result from applying NMO using different velocities. This is illustrated in Figure 3-33 where the CMP gather is shown along with 11 panels (on the right) that show the stacks that result from the velocity trends shown as black lines in the coloured panel on the left. The colours represent the “semblance” of the traces after NMO correction at different velocities. Semblance is defined as:

$$semblance = \frac{1}{m} \frac{\sum_t (\sum_{i=1}^m f_{i,t(i)})^2}{\sum_t \sum_{i=1}^m f_{i,t(i)}^2} \quad 3.5$$

where m is the number of traces in the stack, \sum_t is the sum over a defined time window and f is the trace amplitude. A stacking velocity that results in a high semblance is indicative of a velocity that best aligns trace peaks and troughs and is likely a good velocity pick.

Stacking velocities were manually picked using semblance and velocity-stack panels as guides; illustrated in Figure 3-33. Velocities were picked every 25 CMP's (62.5 m) and the resulting velocity model is illustrated in Figure 3-34. The model was smoothed to yield the final stacking velocity (Figure 3-35) that was used to remove NMO. An example of an NMO-corrected CMP gather is illustrated in Figure 3-36.

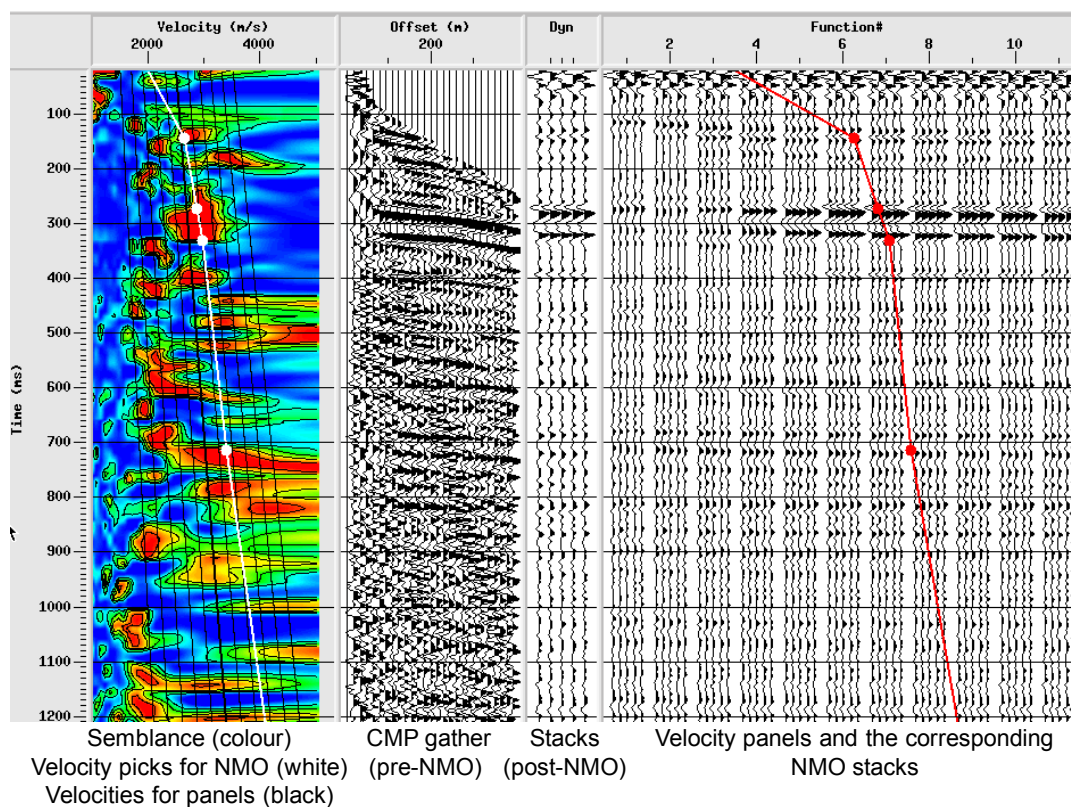


Figure 3-33: Stacking velocity picks with semblance and velocity-stack panels.

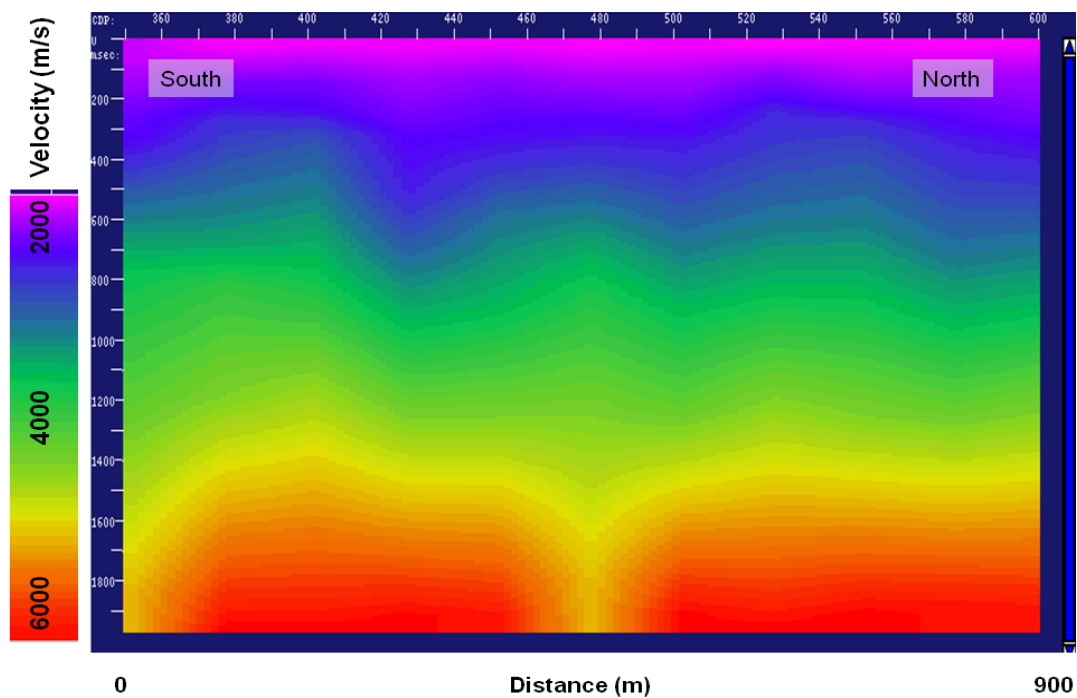


Figure 3-34: Initial stacking velocity model established from velocity picking.

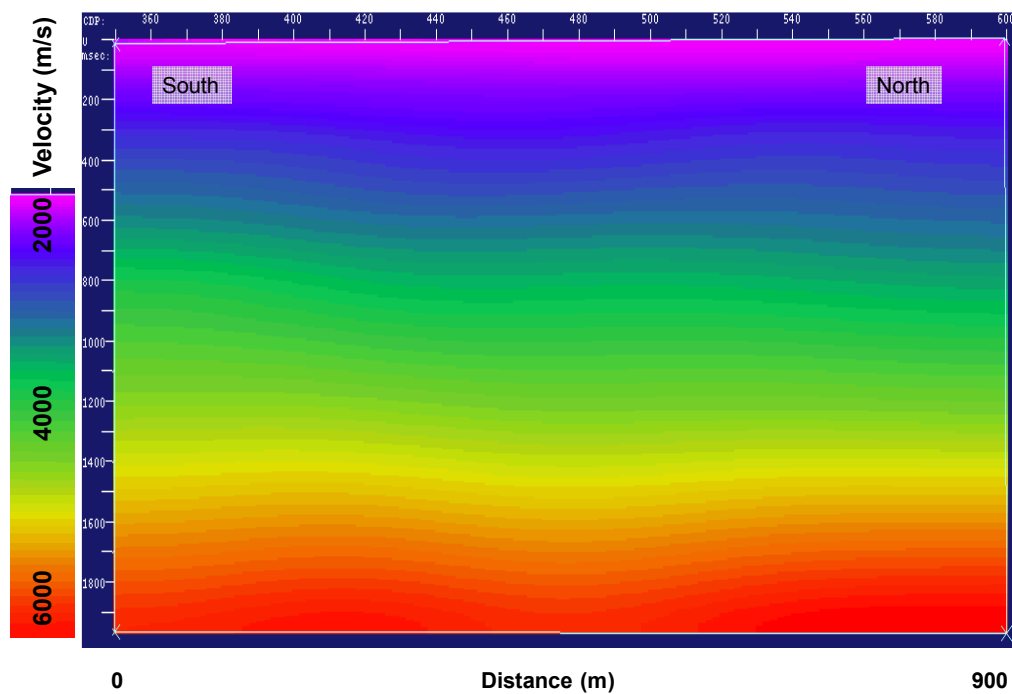


Figure 3-35: The smoothed model of stacking velocities.

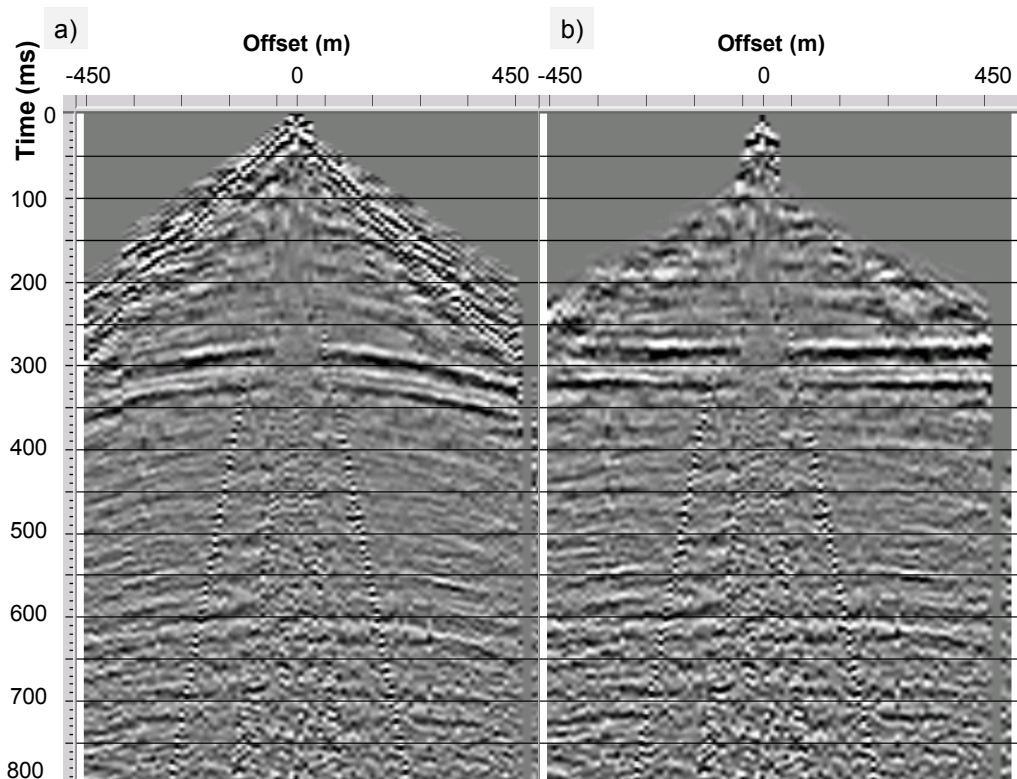


Figure 3-36: A CMP gather (a) before and (b) after NMO removal and application of the offset-dependant mute function.

Trace amplitudes were then corrected for variations that would be consistent in terms of the source or receiver point. This step corrects for source locations that are not as well coupled to the ground or receivers that are not as responsive as others. These variations should be surface consistent and were corrected with a surface consistent amplitude correction.

The data were stacked to yield the section shown in Figure 3-37. Significant noise is evident at the south end of the survey, especially in the events around 300 ms, due to the low fold in this area. In addition, random noise is visible throughout the section. F-x deconvolution, which acts like a trace-to-trace prediction filter, was applied in order to remove some of the lateral noise. The result is shown in Figure 3-38.

Binning traces by common mid-point (CMP) assumes that the reflectors are perfectly horizontal and that they do not scatter the wavefront beyond the simple reflection where the incidence/reflection angle are equal. Dipping reflectors will reflect the wavefront at equal incidence/reflection angles with respect to the normal to the reflector but the reflection point would not be the mid-point in this case. Also, reflector edges will scatter the wavefront. To compensate for these effects and to create an image that represents the true geometry and reflection strength of reflection points, seismic data are migrated.

In this case, the data were migrated post-stack using a Kirchhoff 2D time migration algorithm. Kirchhoff migration sums data amplitudes over equal travel time surfaces that are calculated from the given velocity model (in this case using the stacking velocities of Figure 3-35). The amplitudes in the sum are weighted by the angle of reflector obliqueness and, in the case of 2D migration, a 45° phase shift must be introduced into the summation to compensate for the fact that the data were collected in a 3D world, whereas the summation is only over 2D equal travel time. The migrated section is shown in Figure 3-39.

Because it was assumed in advance that reflector dip angles were less than 45° , the summation was restricted to obliquity angles up to 45° . This reduces computation time and because seismic events that dip at angles greater than 45° do not migrate, the

migration serves as a dip filter. This can be seen in comparing the migrated section of Figure 3-39 to the pre-migrated section of Figure 3-38. Note that the steeply dipping noise in the stack is effectively eliminated in the migrated section.

The migrated data were also filtered with a 5-10-100-110 Hz bandpass filter, and the trace amplitudes were normalized to the RMS amplitude of a trace in the centre of the section in a time window from 200 – 800 ms.

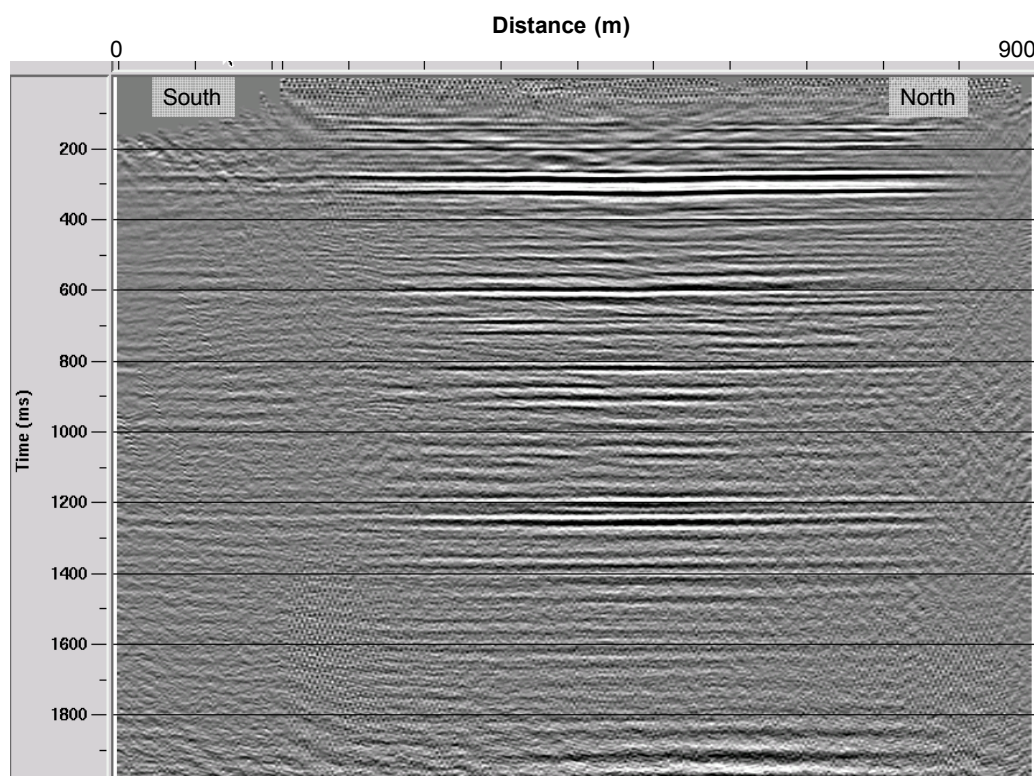


Figure 3-37: The complete seismic section after CMP stacking. The Ardley Coals are the prominent set of reflections around 300 ms.

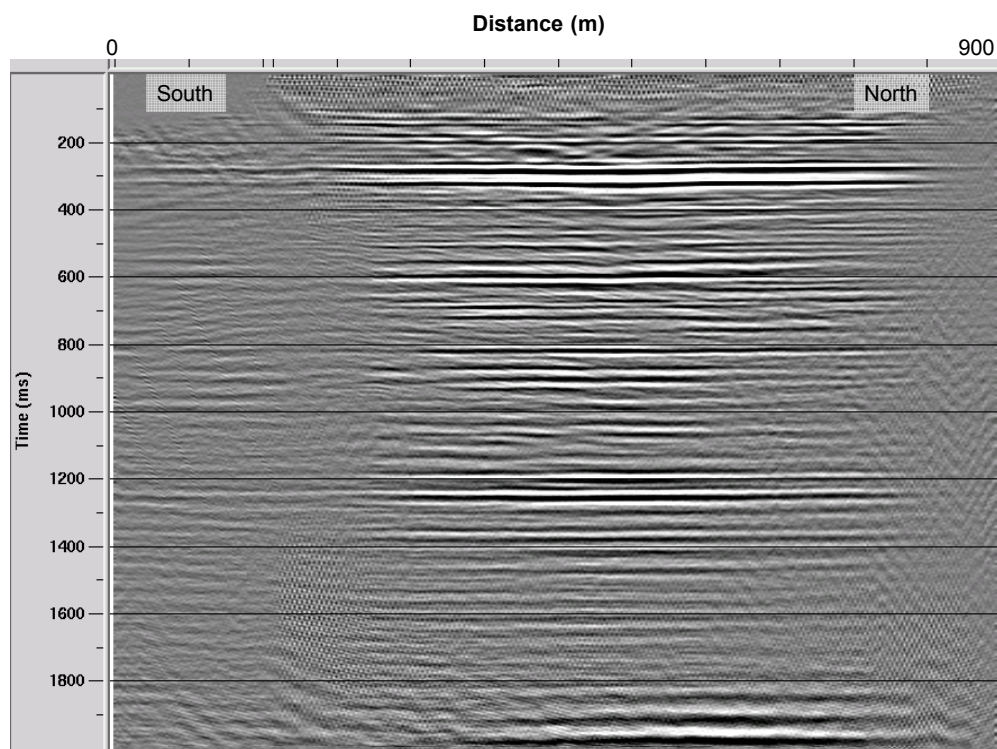


Figure 3-38: Stacked section after applying F-x deconvolution which reduces the incoherent lateral noise.

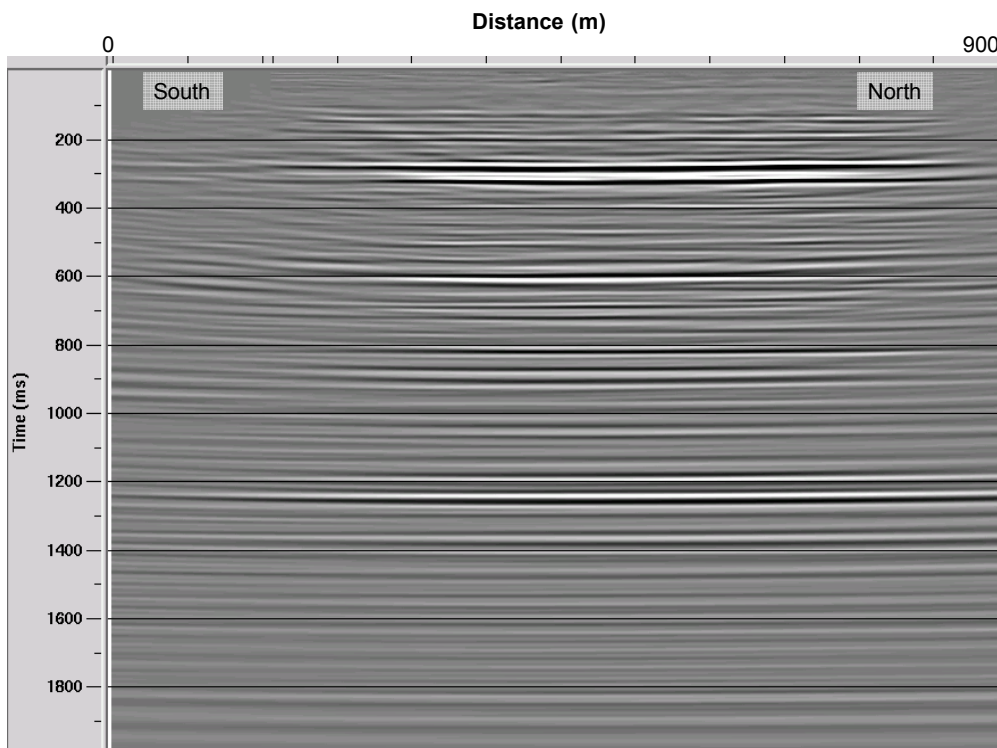


Figure 3-39: Section after post-stack Kirchhoff time migration.

3.5.3 Wavelet Estimation

Following the same procedure as the June 2006 data, a constant-phase wavelet was extracted from the data as shown in Figure 3-40. A normal incidence convolutional synthetic seismogram was constructed with the extended reflectivity well log from 102/7-28 and this wavelet. The zero-phase version of this wavelet gave a synthetic seismogram that could be tied to the reflections of the Ardley Coals to give an estimation of the time-to-depth relationship.

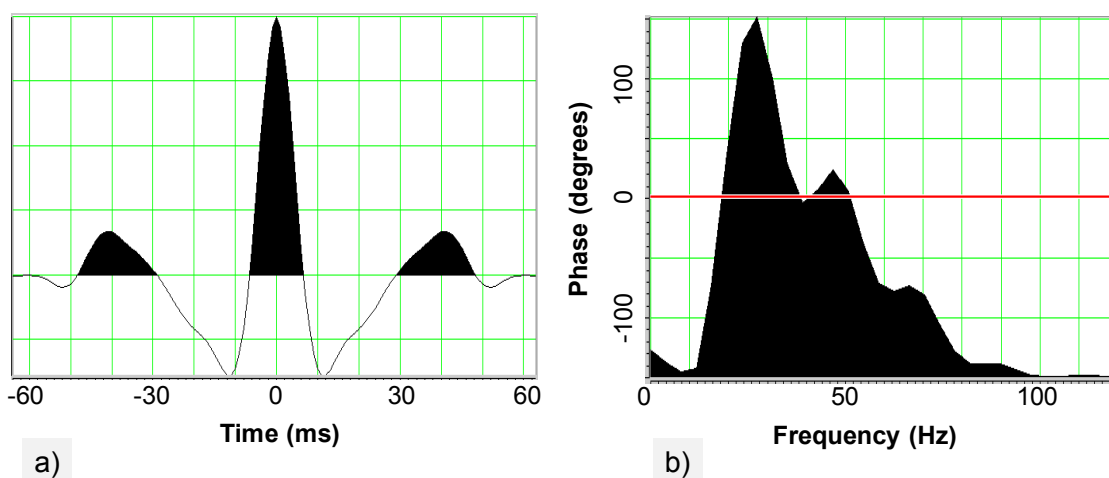


Figure 3-40: (a) The zero-phase wavelet extracted from the March 2007 migrated section using a window from 200 – 800 ms and the 50 CMPs nearest the 102/7-28 well, and (b) the amplitude and phase spectra.

Another method of estimating the embedded wavelet is to find the filter that best matches the synthetic seismogram from the reflectivity log to the seismic data using a least-squares method matching filter method (Hampson Russell Software online theory). Using the time-to-depth relationship that had been established, wavelet estimation was attempted using this matching filter method. However, a challenge in this project is that there is only a short window over which the seismic data is full fold and where the seismic data ties to the original well log from 102/7-28. As seen in Figure 3-36, the fold is high between 150 – 200 ms. On the other hand, Figure 3-10 shows that the petrophysical well data from 102/7-28 only extends to approximately 40 ms below the

base of the Ardley Coal Zone after which data has been spliced onto the 102/7-28 log from another well. Although it is expected that the donated log should help to interpret seismic events below the Ardley Coal Zone, it is not expected that the full length synthesized well should give a seismic-to-well tie of sufficient quality to allow wavelet estimation via a matching filter. Therefore, the window of correspondence between high fold seismic data and original well log data is a 220 ms window from roughly 150 – 370 ms for this survey. Although this is a short window, and standard practice suggests a longer window is recommended, the most believable seismic-to-synthetic tie in the Ardley Coal Zone was achieved by restricting the wavelet extraction window to the interval from 150 – 370 ms. The estimated wavelet is illustrated in Figure 3-41 which shows that the dominant period of the wavelet is about 24 ms.

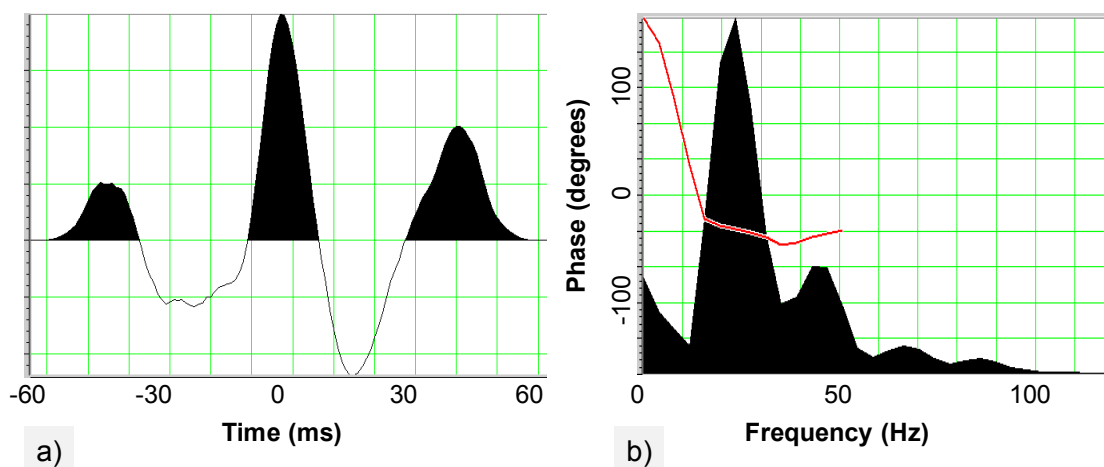


Figure 3-41: (a) The matching filter wavelet and its amplitude and phase spectra extracted by matching the 102/7-28 well to the migrated data in a window from 150 – 370 ms, and (b) the amplitude and phase spectra.

A synthetic seismogram was created using the match filter wavelet from Figure 3-41 and the extended 102/7-28 well log and its tie to the migrated section is illustrated in Figure 3-42, in which the seismic events of the Lower and Upper Ardley Coals have been correlated. Also visible in the section are seismic events at 600 ms and at 800 ms which may represent reflections from the top of the Belly River Formation and the Lea Park Formation, respectively. Given the arrival time of the event at 600 ms which is twice the

approximate arrival time of the Ardley Coal reflections, it is also possible that the event at 600 ms is a multiple reflection between the Ardley Coals and the ground surface. The lack of well-to-seismic correlation at events below the Ardley Coals might also be explained by the fact that the well data below 370 ms has been donated from the 100/05-31-04607W5 well which is approximately 4.5 km from 102/7-28 and may not truly represent the geology imaged by the seismic survey.

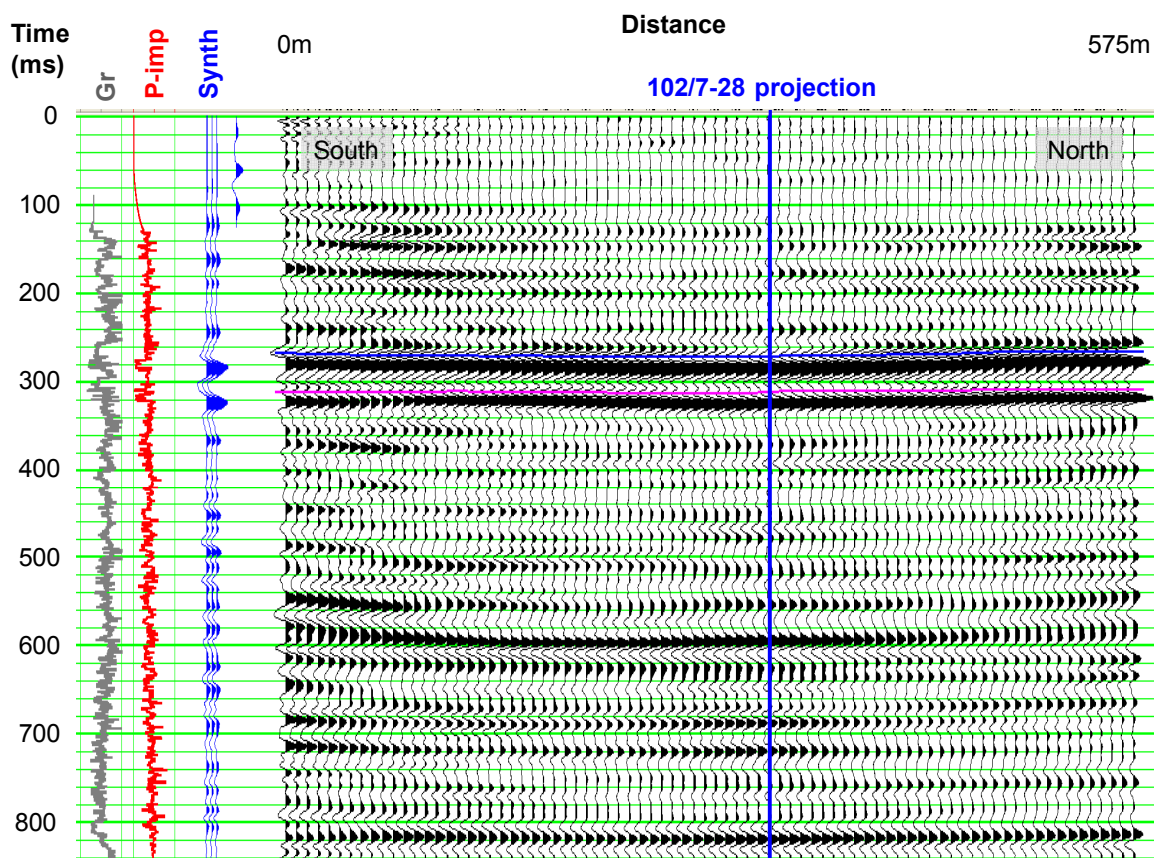


Figure 3-42: The migrated seismic section showing the seismic-synthetic tie and the interpretation of the Upper and Lower Ardley Coal events.

Figure 3-43 shows a detailed view of the synthetic-seismic tie at the Ardley Coal Zone events. As expected with the bandwidth and dominant period of the embedded wavelet, none of the coal zones are resolved. There are no distinct events for the top and bottom of the Lower Ardley Coal Zone or the sub-zones of the Mynheer or Silkstone coals.

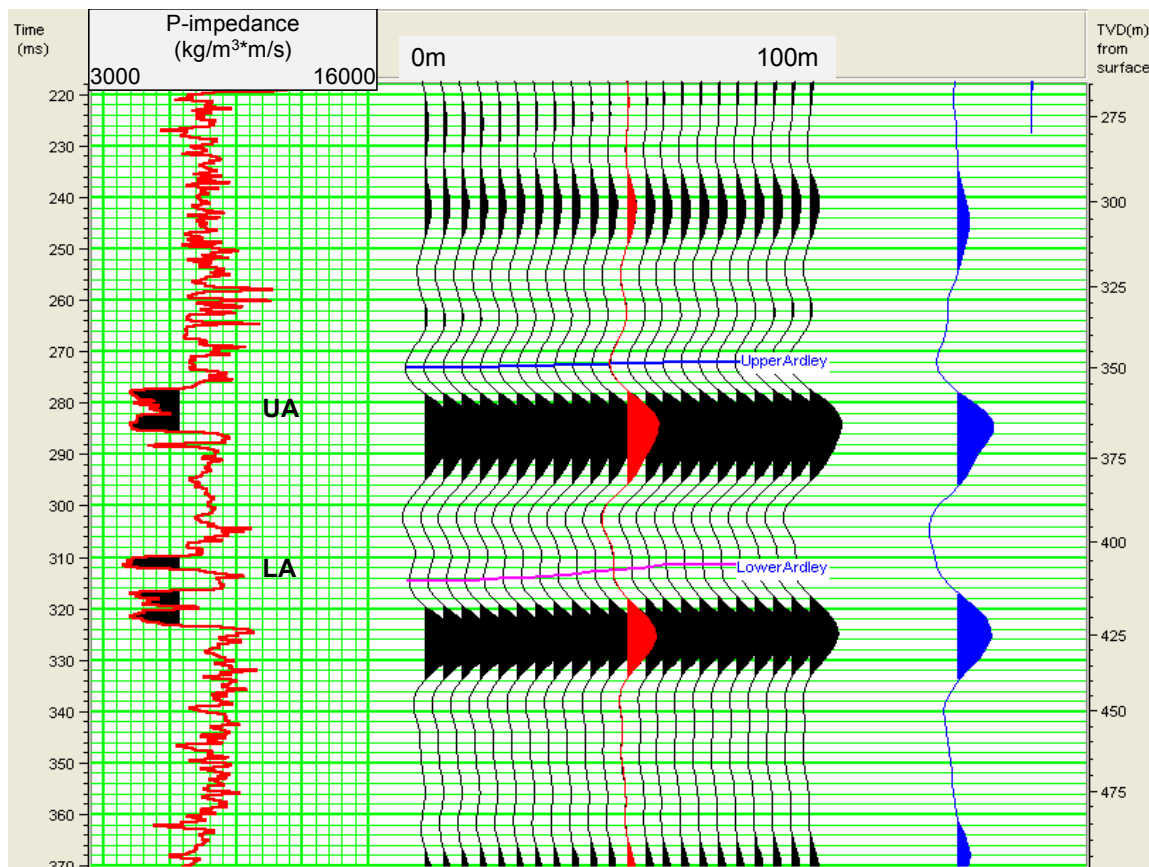


Figure 3-43: The synthetic-seismic tie and well tie in the Ardley Coal Zone using the matching filter wavelet.

3.5.4 Conclusions from the March 2007 Survey

Several conclusions can be drawn from the March 2007 survey:

- The frequency content in the field data appeared to have a more balanced energy spectrum in the frequency band 25 – 50 Hz, relative to the June 2006 data which showed a distinct drop off in energy above 25 Hz. The increased high frequency content is likely related to better source and receiver coupling as well as reduced attenuation in the frozen earth in the winter March 2007 survey.
- The data acquired in March 2007 again confirmed that the near offset data was contaminated by source noise and that at offsets greater than 500 m the refracted first arrivals contaminated reflections from the Ardley Coals. Radial trace filtering

was reasonably successful at reducing the contamination due to these coherent noises.

- Gabor deconvolution was very effective in enhancing the high frequencies in the data and the finally migrated section showed effective bandwidth up to 100 Hz with a reasonably constant-phase extracted wavelet.

Ultimately, the utility of the 2D surveys is to gauge the capabilities of the seismic method to characterize the thin zones of the Ardley Coals in advance of the 3D survey and to assist in designing an efficient acquisition and processing program for the 3D survey. The results show that while the data quality and frequency content should be adequate to differentiate the Upper and Lower Ardley Coals, frequency content limits may prevent resolution of the thinner subzones of the Ardley Coals. Additionally, the results show that offsets beyond 500 m may not be useful.

Chapter Four: 3D – Acquisition, Processing and Interpretation

4.1 Introduction

A 3D survey was acquired at the Alder Flats project site in June of 2007. The survey coverage encompassed the 102/7-28 and 100/7-28 well. Although the survey was originally intended to form the baseline survey for a time-lapse study to track the injection of CO₂, no monitor survey has been conducted. However, as discussed in Chapter 1, because 180 tonnes of CO₂ had been injected in September of 2006, analysis was directed at determining if any footprint of the injected CO₂ could be detected with seismic data.

This chapter discusses the data acquisition, processing flow, and interpretation of the vertical component seismic data with particular attention paid to the reflection character of the Lower Ardley Coal Zone. The horizontal component data is discussed in Chapter 5.

4.2 Survey Design

Ideally in a 3D survey, each CDP will be sampled evenly by the survey fold and the range, distribution and azimuth of source/receiver offsets. Since ideal sampling is not possible, a survey layout is designed with the intent to minimize the bias or asymmetry in the CDP sampling program.

Before commencing with the field work, the survey parameters were assessed using the CREWES QUADDES program. The vertical component survey was designed to be 560 x 560 m with 10 receiver and 10 source lines each spaced 60 m apart. The receiver and source interval was 10 m, the CDP bin size was 5 x 5 m, and both the source and receiver intervals were offset from the line intersections by 5 m. The maximum offset for the assessment was assumed to be 500 m because, as demonstrated in Chapter 3, reflections from the Ardley Coals at offsets greater than 500 m are typically contaminated by refracted energy.

The survey layout design and the corresponding fold map for a reflector at 400 m depth are shown in Figure 4-1 which shows that the fold drops below 10 within

approximately 30 – 80 m of the survey perimeter. The offset coverage (Figure 4-2) shows that the minimum offset is less than 100 m throughout the survey, but that maximum offsets above 400 m are achieved only in the central region of the survey. However, while the maximum offset in the central regions of the survey is high, Figure 4-2(c) shows that there is modest non-uniformity in offset ranges in this region and that the acquisition pattern may leave a footprint in the survey. Figure 4-3 shows a rating of the quality of the distribution of source/receiver offsets and azimuths. The azimuth distribution quality is high in the central regions of the survey, but the offset distribution again imprints a signature in the CDP sampling pattern.

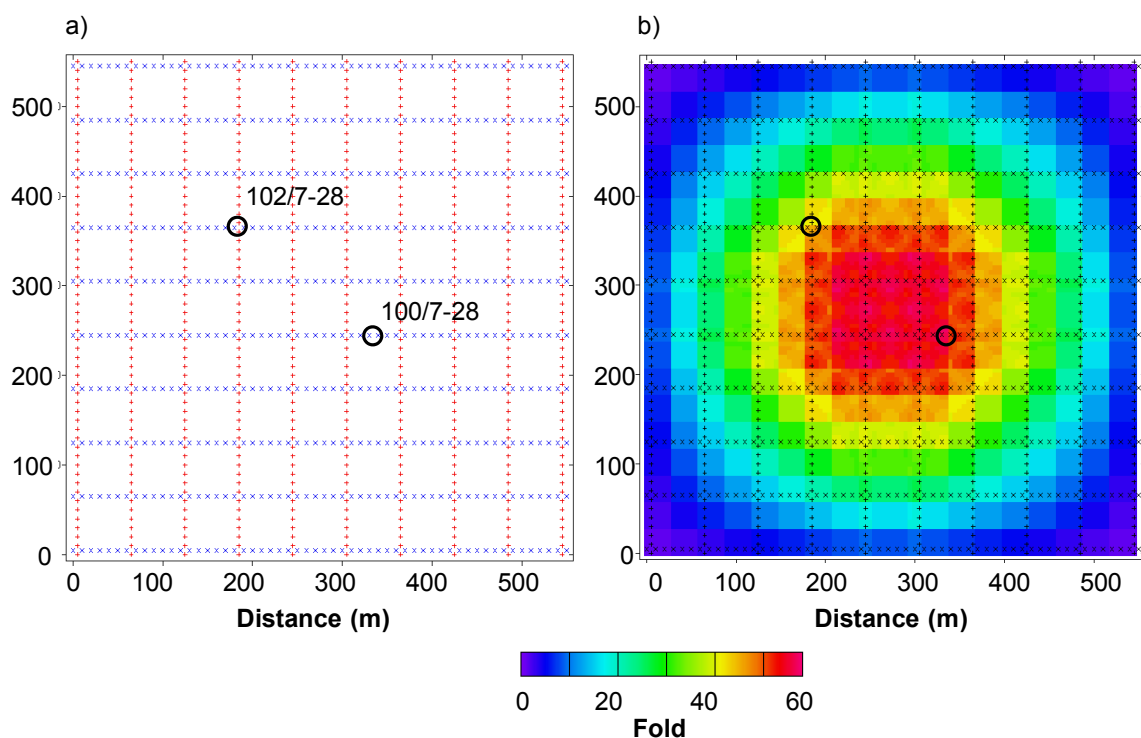


Figure 4-1: (a) The survey design for the vertical component survey, and (b) the associated fold map. Source lines (red) run north-south and receiver lines (blue) run east-west. The black circles show the locations of the 102/7-28 and 100/7-28 wells.

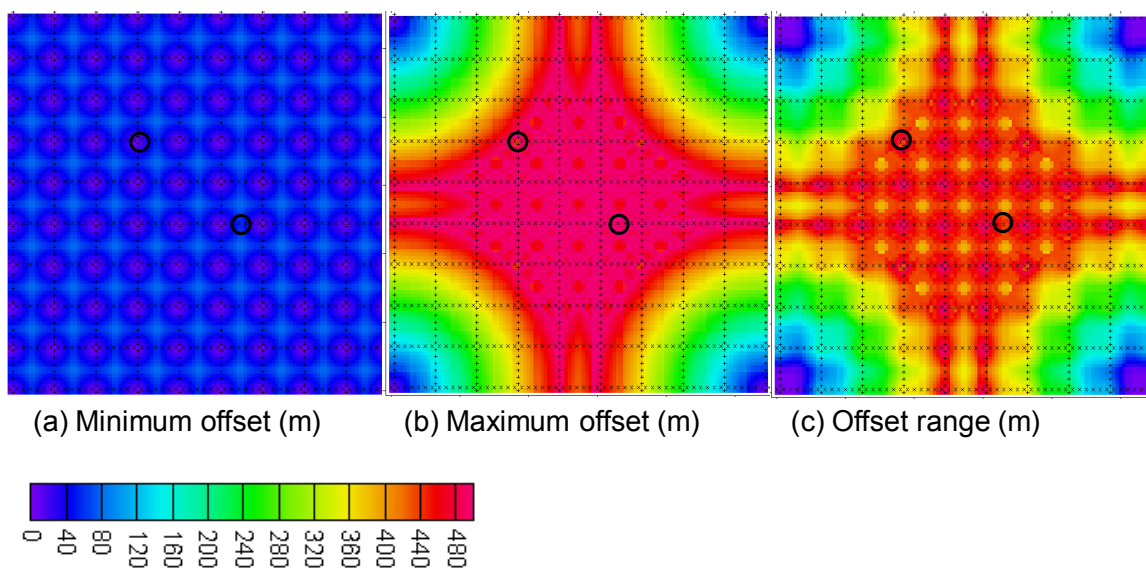


Figure 4-2: Maps of the offset attributes for the survey design. The black circles show the location of the 102/7-28 and 100/7-28 wells.

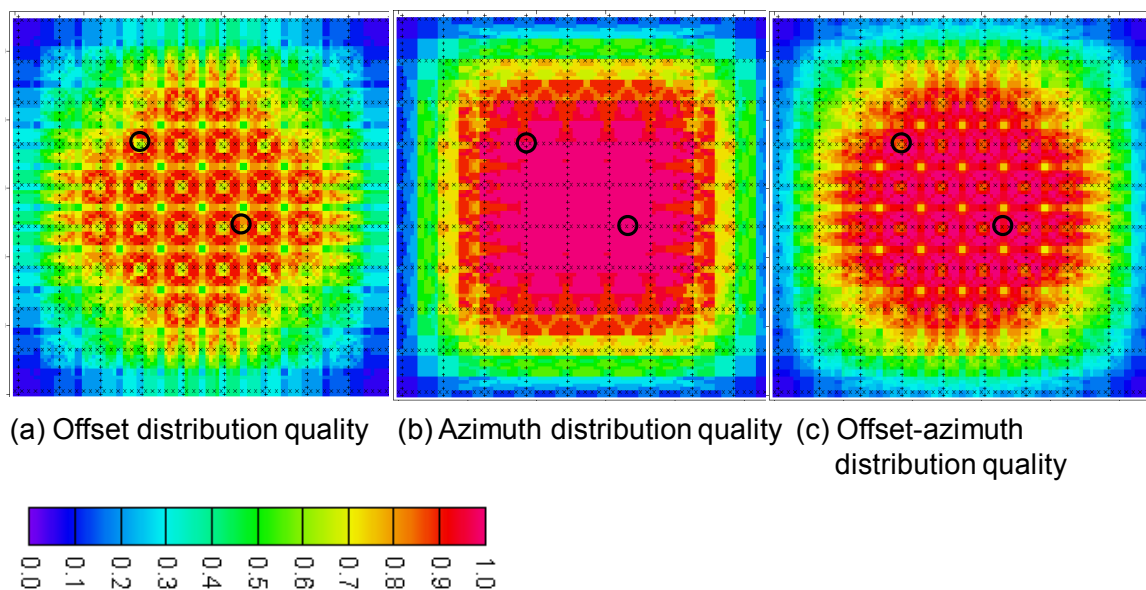


Figure 4-3: Maps of the offset and azimuth distribution quality for the survey design. The black circles show the locations of the 102/7-28 and 100/7-28 wells.

4.3 Acquisition

The acquisition parameters for the 3D survey, acquired on June 6 – 8, 2007, are listed in Table 4-1. As planned, the entire patch of receivers was live during the entire shoot. An areal view of the layout and the actual layout are illustrated in Figure 4-4 and Figure 4-5. Pipeline laybacks, well head infrastructure, a pond in the southeast corner of the spread, and other obstacles prevented the source and receiver grid from being perfectly regular. As discussed further in Chapter 5, the survey included acquisition of a single line of 3C geophones on the east-west receiver line that intersected the 102/7-28 well. The three-component geophones took the place of the vertical component geophones along this line.

Table 4-1: Acquisition parameters for the June 2007 3D vertical component survey.

Source	EnviroVibe 10-180 Hz – 4 sweep diversity stack
Receiver line orientation	10 lines: East-west
Receiver line and receiver spacing	60 m line spacing and 10 m receiver spacing
Receivers	1C SM-24 Marsh phone (10 Hz dominant) and I/O sensor SM-24 3C geophones (single line)
Source line orientation	10 lines: North-south
Source line and source spacing	60 m line spacing and 10 m source spacing
Sweep length	12 second sweep
Listen time	14 seconds
Correlated record length	2 seconds
Ground conditions	Dry summer
Patch live	All



Figure 4-4: The survey layout in the field. Source lines run north-south and receiver lines run east-west.

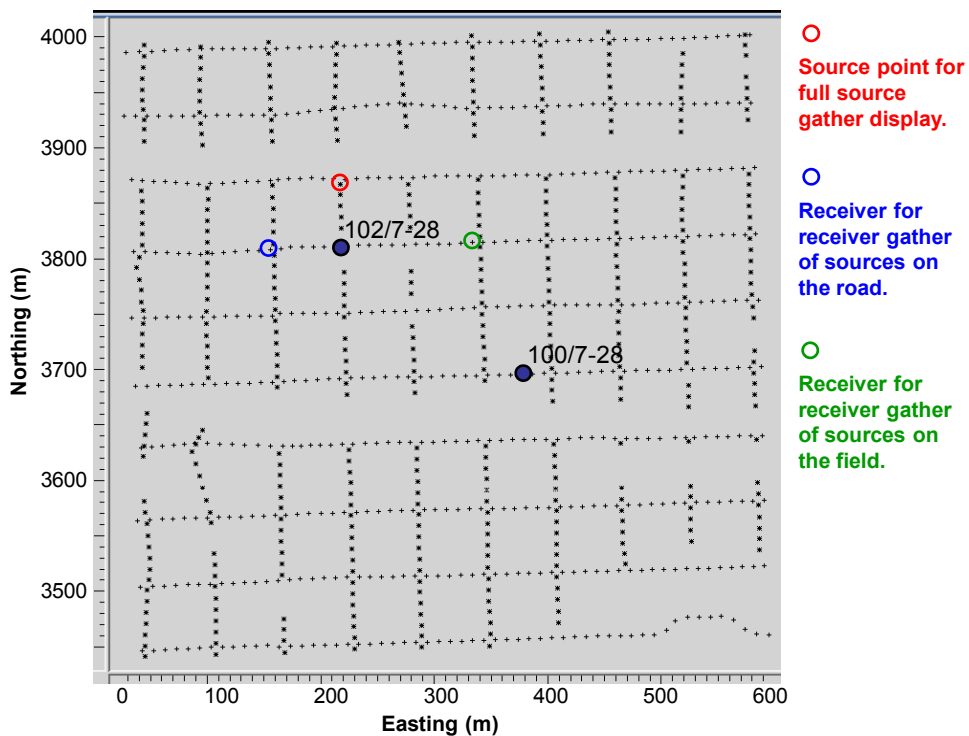


Figure 4-5: The actual layout for the vertical component survey. The coloured circles show the locations of sources or receivers for the gather in the following figures.

Figure 4-6 shows a complete shot gather for the source point labelled in Figure 4-5. The amplitudes are dominated by the first break refracted energy and the late arriving ground roll. Figure 4-7 shows the same source gather with a 200 ms window automatic gain control applied to amplify other events such as the Ardley Coal reflection events around 300 – 400 ms. Again the reflection events of the Ardley Coals are contaminated by direct source noise (air blast and ground roll) at the near offsets.

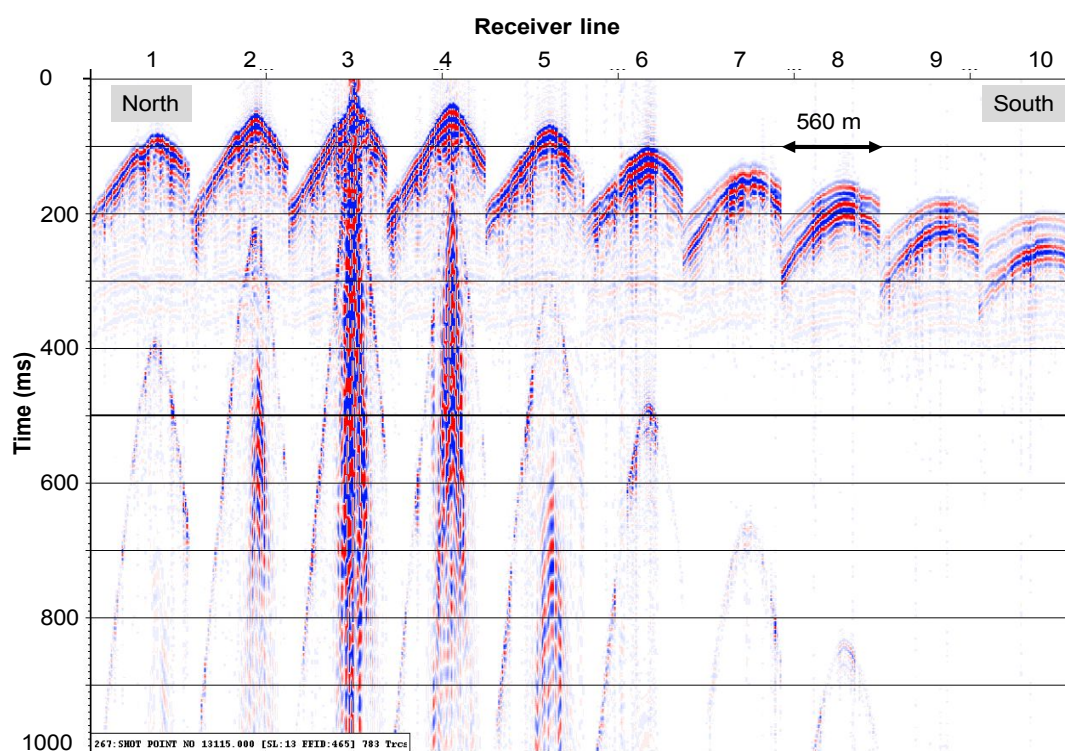


Figure 4-6: A complete source gather with no data enhancement. The source is on receiver line #3.

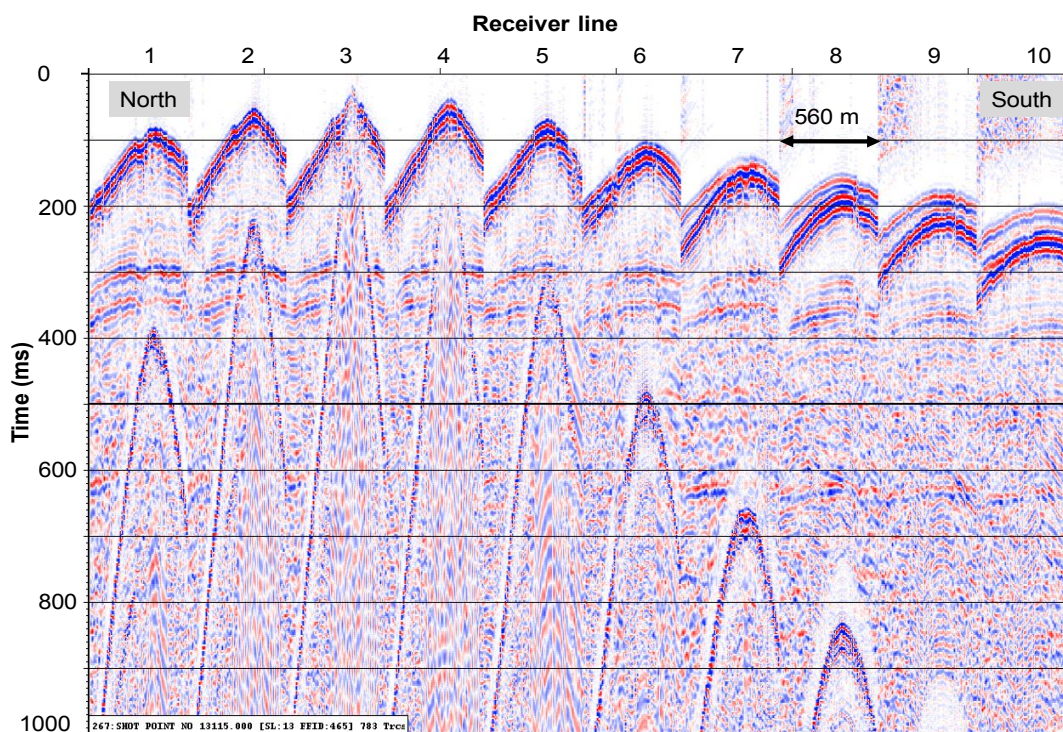


Figure 4-7: A complete source gather with a 200 ms window automatic gain control. The source is on receiver line #3.

A partial receiver gather of raw data from the survey is shown in Figure 4-8. The gather is for the receiver immediately west of the north-south road and immediately west of the 102/7-28 well as indicated in Figure 4-5. The gather includes only sources positioned along the road. The amplitude spectrum for the data in the blue box in Figure 4-8 is illustrated in Figure 4-9. The equivalent figures for a receiver gather where the receiver and the sources are in the grassy field (location shown in Figure 4-5) are illustrated in Figure 4-10 which show the receiver gather and Figure 4-11 which shows the amplitude spectrum. Overall, the data quality does not appear to be distinctly different between the gather on the road and the gather in the field.

The gather on the road has an analogue in each of the June 2006 and March 2007 2D surveys (Figures 3-5 and 3-14). In comparing the amplitude spectra between all of the surveys, the summer surveys appear to show a more pronounced peak in the recorded data at 25 Hz whereas the winter data has a more broadband peak between 25 – 50 Hz, again likely explained by the frozen ground conditions during the winter survey.

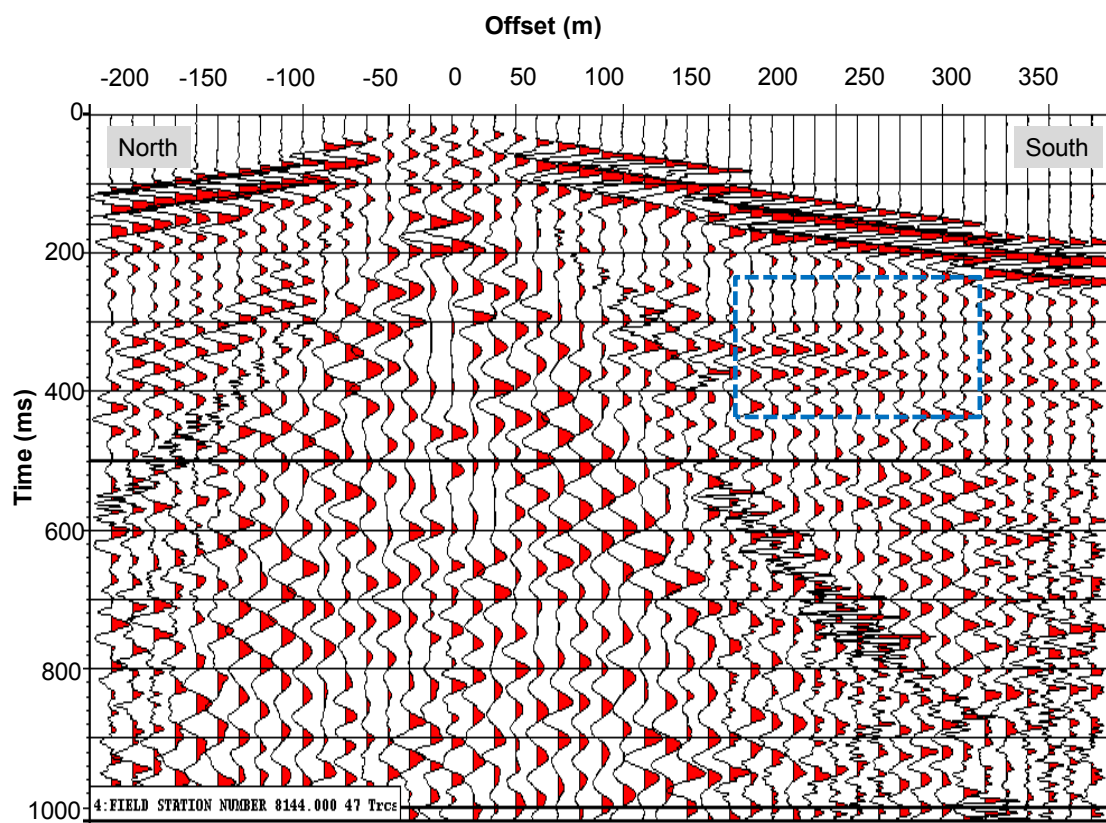


Figure 4-8: A raw receiver gather from the June 2007 3D survey. The gather is for the receiver beside the north-south road nearest the 102/7-28 well and the sources are those along the north-south road.

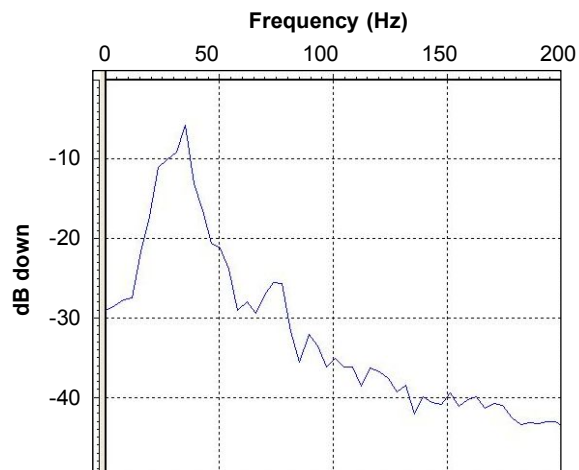


Figure 4-9: The amplitude spectrum for data in a 180 ms window around the Ardley Coal events in Figure 4-8.

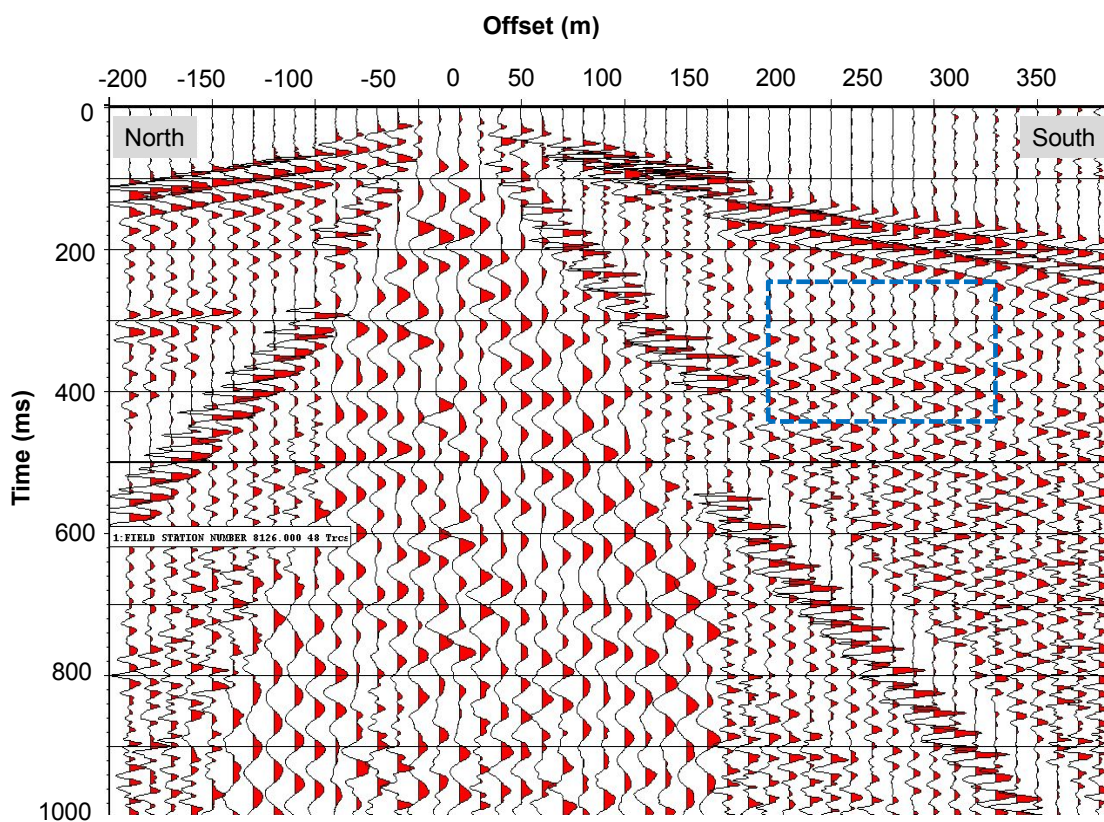


Figure 4-10: A raw receiver gather from the June 2007 3D survey. The gather is for a receiver in the grassy field with all sources in a north-south line in the grassy field.

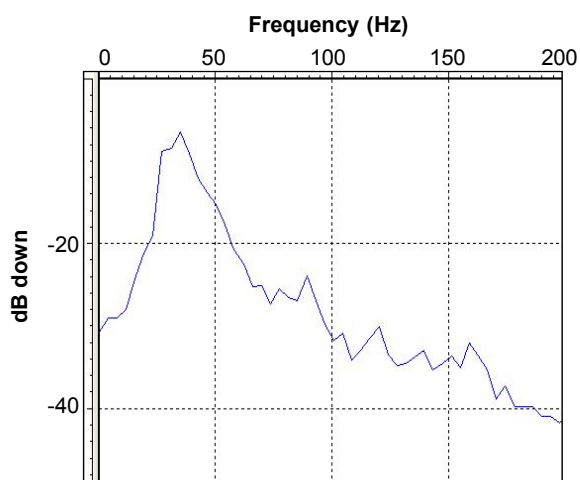


Figure 4-11: The amplitude spectrum for data in a 180 ms window around the Ardley Coal events in Figure 4-10.

4.4 Data Processing

The data were processed by Sensor Geophysical Ltd. using a flow intended to preserve true amplitude. The flow, listed in Table 4-2, avoids the use of short length automatic gain control and time varying spectral whitening. The geometry for the vertical component data was processed as 111 inline (east-west) bins and 110 cross-line (north-south) bins giving 5 x 5 m CMP bins. A fold map, generated by quantifying the number of traces in each CMP bin in the pre-stack gathers, is illustrated in Figure 4-12 which shows that the fold drops below 10 within approximately 30 – 80 m of the survey perimeter. Some lineation patterns are evident in the fold distribution. Also, some asymmetries result from source and receiver locations that were missed due to obstacles such as wellheads, pipelines, ponds and foliage.

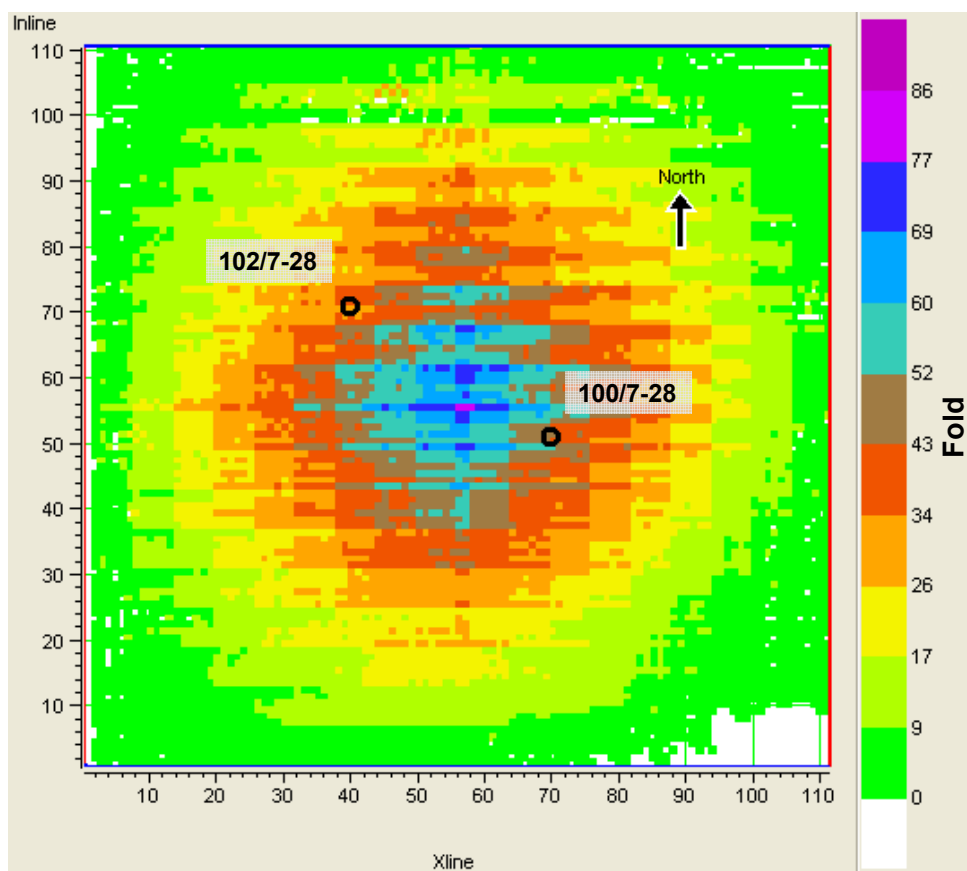


Figure 4-12: The fold attained in the vertical component data.

Table 4-2: The processing flow for the vertical component data.

Flow step	Parameters
Geometry bin spacing	5m x 5m
Trace edit and noise attenuation	
Offset amplitude recovery	No array correction No emergence angle correction 4 dB/second correction
Refraction and elevation statics	Replacement velocity was 2500 m/s
Air blast attenuation	Two passes Velocity of energy attenuated = 340 m/s Air blast enhancement filter=25-40-250-280 Hz
fk filter	Two passes Vibroseis ground roll fk filter
Q compensation	Use velocities from data base (second pass processing)
Surface consistent deconvolution	Shot, Receiver, Offset 100 ms operator length Design window: 84-1500 ms at 5m 485-1600 ms at 770m
Vibroseis decon compensation	
NMO correction	
Surface consistent amplitude scaling	Shot and receiver
Offset consistent gain control	Sensor Geophysical proprietary process
Stack	
F-XY deconvolution	# inline/crossline in filter = 3 # inline/crossline in design window = 9 Time window length = 100 ms

Finite difference 3D time migration	65 degrees
Time varying band pass filter	to 500 ms: 5-10-70-90 Hz after: 10-15-40-60 Hz
AGC	1.0 sec operator length

Several significant differences can be noted between the processing flow employed for the 3D data and for the March 2007 2D data:

- In the 3D data the coherent noise related to the air blast and surface waves were reduced by fk filtering, whereas the radial trace filtering tool was used for the March 2007 2D. As discussed in Chapter 3, fk filtering method attenuate or enhance all events, noise or otherwise, that have similar frequency and wavenumber, whereas radial trace filtering can be used to target specific events.
- For the 3D data a surface consistent spiking deconvolution step was used, whereas for the March 2007 2D data a Gabor deconvolution step was used that was not surface consistent.
- In processing the 3D data, Q compensation was applied whereas it was not in the March 2007 2D.
- For the 3D data a vibroseis deconvolution compensation process was used. The intention of this step is to remove any residual phase distortion that may remain after surface consistent spiking deconvolution as a result of the mixed-phase nature of the vibroseis field data. Processing of the March 2007 2D data did not account for the mixed phase nature of the field data.
- The 3D data was time migrated with a finite-difference algorithm, where a Kirchhoff time migration process was applied to the March 2007 2D data.
- In order to minimize the amplitude artefacts introduced into the 3D data amplitudes, no attempt was made to balance the amplitudes after stacking or migration. The trace amplitudes were equalized after migration in the case of the March 2007 2D data.

4.5 Interpretation Vertical Component Post Stack

4.5.1 Base Map

The migrated 3D seismic volume is depicted in Figure 4-13 and a time slice through the volume at 300 ms is illustrated in Figure 4-14. The figure also shows the location of a north-south crossline #40 and an east-west inline #71 that intersect the 102/7-28 well. Unless otherwise stated, figures in this thesis that show sections from the volume will show either of these two sections. The sections themselves are depicted in Figures 4-15 and 4-16.

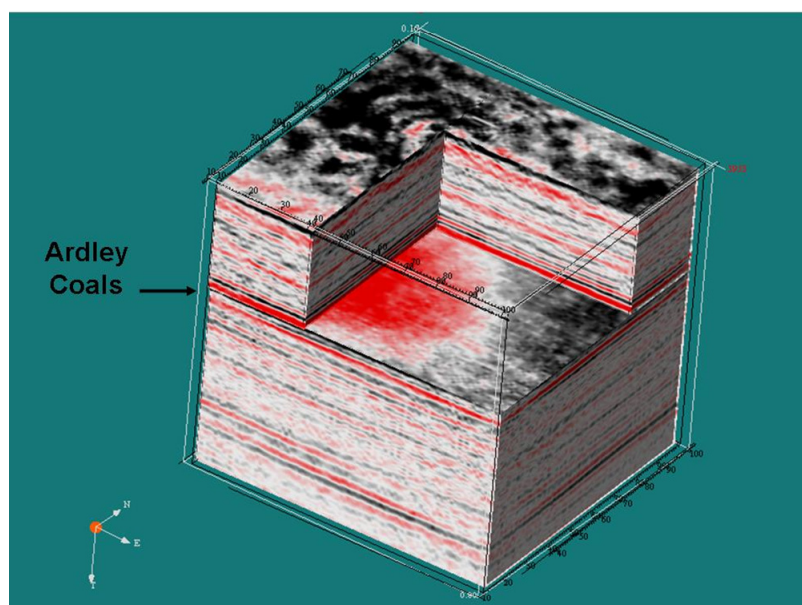


Figure 4-13: The migrated 3D PP data volume showing a chair display with a time slice at the level of the Ardley Coals.

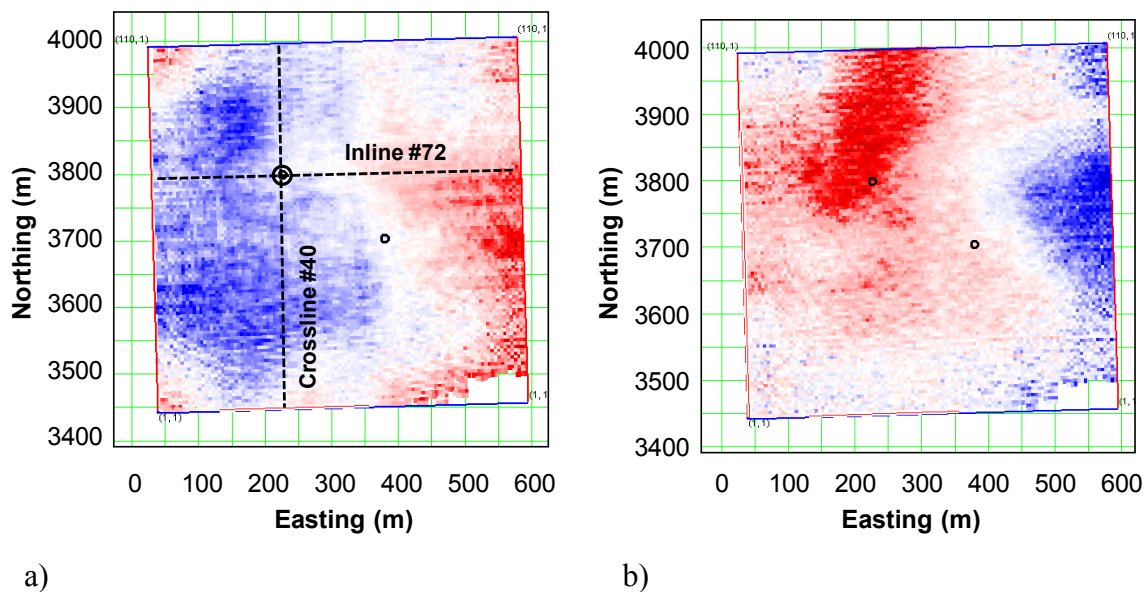


Figure 4-14: A time slice at (a) 250 ms and (b) 300 ms through the seismic volume. Inline #71 and crossline #40 intersect the 102/7-28 well and are often referred to in this thesis.

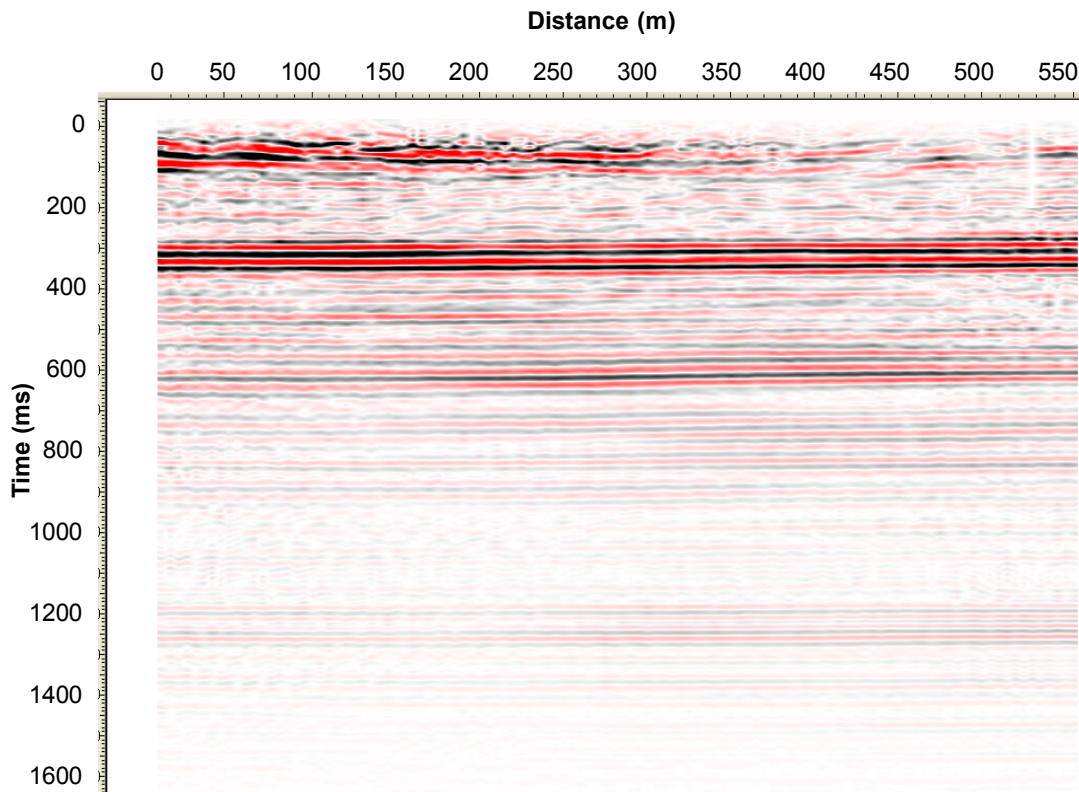


Figure 4-15: Cross section from the 3D volume showing Inline #71. The Ardley Coal events are between 300-350 ms.

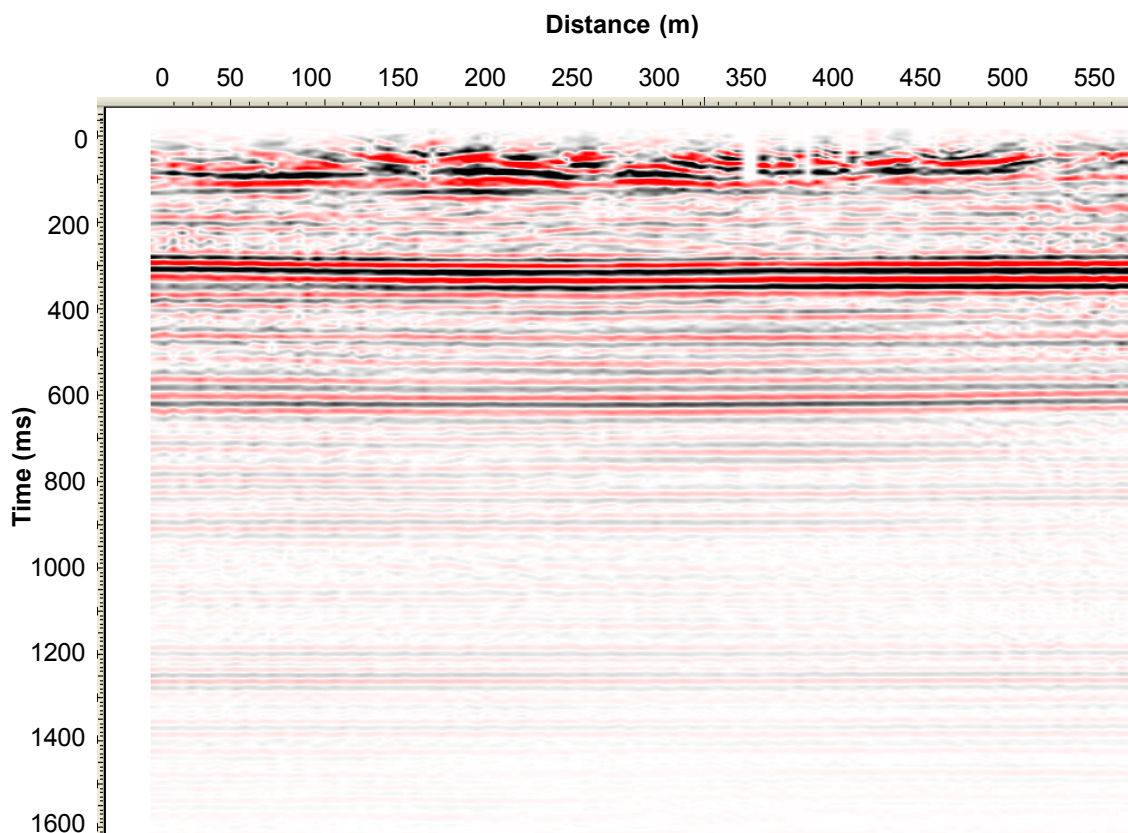


Figure 4-16: Cross section from the 3D volume showing Crossline #40. The Ardley Coal events are between 300-350 ms.

4.5.2 Wavelet Estimation

The autocorrelation of several traces near the centre of the survey over a time window from 200 – 800 ms gave a constant (zero-) phase estimate of the wavelet. With this wavelet a synthetic seismogram was created and a tentative time-depth tie was achieved by correlating significant reflection events between the seismic and synthetic seismogram. The cross-correlation in a window from 180 – 380 ms (encompassing the Ardley Coal reflections) was 0.83 using this wavelet. The zero-phase wavelet extracted using this technique and its amplitude and phase spectra are illustrated in Figure 4-17. The wavelet shows energy up to 80 Hz; however the energy is significantly diminished above 50 Hz. To check that this bandwidth is truly representative of the signal bandwidth, the amplitude spectrum found from the Fourier transform of each trace in a section from

the 3D volume is illustrated in Figure 4-18. The figure confirms that the signal is bandlimited between 10 – 50 Hz.

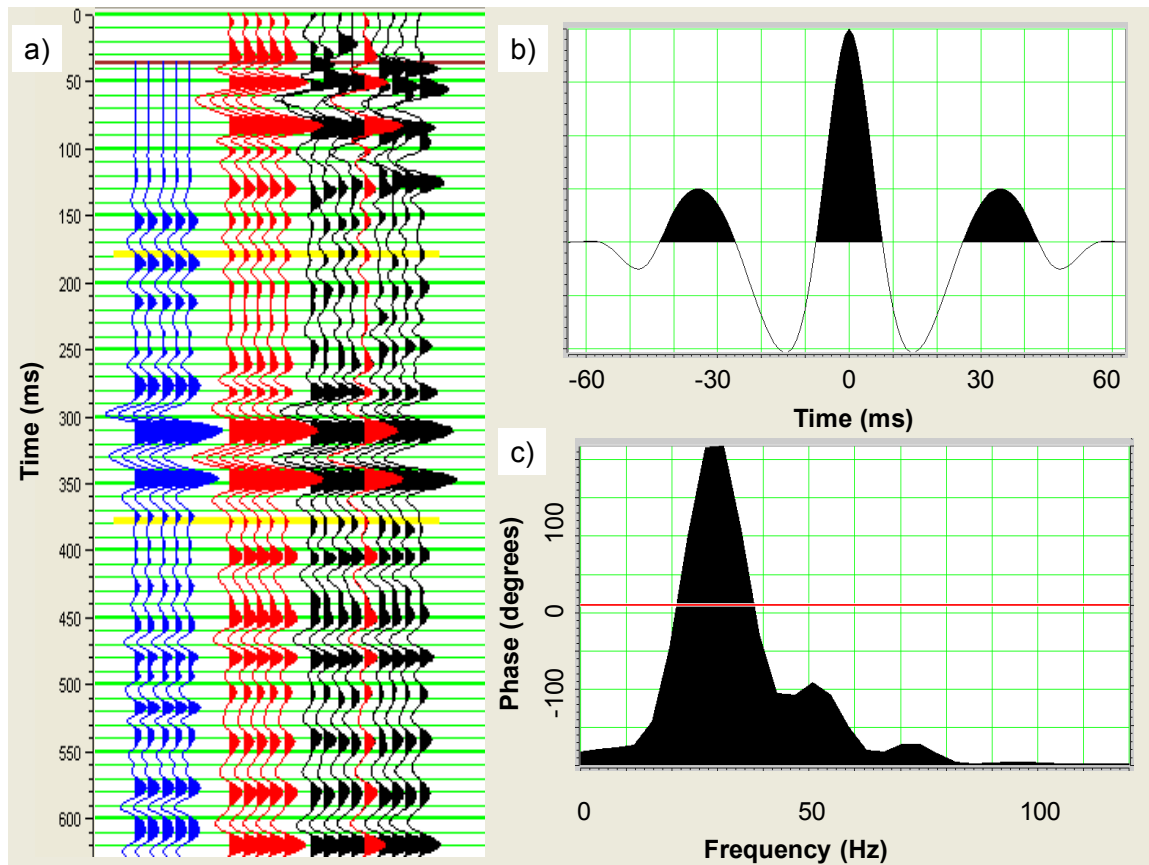


Figure 4-17: The tie between the synthetic seismogram and seismic data achieved with the wavelet extracted using the autocorrelation of the traces over a window from 180 – 800 ms. (a) The blue traces are synthetic seismograms, the red traces are a single composite of the black trace actual data. (b) the wavelet and (c) the amplitude and phase spectra.

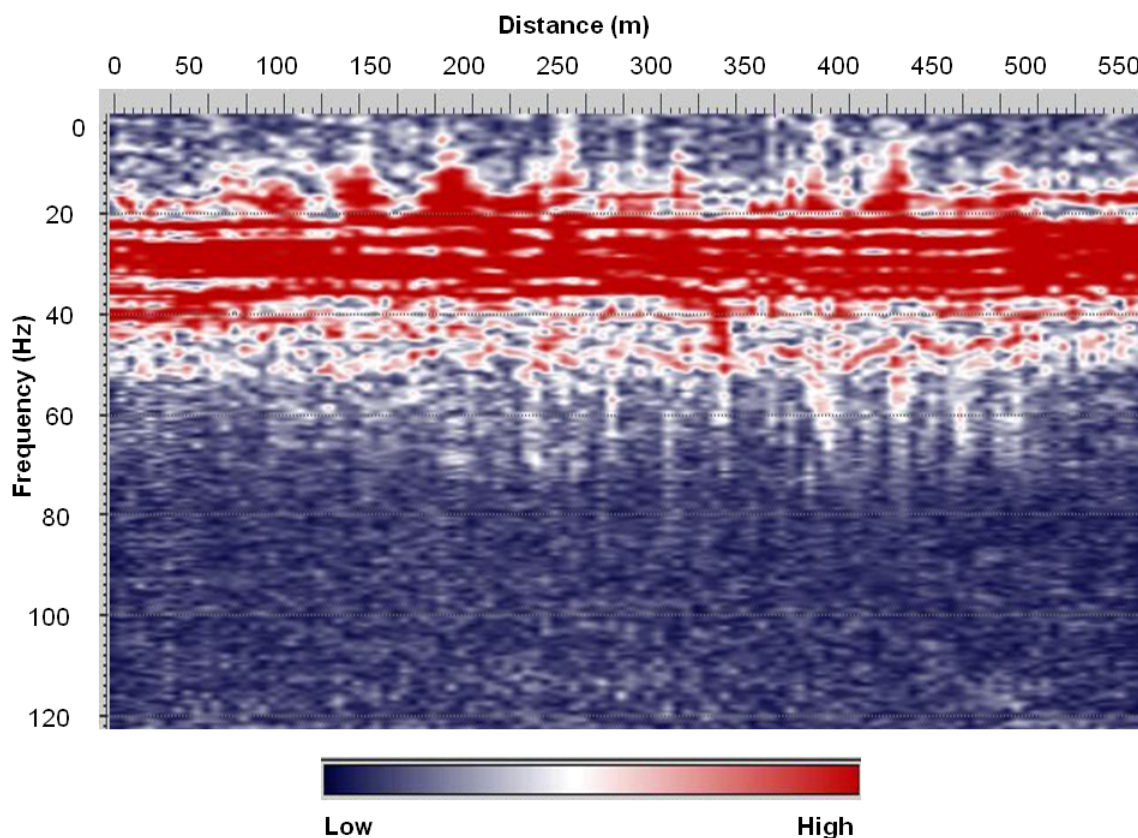


Figure 4-18: The amplitude spectrum of each trace in crossline #40 section that intersects the 102/7-28 well.

The Ardley Coal events are represented by a dominant trough/peak doublet that ties quite well to the synthetic seismogram (Figure 4-17). An attempt to improve the tie in zones other than the Ardley Coals resulted in significant and unacceptable shifts in the time-depth relationship. Since the ultimate objective is to analyze the Ardley Coal reflections, the tie in this zone alone was believed to be adequate.

After initially estimating the time-depth relationship, a second estimation of the embedded wavelet was attempted by finding the filter that best matched, in a least-squares sense, the well data reflection series to the seismic data (Hampson Russell Software online theory). The filter is limited and tapered in time to give the wavelet estimation. An initial wavelet was extracted, then the synthetic-to-seismic tie was re-evaluated, and finally a revised wavelet was extracted. With this final “match filter wavelet”, the synthetic-to-seismic cross-correlation is 0.92 over a window from 180 –

380 ms. The synthetic-to-seismic tie and the extracted wavelet are shown in Figure 4-19. Again, events in the Ardley Coal Zone tie well between the synthetic and seismic data, but events at earlier and later times are not as easily correlated. This is likely due to the low fold of the seismic data at early times and that events at times later than the Ardley Coals correlated to the well where the data have been spliced from the 5-31-46-7W5M well.

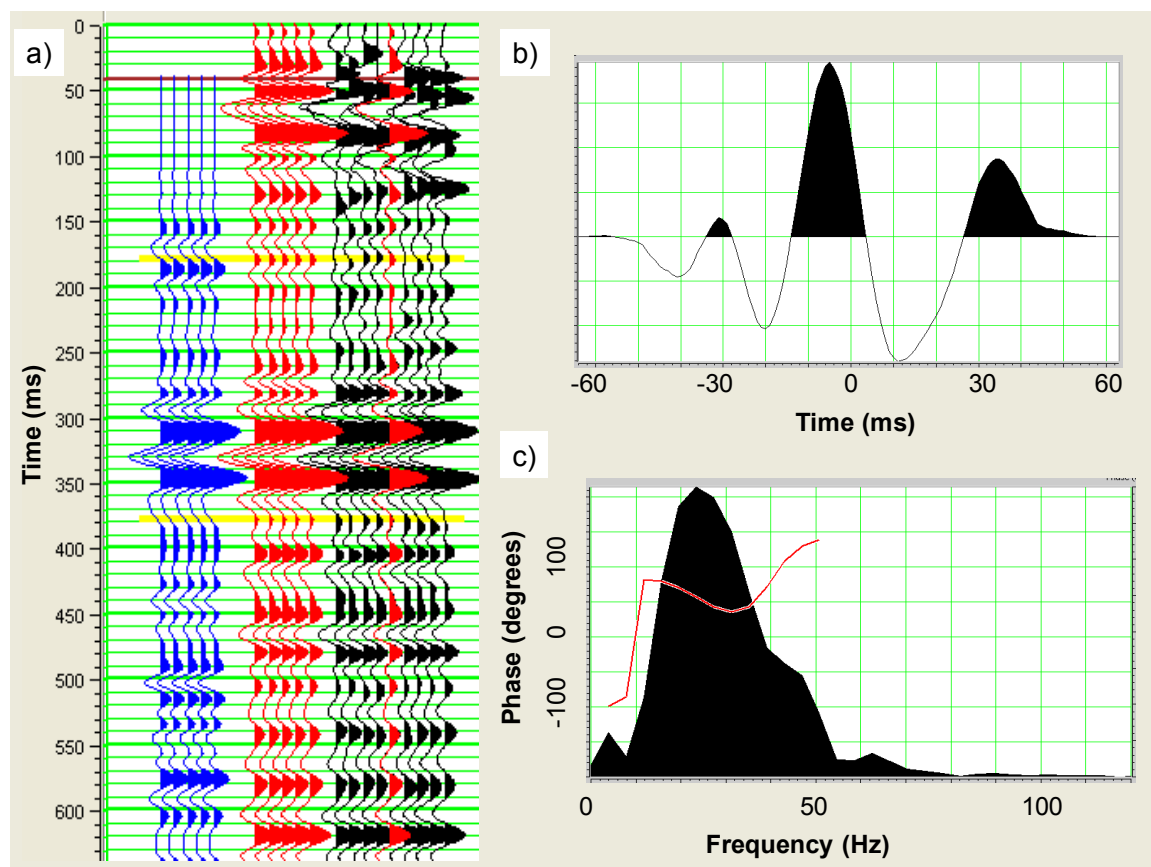


Figure 4-19: The tie between the synthetic seismogram and seismic data achieved with the wavelet extracted as a matching filter between the 102/7-28 well reflectivity log to the seismic data over a window from 180 – 380 ms. (a) The blue traces are synthetic seismograms, the red traces are a single composite of the black trace actual data. (b) the wavelet and (c) the amplitude and phase spectra.

The wavelet shows energy up to 80 Hz, but again the energy is significantly diminished above 50 Hz. Also, the wavelet has a dominant period of approximately 30 ms. Figure 4-20 shows the tie between the synthetic seismogram and the seismic data in

the time window of the Ardley Coal Zone. The figure shows that the Lower and Upper Ardley Coal Zones are resolved as distinct events, but the Silkstone and Mynheer zones of the Lower Ardley Coal Zone are not resolved. This is not surprising since, as indicated in Table 3-1 and 3-2, the Silkstone and Mynheer coals as well as the shale package between them would be at or below the absolute resolution limit ($\lambda/8$) for a wavelet with a 30 ms dominant period.

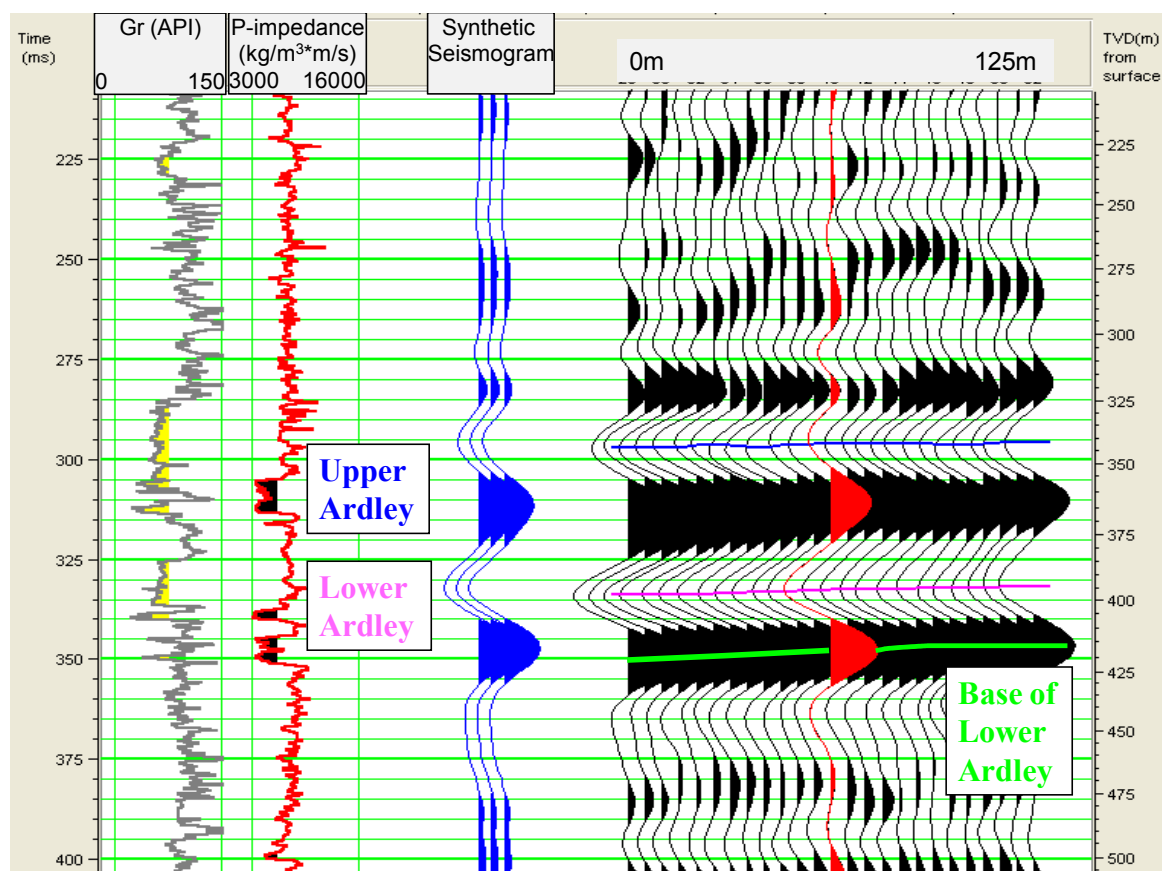


Figure 4-20: The tie between the synthetic seismogram and seismic data with a comparison to the P-impedance well log in the Ardley Coal Zone. Events are picked for the Upper Ardley Coals, the top of the Lower Ardley Coals, and the base of the Lower Ardley Coals.

4.5.3 Interpreted Seismic Events

With the well data tied to the seismic data, the Lower and Upper Ardley Coal events were picked in the seismic volume. The interpretation is illustrated in Figure 4-21

and Figure 4-22. The north-south section in Figure 4-22 also demonstrates deterioration in the consistency of the reflection data of seismic “peak” event below the Lower Ardley Coals at the south end of the survey (at about 350 ms). The deterioration is not seen at the east, north, or west edges of the survey and is not likely due to the low fold edge effect. It may be related to subsurface conditions, but a corresponding wave form character is not as easily discerned in either of the 2D data sets.

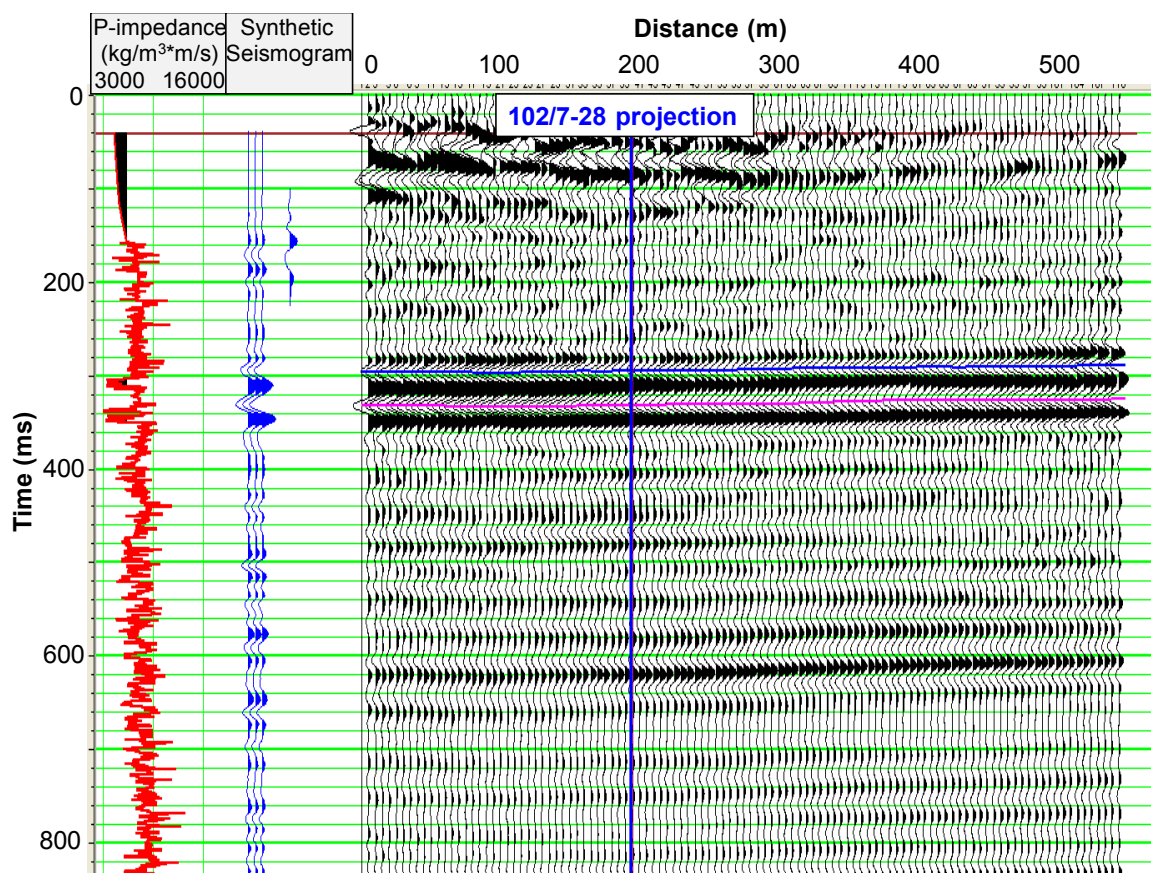


Figure 4-21: The east-west section that intersects the 102/7-28 well and the tie to the well data and synthetic seismogram.

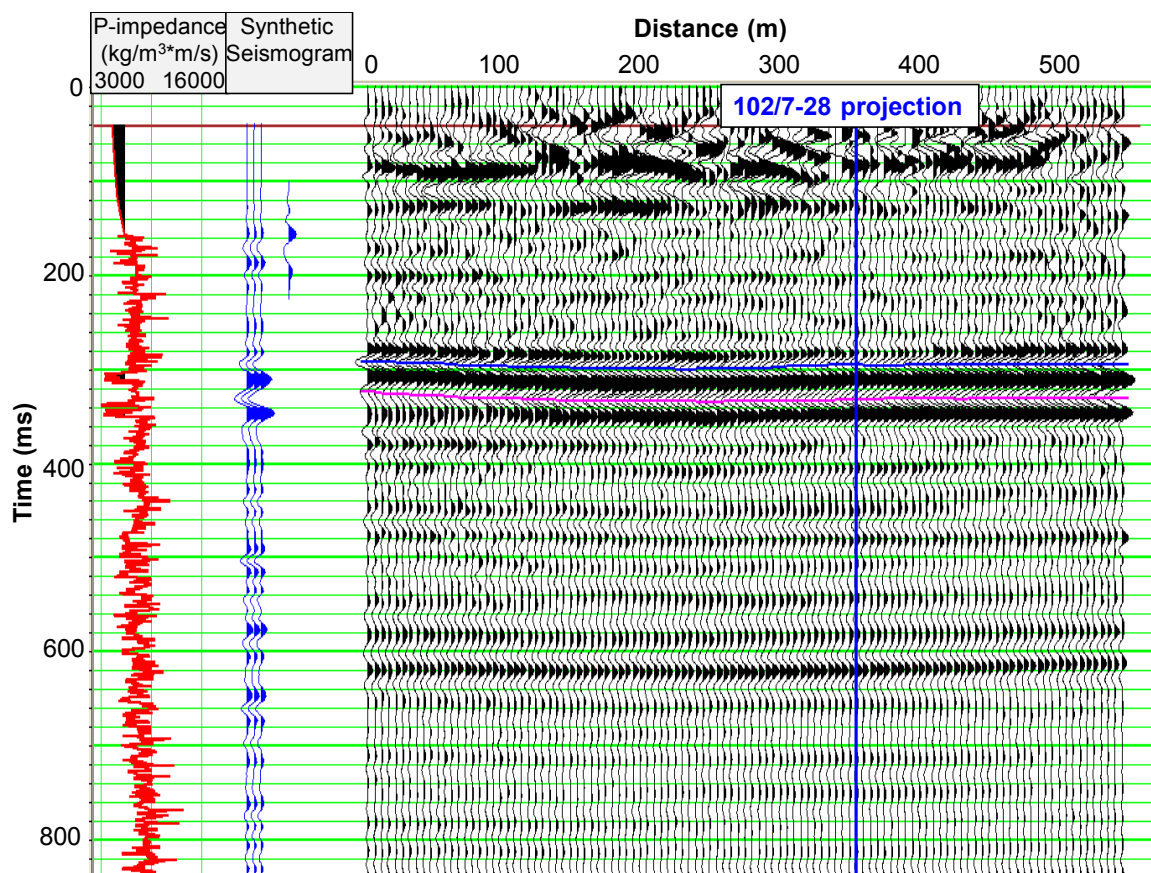


Figure 4-22: The north-south section that intersects the 102/7-28 well and the tie to the well data and synthetic seismogram.

4.5.4 Ardley Coal Time Structure and Amplitude Maps

The time structure maps of the Upper and Lower Ardley Coal seismic horizon (Figure 4-24 and Figure 4-23; respectively) show an overall dip to the south-west and a shallow synclinal saddle with its base in the south-west quadrant of the survey for each horizon. The relief of this saddle is approximately 10 ms TWT for each horizon. Assuming an approximate velocity of 3000 m/s for rocks in the Ardley Coal Zone, this relief would correspond to 15 m of relief which is consistent with the scale of relief between wells in the geological cross-sections in Figures 2-6 and 2-7. Figure 4-25 shows the time structure of the “peak” below the Lower Ardley Coal pick which ties to the base of the Lower Ardley Coal Zone (the horizon pick is shown in Figure 4-20).

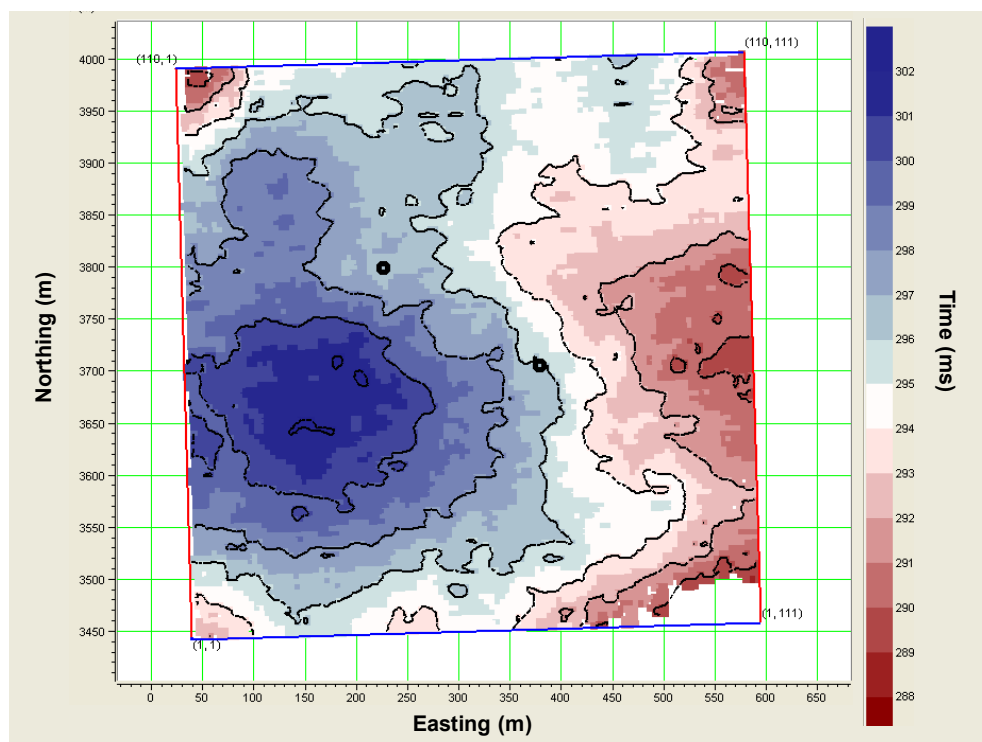


Figure 4-23: The time structure of the top of the Upper Ardley Coal horizon.

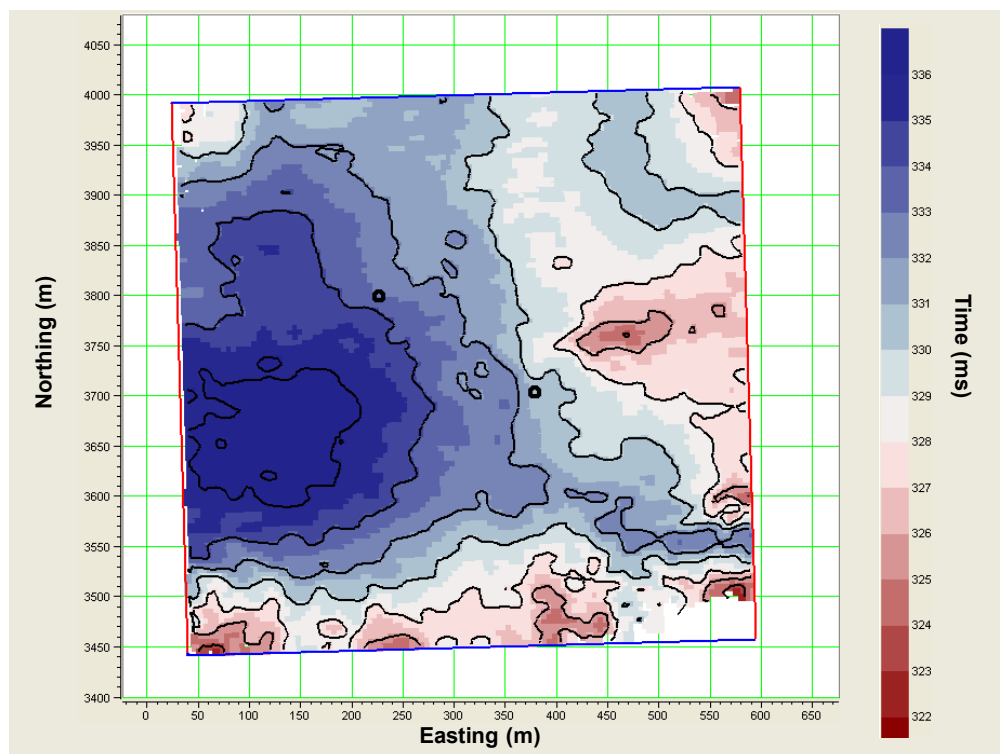


Figure 4-24: The time structure of the top of the Lower Ardley Coal horizon.

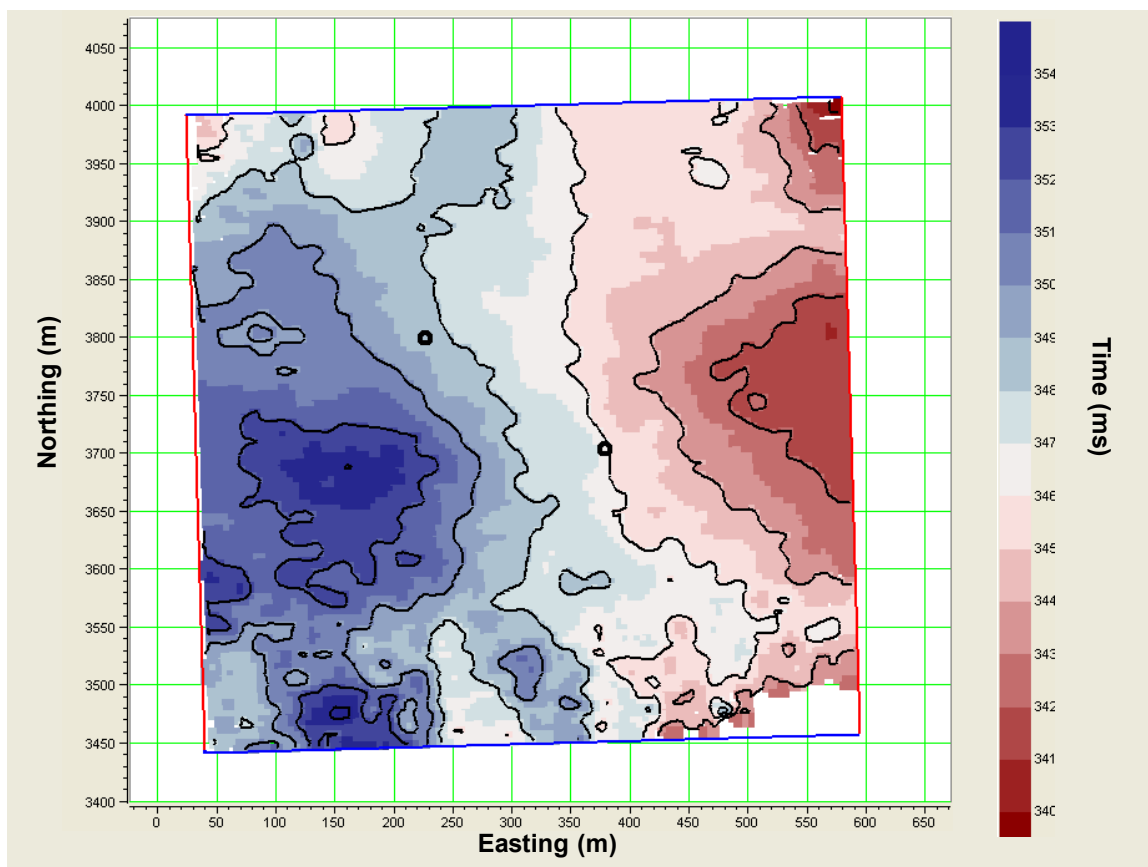


Figure 4-25: The time structure of the base of the Lower Ardley Coal event.

The isochron between the Upper and Lower Ardley Coal trough events (Figure 4-26) shows a fairly constant time thickness between these horizons. Similarly, the isochron between events of the top and base of the Lower Ardley Coal Zone (Figure 4-27) shows that the variation is on the order of 14-18 ms TWT in the central area of the survey.

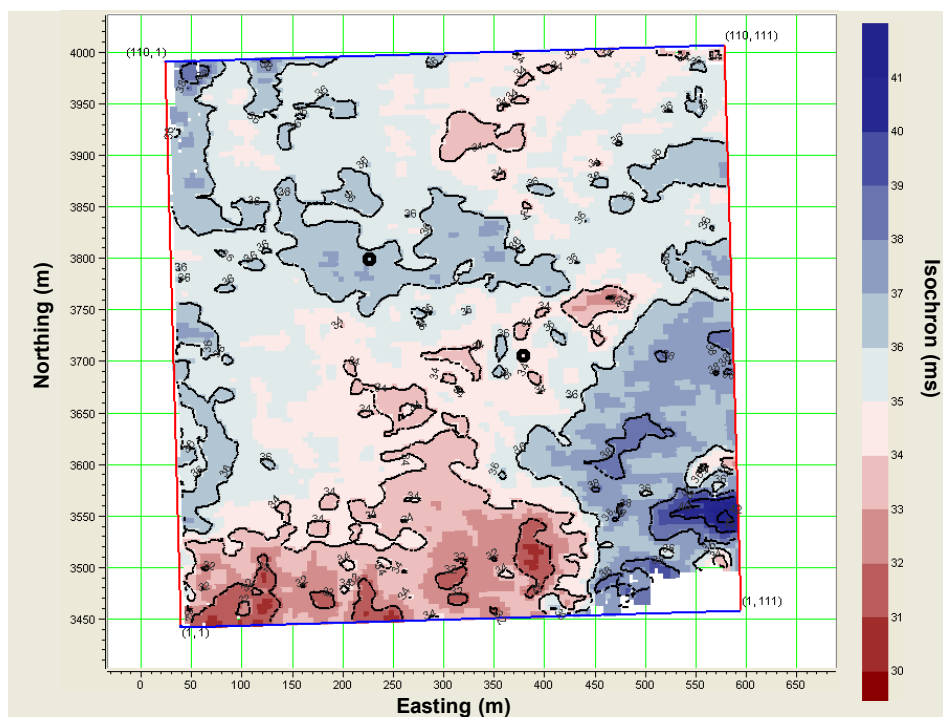


Figure 4-26: The isochron between the Upper and Lower Ardley Coal horizons. Smoothing has been applied to the map.

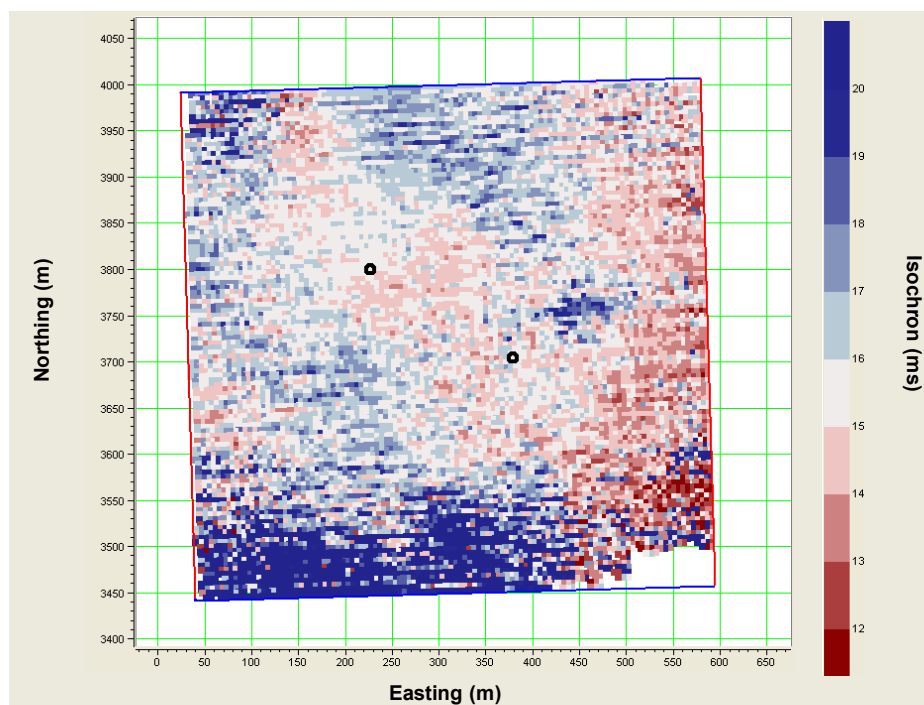


Figure 4-27: The isochron between the top and base of the Lower Ardley Coal events. No smoothing has been applied to the map in order to preserve fidelity of the data.

The minimum amplitude of the Lower and Upper Ardley Coal seismic horizons (troughs) are illustrated in Figure 4-28 and Figure 4-29, respectively.

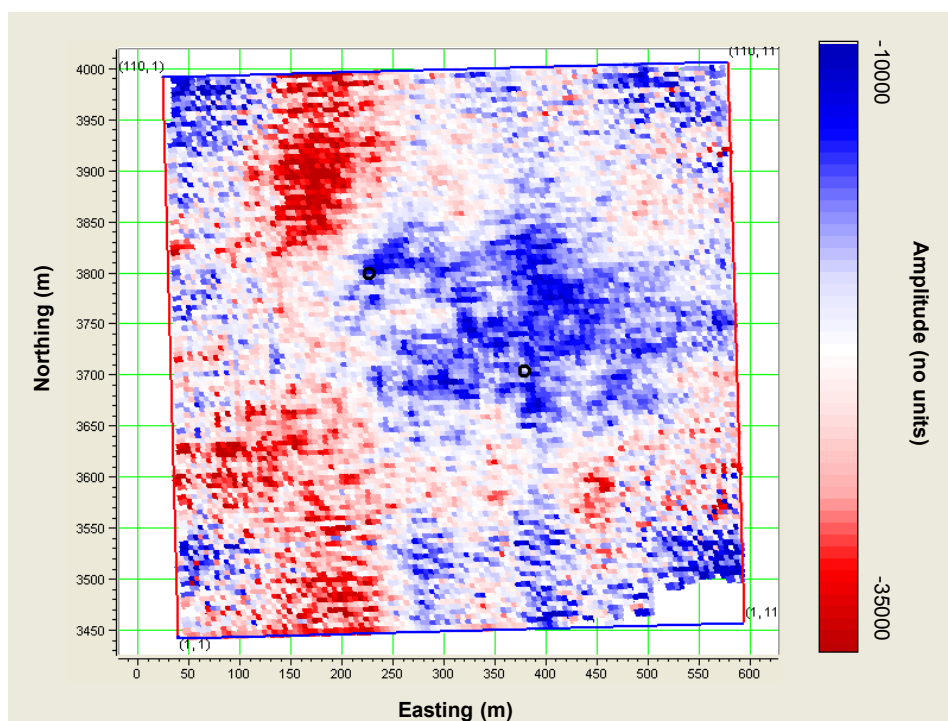


Figure 4-28: The minimum amplitude of the Upper Ardley Coal seismic trough event.

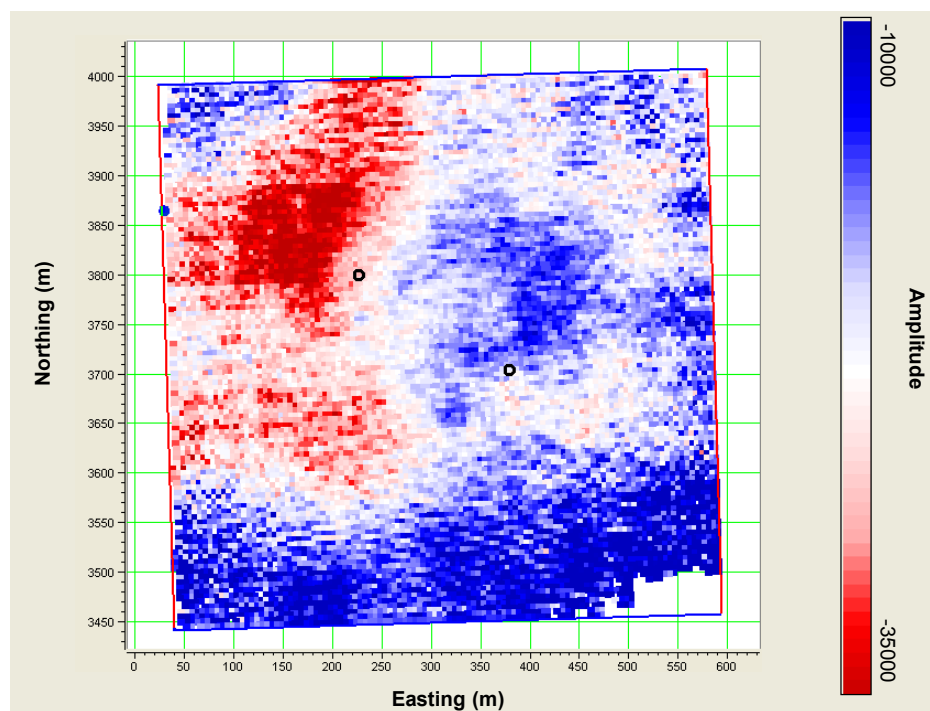


Figure 4-29: The minimum amplitude of the Lower Ardley Coal seismic trough event.

The isochron between seismic events, as well as event amplitudes, are difficult to interpret because of thin-bed tuning and waveform variability. However, if the CO₂ that was injected into the Mynheer Coal zone caused a velocity or reflectivity anomaly in the Lower Ardley Coal Zone, it might present itself as either an anomalous time-thickness between the top and base of the Lower Ardley or an amplitude anomaly in the Lower Ardley horizon. No such anomaly is immediately obvious.

4.6 Pre-stack Data Interpretation

Amplitude variation with offset (AVO) of the 3D vertical component data were analysed to inspect for trends. Because the AVO at an interface is a function of the difference in the P-wave velocity (V_p), S-wave velocity (V_s), and density between the bounding media, AVO data can be inverted to estimate a number of rock properties. The Zoeppritz equations are analytic solutions to the variations in reflectivity with angle of incidence. However, the Zoeppritz equations are complex and not easily applied to the analysis of AVO data. Shuey (1985) provided a convenient approximation to the Zoeppritz equations for PP waves that is valid for boundaries across which there are small reflection coefficients and restricted angles of incidence:

$$R_{pp}(\theta) \approx A + B \sin^2 \theta \quad 4.1$$

where

R_{pp} = the P-wave reflectivity as a function of incidence angle (θ)

A = the normal incidence P-wave reflection coefficient = $\frac{\rho_2 V_{p2} - \rho_1 V_{p1}}{\rho_2 V_{p2} + \rho_1 V_{p1}}$

$$B = A \left[D - 2(1 + D) \frac{1 - 2\sigma}{1 - \sigma} \right] + \frac{\Delta\sigma}{(1 - \sigma)^2}$$

$$D = \frac{\Delta V_p / V_p}{\Delta V_p / V_p + \Delta \rho / \rho}$$

$$\sigma = \frac{\sigma_2 + \sigma_1}{2} = \text{mean Poisson's ratio of the two media}$$

$$\Delta\sigma = \sigma_2 - \sigma_1$$

ρ = mean density of the two media

$$\Delta\rho = \rho_2 - \rho_1$$

V_p = mean P-wave velocity of the two media

$$\Delta V_p = V_{p_2} - V_{p_1}$$

In the linear equation 4.1, A is the normal incidence reflection coefficient, and B is the PP “AVO gradient”. This linearization of the PP reflection coefficient as a function of incident angle allows for convenient AVO analysis in terms of an AVO intercept (A) and the gradient (B).

Three typical CDP gathers are illustrated in Figure 4-30 which show that consistent amplitude variation with offset is not obvious in the raw gathers. In order to increase signal-to-noise, traces were stacked into common offset bins (30 m wide) that included traces from the nearest two CDP locations in the inline and cross-line directions. Examples of the resulting super gather from two locations on inline #71 (around crosslines #40 and #63) are illustrated in Figure 4-31 which shows that the AVO behaviour of the gathers is more obvious after partial stacking. The absolute amplitude of the Lower Ardley Coal trough event generally decreases with offset (i.e. it is a trough event and has a positive gradient). However, the figure shows that at near offsets, the trace amplitudes are often anomalously high or erratic. This phenomena is likely a result of residual direct source noise in the gathers that could not be attenuated in data processing.

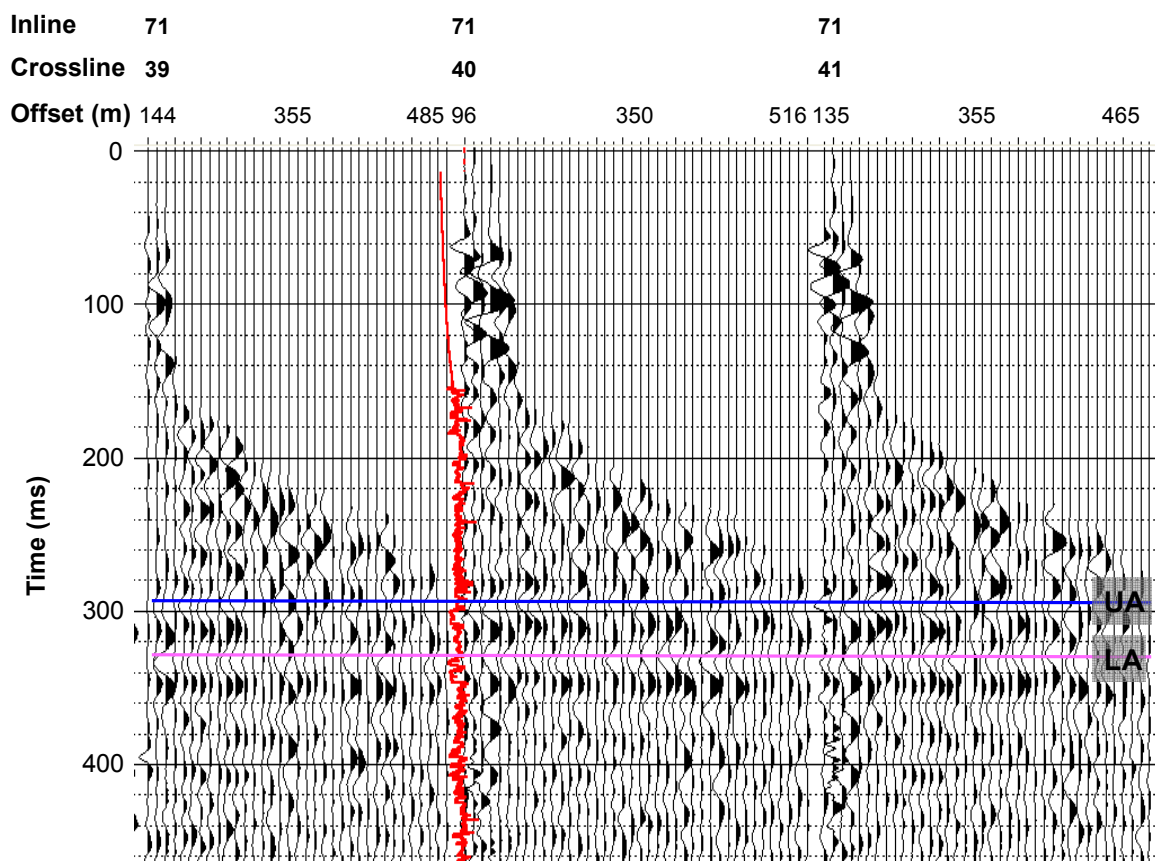


Figure 4-30: Three CDP gathers near the 102/7-28 well. The Upper Ardley (UA) and Lower Ardley (LA) Coal events are highlighted and the log is the acoustic impedance.

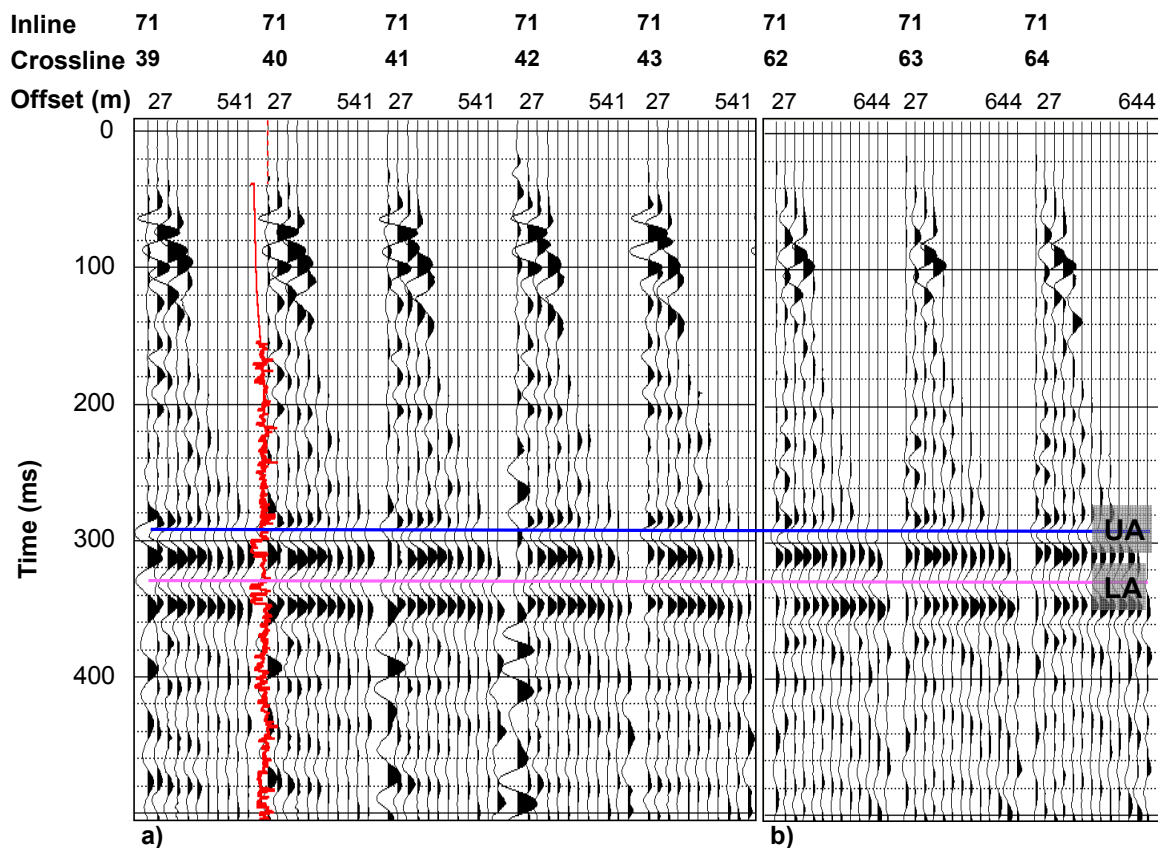


Figure 4-31: Super gathers showing traces that are binned from neighbouring CDP locations into stacks with common offsets. All gather are from inline #71. (a) shows gathers near the 102/7-28 well (crossline # 39-43) and (b) shows gathers from further east at crossline # 62-64. The Upper Ardley (UA) and Lower Ardley (LA) Coal events are highlighted and the log is the acoustic impedance.

Following the work of Ostrander (1984), a similar improvement was made by pre-stacking the data into common angle gathers and again stacking neighbouring CDP's to give an estimate of the amplitude variation with angle (AVA). The angles of incidence were calculated using the velocity model derived from the sonic log for the extended 102/7-28 well, that assumes a smooth gradient from the top of the log data to the surface velocity of 2000 m/s. Example angle gathers are illustrated in Figure 4-32, from two locations in the survey. The gathers near the 102/7-28 well show an overall decrease in absolute amplitude with increasing incidence angle for the Upper and Lower Ardley Coal events. Again, however, the small offset data appears spurious. Near crossline #63, the AVA trend at the Lower Ardley Coal event shows an increase in absolute amplitude with

angle of incidence. These trends are displayed again in Figure 4-33 which shows the maximum absolute amplitude at different angles of incidence for the horizons at the top and base of the Lower Ardley Coals at three CDP locations. The figure shows that the trough corresponding to the top of the Lower Ardley Coals has a positive or a negative AVA gradient in different regions of the volume. This variation may be attributed to subtle differences in the tuning character of the thin beds which will be critically sensitive to slight differences in the ray path angle and travel times at different offsets.

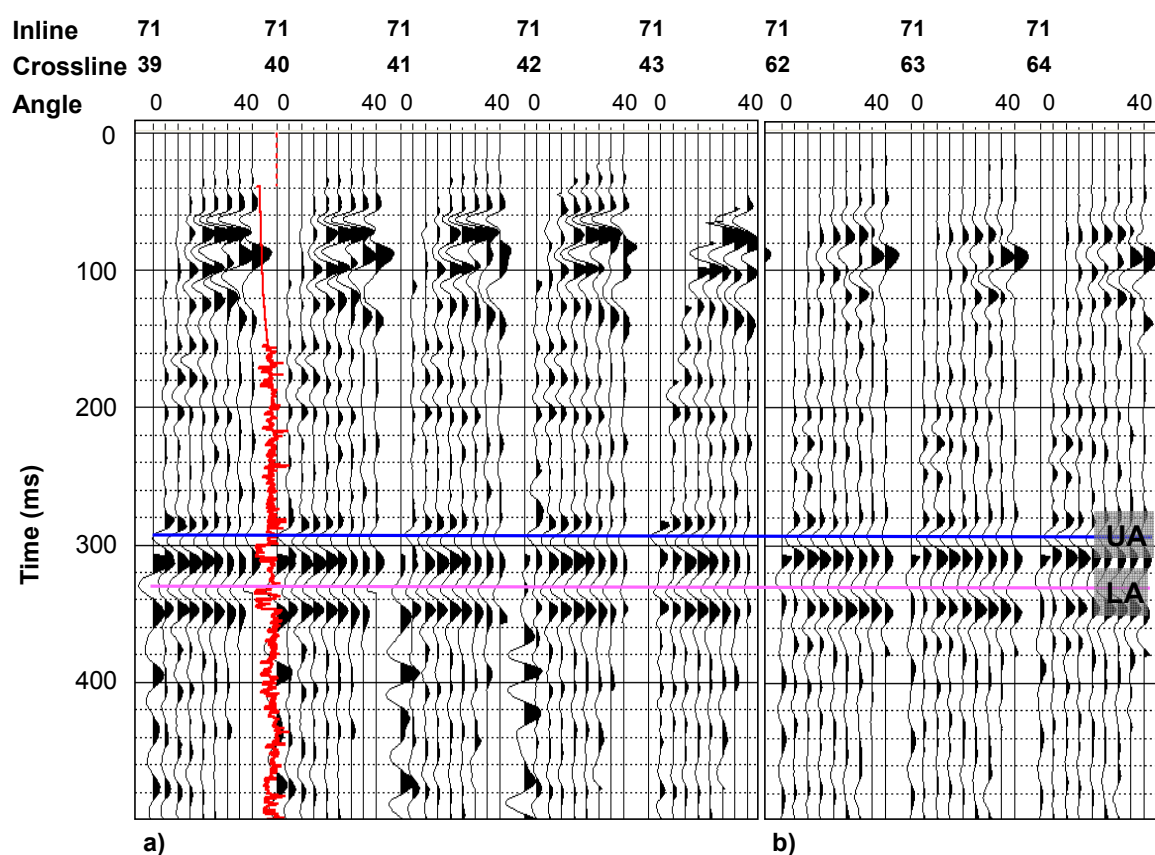


Figure 4-32: The angle gathers showing traces that are binned from neighbouring CDP locations into stacks with equal angles of incidence. All gather are from inline #71. (a) shows gathers near the 102/7-28 well (crossline # 39-43) and (b) shows gathers from further east at crossline # 62-64. The Upper Ardley (UA) and Lower Ardley (LA) Coal events are highlighted and the log is the acoustic impedance.

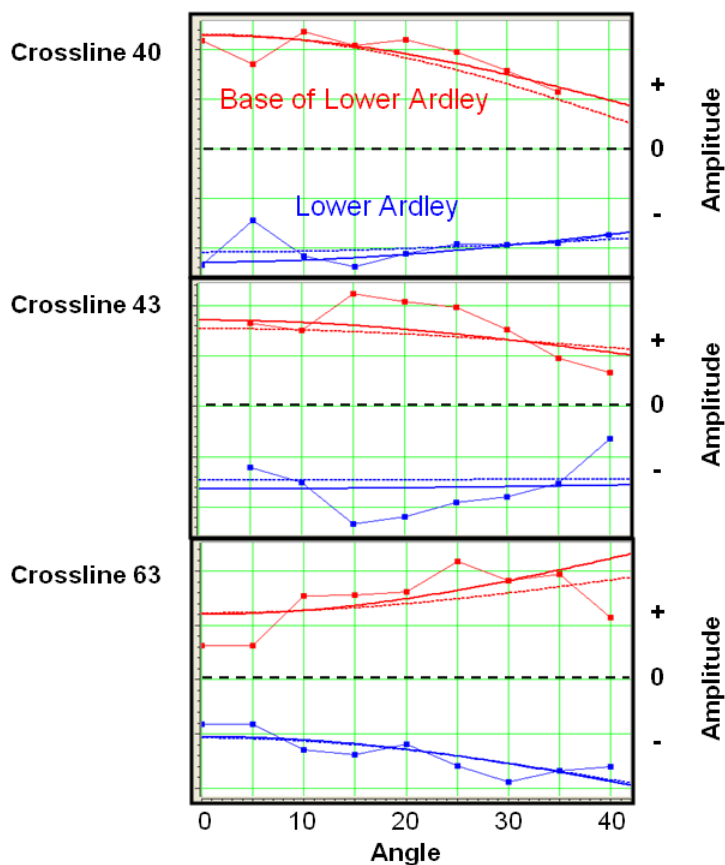


Figure 4-33: The best fit line matching the amplitude variation with incidence angle for data from three CDP locations on inline #71. The red line shows the amplitudes picked from the base of the Lower Ardley peak event (positive amplitudes) and the blue line shows the amplitudes picked from the top of the Lower Ardley trough event (negative amplitudes).

Figure 4-34 and 4-35 shows AVA gradient and intercept maps, respectively, for the trough at the top of the Lower Ardley Coals. These attributes were calculated using only data in the angle range from 15° – 45° . This limited range was selected in order to avoid spurious effects that might occur as a result of the near offset amplitude contamination by coherent source noise. The figure shows a trend of positive AVA gradients throughout most of the volume but with significant regions where the gradient is negative. Again, this may be an indication of subtle heterogeneity in the stratigraphy. The map patterns also show some lineation that correspond to the survey source/receiver lines and may be indicative of acquisition footprint due to unevenness in the offset and azimuth distribution in the acquisition design (as discussed in Section 4.2).

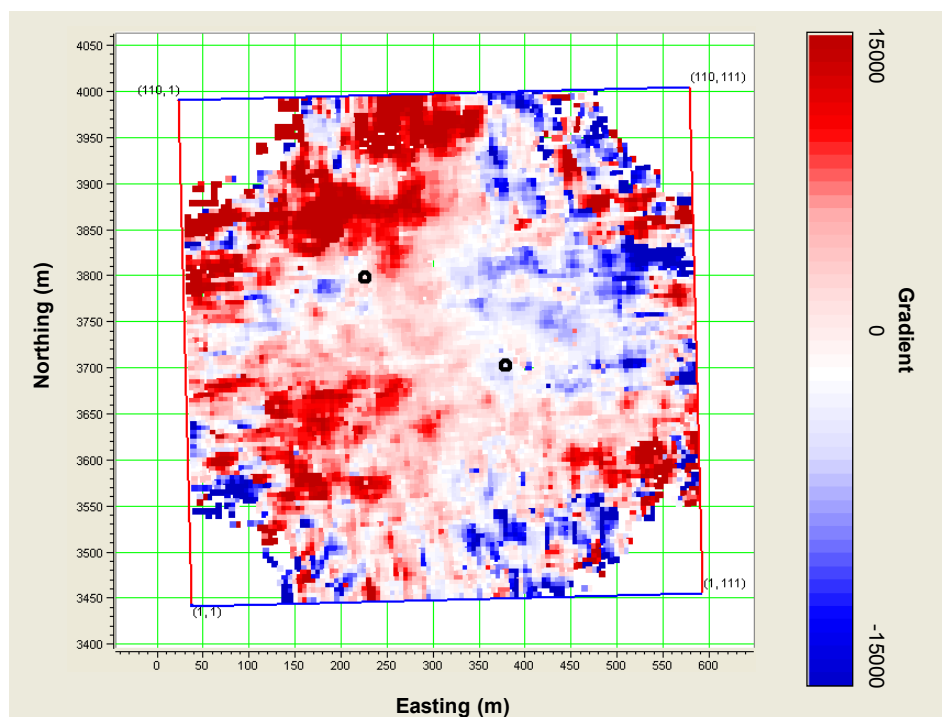


Figure 4-34: The AVA gradient mapped for the Lower Ardley seismic event using only angles of incidence from $15^\circ - 45^\circ$.

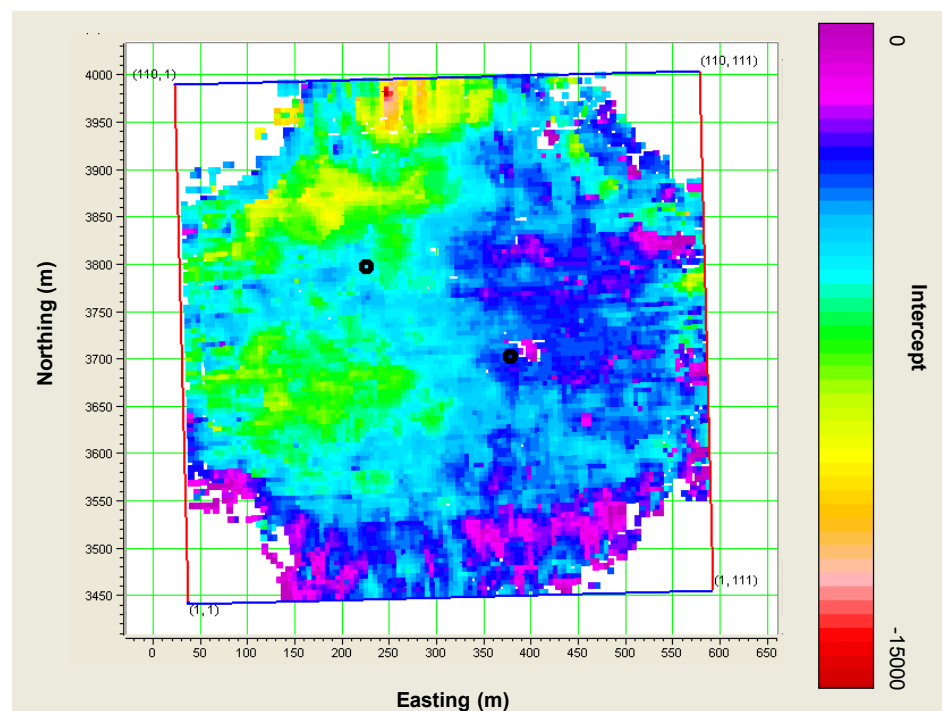


Figure 4-35: The AVA intercept mapped for the Lower Ardley seismic event using only angles of incidence from $15^\circ - 45^\circ$.

4.7 Conclusions

The data from the June 2007 3D survey were processed and resulted in a high quality data volume. The extracted wavelet showed useful energy in the frequency band 10 – 60 Hz which resolved the Lower and Upper Ardley Coal Zones as a trough/peak doublet, but did not resolve the individual members of the Lower Ardley Coal Zone.

The time structure and amplitude of the Lower Ardley Coal Zone event were mapped. The time structure showed an overall dip to the south-west but with a saddle-shaped depression immediately to the south-west of the injection well. Up-dip from the 102/7-28 well is to the northeast. The amplitude of the Lower Ardley Coal event is variable throughout the volume. The maps did not show any overt trends that might be related to the injected CO₂.

Analysis of the pre-stack AVO and AVA data throughout the volume again showed variability in the reflection character of the Lower Ardley Coals. The expected positive AVA gradient was observed in some regions of the survey, however, some regions showed a negative gradient which may be related to the subtle effect of differential tuning with offset and variable stratigraphy. The AVA gradient and intercept maps show some patterning that may be related to acquisition footprint. However, no reflection character is easily related to a signature of the injected CO₂.

Chapter Five: 3D Converted-wave data

5.1 Introduction

In addition to collecting the vertical component PP data during the June 2007 3D survey, a single receiver line of three-component (3C multi-component) geophones was deployed to record the converted PS wave field. The utility of this data, acquisition design, basic processing strategies and interpretation of these data are discussed in this chapter.

5.2 Converted-wave Data

When a compressional (P) wave is reflected at an oblique angle from an impedance boundary in an elastic medium, the reflected energy will propagate not only in the compressional PP mode, but some portion of the energy will be converted to a PS shear-wave mode (Krebes, 2005). In an isotropic medium, the shear (S) mode will propagate via a particle displacement that is polarized in the plane of the incident and the reflected ray paths, but is perpendicular to the direction of propagation. Ray paths of both PP and PS waves bend toward vertical as the upward propagating wave reaches the Earth's surface because wave velocities are typically lowest in the near surface. Thus, the PP wave will result in a vertical particle displacement at the surface whereas the PS wave will result in a horizontal particle motion. In the case of an isotropic medium of horizontal reflectors, the PS particle motion will be radial in the plane of the source-to-receiver line. To record the converted wave field, geophones must measure not only the typical vertical component of motion, but also the horizontal motion component.

In conjunction with a PP data set, a PS data set can improve interpretation in several ways. Although shear waves generally attenuate faster than compressional waves and so have reduced frequency content, Hendrick (2006) showed the very low shear wave velocity of coal intervals compensates for the lower bandwidth and that PS data can provide comparable resolution to that of PP data. Stewart et al. (2002; 2003) discuss how converted-wave data can enable improved lithological estimation by comparing travel times between events that have been registered in both the PP and PS data sets. The

interval travel times indicate V_p/V_s , an important lithology indicator. Additionally, further elastic property estimation and lithologic constraint was achievable by jointly inverting pre-stack PP and PS amplitude data (Margrave et al. 2001).

Because the S-velocity is slower than the P-velocity, the angle of reflection for a PS wave is not the same as the incidence angle. As a result, the midpoint does not correspond to the conversion (PS reflection) point, even for horizontally bedded homogeneous reflectors. In such a scenario, the conversion point (CP) will be closer to the receiver than the source location (Figure 5-1). The position of the CP varies with depth and can be computed from the horizontal slowness of the wavefield.

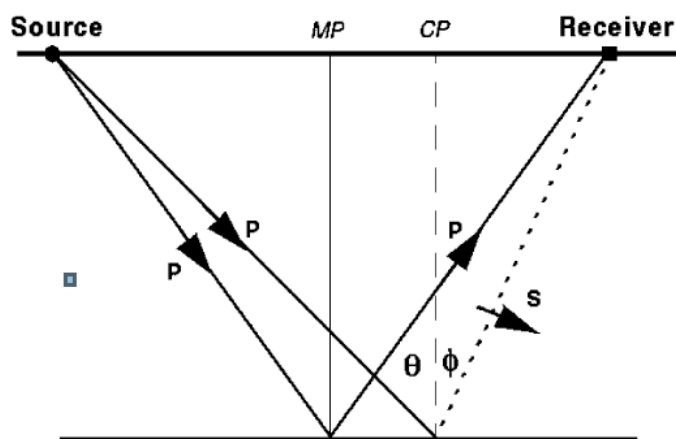


Figure 5-1: A PS reflection at its conversion point (CP) and the PP reflection at its midpoint (MP). The CP is closer to the receiver than the source. (From Stewart et al., 2002).

5.3 Converted-wave Data at Alder Flats

5.3.1 Survey Design and Acquisition

The multicomponent survey layout included a single receiver spread of 3C geophones spread east-west in a line that intersected the 102/7-28 well. Because the line was live during the entire shoot, it formed a sparse 3D survey. The survey design and the resulting 3D fold are illustrated in Figure 5-2 which uses a common conversion point (CCP) bin geometry that is 5 m wide by 20 m long elongated in the north-south direction

and assumes a target at 400 m depth and $V_p/V_s = 2$. The figure shows that the fold will only be appreciable in a region between the wells.

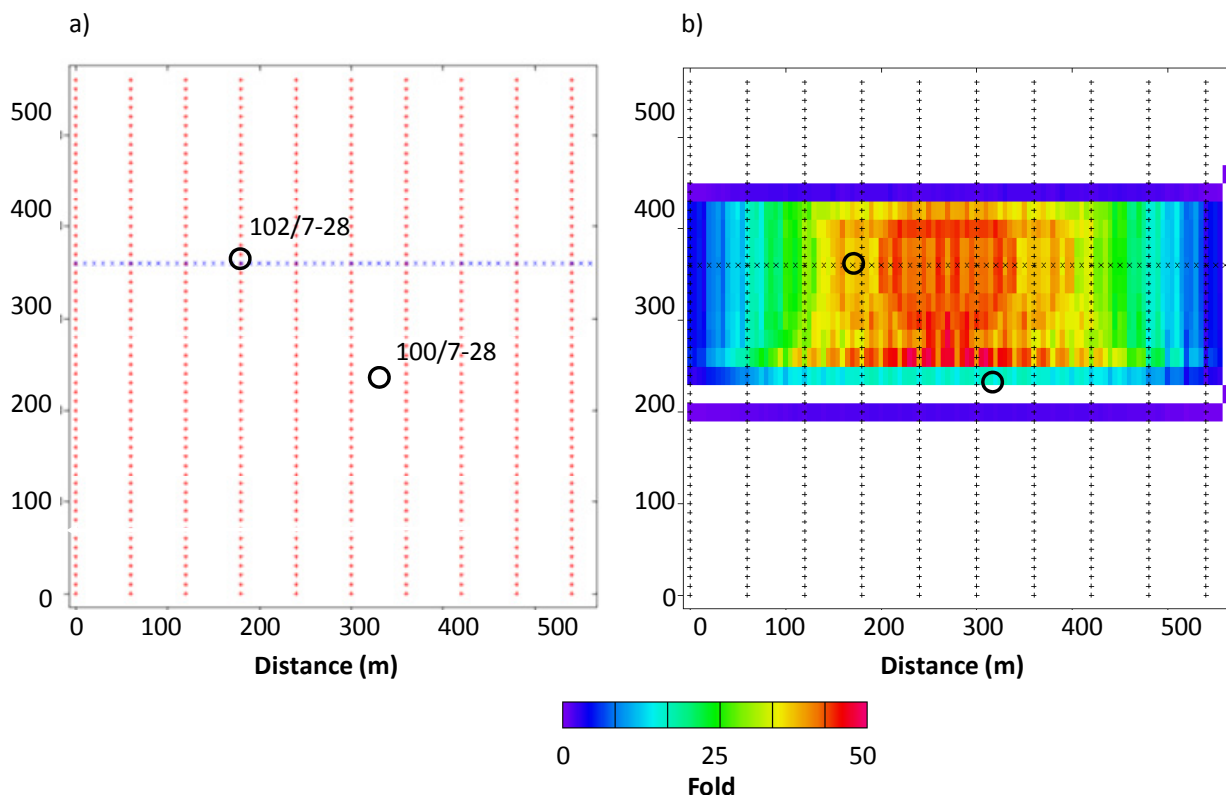


Figure 5-2: (a) The design for the converted-wave survey. Source lines run north-south (red) and the single receiver line runs east-west (blue). (b) The associated fold map.

5.3.2 *Converted-wave Processing*

The radial and transverse data of the single 3C receiver line were processed by Sensor Geophysical Ltd. using a converted-wave processing flow that included time-varying CCP binning. The need for time-varying binning is illustrated in Figure 5-3 which shows that the data recorded by a single receiver will correlate to conversion points that move away from the receiver location with depth but that eventually approach an asymptotic conversion point limit. Because the specific shape of the PS reflection point curve is a function of V_p/V_s , the Alder Flats data were assigned to CCP bins according to a depth-varying V_p/V_s ratio identified by preliminary processing steps. A

balanced wavelet was achieved by applying a time-varying spectral whitening process. Finally, the data were migrated to form a low-fold 3D volume.

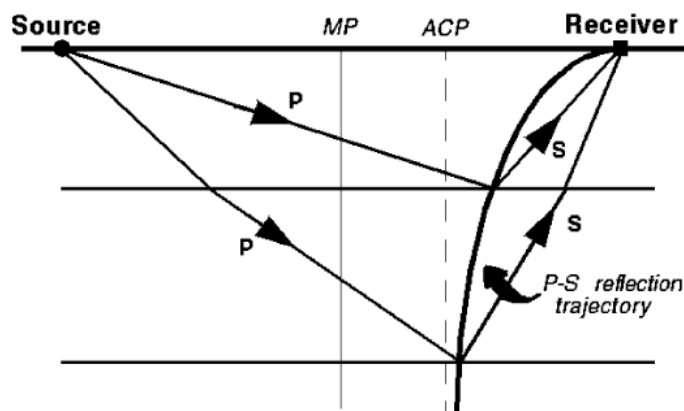


Figure 5-3: The location of the CCP moves away from the receiver location with increasing depth but at the limit of depth approaches an asymptotic conversion point (ACP). From Stewart et al. (2002).

5.3.3 Interpretation of the 3D Data

A PS synthetic seismogram created with the P-wave, S-wave and density logs from the 102/7-28 well is illustrated in Figure 5-4. The figure shows that, with the polarity convention that an increase in shear impedance represents a positive reflection coefficient, the tops of the coal zones are again characterized as troughs.

Figure 5-5 shows a west-east section from the 3D volume with the Upper and Lower Ardley Coal horizons identified. The figure shows that the horizons can only be picked in the central, high-fold regions of the survey. The data in the figure are displayed according to the time that it takes a reflection to propagate as a P-wave downward and an S-wave upward (called PS time). The arrival times are delayed relative to PP arrival times due to the lower velocity of the up-going S-wave.

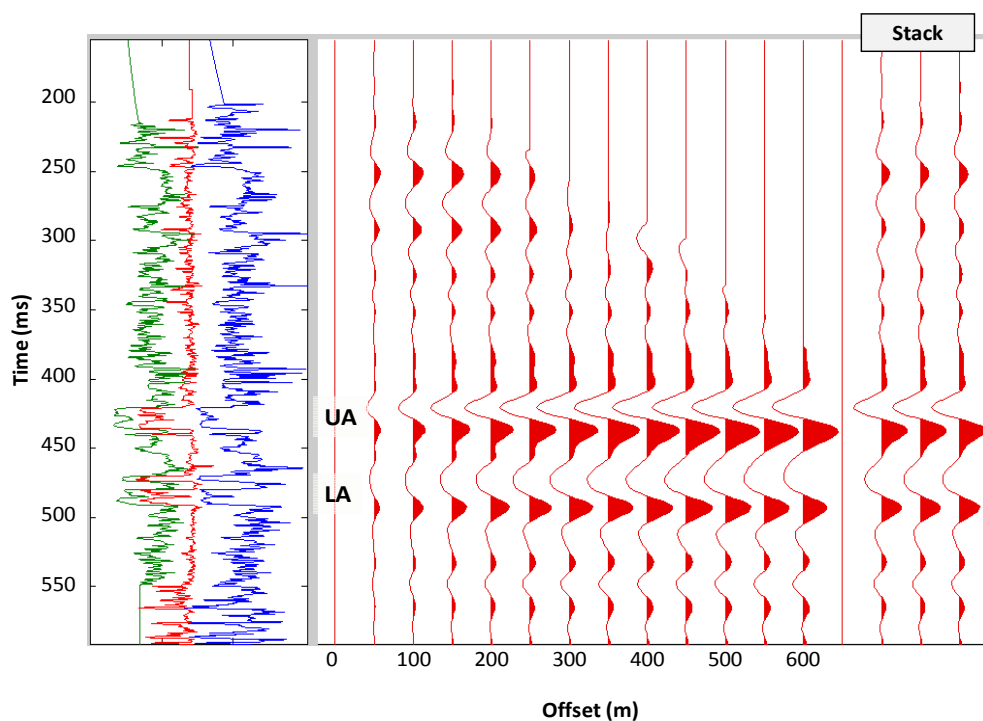


Figure 5-4: An offset gather synthetic seismogram of the radial component converted-wave using a 25 Hz Ricker wavelet. The 3 traces on the left are the stack, repeated 3 times.

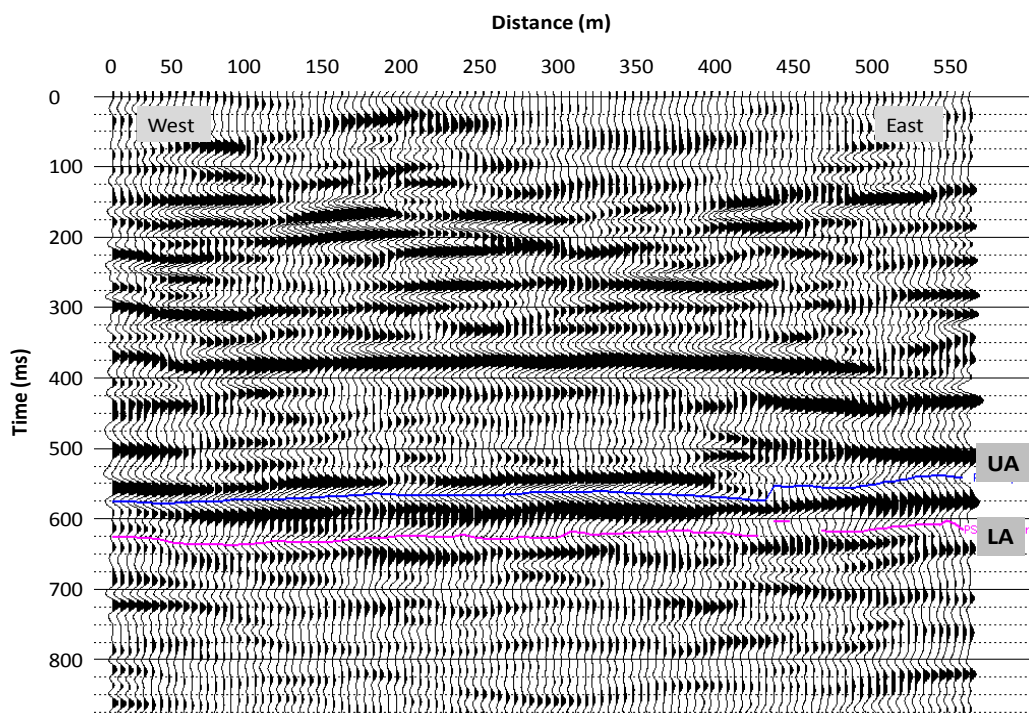


Figure 5-5: A west-east inline (#10) section from the 3D PS data volume showing the picks of the Upper and Lower Ardley Coals. The data are displayed in PS time.

5.3.4 Interpretation of the 2D Stack

In order to improve the fold and thus the image quality, all east-west inlines were stacked together to form the single west-east 2D data section, shown in Figure 5-6. The figure shows that the continuity of the Ardley Coal events is improved relative to the 3D data of Figure 5-5.

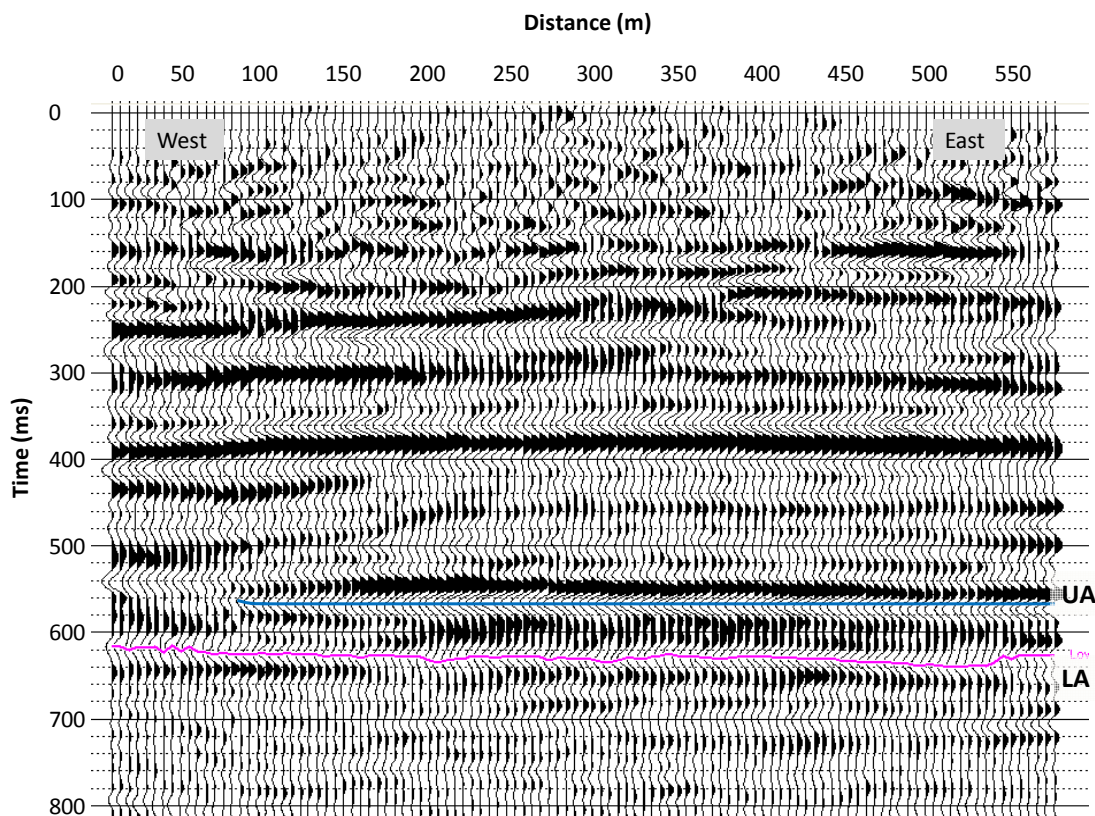


Figure 5-6: The 2D stack of the PS data. The trace is displayed in PS time. The Upper and Lower Ardley horizons are picked.

Figure 5-7 shows the tie between the 2D PS data and the west-east inline #71 section extracted from a version of the 3D PP data volume. Because the PS data had spectral whitening applied to them, the same whitening was applied to the PP data. The data show that the vertical resolution of the PS data is comparable to that of the PP data in the Ardley Coal Zone.

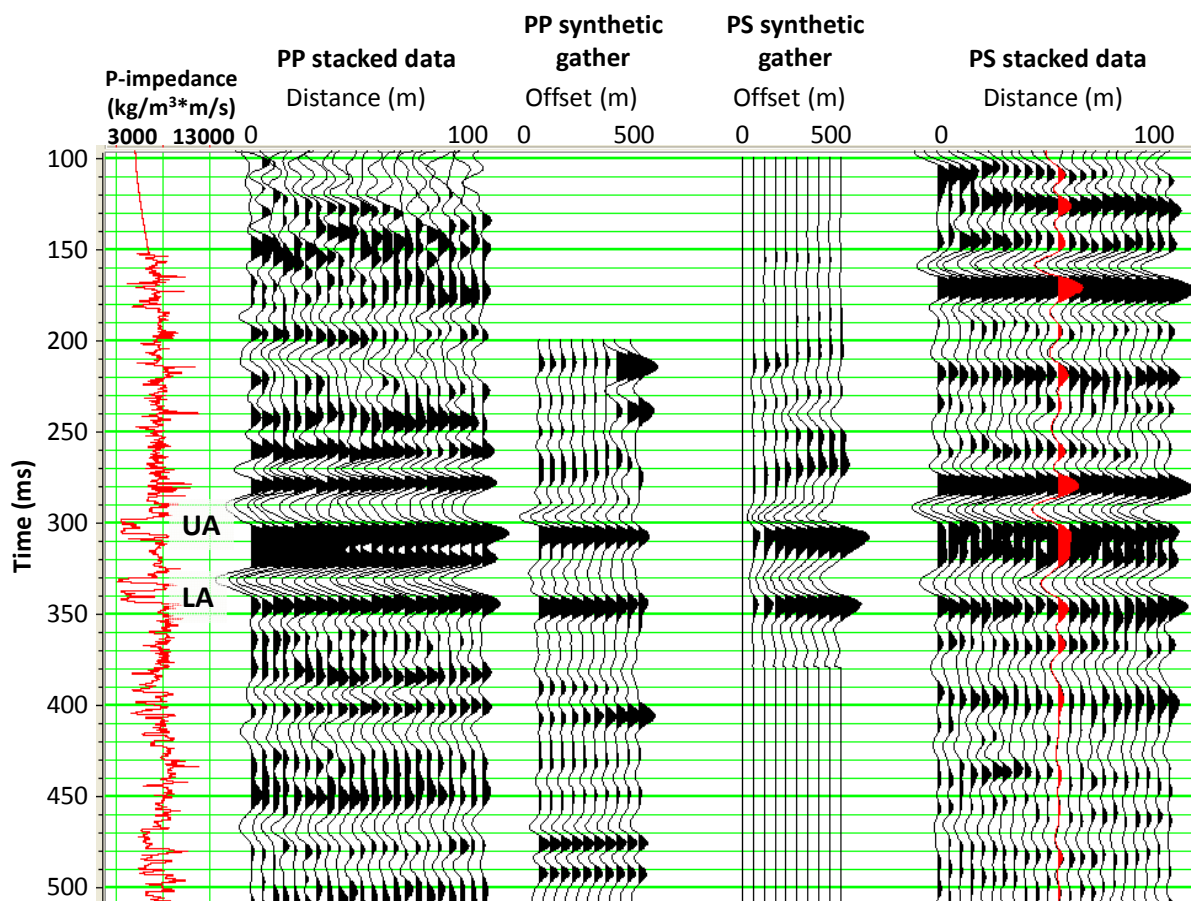


Figure 5-7: The correlation between the PP data and the PS data. The real data are post-stack whereas the synthetic data are pre-stack offset gathers. Each synthetic seismogram was created with a zero-phase wavelet extracted from the respective data sets. The data are displayed in PP time (i.e. the PS arrivals have been time-compressed to match the PP data events).

Figure 5-8 shows V_p/V_s calculated from the difference in the travel time between the Upper and Lower Ardley Coal events in the PP and the PS data. The data shows V_p/V_s ranges between 2.00 – 2.75 in the coal zone. In Chapter 2, petrophysical analysis of the 102/7-28 well logs found the average V_p/V_s for coal was 2.39, which is in concurrence with the values shown in Figure 5-8. V_p/V_s values estimated using this method are very sensitive to picking errors; hence an average value is most relevant. In this case the average V_p/V_s value for the Ardley Coal Zone estimated from the data in Figure 5-8 is 2.27.

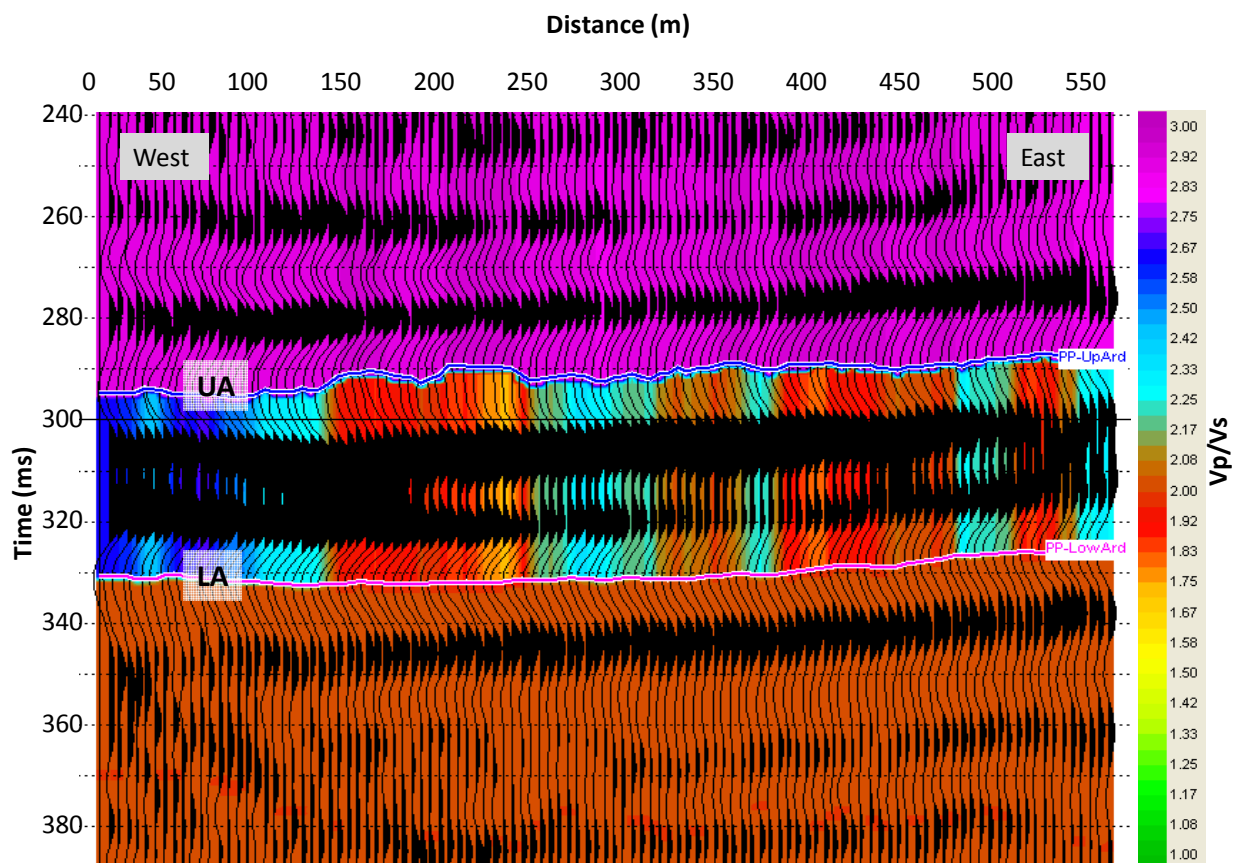


Figure 5-8: V_p/V_s ratio between the Upper and Lower Ardley Coals calculated by registering similar seismic events in the PP and the PS data. The zones above and below the Ardley Coal horizons were assigned constant V_p/V_s . The traces are the PP data displayed in PP time.

5.4 Conclusions

Although the fold of the PS data acquired at the Alder Flats location was low, the data quality was relatively good. The 3D data volume showed identifiable events that could be tied to the Upper and Lower Ardley Coals. The waveform consistency became improved when the data were stacked into a single west-east 2D line. By registering the horizon that ties to the Upper and the Lower Ardley Coals in the PP and the PS data set, V_p/V_s was estimated for the Ardley Coal Zone as a whole, and was found to average 2.27.

Chapter Six: Acoustic Impedance Inversion

6.1 Introduction

This chapter discusses inverting the post-stack vertical component seismic data to estimate the acoustic impedance. The theory and methods of inversion are reviewed. The Alder Flats data is inverted with a model-based least-squares method and a mixed-norm constrained sparse spike method. The results are used to quantitatively interpret the rock properties of the Ardley Coals. Additionally, synthetic modelling is conducted in order to understand the effect that short-path multiples might have on the seismic data and the inversion result.

6.1.1 The Utility of Acoustic Impedance Inversion

Acoustic impedance (P-impedance, Z_p , Z or AI) is defined as the product of compressional wave velocity (v_p) and density (ρ):

$$Z_p = v_p \times \rho$$

Because both velocity and density are indicators of lithology, fluid content, porosity and other petrophysical properties, a quantitative estimate of acoustic impedance from seismic data can be used to characterize petrophysical properties of the subsurface. If a seismic trace is treated as a filtered estimate of the earth's layered normal incidence reflectivity, the trace only gives information about the boundary between layers, not the layers themselves. However, since the normal incidence reflection coefficient (r_i) at the i^{th} interface of two layers is given by:

$$r_i = \frac{Z_{i+1} - Z_i}{Z_{i+1} + Z_i}, \quad 6.1$$

the data from a seismic trace can be used to give an acoustic impedance estimate of the reflecting layers.

Inversion estimates of acoustic impedance provide several advantages over interpretation of the stacked traces themselves (Latimer et al., 2000; Veeken and Da Silva, 2004):

1. Acoustic impedance inversions incorporate well information into the parameter estimate which includes low frequency information that is not available in the seismic data alone.
2. In estimating acoustic impedance of a layer, an attempt to remove the wavelet is made which can reduce wavelet side lobe and tuning effects.
3. Seismic data is a band-limited estimation of the reflectivity at the interface between layers, while an acoustic impedance estimate, although also band-limited, is a property of the rock layers themselves.
4. The layer based acoustic impedance rock property is more easily correlated with well data which is also layer based information (as opposed to layer interface information).
5. Because acoustic impedance is a rock property, it can be more easily related to other petrophysical properties such as fluid content and porosity.

Although there are other types of impedance (i.e. shear, elastic, etc.), the remainder of this thesis only discusses acoustic impedance. For the sake of brevity “acoustic impedance” is shortened to “impedance”.

6.2 Methods of Inversion

Multiple methods of inverting post-stack seismic traces to find impedance have been developed. Russell and Hampson (1991) reviewed the band-limited method, the model based method, and the sparse spike method and showed that each has its advantages and disadvantages.

6.2.1 Band-limited Inversion

The band-limited method was first proposed by Lindseth (1979). Normal incidence reflectivity at a boundary interface is given as by equation 6.1 which can be rearranged to give:

$$Z_{i+1} = Z_1 \prod_{j=1}^i \left(\frac{1+r_j}{1-r_j} \right) \quad , \quad 6.2$$

where r_i is the reflection coefficient at the i^{th} interface and Z_i is the impedance of the i^{th} layer. Thus if the impedance of the first layer is known and the reflection coefficients of the subsequent layers are known, the impedance of any layer can be estimated. Treating the seismic trace as an estimate of the reflectivity, the trace can be inverted to yield an impedance estimate.

Another approach to estimating impedance is to use an approximation of equation 6.1:

$$r(t) \approx \frac{1}{2} \frac{d[\ln Z(t)]}{dt} \quad 6.3$$

Notably, this approximation assumes that $|r| < 0.3$ (Lines and Newrick, 2004). Equation 6.3 can be integrated to give:

$$Z(t) = Z(0) \exp \left[2 \int_0^t r(u) du \right] \quad 6.4$$

and again the impedance can be estimated from the reflection series alone if the $Z(0)$ is known. In recognition that the seismic trace lacks content at the low end of the frequency spectrum, the low frequency trend is introduced into the solution by adding the low frequency high-cut filtered impedance estimate from regional well data. The advantage of the band-limited inversion method is its simplicity. The principal disadvantage is that it does not account for the wavelet embedded in the seismic trace.

6.2.2 Model-based Inversion

Improved impedance inversions incorporate information about the wavelet. One of the Hampson Russell Software (HRS) inversion methods is a model-based inversion. Cooke and Schneider (1983) were the first to use such a method to solve for acoustic impedance from post-stack seismic data. In general, the method uses an initial guess model of the impedance which is used in an objective function that includes consideration of the extracted wavelet. The initial model incorporates low frequency information from local wells. The objective function is minimized by iterative

perturbation of the model which results in a reasonable solution if the initial guess is within the region of global convergence of the objective function.

The HRS technique is a highly evolved method that minimizes the following objective function (HRS Strata Theory):

$$\mathbf{e} = (\mathbf{T} - \mathbf{wDL}) \quad 6.5$$

where \mathbf{e} is the residual difference (in vector notation) between the seismic trace \mathbf{T} and the trace resulting from the model data, \mathbf{wDL} , where \mathbf{w} is the convolutional wavelet matrix for an n sample wavelet:

$$\mathbf{w} = \begin{bmatrix} w(1) & 0 & \dots \\ w(2) & w(1) & \dots \\ \vdots & w(2) & \dots \\ w(n) & \vdots & \dots \\ 0 & w(n) & \dots \\ \vdots & 0 & \dots \\ 0 & \vdots & \ddots \end{bmatrix},$$

\mathbf{L} is a vector consisting of the logarithm of impedance for m model samples:

$$\mathbf{L} = \begin{bmatrix} L(1) \\ L(2) \\ \vdots \\ L(m) \end{bmatrix} \quad \text{where } L(i) = \log(Z(i)), \text{ and } Z(i) \text{ is the impedance model,}$$

and \mathbf{D} is an $m-1$ by m derivative matrix where m is the number of layers to be solved for and $m-1$ is the number of reflection coefficients, given as:

$$\mathbf{D} = \frac{1}{2} \begin{bmatrix} -1 & 1 & 0 & 0 & 0 & \dots \\ 0 & -1 & 1 & 0 & 0 & \dots \\ 0 & 0 & -1 & 1 & 0 & \dots \\ \vdots & & & & & \ddots \end{bmatrix}.$$

Note that m , the number of impedance layers to be solved for, does not need to equal the length of \mathbf{T} (i.e. the solution impedance model may have fewer layers than there are time samples in the seismic trace being inverted).

The sum of the square of the errors is given by:

$$\mathbf{e}^T \mathbf{e} = (\mathbf{T} - \mathbf{wDL})^T (\mathbf{T} - \mathbf{wDL}) \quad . \quad 6.6$$

Using linear inverse theory (see Aster et al., 2005), minimizing $\mathbf{e}^T \mathbf{e}$ leads to the “normal equation” (with a stabilization factor, α):

$$((\mathbf{D}^T \mathbf{w}^T \mathbf{wD}) + \alpha \mathbf{I}) \mathbf{L} = \mathbf{D}^T \mathbf{w}^T \mathbf{T} \quad . \quad 6.7$$

However, rather than solving equation 6.7 directly for \mathbf{L} , a solution estimate is found by iterative refinement of a guess at the correct model until $\mathbf{e}^T \mathbf{e}$ is minimized. An initial guess model is seeded in equation 6.7 for \mathbf{L} which includes the low frequency trend from regional wells. Conjugant gradient iteration of \mathbf{L} then minimizes $\mathbf{e}^T \mathbf{e}$. Because the solution to equation 6.7 is non-unique (i.e. there are an infinite number of models that can minimize $\mathbf{e}^T \mathbf{e}$), constraints are introduced that restrict the possible solutions. In the HRS “hard-constraints” algorithm, constraints are imposed on the upper and lower bounds for the impedance estimates. The program allows the user to define the bounds as a percentage of the average impedance of the initial guess model.

The HRS theory manual notes that the algorithm has the property that components of the initial guess model that are not resolved by the data tend to be carried through from the initial guess. Thus the frequency trend below the seismic band, introduced in the initial guess model, is carried through to the final solution, as are high frequencies above the seismic band if they are not filtered away from the initial model prior to the inversion. Sparsity in the inversion can be achieved via the assumption of a finite number of discrete layers within the inversion window.

6.2.3 Sparse Spike Inversion

The generalized linear inversion approach to impedance estimation assumes that the errors (equation 6.5) are distributed according to a Gaussian distribution and the method attempts to minimize the L_2 -norm given by equation 6.6 (the method of least-squares).

However, several authors have shown that an optimal deconvolution of the wavelet from a seismic trace is achieved by minimizing an L_1 -norm objective function (Levy and Fullagar, 1981). The argument is that the reflectivity of interest in a seismic trace is best modelled as a series of isolated reflectivity spikes embedded in a greater number of low amplitude, noisy spikes. A solution that minimizes an L_1 -norm will draw out the fewest layers and only the major layer boundaries. Also, the introduction of the additional knowledge that the reflectivity series is best modelled by a sparse spike train reduces the non-uniqueness problem of the inversion (Oldenburg et al., 1983). The function to be minimized is:

$$J = \sum_{t=0}^{t_{\max}} |r(t)| .$$

Oldenburg et al. (1983) demonstrated a method that solved for a sparse reflectivity series, while still modeling the seismic data. The method then used equation 6.2 to find the impedance. The solution was also shown to be more accurate in the presence of noise by introducing upper and lower impedance bounds.

(Author's note: HRS Strata includes a tool for doing a sparse spike inversion, however, it was not used as a part of this thesis).

6.2.4 Mixed-norm Inversion

Debye and van Riel (1990) made the argument that the seismic trace should be modelled as a combination of a series of spikes that are distributed according to a sparse distribution and a series of noisy events distributed according to a Gaussian distribution. They claimed that a best estimate of the reflectivity series is found by minimizing a mixed-norm objective function:

$$J = L_p(\mathbf{r}) + \lambda L_q(\mathbf{T} - \mathbf{w}\mathbf{r})$$

where p and q are the number of the norm to be minimized and λ is a weighting factor between the two terms. p is set to 1 to solve for a sparse spike series and q is set to 2 to model noise as normally distributed events. λ , also called the trade-off parameter, weighs between solving for a sparse spike series and a series that matches the seismic trace as closely as possible in a least squares sense. A small λ value gives a large penalty on the

estimated reflectivity and implies a large estimation of the noise in the data. When using this method of estimating reflectivity, the selection of an appropriate value for λ is essential. To select the appropriate value, traces at a location where well data is available are inverted using multiple values of λ . The optimal value is believed to be the smallest λ that provides a match between the model and the data. Such a value is as sparse as possible while still modelling the data. The choice can also be evaluated by comparing the inversion result to the known well impedance.

The final L_2 -norm term contains residuals which account for random noise as well as failures of the mathematical model such as the fact that the full stack doesn't equal the normal incidence reflectivity, that the convolution model doesn't truly model the earth's seismic response, that there are errors in the estimated wavelet and other possible discrepancies between the model and reality.

6.3 Acoustic Impedance of the Ardley Coals

6.3.1 Petrophysics at Well Log Resolution

Figure 6-1 shows the cross-plot of impedance and V_p/V_s ratio for the 102/7-28 well logs from 300 – 475 m (KB). The cross-plot space has been divided into regions that delineate coal, sandstone and shale lithologies and Figure 6-2 shows the resulting lithology log. Coals are easily identified in a region of low impedance with a cut-off of less than 6.0×10^6 kg/m³*m/s. Separation of the siliciclastics into sandstones and shales is less obvious in the cross-plot because the two lithologies overlap, however, the lithology boundaries in Figure 6-1 have been selected in order to roughly match the bulk lithology trends shown discussed in Chapter 2.

Notably in Figure 6-1, while differentiating sandstones and shales would require an estimation of both impedance and V_p/V_s , coals can be easily identified by the single impedance parameter with the (high) cut-off of 6.0×10^6 kg/m³*m/s. Also, because impedance is fundamentally a function of density and wave-velocity, which in turn is a function of bulk modulus, shear modulus and density, the impedance of the coals might be changed by the injection of CO₂ and an impedance estimate might be able to locate coal affected by the injected CO₂.

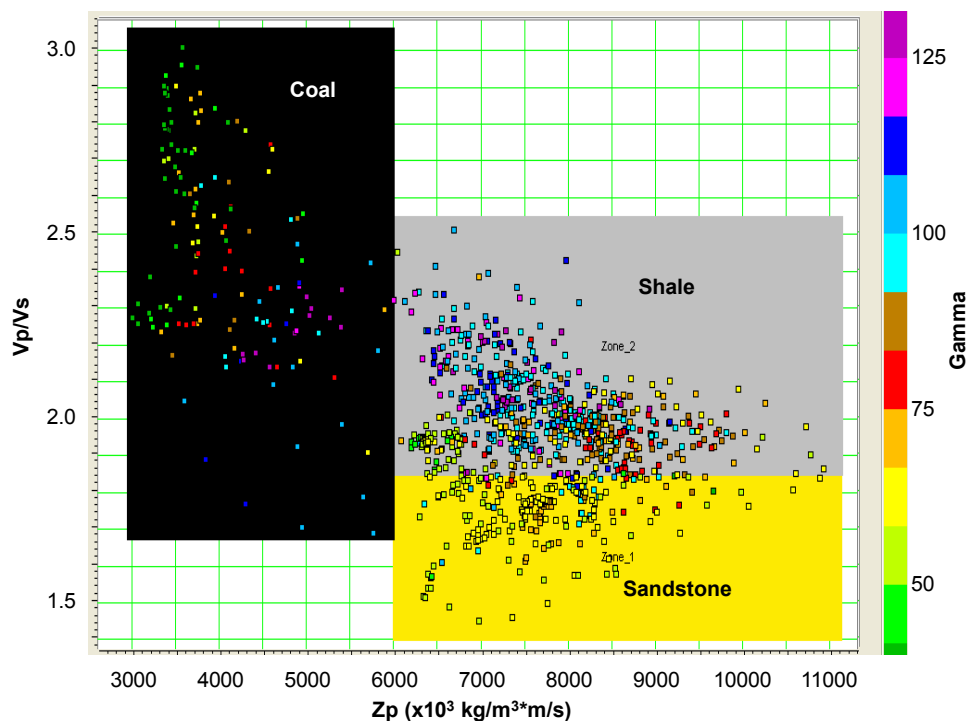


Figure 6-1: A cross-plot of impedance and Vp/Vs with gamma values in colour for 102/7-28 from 300 - 475 m (KB). Lithologies are blocked into coals, sandstones and shales in cross-plot space.

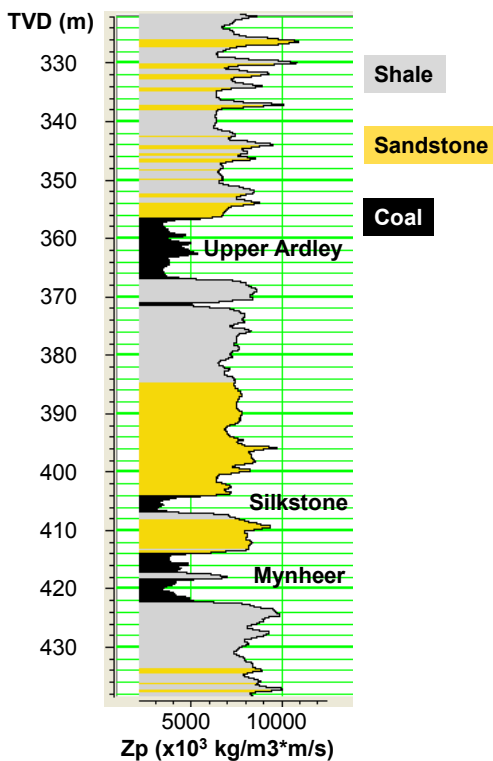


Figure 6-2: The lithology log from in the vicinity of the Ardley Coal Zone for 102/7-28.

Figure 6-1 also shows that within the coal lithology, there is a linear trend with the gamma response. Figure 6-3 illustrates this trend in a cross-plot of impedance versus gamma response. The coal lithology follows a trend of increasing impedance with increasing gamma response. The lower impedance, lower gamma zones correspond to the more pure coal lithology and the higher impedance and gamma response indicates shaley coal or coaly shale. The cut-offs are here defined as pure coal with impedance of less than 4.0×10^6 $\text{kg/m}^3 \cdot \text{m/s}$ and shaley coal with a impedance of 4.0×10^6 - 6.0×10^6 $\text{kg/m}^3 \cdot \text{m/s}$. Figure 6-4 shows the lithology log with the sub-lithologies of the coal zones delineated. These sub-lithologies of the coal zones can be delineated by impedance, giving a possible hint in terms of interpreting inverted impedance seismic data in coal zones.

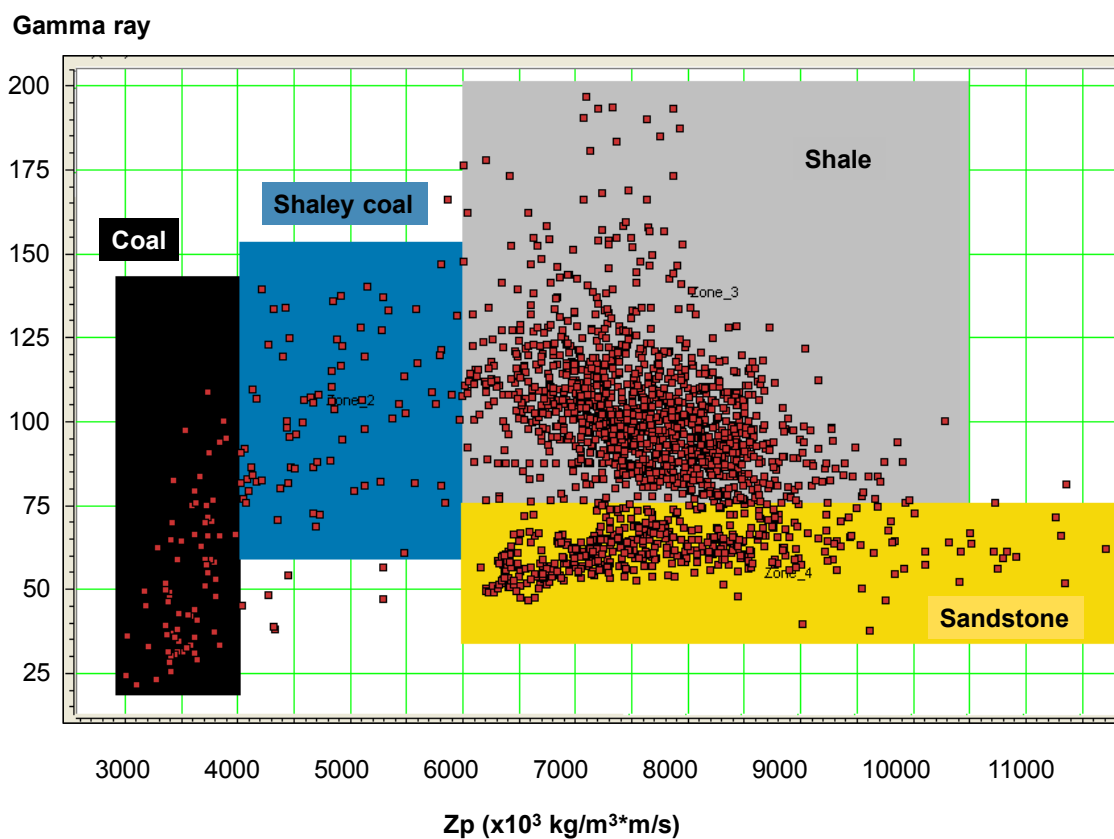


Figure 6-3: Cross-plot of impedance and gamma log response from 300 – 475 m (KB) for 102/7-28.

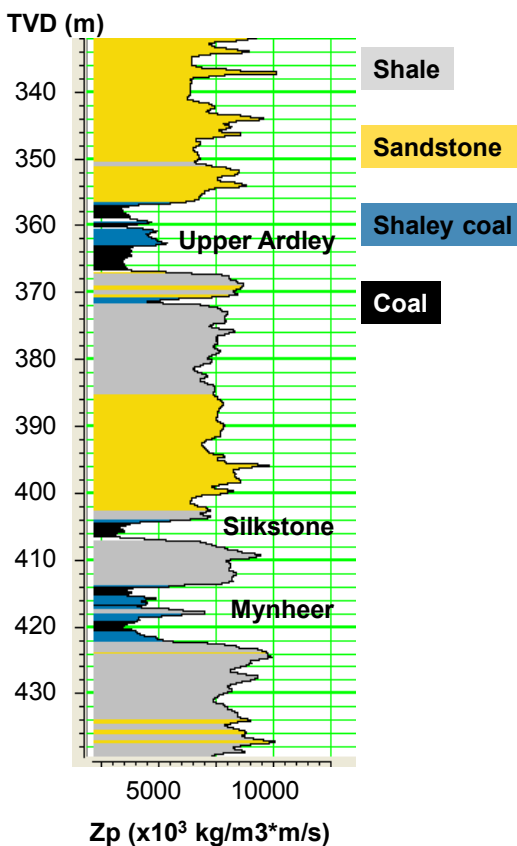


Figure 6-4: Lithology log showing the sub-lithologies of coal in the vicinity of the Ardley Coal Zone for 102/7-28.

6.3.2 *Petrophysics at Seismic Resolution*

The lithology log of Figure 6-2 has been established using the petrophysical properties acquired at well “logging resolution” (i.e. approximately 15 cm – 1 m scale). However, because seismic data is measured in time and with a limited bandwidth, it is reasonable to expect that lithologies derived from seismic impedance data will have lower resolution than those derived from logs. For example, Figure 6-5 shows the same cross-plot as Figure 6-3 but at “seismic resolution”. The log data have been sampled at 1 ms intervals and have been filtered with a 60 – 70 Hz high cut. Using the same lithology cut-offs as in Figure 6-1, Figure 6-6 shows the resulting lithology log along with the impedance log at logging resolution and at seismic resolution. There are two significant changes that result with the band-limiting of the impedance. The first is the reduced

vertical resolution of thin beds. For example, with the truncated bandwidth, the Mynheer and Silkstone Coal zones are no longer resolved as separate zones. The second significant difference is the reduction in the dynamic range of the impedance estimate. For example, the lowest impedance measured after applying the high cut filter is approximately $4.0 \times 10^6 \text{ kg/m}^3 \cdot \text{m/s}$ in Upper Ardley Coal Zone and approximately $5.0 \times 10^6 \text{ kg/m}^3 \cdot \text{m/s}$ in the Lower Ardley Coal Zone. At logging resolution, the impedance of the purest coals is significantly lower at $\sim 3.0 \times 10^6 \text{ kg/m}^3 \cdot \text{m/s}$.

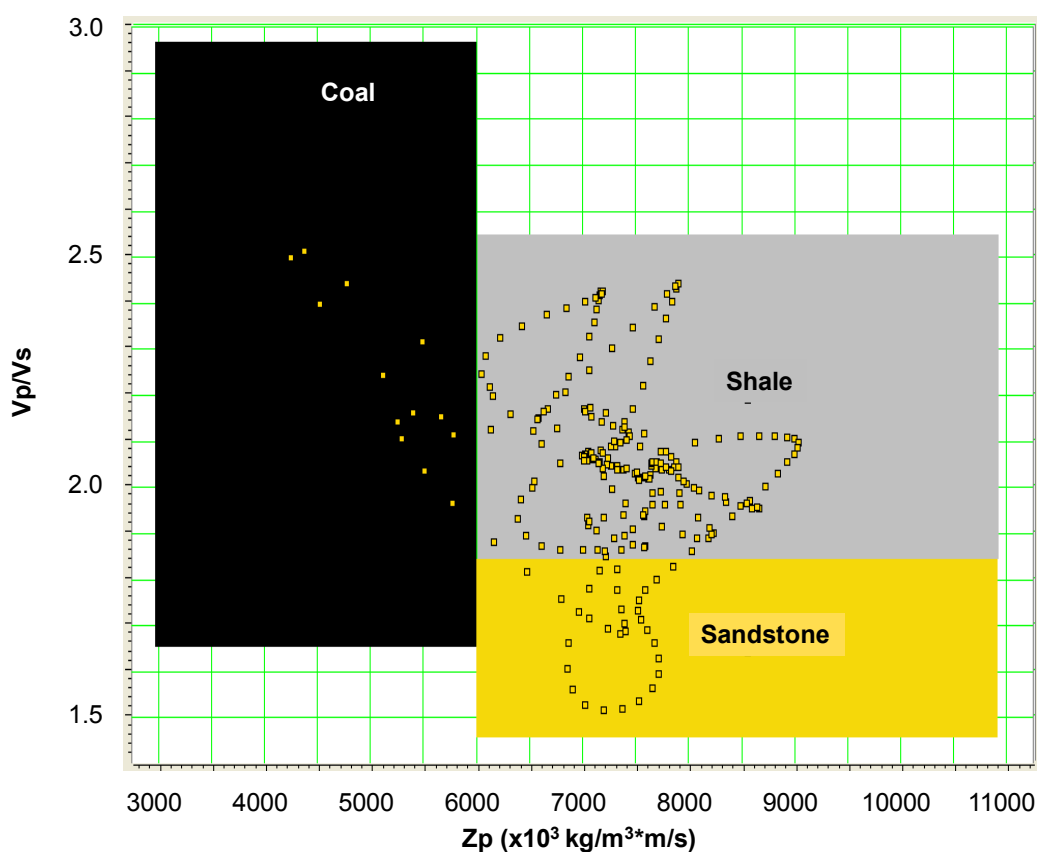


Figure 6-5: A cross-plot of impedance and Vp/Vs for 102/7-28 from 300 - 475 m (KB) at 1 ms sampling with a 60 – 70 Hz high cut filter.

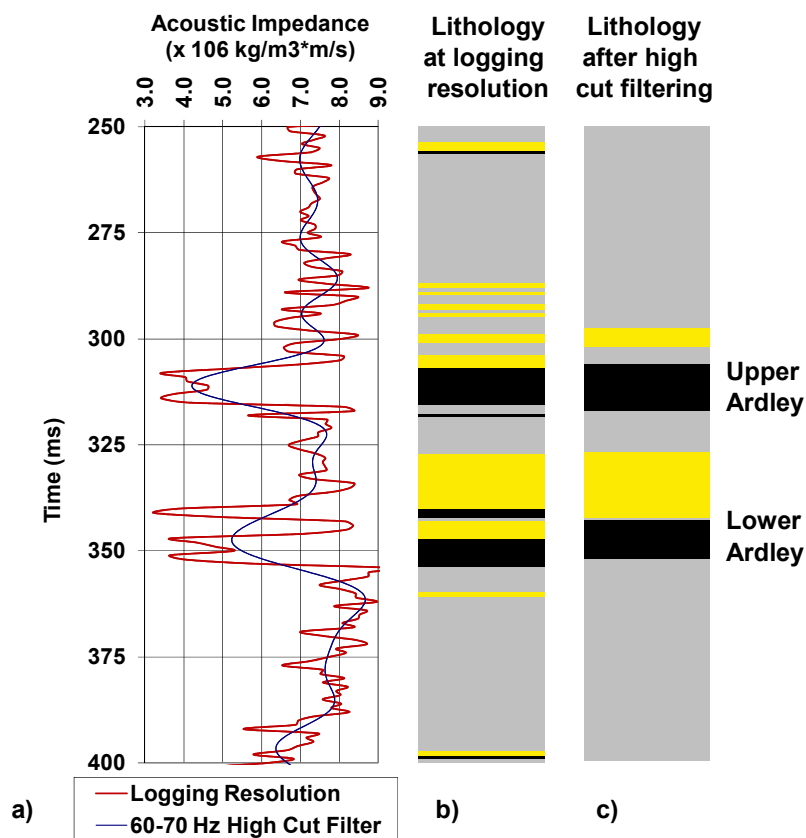


Figure 6-6: (a) The impedance log at logging resolution and with a 60 – 70 Hz high cut filter and the corresponding lithology logs: (b) at logging resolution and (c) after high cut filtering.

6.4 Model Based Inversion of the Alder Flats 3D Data

The workflow for the HRS model-based “hard constraint” inversion method is:

1. Establish the wavelet.
2. Build the initial guess model by interpolating well data throughout the model domain following specified seismic horizons.
3. Low pass filter this initial guess model to the frequency band below the wavelet bandwidth.
4. Test the parameters for the inversion: the pre-whitening value, the number of iterations, the size of the time blocks for the inversion solution, and the bounds for the constraints to be imposed (listed as a percentage of the average impedance of the input initial guess model). Testing is conducted at well locations where the

actual impedance values are known and can be compared to the inverted impedance. The parameters are tuned to reduce the residual difference between the logged impedance and the inverted impedance.

5. Run the inversion. The wavelet amplitude is scaled as a part of the inversion process.
6. Inspect the results and the residual difference between the seismic trace and the synthetic that is created with the inverted impedance model.

Two estimates of the wavelet have already been established as described in Chapter 4. The matching filter wavelet was used for inversion because it generates a zero-offset synthetic seismogram with the better cross-correlation with the seismic data. The wavelet is illustrated again in Figure 6-7.

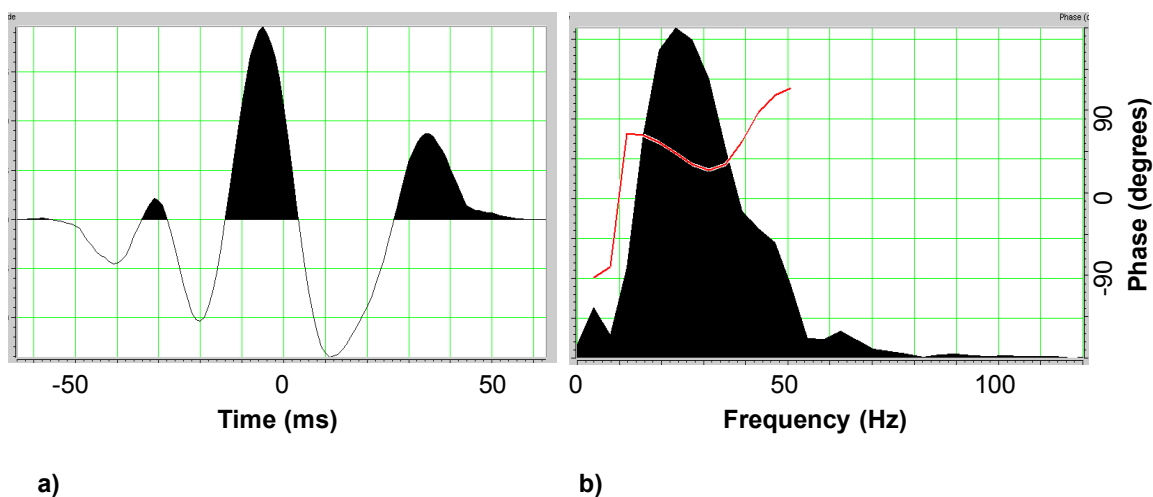


Figure 6-7: (a) The match filter wavelet used for the model-based inversion and (b) the amplitude and phase spectra.

6.4.1 Low Frequency Initial Guess Model

The initial guess model was based solely on the calculated impedance at log resolution from the 102/7-28 well. Although the 100/7-28 well is in the survey limits, as noted earlier, the p-wave velocity was not logged in the well, and an accurate impedance log could not be estimated. Therefore, the 102/7-28 well impedance log was extrapolated

throughout the survey domain as the initial guess model. In order to account for the geological structure of the domain, the log was extrapolated along the seismic horizon of the Lower Ardley Coal zone. Use of a single horizon to guide the extrapolation is believed to give an accurate initial guess model because the stratigraphy is relatively uniform throughout the domain. The initial guess model, at log resolution is illustrated in Figure 6-8.

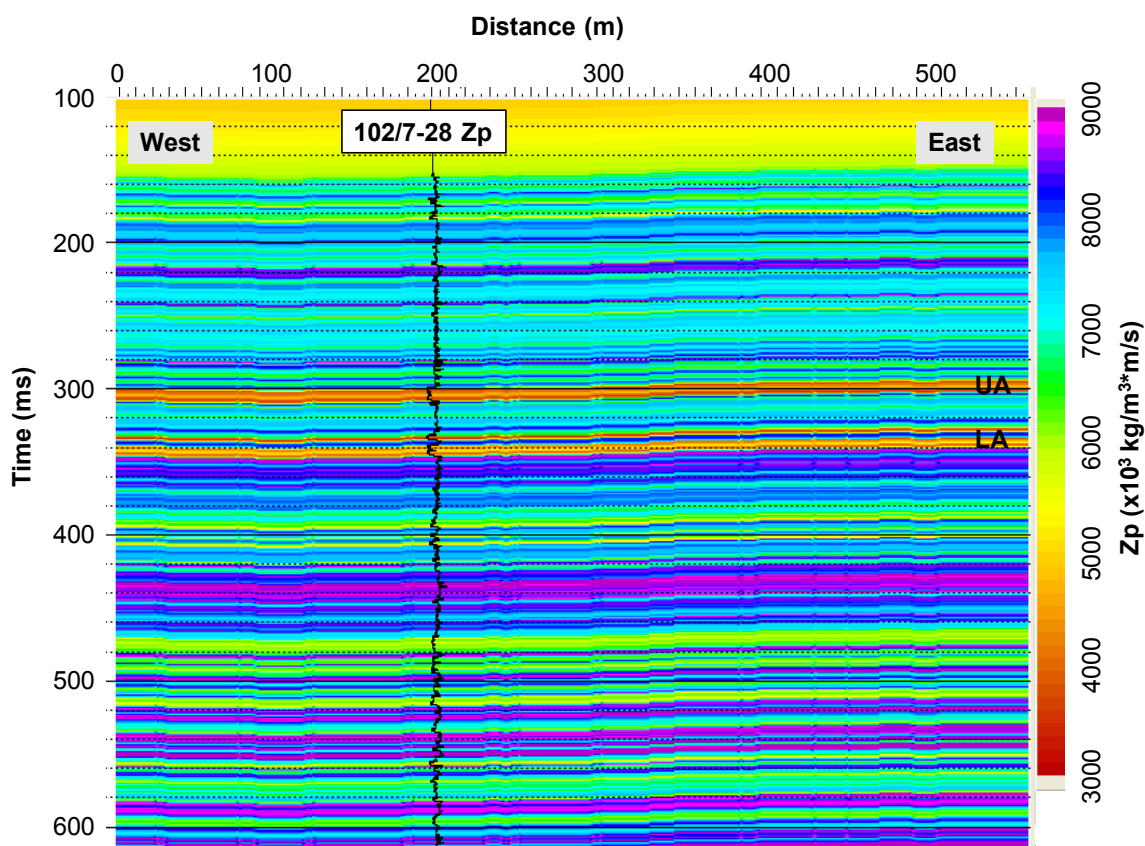


Figure 6-8: The initial guess impedance model at log resolution (inline 71).

As noted above, components of the initial guess model that are not resolved by the seismic data are carried through the inversion algorithm. If the model at log resolution was used as the initial guess model, it would be difficult to know what detail in the inverted impedance estimate had come from the data and what had simply been carried through from the initial guess. Therefore, the initial guess was low pass filtered at 10-15 Hz, the frequency band below the band of the seismic data. This low frequency

model was used as the initial guess model for the conjugate gradient perturbation of the impedance model. The inversion solution should then minimize the squares of the errors (equation 6.6) as long as the low pass filtered initial guess model is within the region of convergence. The low passed initial guess model is illustrated in Figure 6-9.

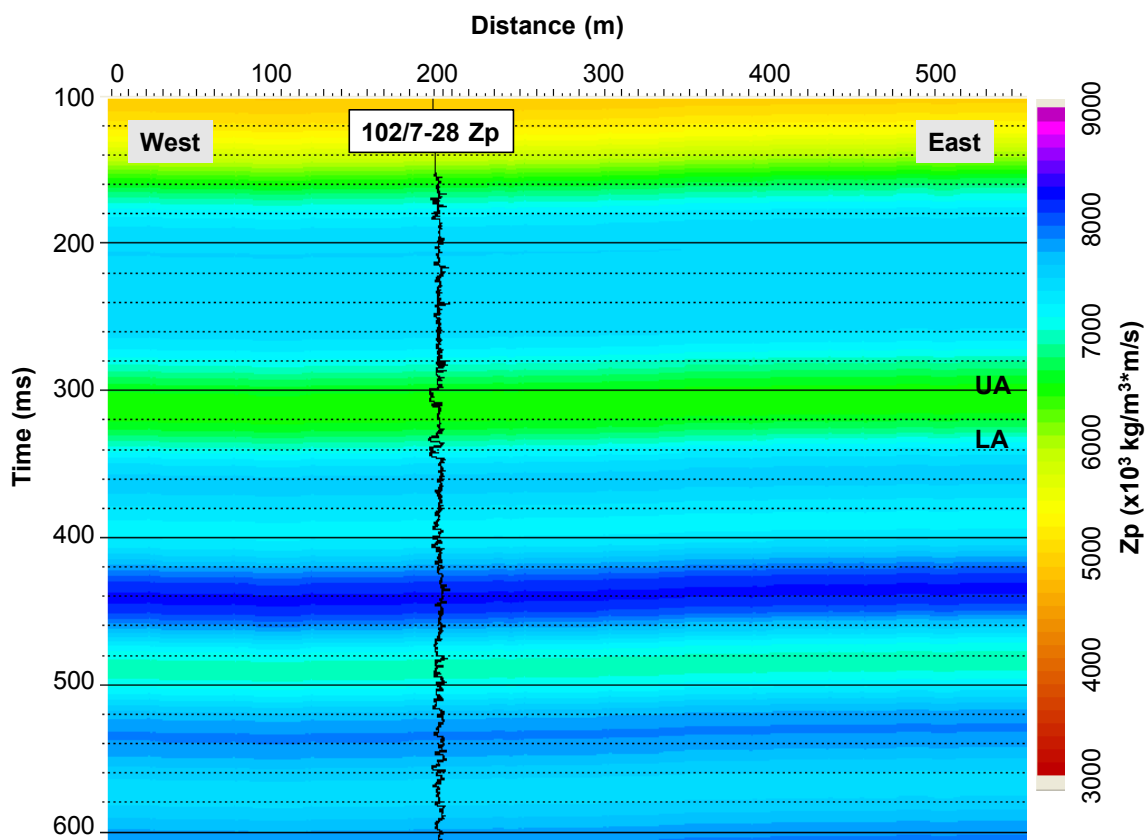


Figure 6-9: The initial guess impedance model after low pass filtering 10-15 Hz (inline 71).

6.4.2 Inversion Parameter Testing

The inversion was then run on the traces nearest the 102/7-28 well. The result was compared to the impedance log from the well, and individual parameters were adjusted until the error difference between the log impedance and the inverted impedance was minimized. The parameters were tested in a more or less *ad hoc* way and the elected values are listed in Table 6-1. The model-based constraint was set to 100% of the average impedance from the initial guess model which is the least constrained setting.

Additionally, the inversion was set to invert each trace independently of the other traces in order to minimize spatial averaging and retain as much lateral resolution as possible.

Table 6-1: Parameters used in the model-based impedance inversion

Parameter	Value
Percentage of the average impedance from the initial guess model used as a constraint for the solution impedance.	100%
Block size	1 ms
Stability factor	0.02
Number of iterations	10

The pre-whitening parameter for the inversion was selected by gradually increasing the value until the inverted solution seemed to be stable (i.e. no great change in the error or the inversion trend resulted with further increases in the pre-whitening). The final inverted impedance is compared to the 102/7-28 well impedance log in Figure 6-10 and the residual error (difference between the inverted impedance and the well log impedance) and the cross-correlation between the synthetic seismogram of the inverted impedance and the actual seismic trace are listed in Table 6-2.

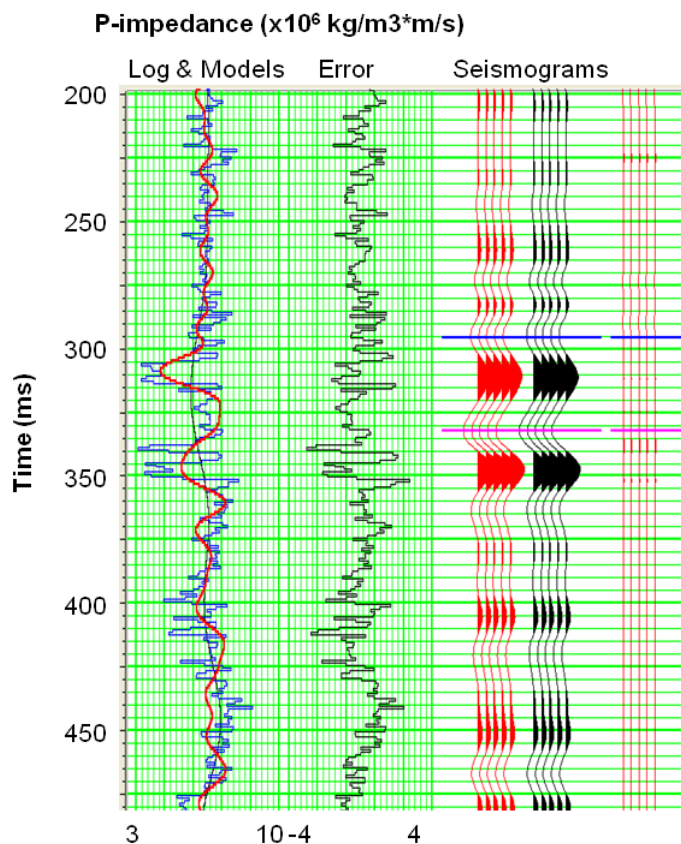


Figure 6-10: Analysis of the inverted impedance estimation at the 102/7-28 well location. In the left track, the blue curve is the log impedance, the black curve is the initial guess impedance, and the red trace is the inverted impedance. The middle track black curve is the error in the impedance estimate. On the right, the red seismogram is the synthetic generated from the impedance inversion and the black seismogram is the actual seismic data and the traces on the far right is the difference between the red and black seismogram.

Table 6-2: The impedance error and synthetic-seismic correlation after impedance inversion at the 102/7-28 well location using the parameters from Table 6-1 (100-600 ms)

	Value for the match filter wavelet
Impedance error	1018.3
Synthetic-to-data seismogram cross-correlation	0.9933

6.4.3 Inversion and Wavelet Scaling

With these parameters, the inversion was then run on the full 3D data set. The first automated step in the inversion algorithm is scaling of the wavelet. In order to scale the impedances correctly in equation 6.7, the absolute amplitude of the wavelet must be known. The wavelet shape has already been established, however the absolute amplitude has not. To solve for the wavelet amplitude, the unscaled wavelet \mathbf{w} is convolved with the unfiltered reflectivity of the initial guess model (\mathbf{r}) and then correlated with \mathbf{w}^T to give: $\mathbf{w}^T \mathbf{w} \mathbf{r}$ (HRS Strata Theory). The RMS value of the ten largest amplitude peaks and troughs from this series is found:

$$avgModelAmp = \sqrt{\left(\frac{1}{10}\right) \sum_{i=1}^{10} (w^T wr)_i^2} \quad .$$

Also, $\mathbf{w}^T \mathbf{T}$ is calculated (where \mathbf{T} is the seismic trace) and the RMS value of the ten largest amplitude peaks and troughs of this series is found:

$$RMS_TraceSize = \sqrt{\left(\frac{1}{10}\right) \sum_{i=1}^{10} (w^T T)_i^2} \quad .$$

The ratio:

$$Scaling = \frac{avgModelAmp}{RMS_TraceSize}$$

is used to scale the wavelet.

A key parameter used in scaling the wavelet is which seismic trace(s) \mathbf{T} to use in the scaling algorithm. Because the seismic trace amplitudes were not equalized during the processing flow, the wavelet amplitude may not be consistent throughout the seismic data volume. This is illustrated Figure 6-11 which shows the RMS of the seismic trace amplitude in a window from 150 ms above to 500 ms below the Upper Ardley Coal horizon. Over a window of this size, the RMS values should be fairly uniform, but they are not because the amplitudes were never equalized. Therefore, the inversion algorithm was parameterized to scale the wavelet for each trace individually.

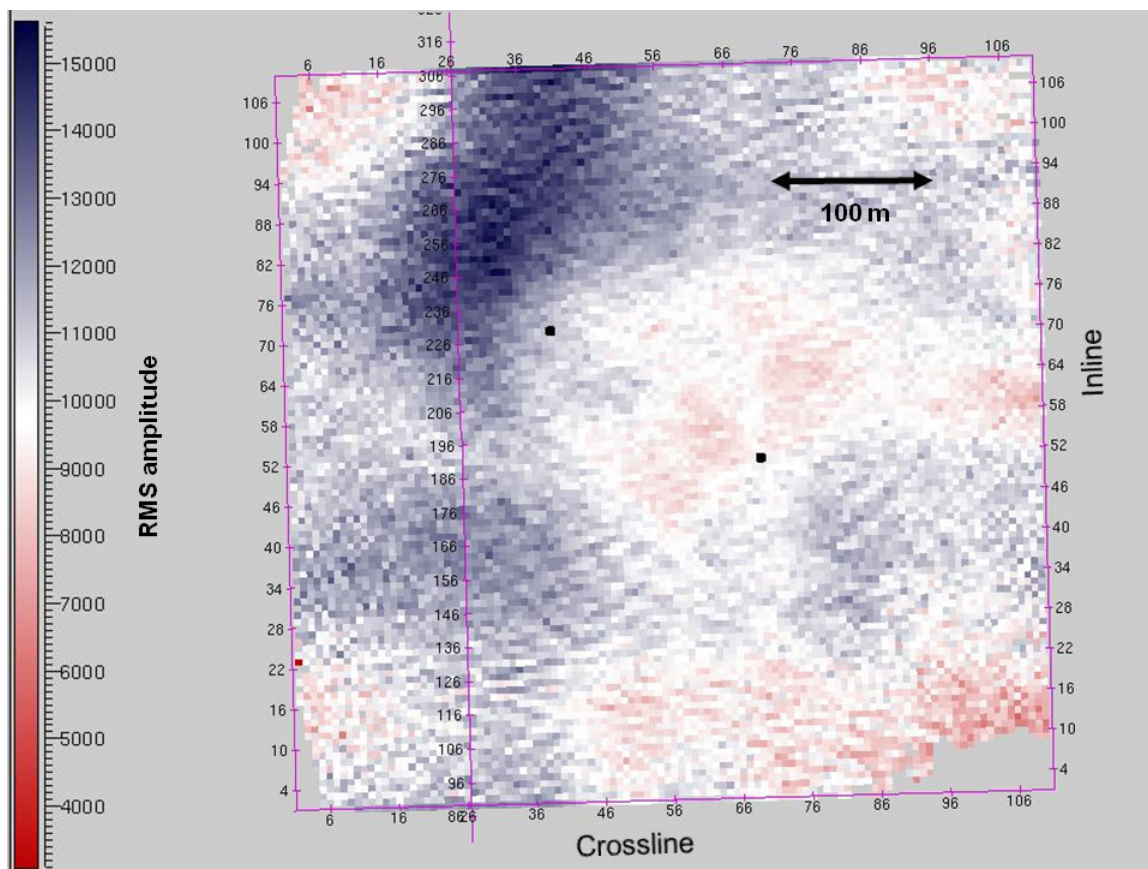


Figure 6-11: The RMS of the trace amplitudes in the 3D data in a window from 150 ms above the Upper Ardley Coal horizon to 500 ms below the Upper Ardley Coal horizon.

The results after inversion are illustrated in Figure 6-12. The figure can be compared to the low frequency initial guess model in Figure 6-9. Two layers of low impedance occur after 300 ms which are the Lower and Upper Ardley Coals.

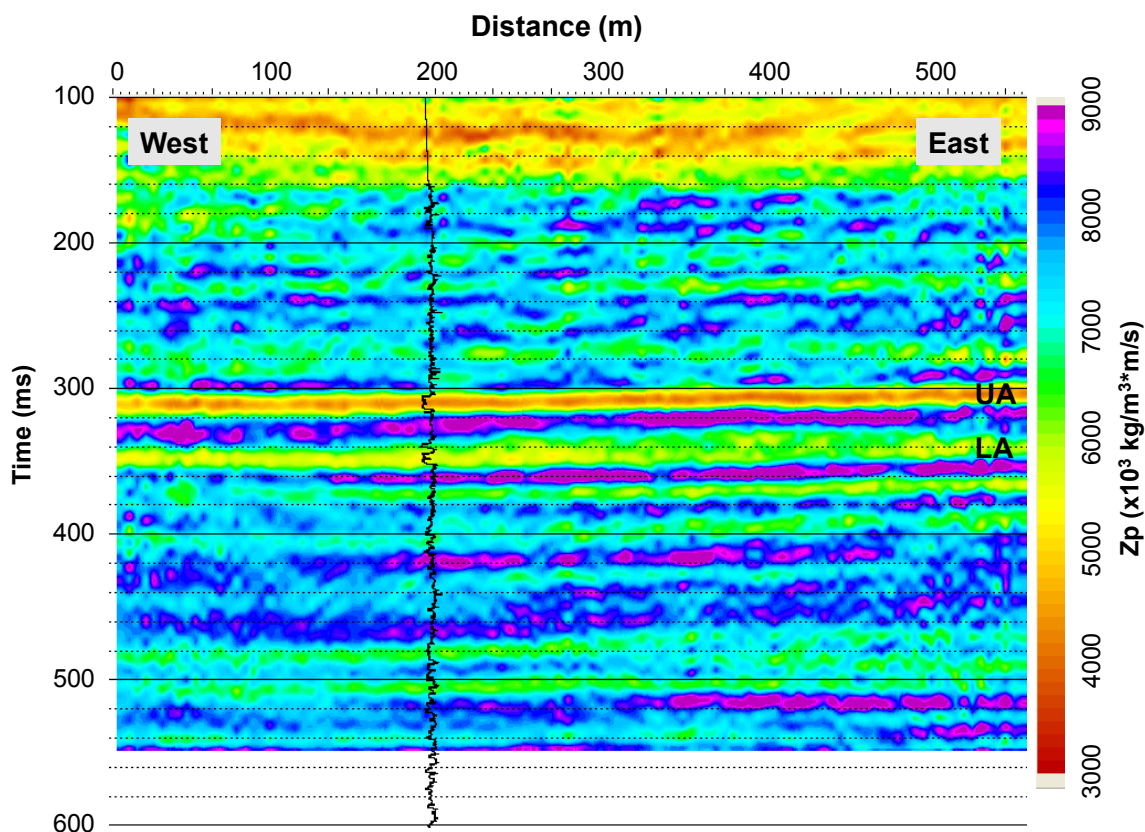


Figure 6-12: The inverted impedance (inline 71) with the impedance log from 102/7-28 superimposed.

6.4.4 Interpretation

A closer inspection of the inversion of the Ardley Coal Zone is illustrated in Figure 6-13. Several trends are noteworthy. The Upper Ardley Coals are represented by a strong zone of low impedance that ties acceptably in time with the well impedance log. The event is laterally continuous and of uniform thickness, as intuitively expected. However, the Lower Ardley Coal impedance event does not show consistency or constant thickness. At the south end of the survey, the zone of low impedance is very much smeared out and using a lithology cut-off value of $6.0 \times 10^6 \text{ kg/m}^3 \cdot \text{m/s}$ the coal zone effectively disappears. This phenomena can be related to the erratic character of the seismic trace at the Lower Ardley horizon in the south end of the survey. As noted in Chapter 4 this erratic trace character may be a related to the geology or it may be simply an unexplained data error. However, in the vicinity of the 102/7-28 well, the inversion

seems intuitively robust. The Mynheer and the Silkstone zones are not resolved as individual low impedance zones, but this is expected given the band-limited nature of the wavelet and the inversion.

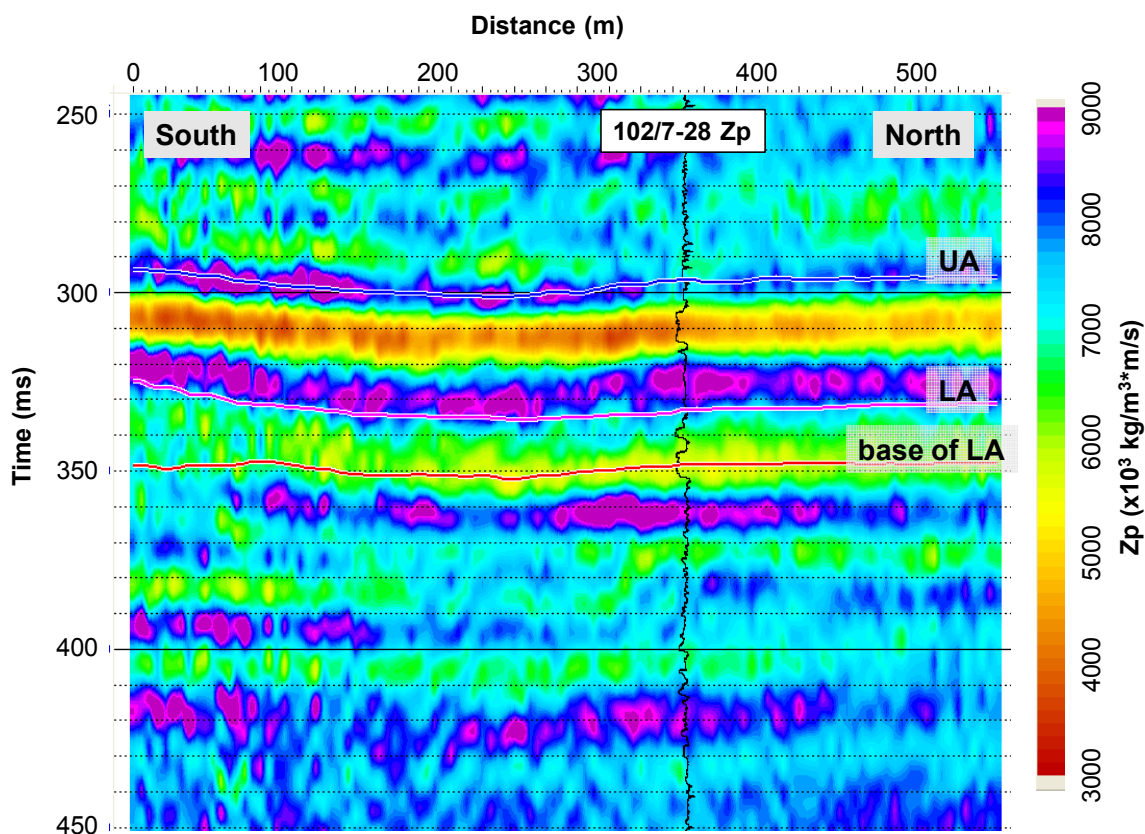


Figure 6-13: The inverted impedance (crossline 40) with the impedance log from 102/7-28 superimposed. The horizons are those picked from the seismic.

Figure 6-13 shows that there is a low impedance zone in the Lower Ardley coals starting near the 102/7-28 well location. This anomaly is mapped in Figure 6-14 which shows the average impedance in a window 2 – 12 ms above the “base of Lower Ardley” seismic horizon (Figure 6-13). The map shows a distinct low impedance anomaly immediately to the northeast of the 102/7-28 well. The anomaly covers an elliptical area with major and minor axis lengths of approximately 65 m x 25 m (an area equivalent to 1276 m²).

The size of the anomaly and its location suggest that it could be related to the injected CO₂. As noted in Chapter 1, the project engineers note that if the CO₂ entered the full thickness of the Lower Ardley Coal Zone, the area of the region contacted by CO₂ would be 1,495 m² and that if the region were circular around the injection well (102/7-28) the equivalent radius would be 21.8 m. Also, because the dominant natural fracture direction and the anticipated orientation of the hydraulically stimulated fracture trends southwest-to-northeast, the preferential permeability pathway is expected to be southwest-northeast and any injected fluid would move along that axis. Furthermore, a gaseous fluid would likely move up-dip due to buoyancy, which is to the northeast relative to where 102/7-28 penetrates the Lower Ardley Coals (see Figure 4-24). Thus, the anomaly's location, shape and size suggest that it could be related to the injected CO₂.

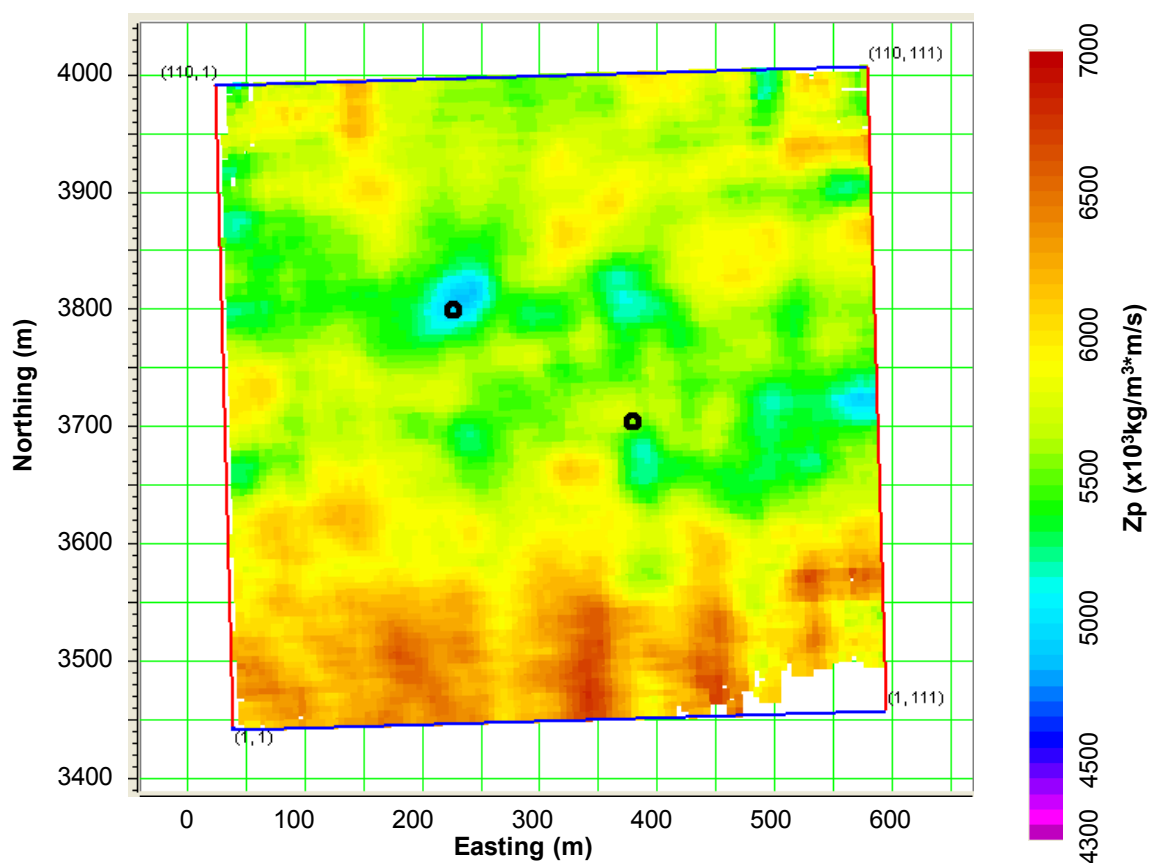


Figure 6-14: A map of the mean impedance in a 10 ms window through the Lower Ardley impedance zone.

One method to evaluating the quality of an inversion result is to look at the residual difference between seismic data and the synthetic seismogram that is created from the inverted impedance estimation to ensure that the data are being successfully reproduced by the model. Figure 6-15 illustrates the residual difference which is low throughout the data volume.

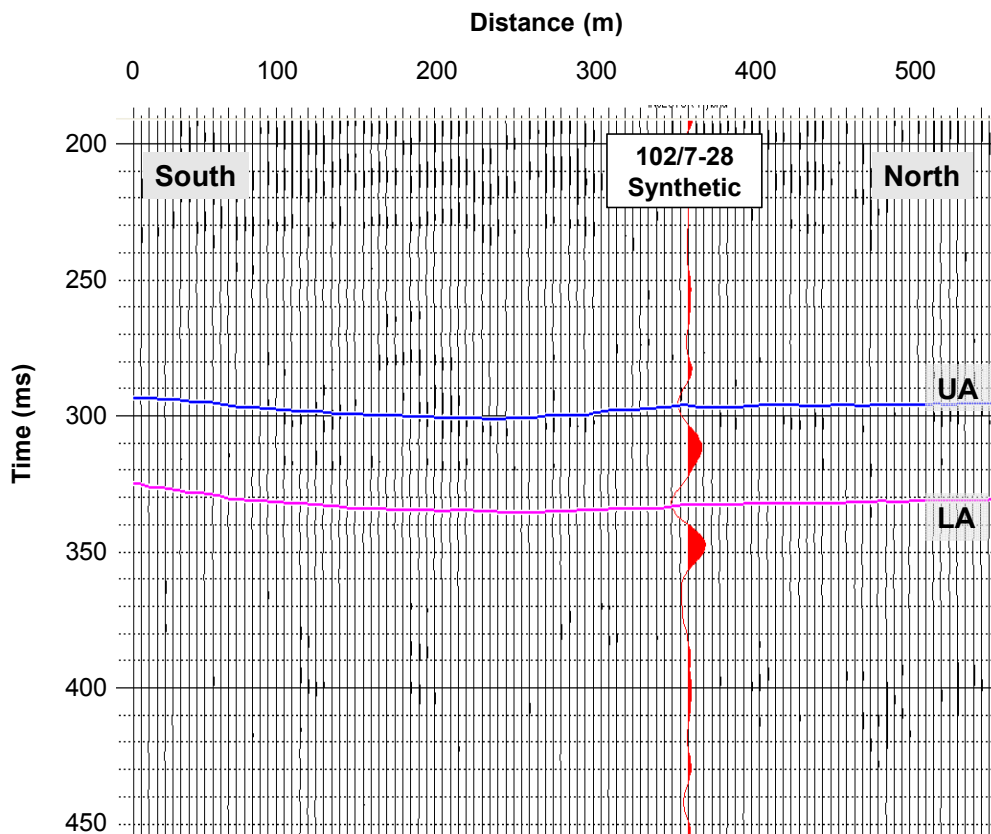


Figure 6-15: The residual difference between the seismic traces and the synthetic seismogram created from the impedance estimation (crossline 40).

Another method of evaluating the quality of the inversion is to compare the impedance estimate to the known impedance at well locations. However, since the impedance estimate is band-limited, it is important to compare the inversion result to a band-limited version of the well log. A cross-plot of the inversion impedance values and the 102/7-28 impedance log values that have been filtered with a high-cut of 60-70 Hz is

illustrated in Figure 6-16. The plot shows a 1:1 slope which confirms that the inversion scaling is unbiased.

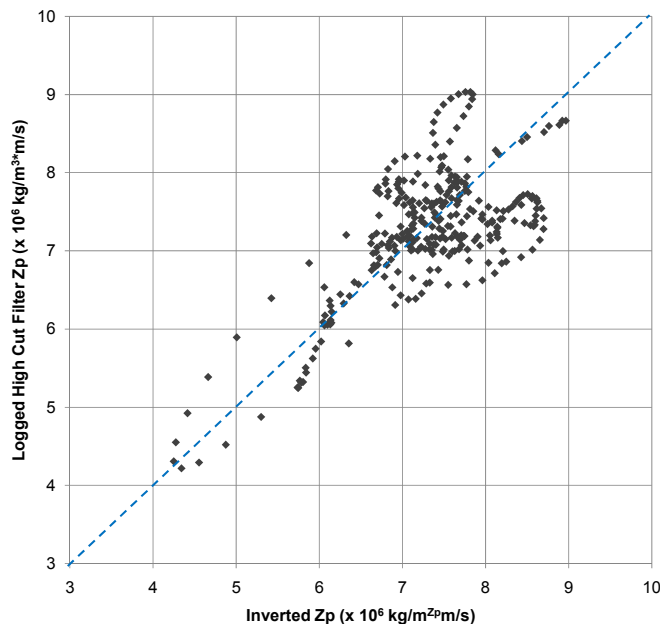


Figure 6-16: Cross plot of the impedance inversion estimate values and the 102/7-28 well log impedance values after high cut filtering (60-70 Hz).

6.5 Mixed-norm Constrained Sparse Spike Inversion of the Alder Flats 3D Data

In order to verify the inversion results, the inversion was run with a different algorithm. The Jason Geoscience Workbench (JGW) uses a mixed-norm inversion algorithm called a Constrained Sparse Spike Inversion (CSS inversion). The CSS inversion was used to invert the Alder Flats data.

The workflow for inversion with JGW is:

1. Estimate the wavelet shape and amplitude using the CSS inversion algorithm in reverse.
2. Build a low frequency trend model by interpolating well data throughout the model domain following specified seismic markers.
3. Test the λ norm-weighting parameter.
4. Identify the inversion constraints.
5. Run the inversion.

6. QC the results:

- compare the residual difference between the seismic trace and the synthetic that would be created with the inverted impedance mode,
- compare the amplitude of the inverted impedance to the well logs.

6.5.1 Wavelet Estimation

The JGW uses another technique to estimate the wavelet in the seismic data. The tool finds the wavelet that will best produce the log reflectivity from the seismic data using the CSS inversion. The estimated wavelet extracted from 200 – 400 ms is illustrated in Figure 6-17. The amplitude spectrum is roughly comparable to the match filter wavelet.

A QC (quality control) of the wavelet is to compare the amplitude spectrum of the wavelet in the Fourier domain with the spectrum of the seismic data. The wavelet's spectrum should not be too dissimilar to the seismic's spectrum for a white Earth but should be shifted with respect to that for the seismic for a coloured Earth. Figure 6-18 illustrates the comparison and shows that the wavelet spectrum is roughly a smoothed version of the seismic spectrum. The seismic spectrum has more peaks and troughs but this is expected since the reflectivity series spectrum also shows many peaks and troughs (Figure 6-19). Windowing and tapering the wavelet in the time domain smoothes the wavelet spectrum in the Fourier domain and so the window length and taper must be selected carefully. Figure 6-18 shows that the wavelet spectrum does represent a smoothed and shifted version of the band-limited reflectivity series and is accurately parameterized.

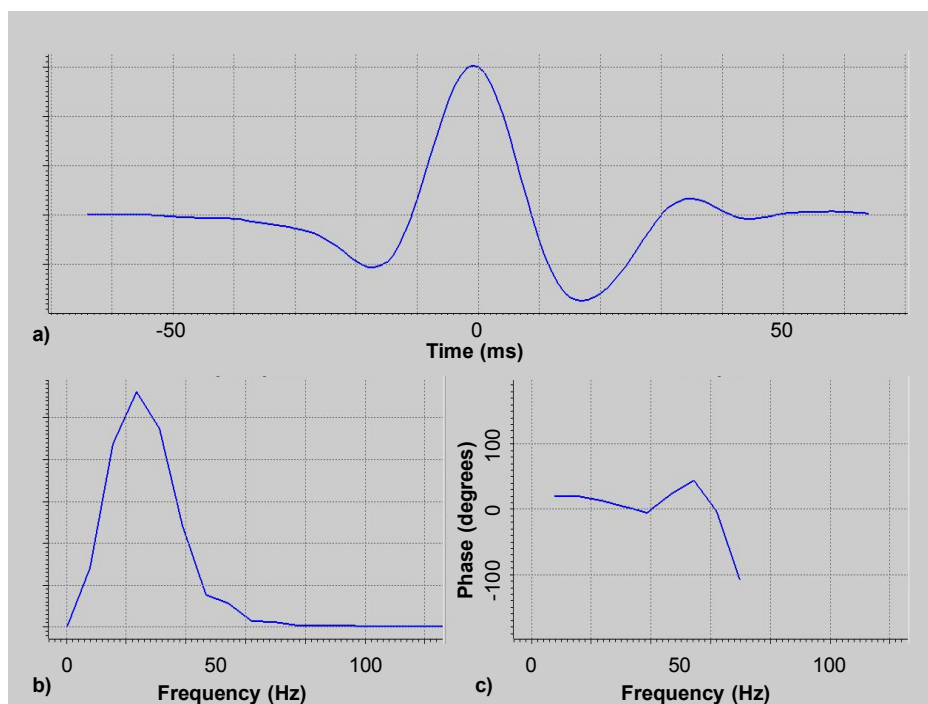


Figure 6-17: (a) The wavelet estimated using the CSS inversion, (b) the amplitude spectrum and (c) the phase spectrum.

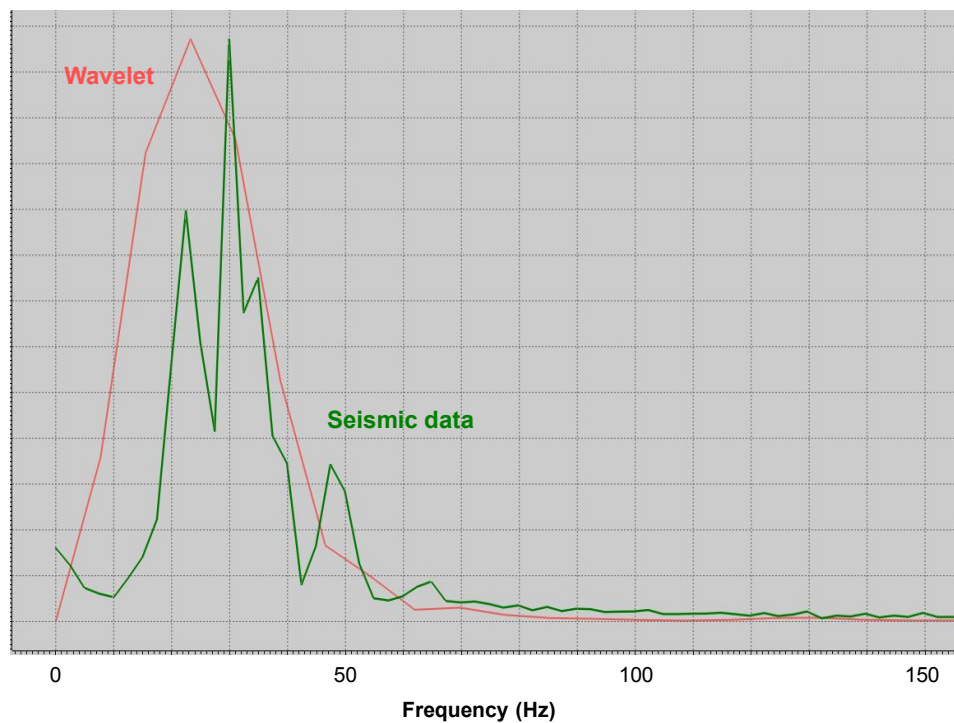


Figure 6-18: The amplitude spectrum of the wavelet and the seismic data.

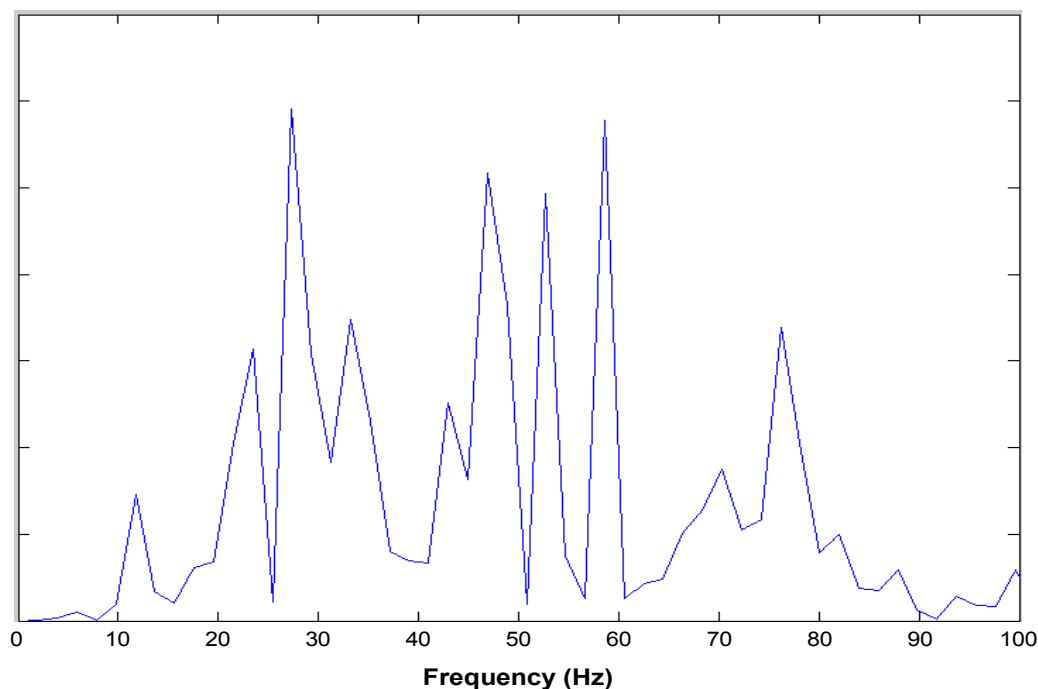


Figure 6-19: The amplitude spectrum of the reflectivity series from the 102/7-28 well logs generated from a 512 ms time series with 1 ms sampling and an 80-100 Hz high-cut filter.

Although the CSS inversion can accommodate a spatially varying wavelet, it is convenient to assume that there is a single wavelet with a constant amplitude throughout the seismic volume. For this to be valid, it is important that the amplitudes of the seismic data are balanced from trace to trace. As discussed in Section 6.4.3, the data showed a significant variation in RMS amplitude in a long time window around the Ardley Coal reflection events which indicated that the trace amplitudes were not equally balanced. Therefore the RMS amplitudes were normalized over this 650 ms window before proceeding with the inversion.

6.5.2 Setting the Inversion Parameters

The CSS inversion minimizes a mixed norm objective function as discussed in Section 6.2.4. The mixed norm objective function is:

$$J = L_p(\mathbf{r}) + \lambda L_q(\mathbf{T} - \mathbf{w}\mathbf{r}) + L_1(\text{low freq. residuals})$$

where λ balances the cost of the first term that seeks the sparsest reflectivity series possible and the second term that seeks to minimize the difference between the seismic trace and the model trace (wavelet convolved with the solution reflectivity series) in a least squares sense. The choice of λ depends upon the level of noise in the seismic trace and is a critical parameter to adjust. If λ is too small, the reflectivity will be sparse, but the model will not closely match the seismic data. However, if λ is too large, the model will match the trace very well, but there will be too many reflection coefficients in the solution series, some of which will merely model the noise. The key is to find the λ value that just matches the seismic. Figure 6-20 shows two methods of evaluating the correct choice of λ . Figure 6-20a shows the seismic trace and the residual between the model trace and the seismic at the same amplitude scale. Setting λ to 10 appears to be the lowest level that produces a small residual. Figure 6-20b shows the resulting impedance inversion for several traces and compares it to the well log impedance values. Again a λ value of 10 produces an adequate match between the inversion impedance and the well log impedance. λ was set to 10 in the inversion.

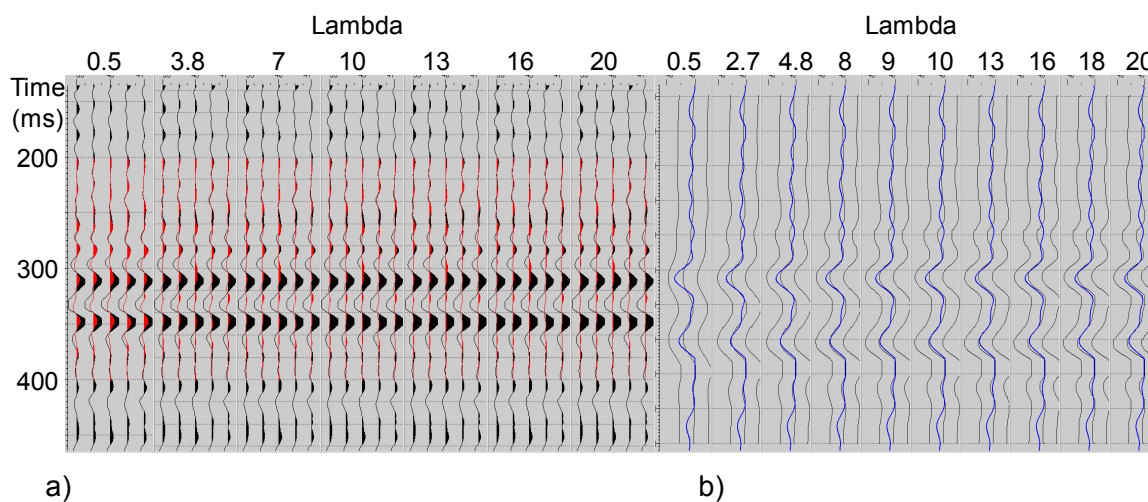


Figure 6-20: Testing the λ value. (a) the seismic (black) and the residual (red) in the time domain and (b) the inverted impedance (black) compared to the well log impedance (blue).

The third term in the objective function softly constrains the low frequencies in the inversion to match the initial *a priori* low frequency model. The CSS inversion objective function also includes an optional constraint that constrains the solution to stay within a specified range of the solutions in adjacent CDP bins. This introduces stability in the inversion and results in a smoother inversion result bin-to-bin. The inversion was constrained in this way.

The solution to the inversion is a reflectivity series. The impedance is estimated using equation 6.2 and constraints from the low frequency model. Finally, the estimated impedance is merged with the low frequency model to produce the inverted impedance. The frequency at which to merge the estimated impedance with the low frequency model must be specified. The low frequency model used in the CSS inversion was identical to the model illustrated in Figure 6-9 which was filtered with a 10-15 Hz filter. This was an appropriate merging band since the vibroseis sweep started at 10 Hz.

6.5.3 Inversion QCs

Figure 6-21 shows the inverted impedance and the band-limited impedance well log from 102/7-28. As before, in the crossline direction (north-south) the impedance in the Upper Ardley Coal Zone is consistent across the survey, but in the Lower Ardley Coal Zone the impedance estimate shows the same deterioration in consistency seen in the HRS inversions at the south end of the survey. The inverted impedance estimate is illustrated along side the original seismic data in Figure 6-22. Figure 6-22 also shows that the horizons for the Lower and Upper Ardley Coal Zones can be picked either on the seismic troughs or on the impedance data using a 6.0×10^6 kg/m³*m/s cut-off.

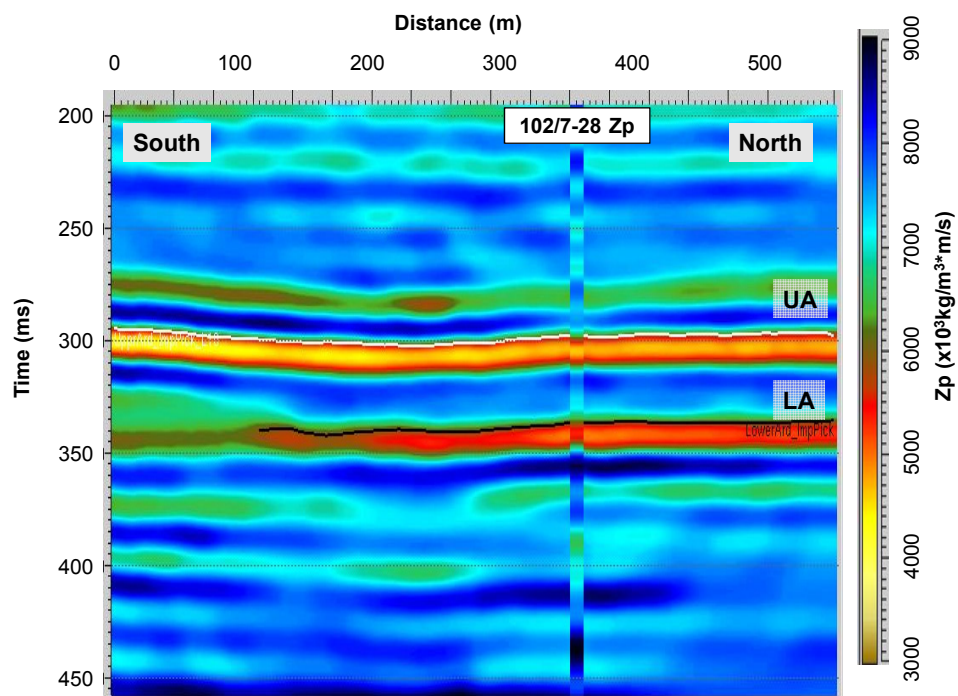


Figure 6-21: The inverted impedance (crossline 40).

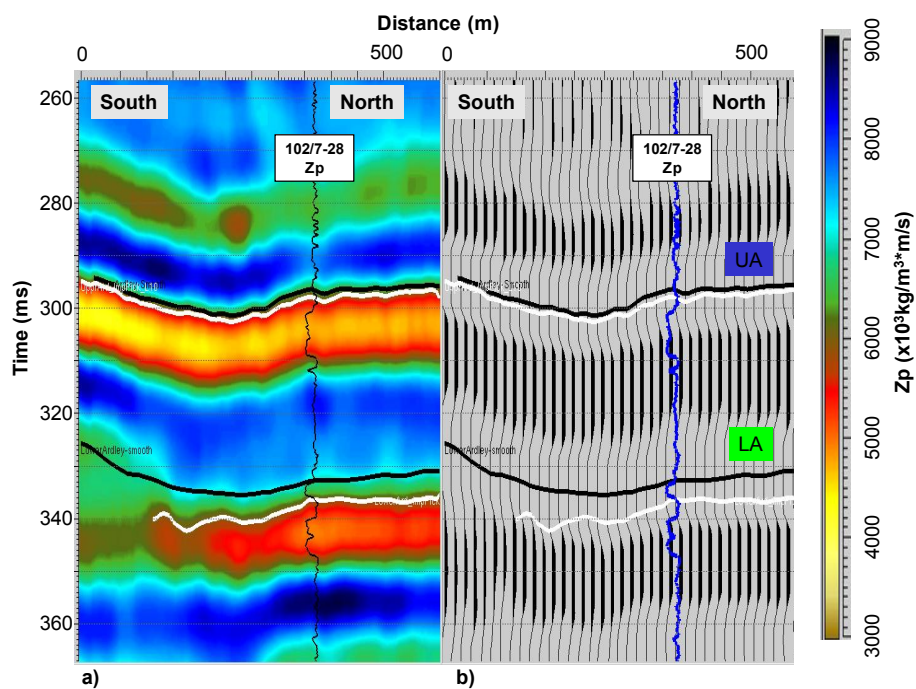


Figure 6-22: (a) The inverted impedance (crossline 40) and (b) the original seismic. Lower and Upper Ardley Coal horizon picked on seismic (black) and on the impedance data $6.0 \times 10^6 \text{ kg/m}^3 \cdot \text{m/s}$ cut-off (blue).

The cross-correlation between the synthetic seismograms generated from the inverted impedance and the original seismic traces over a 200 ms window around the Ardley coals (Figure 6-23) is higher than 0.9 throughout most of the survey indicating a good match. Figure 6-24 shows the residual difference between the original seismic data and the seismogram generated from the inversion impedance with the original seismic superimposed (each at the same scale). The residual is low relative to the seismic especially in the window of the Ardley coals.

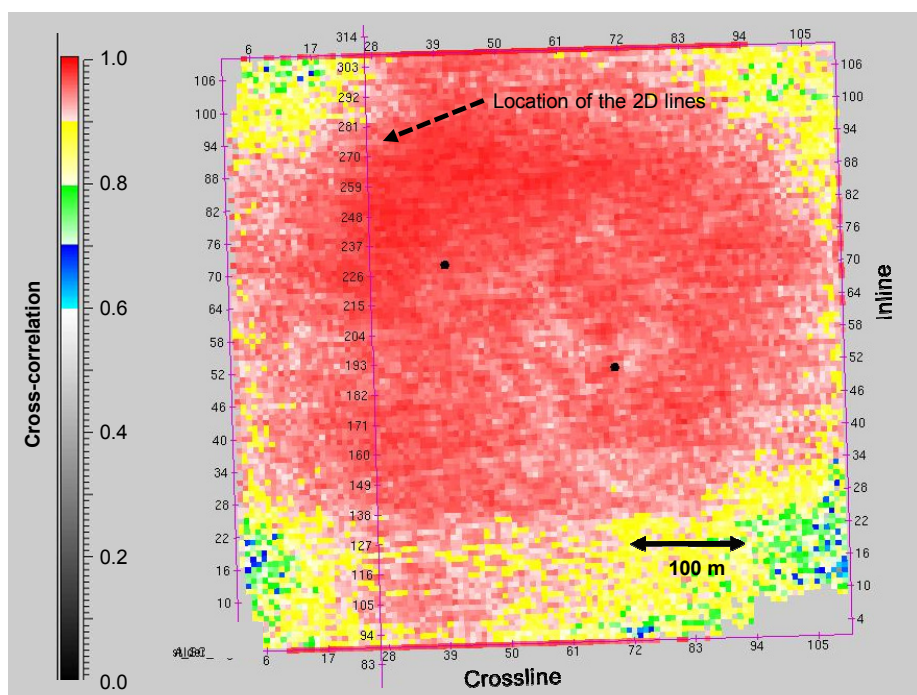


Figure 6-23: Inverted synthetic seismogram cross-correlation with the seismic data.

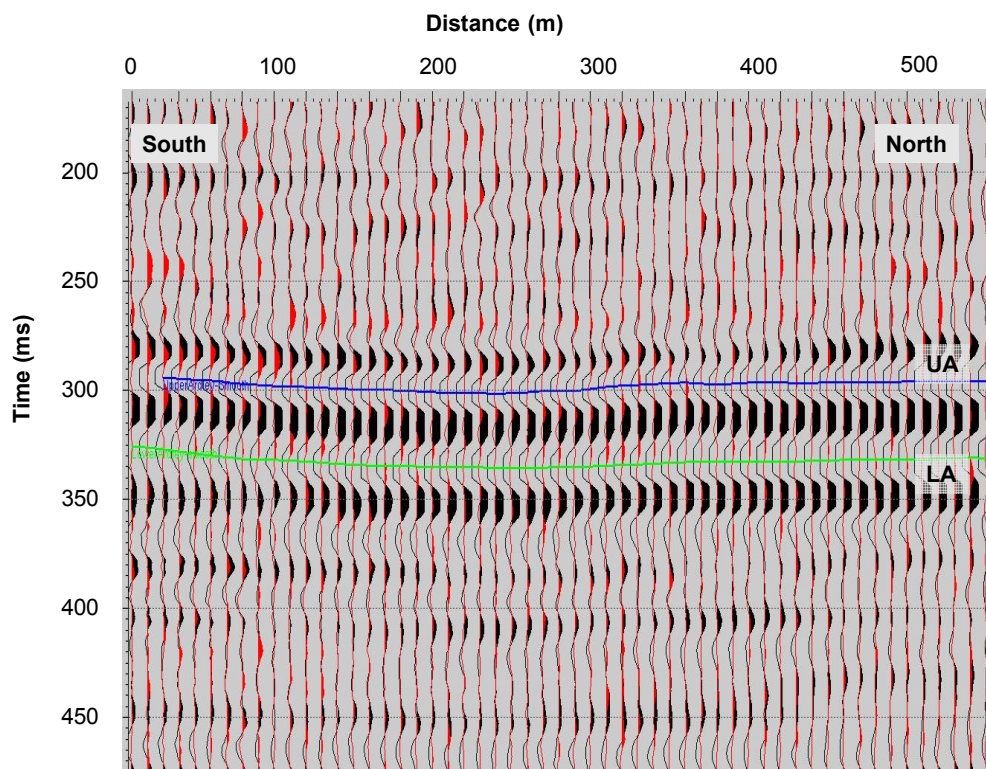


Figure 6-24: The seismic data (black) and the residual error (red) plotted at the same amplitude scale (crossline 40).

The scale of the inverted impedance is compared to a band-limited version of the well log impedance in Figure 6-25 which shows that the inverted impedance is slightly higher in the Upper Ardley Coal Zone and is slightly lower in the Lower Ardley Coal Zone than the high cut filtered well log impedance. However, overall, the amplitude is approximately correct. Figure 6-26 shows the cross-plot of the inverted impedance estimates to the band-limited well log impedance values. The trend shows a 1:1 slope indicating an unbiased and properly scaled impedance estimate.

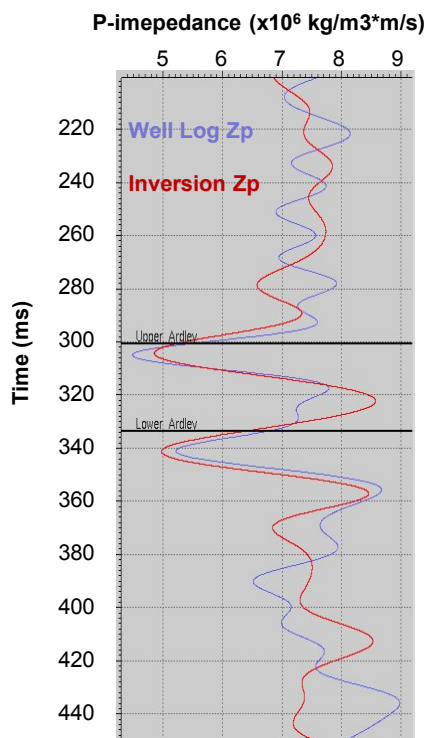


Figure 6-25: The inverted impedance and the 102/7-28 well log impedance with a 60-70 Hz high cut filter.

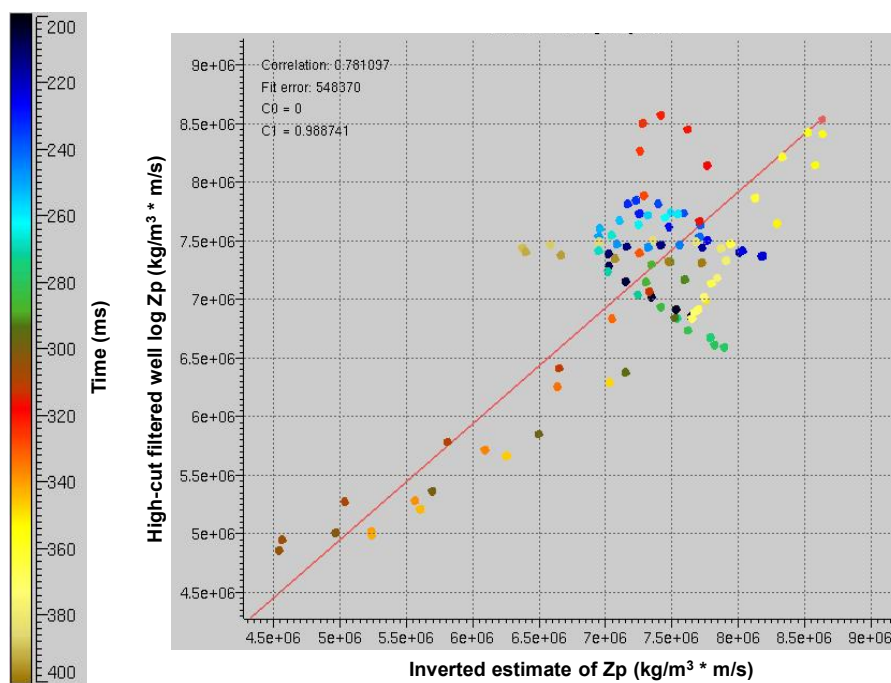


Figure 6-26: The cross-plot of the inverted impedance and the well log impedance after high cut filtering (60-70 Hz).

6.5.4 Interpretation

Figure 6-27 shows a close scrutiny of the inversion results. In Figure 6-27a the impedance well log with a 60-70 Hz high cut filter is superimposed on the inverted impedance result. Figure 6-27c shows the reflectivity result of the CSS inversion. It is interesting to note that although the Mynheer and Silkstone coals zones were not resolved as separate events in the seismic data or the impedance estimate, there is a subtle event in the estimated sparse spike reflectivity series (Figure 6-27c) that could be tied to the thin zone of the Silkstone coal zone.

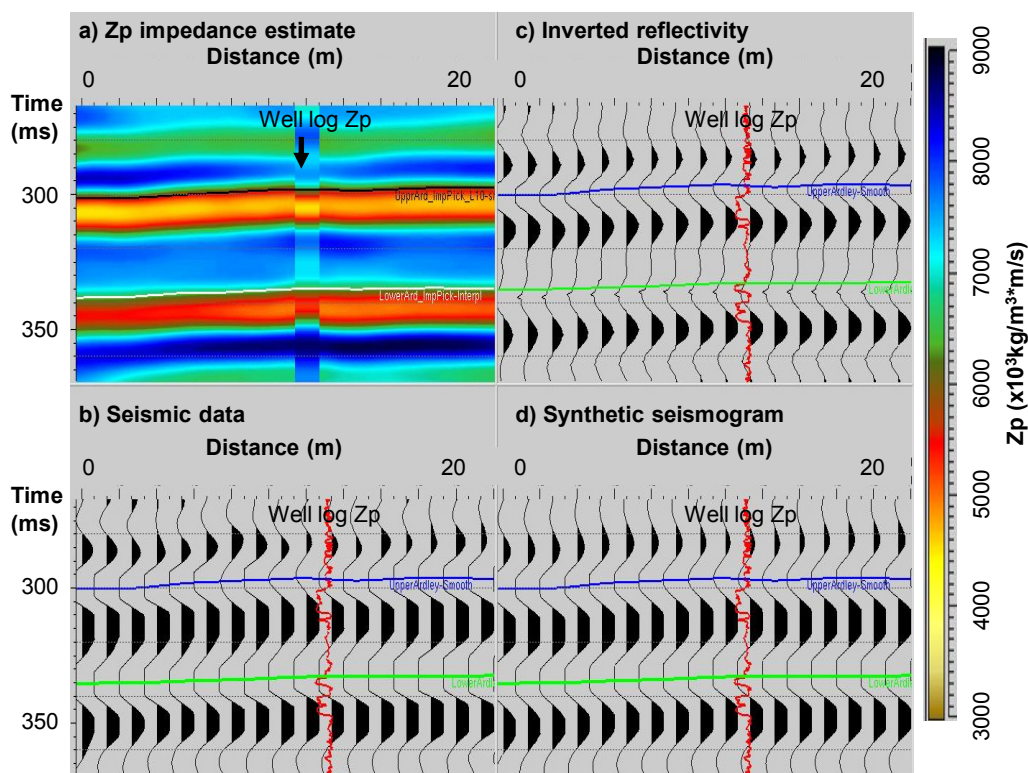


Figure 6-27: (a) The inverted impedance with the well log impedance after 60-70 Hz high cut filtering, (b) the original seismic, (c) the inverted reflectivity, and (d) the inverted synthetic seismogram (a portion of crossline #40).

Horizon slices at 1 ms increments to the Lower Ardley Coal Zone seismic horizon are mapped in Figure 6-28. The slices effectively step through the impedance of the Lower Ardley Coal Zone. At a horizon that is 10 ms below the Lower Ardley horizon a

low impedance anomaly is evident around the 102/7-28 well. Figure 6-29 illustrates this slice again and the temporal location of the slice. The anomaly is to the northeast of the well in exactly the same location that it was observed in Figure 6-14. Its approximate areal extent is approximately 1800 m², which again compares favourably with the expected 1,495 m² size of the CO₂ flood predicted by the project engineers. Again, the location is along strike with the southwest-to-northeast fracture trend and up-dip of where 102/7-28 penetrates the Lower Ardley Coals.

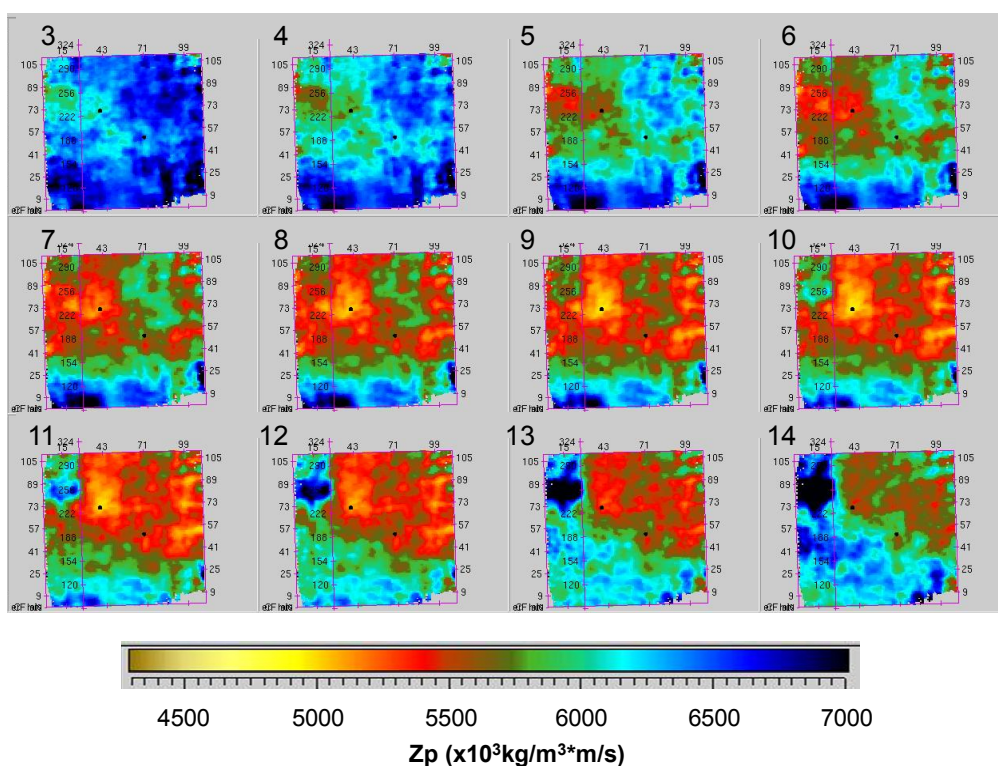


Figure 6-28: 1 ms steps through the inverted impedance of the Lower Ardley Coal Zone from 3 - 14 ms below the Lower Ardley Coal seismic pick horizon.

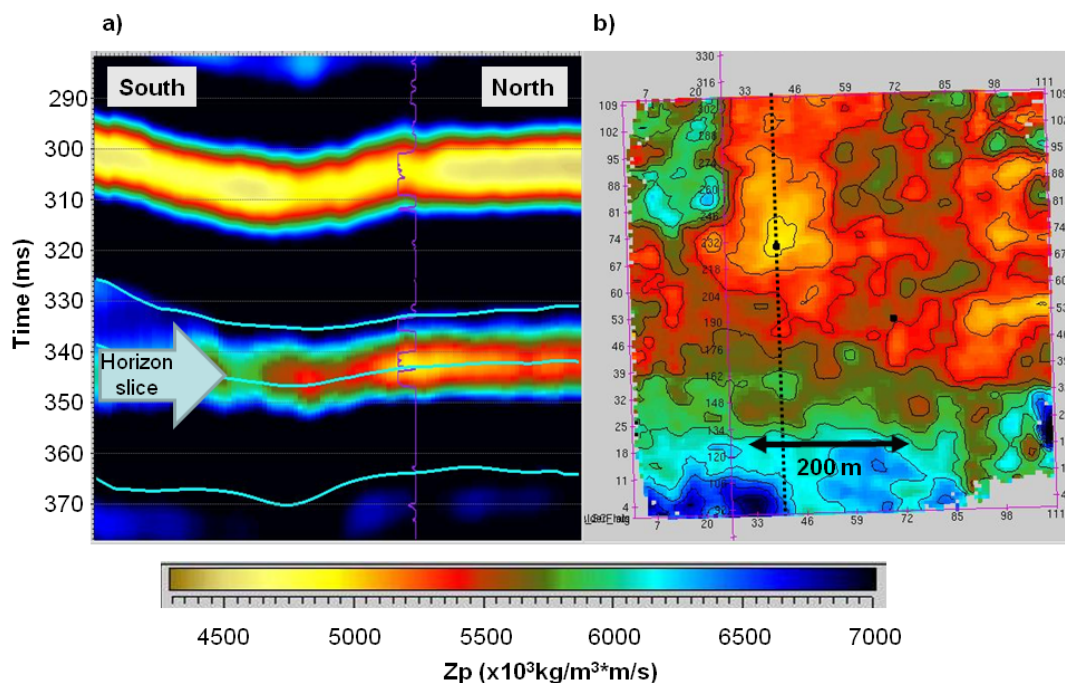


Figure 6-29: Examination of a horizon slice through the middle of the Lower Ardley Coal low impedance zone. (a) crossline #40 showing the slice location and (b) the slice. Crossline #40 is the black dotted line in (b).

The mean impedance in a 10 ms window below the Lower Ardley Coal horizon picked from the impedance volume (using the $6.0 \times 10^6 \text{ kg/m}^3 \cdot \text{m/s}$ cut-off) is illustrated in Figure 6-30. Again the anomaly is evident. Figure 6-31 illustrates a 3D rendering of all impedance samples that are less than $5.0 \times 10^6 \text{ kg/m}^3 \cdot \text{m/s}$ and that are connected to at least 49 other similar samples (i.e. clusters of 50 or more connected impedance voxels less than $5.0 \times 10^6 \text{ kg/m}^3 \cdot \text{m/s}$). The sheet of the Upper Ardley Coal Zone is obvious at the top of the volume where the thickness of the coal zone has resulted in this very low impedance estimate. The figure also shows the extent of the very low impedance anomaly cluster in the Lower Ardley Coal Zone.

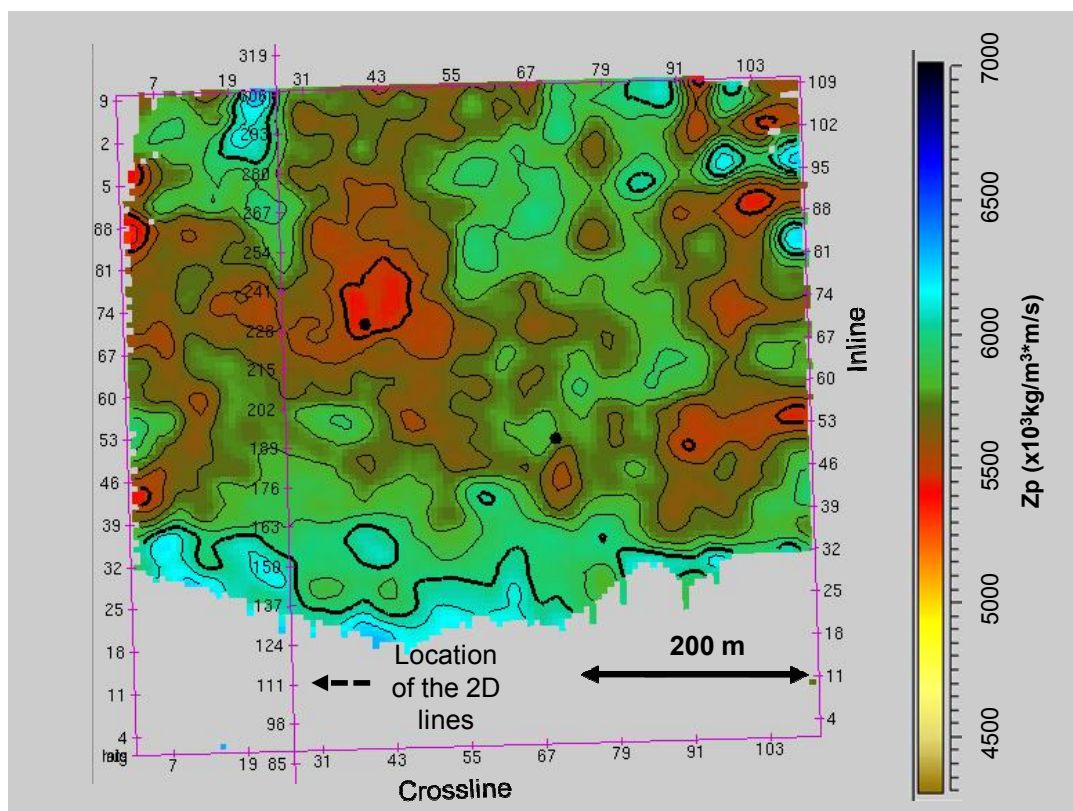


Figure 6-30: The mean impedance in a 10 ms window below the Lower Ardley horizon picked from the impedance volume.

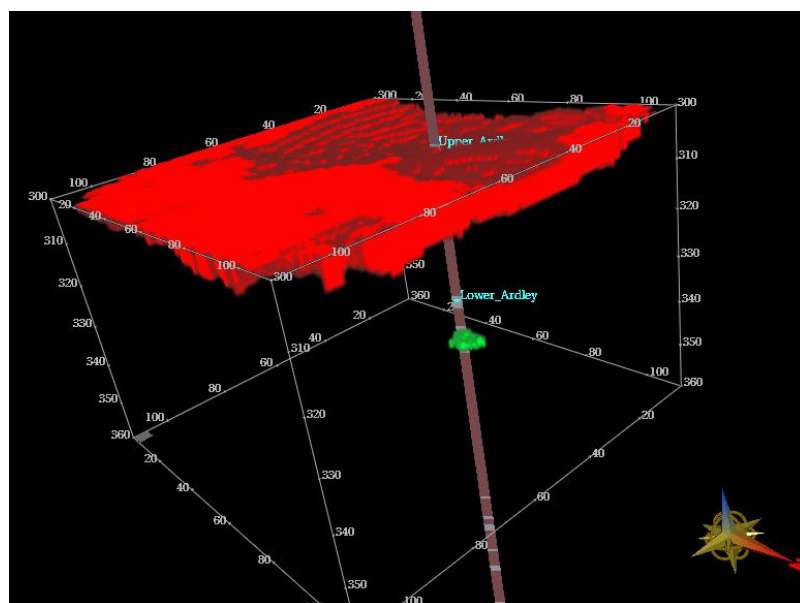


Figure 6-31: 3D rendering of the clusters of area where the impedance is less than $5.0 \times 10^6 \text{ kg/m}^3 \cdot \text{m/s}$. Note the Upper Ardley Coal forms the large cluster in red, while a sole cluster exists in the Lower Ardley Coal Zone (green).

It is interesting to note that the time separation of the low impedance zones of the Upper and Lower Ardley Coals in the inversion result is slightly larger than the separation exhibited in the bandpassed impedance log (e.g. Figure 6-21). The reason for this is not known, but may be due to a phase delay resulting from short-path intra- and inter-bed multiples discussed in the next section.

6.6 Short-period Multiples

The seams of the Ardley Coal Zone and the inter-bedded shales, siltstones, and sandstones form a series of high reflection coefficients. Such a sequence of beds will generate not only high amplitude primary reflections, but also short-period inter-bed and intra-bed multiple reflections and mode conversions. The build-up of multiple energy has been shown to distort the wavelet from seismic horizons below coals (e.g. Coulombe and Bird, 1996; Perz, 2001). Such distortion could be problematic for the Alder Flats study which focuses on the quantitative interpretation of seismic reflection amplitudes corresponding to the deepest zone of the Ardley Coals. This consideration motivated an investigation of the potential effect of short-path multiples on the reflection data from the Ardley Coals.

Schoenberger and Levin (1974, 1978) investigated the effect of short-path multiples on the seismic response of cyclically bedded coal seams. Their work showed that while the downward propagating energy of the primary pulse is diminished by high reflectivity and low transmission coefficients across the strata boundaries, the down-going energy of the multiple train may compensate for the loss of the primary pulse energy and in some cases the energy of the delayed multiple arrivals may exceed that of the primary arrivals. Figure 6-32 illustrates an example time sequence of the primary pulse and the delayed pulses from the multiple train. Fogg (2001) found that coals deep in a cyclic sequence may be imaged entirely by short-path multiple energy. The energy delay has the net effect of reshaping the wavelet with lower energy at higher frequencies and increased energy at lower frequencies. Additionally, there is a delay in the arrival of the net signal pulse. The reshaping of the wavelet with interference from multiple energy results in an

apparent attenuation that is effectively indistinguishable from the intrinsic attenuation of the rocks.

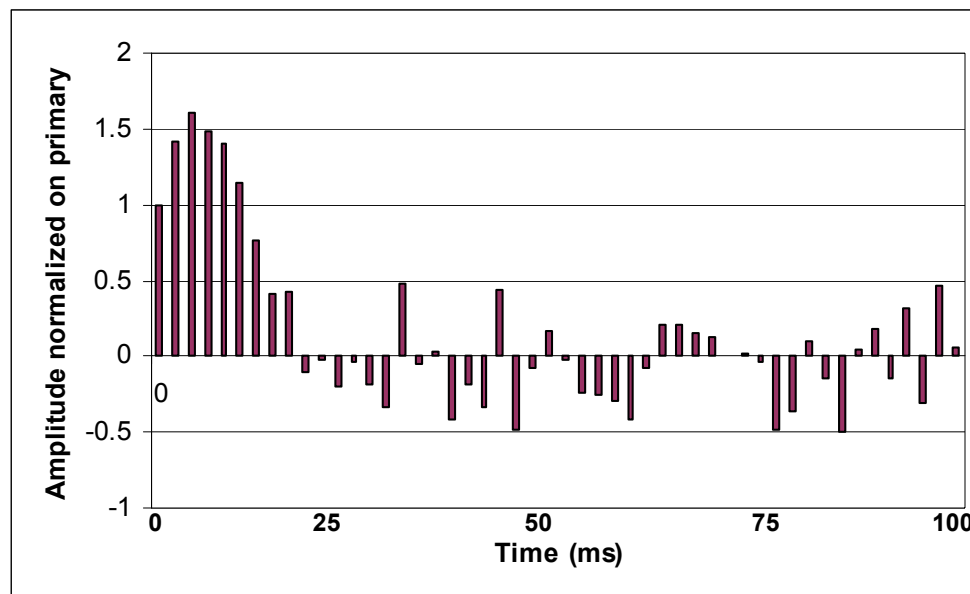


Figure 6-32: An example that illustrates how the initial pulse at time zero can be dominated by delayed arrivals of short-path multiple pulses after the wave transmits through a series of coal seams (after Schoenberger and Levin, 1974).

To investigate whether short-path multiples have a significant effect on the trace waveform in the Alder Flats data, synthetic seismograms were modelled, using the reflectivity method, which calculates the full elastic wave response of a stratified earth including all multiples and mode conversions (Fertig and Müller, 1977; Müller, 1985). The method, as implemented by Hampson Russell Software, was used to generate synthetic seismograms with and without multiples (and mode conversions) for comparison. Figure 6-33 shows offset and stacked modelled seismograms created using a 5-10-50-60 Hz Ormsby zero-phase wavelet and included a modelled depth range of 200 - 800 m that encompassed the Ardley Coals. The offset gather included 10 offsets up to a maximum offset distance of 500 m.

Focusing on the post-stack data, events at earlier times than the coal zone are relatively unaffected with the inclusion of multiples. For example, the arrival time and amplitude of the top of the Upper Ardley event is unaffected (shown at the dotted red line

in Figure 6-33). However, the amplitudes and arrival times at the level of the Lower Ardley event show some distortion in amplitude and phase with the inclusion of multiples. For example, the amplitude of the trace peak at the base of the Lower Ardley Coals has increased amplitude and the zero-crossing following the peak (shown at the blue line in Figure 6-33) is delayed by 3 ms with the inclusion of multiples. This difference in the signal response between the top and the bottom of the coals indicates that the effective wavelet (Equation 3.3) is time-varying across the coals as a result of the interference from the multiple train.

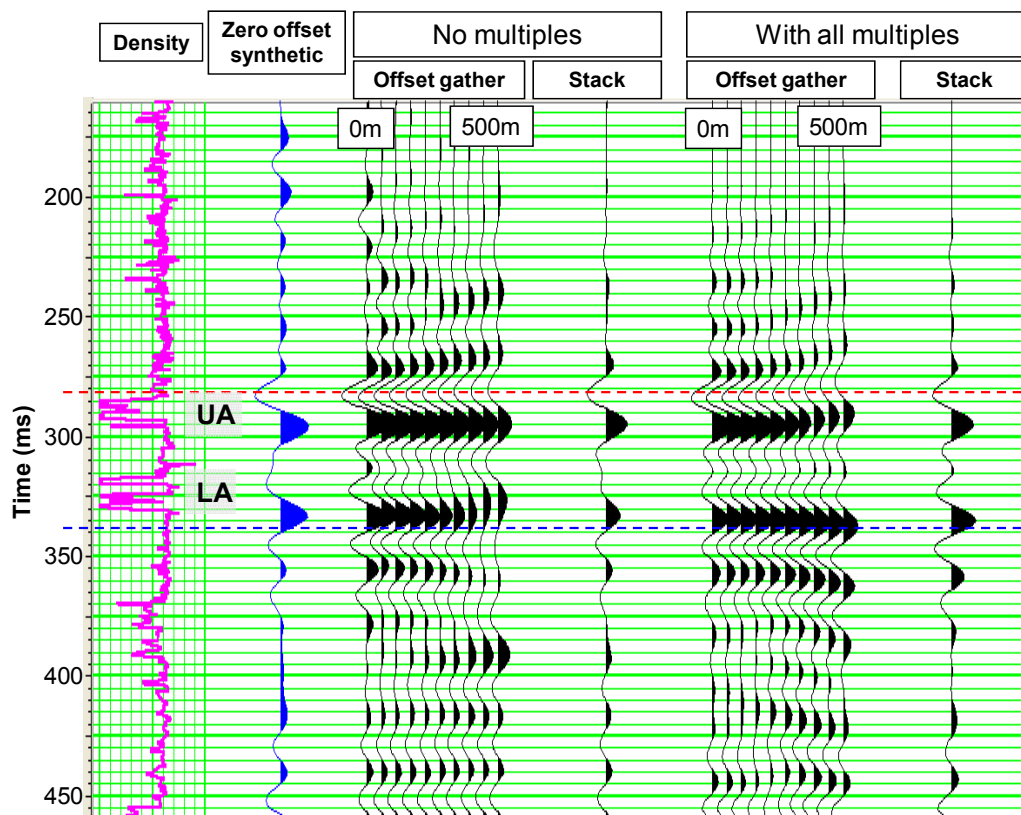


Figure 6-33: Synthetic seismograms showing the effect of short-path multiples and mode conversions by comparing gathers and stacks with and without including multiples in the model. All models were created with a zero-phase 5-10-50-60 Hz Ormsby wavelet. The dotted lines are constant time lines for comparing the phase of the different models.

6.7 Deconvolving the Multiple Train

Standard processing flows include a deconvolution step which attempts to recover the reflectivity series that has been convolved with some unknown effective wavelet. Since the effect of short-path multiples is to create some phase distortion of the wavelet, deconvolution may be successful in removing the amplitude and phase effects of the recorded wavelet. In so doing, the true reflectivity series may be extracted from the original source wavelet and the effects of the multiple train. This hypothesis is investigated in this section using synthetic examples. The model data, constructed with all multiples and a known wavelet, were deconvolved with the algorithms used in the processing flows described in earlier chapters. The results were then compared to idealized data sets constructed with a known wavelet but without multiples.

Spiking deconvolution, which has been used in several flows to process the Alder Flats data, was investigated. However, the time-varying nature of the effective wavelet could be problematic for this approach. As illustrated with the synthetic modelling above, the wavelet may be rapidly time-varying due to the apparent attenuation resulting from multiples. Any form of attenuation (either intrinsic or multiple-generated) changes the source wavelet's shape as the signal propagates through the earth (Kearey and Brooks, 1991), resulting in a time-varying wavelet. A short fall of spiking deconvolution is that it assumes the wavelet is stationary in time. Alternatively, Gabor deconvolution is designed to account for the time-varying nature of the effective wavelet and may be more adept at deconvolving the multiple train in the Ardley Coals seismic data. The utility of both spiking and Gabor deconvolution were investigated.

6.7.1 Zero-phase deconvolution

Zero-phase deconvolution is considered first. Zero-phase spiking and Gabor deconvolution were applied to the offset synthetic data shown in Figure 6-33 which was modelled with a zero-phase wavelet. The parameters for the spiking deconvolution are listed in Table 6-3. The time window for the operator design included the coal events. Parameters for deconvolution using the Gabor algorithm were selected in order to capture the time-varying effect of intrinsic and apparent absorption in the coal sequence. The

parameters of two variations of the Gabor deconvolution are listed in Table 6-4. The first parameterization has a larger Gaussian time window and a greater temporal increment between windows than the second parameterization. The second Gabor deconvolution design is intended to address rapidly varying wavelet effects, while the first parameterization would smooth time-varying effects to a greater degree.

Table 6-3: Parameters for the spiking deconvolution

Deconvolution operator length	0.1 sec
Time gate for operator design	0.2 to 0.9 sec
Operator white noise level	0.001

Table 6-4: Parameters for the Gabor deconvolutions

	Parameterization #1	Parameterization #2
Size of Gaussian temporal window	0.5 sec	0.3 sec
Temporal increment between windows	0.01 sec	0.002 sec
Smoothing	Hyperbolic	Hyperbolic
Stability factor	0.001	0.001
Size of frequency smoother	20 Hz	20 Hz

Figure 6-34 shows the zero-offset convolutional synthetic seismogram with no multiples (trace #1), the stack of the no-multiples offset reflectivity model (trace #2), the stack of the reflectivity model data with all multiples (trace #3), the stack after spiking deconvolution of the model with multiples (trace #4), the stack of the model with multiples after the first parameterization of Gabor deconvolution (trace #5), and the stack of the model with multiples after the second parameterization of Gabor deconvolution (trace #6). While spiking deconvolution does not account for a time-varying wavelet, the stationary wavelet assumption may be appropriate since the deconvolved result improves the match to the no multiples trace (#2), as shown in Figure 6-34. The figure also shows that the first parameterization of the Gabor deconvolution produces a better match to the

no-multiples trace (trace #2). In all cases there is a slight phase delay in the arrival time of the Lower Ardley event if multiples are included.

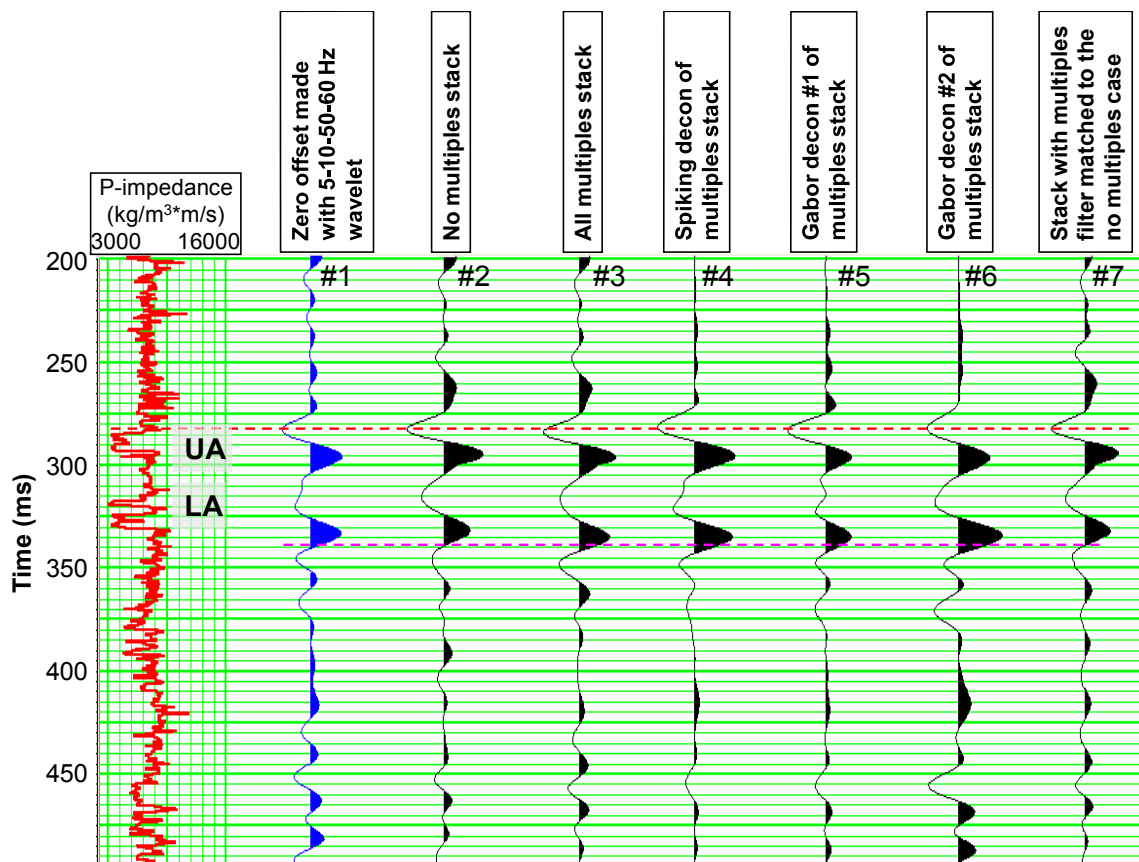


Figure 6-34: Traces produced by stacking offset synthetic data to evaluate the effectiveness of several methods of deconvolution

To compare their effectiveness, the traces after deconvolution should be compared to the trace generated with the no multiples model (trace #2). A visual comparison of the traces shows that after both the spiking and first Gabor deconvolution, there is a slight amplitude and phase distortion, while the second Gabor deconvolution shows a poor match to the no-multiples trace. To compare the results quantitatively, the cross correlation of each of the post-deconvolution traces was calculated over a window from 200 - 400 ms, encompassing the coal events. The spiking deconvolution trace resulted in a cross correlation of 0.84. The first parameterization of the Gabor deconvolution resulted in a cross correlation of 0.80 and the second parameterization of the Gabor deconvolution

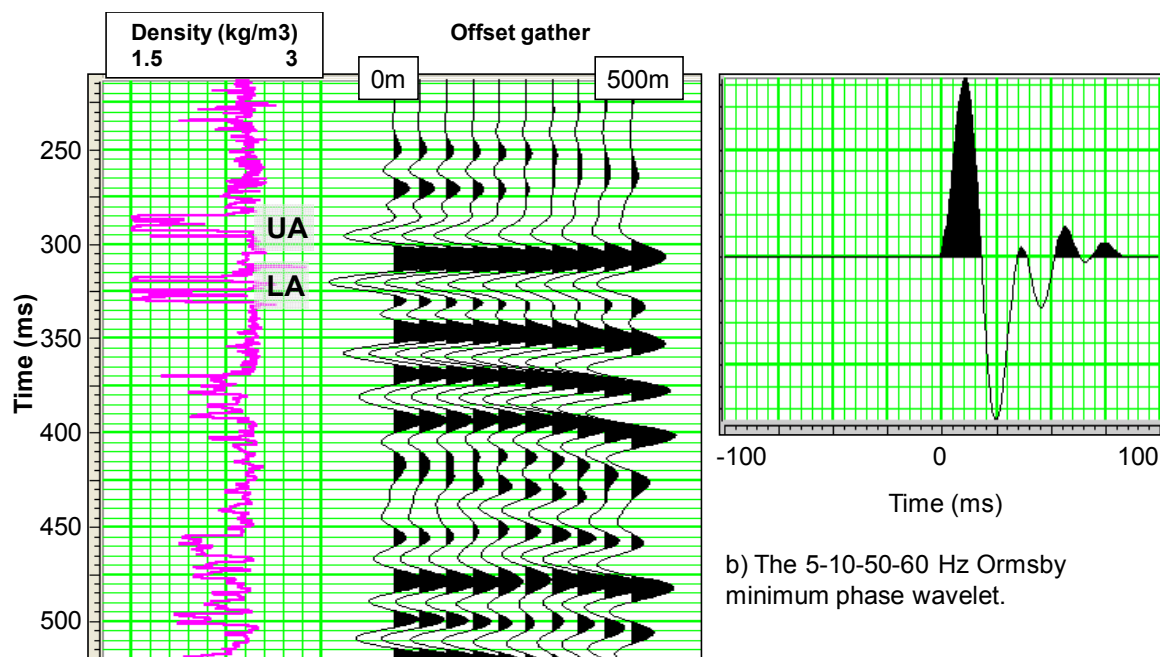
resulted in a cross correlation of 0.67. Based on this information, it appears that the spiking deconvolution, as parameterized, in this experiment is slightly superior to the other methods at removing the effect of multiples in the data.

Another approach to remove the effect of multiples was to construct a Weiner match filter to match the stacked trace with multiples to the stacked trace without multiples. Such a filter, once designed with synthetic data, could then be applied to real data to remove the effect of multiples. A match filter was designed over the time window from 250-400 ms for traces #2 and #3 in Figure 6-34 and applied to the trace with multiples (#3). The resulting trace is illustrated as Trace #7 in Figure 6-34. The cross correlation between Trace #2 and Trace #7 over the window from 200-400 ms is now 0.94. While this method of removing the effect of multiples appears to be quite effective in zero-phase synthetic data, the matching filter is highly model driven and spurious effects of applying the filter to real data are hard to predict. This method should therefore only be used with an understanding of its potential risks.

6.7.2 Minimum phase deconvolution

Field data, assumed to be minimum phase, are conditioned with minimum phase deconvolution in an attempt to normalize the amplitude spectrum and “zero” the phase of the embedded wavelet. Again, it is appropriate to investigate the effectiveness of minimum phase deconvolution on synthetic data with multiples. A data set was modelled using the reflectivity method assuming a minimum phase 5-10-50-60 Hz Ormsby wavelet and including all multiples, illustrated in Figure 6-35. Then the pre-stack synthetic data was conditioned with both a minimum-phase spiking deconvolution and Gabor deconvolution. The parameters for the deconvolutions are the minimum-phase equivalents of those listed in Table 6-3 and Table 6-4. The results, after stacking, are illustrated in Figure 6-36. The stack of the “no-multiples” synthetic and the “all multiples” synthetic data sets created with a zero-phase 5-10-50-60 Hz Ormsby wavelet are provided for comparison. All of the deconvolved traces have amplitude and phase distortions and none of the deconvolutions show a distinctly superior result when

compared to the no-multiples trace. It appears that all of the deconvolution tests left residual phase and amplitude distortions in the embedded wavelet.



a) The density log and synthetic seismogram up to 500 m offset

b) The 5-10-50-60 Hz Ormsby minimum phase wavelet.

Figure 6-35: (a) A synthetic offset gather created with (b) a minimum phase 5-10-50-60 Hz Ormsby wavelet and including all multiples.

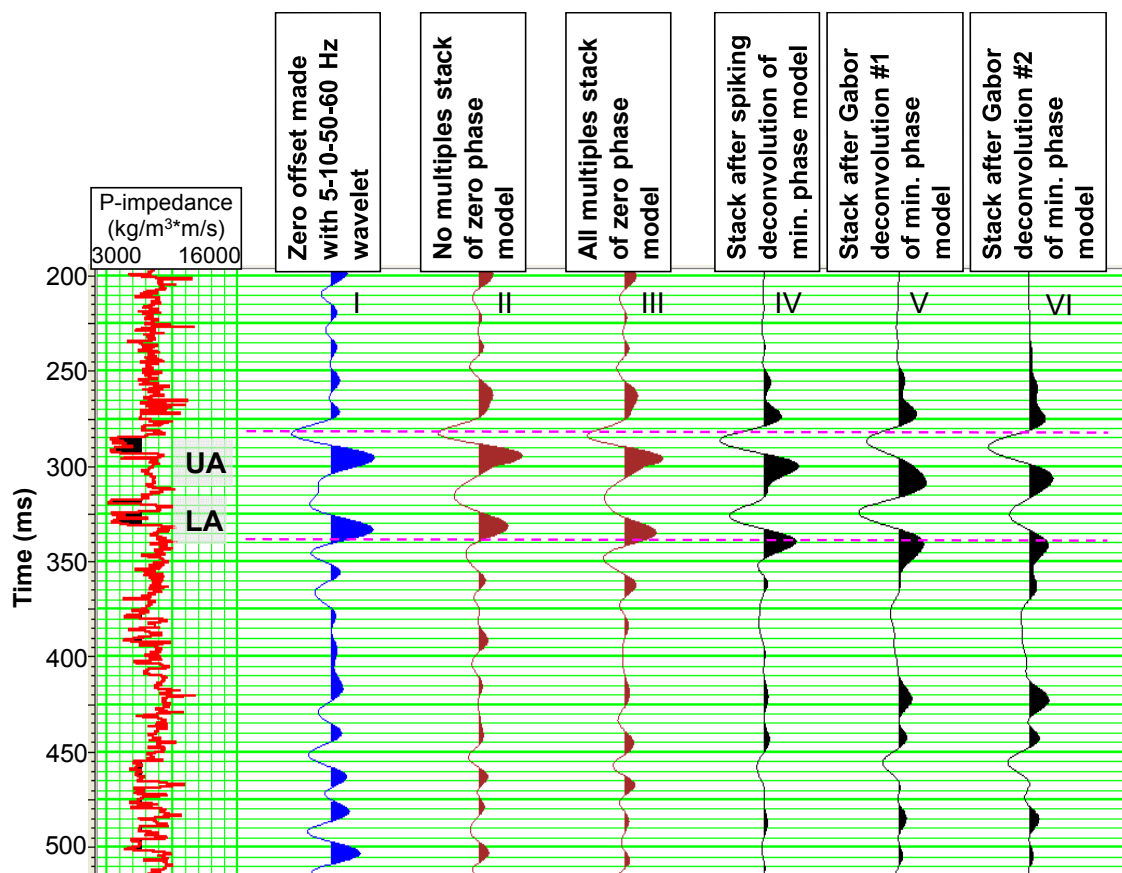


Figure 6-36: A comparison of deconvolving minimum phase synthetic seismograms. The brown traces are stacks of model data created with a zero-phase wavelet and the black traces are stacks of minimum phase synthetic data that has been deconvolved.

6.7.3 Acoustic impedance estimates after deconvolution

One objective of the Alder Flats study is to use the data for impedance inversion. To invert seismic data for impedance estimates, the embedded wavelet must be known *a priori* (Avseth et al., 2005). If a robust wavelet can be established, any residual wavelet phase and amplitude distortions remaining in the data after deconvolution may be accounted for in the inversion. However, the algorithms also assume that the wavelet is time-invariant. While theoretically incorrect, this assumption may be justified if the deconvolution processing step is successful at removing the wavelet in a local sense. It is therefore important to investigate whether deconvolution has resulted in a stable and robust wavelet, at least in a localized sense, and whether the resulting data can be reliably inverted to yield accurate impedance estimates.

The traces that resulted from each synthetic deconvolution shown in Figure 6-36 were used in a model-based post-stack inversion for acoustic impedance (section 5.2.2 discusses model-based inversion). The intent was to compare the results of the three deconvolutions in terms of their ability to reproduce the impedance curve that was used as the original input to create the synthetic seismograms. The inversion results are illustrated in Figure 6-37. The inversions after the minimum phase deconvolutions should be compared to trace (a) in Figure 6-37 which results from inverting the idealized no-multiples, zero-phase synthetic seismogram. Also shown in the figure is the inversion resulting from a zero-phase synthetic seismogram created with all multiples (inversion (b) in Figure 6-37). The residual error calculated by differencing the original impedance log and the inverted impedance result (between 200-450 ms) is also shown in Figure 6-37. Of the three deconvolution methods, the inversion error is least for the trace produced from the first Gabor deconvolution, followed by the inversion error resulting after spiking deconvolution. Either of these deconvolution results produce reasonably accurate estimates of the impedance in the coals. The second Gabor deconvolution trace did not produce as acceptable an inversion estimate as the first 2 methods.

Figure 6-37 shows that the impedance estimate from the traces that included multiples (traces III to VI) show a slight time delay of the low impedance zone of the Lower Ardley Coals while the low impedance zone of the Upper Ardley Coals is correctly tied in time. This is not surprising because it has already been noted that multiples have the effect of introducing a slight phase delay in the Lower Ardley Coal reflection event and may explain the slightly exaggerated isochron between the coal zones seen in the inversion of the field data.

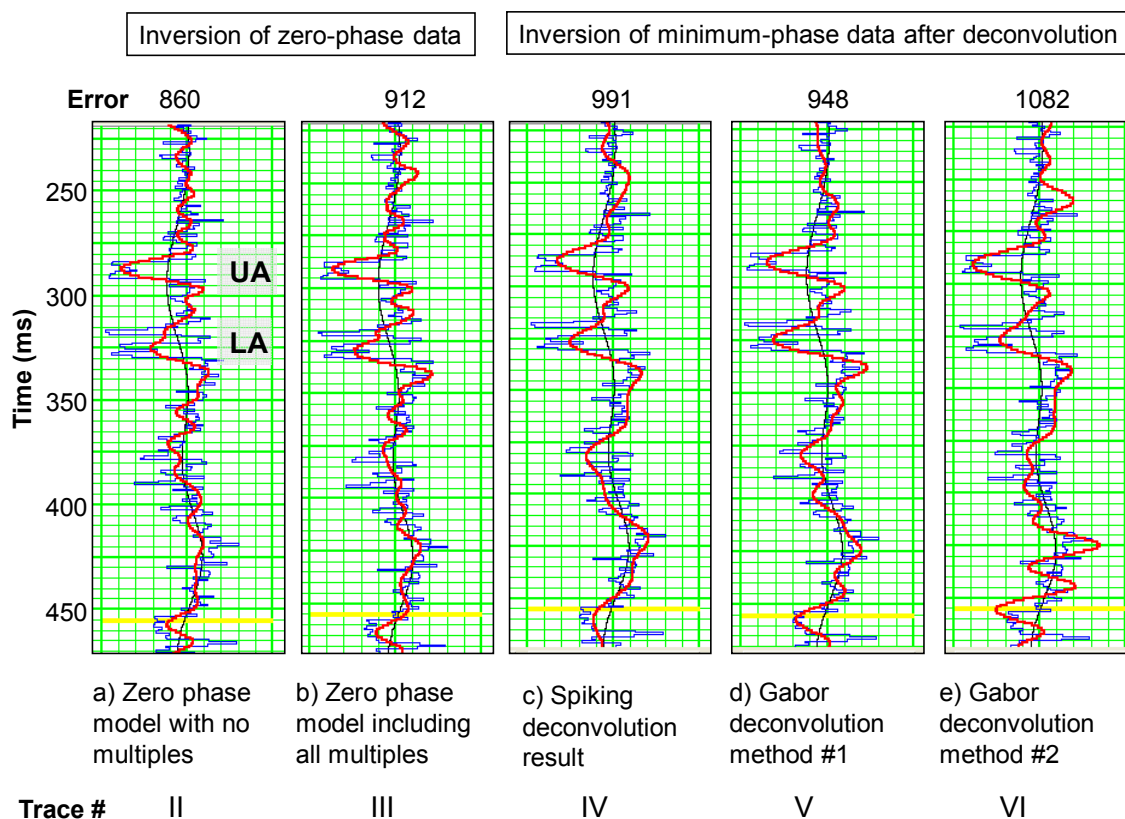


Figure 6-37: Comparison of the post-stack acoustic impedance inversion of various traces. Inversion a) and b) are based on the traces produced with a zero-phase wavelet. Inversions c), d), and e) are based on the deconvolved minimum phase data. The blue curve is the real log impedance, the black curve is the initial guess model for the inversion (10 Hz high cut), and the red curve is the inversion result. The error value is the residual difference between the log curve and the inverted curve between 200-450 ms.

6.8 Petrophysical Interpretation of the Anomaly

Both the model-based and CSS inversion results show a low impedance anomaly around the 102/7-28 well in the Lower Ardley Coal Zone. The size, shape, and location of the anomaly correspond to the expected imprint of the 180 tonne CO₂ flood.

Figure 6-29 illustrates that the impedance measured in the Lower Ardley Coal anomaly reaches low values that are less than 5.0×10^6 kg/m³*m/s while the rest of the Lower Ardley Coal Zone the impedance estimate is in the range of $5-6 \times 10^6$ kg/m³*m/s. Figure 6-6 showed a band-limited version of the impedance log from the 102/7-28 well and demonstrated that the minimum impedance in the 102/7-28 well was greater than

$5.0 \times 10^6 \text{ kg/m}^3 \cdot \text{m/s}$ after high cut filtering. This discrepancy between the well logged impedance estimate and the impedance estimate from inversion in the Lower Ardley Coal Zone suggests that the impedance may have been lowered in the vicinity of the 102/7-28 well after the logging data was acquired.

Figure 6-38 shows the 102/7-28 impedance well log at “logging resolution” and at “seismic resolution” (after application of a 60-70 Hz high cut filter). The band-limited impedance log is higher than $5.0 \times 10^6 \text{ kg/m}^3 \cdot \text{m/s}$. Also shown is a log where the impedance of the Mynheer coal zone has been lowered uniformly by 10%. The reduced impedance log after application of the high cut filter is also shown. It indicates that a 10% reduction in the impedance of the Mynheer coals would be enough to change the band-limited impedance estimate to just less than $5.0 \times 10^6 \text{ kg/m}^3 \cdot \text{m/s}$.

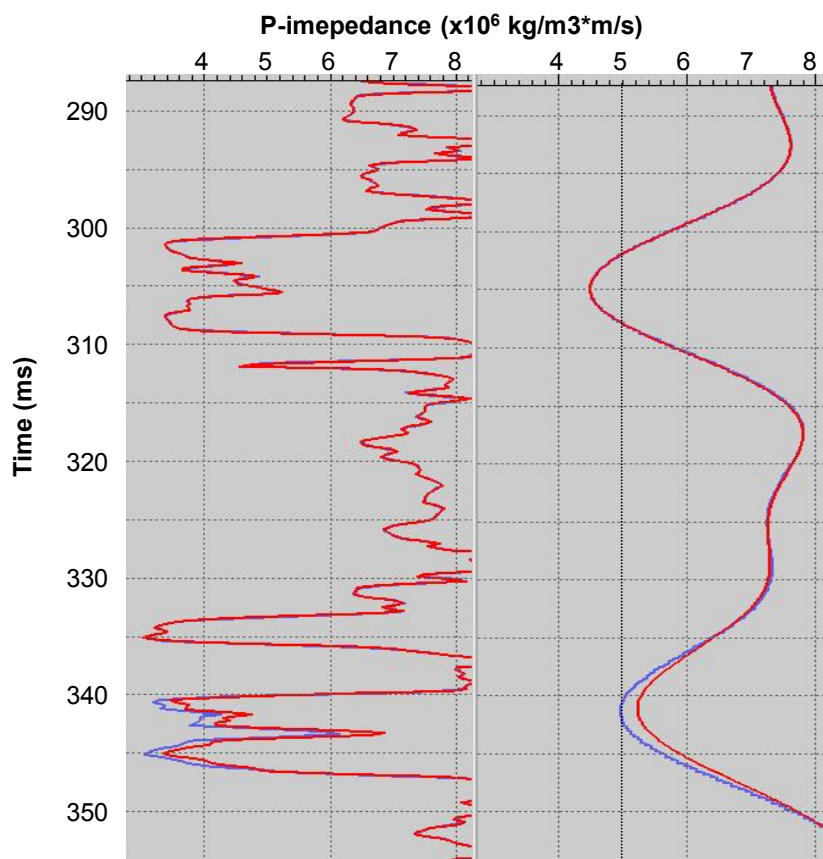


Figure 6-38: The original impedance log from the 102/7-28 well (red) and the log adjusted by a 10% reduction in impedance in the Mynheer coal zone (blue). The curves are at log resolution on the left and with a 60-70 Hz high cut filter on the right.

It is reasonable to ask whether a fluid substitution of water for gaseous CO₂ in the coals' macroporosity cleat system could account for the level of anomaly observed in the measured impedance of the Lower Ardley coals if calculated with the Gassmann model.

The Gassmann fluid substitution model, introduced in Chapter 2, assumes that fluid substitution occurs only in the macro-porosity of the coal. The Mynheer coals in their original state were likely water saturated and the logged data was used to find the water saturated elastic properties. The average velocity and density values from Table 2-1 were used to find the average values for the water saturated rock listed in Table 6-5. Again, the shear modulus of the rock was assumed to be unchanged by a substitution of fluids, and so the dry shear modulus and the shear modulus when the coal macro-porosity was filled with CO₂ is the same as the shear modulus measured with the petrophysical logs. The bulk modulus and density of water and CO₂ were calculated using methods described by Batzle and Wang (1992). The fracture porosity was assumed to be 1%, as indicated by Mavor and Faltinson (2008).

Estimating a bulk modulus for the dry rock frame (k_{fr}) is difficult. Ideally, lab measurements of the dried frame would be available. Alternatively, literature values could be used. Yu et al. (1993) showed that the bulk modulus of air dried bituminous coal was approximately 10% less than water saturated coal at 8 MPa confining pressure. It was assumed that the bulk modulus of the dry coal frame is 10% less than the water saturated bulk modulus for the Ardley Coals as well.

Again, the Gassmann equation from Section 2.5.2 is:

$$\frac{K_{sat}}{K_0 - K_{sat}} = \frac{K_{fr}}{K_0 - K_{fr}} + \frac{K_f}{\phi(K_0 - K_f)} \quad 6.8$$

With ϕ , k_{sat} , k_{water} , and k_{fr} estimated, equation 6.8 can be used to calculate the bulk modulus of the coal mineral, k_o . All these data are listed in Table 6-5. Equation 6.8 can

be re-arranged to give equation 6.9 which is used to find the bulk modulus of the CO₂ saturated coal.

$$K_{sat} = K_{fr} + \frac{(1 - \frac{K_{fr}}{K_o})^2}{\frac{\phi}{K_f} + \frac{(1-\phi)}{K_o} - \frac{K_{fr}}{K_o^2}} \quad . \quad 6.9$$

Finally the density can be calculated using equation 2.7 which is stated again:

$$\rho = \phi\rho_f + (1 - \phi)\rho_{fr} \quad . \quad 6.10$$

The velocity and density values of the fluid saturated coals give the impedance, which for the water saturated coals is 4.61x10⁶ kg/m³*m/s and for the gaseous CO₂ saturated coals is 4.43x10⁶ kg/m³*m/s. This corresponds to a 3.9 % decrease in impedance when water is replaced by gaseous CO₂ in coals.

Table 6-5: The average elastic properties of the Mynheer coals used to model the substitution of water for gaseous CO₂ using the Gassmann method.

ϕ (macro)	0.01
V_p (water saturated)	2567 m/s
V_s (water saturated)	1097 m/s
ρ_{sat} (water)	1797 kg
k_{sat} (water)	8.96 GPa
μ_{sat} (water) = μ_{dry} = μ_{sat} (CO ₂)	2.16 GPa
k_{water} (16.6 °C, 1.73 MPa, 1931 ppm NaCl)	2.4 GPa
k_{CO_2} (16.6 °C, 1.73 MPa)	0.01 GPa
ρ_{water} (16.6 °C, 1.73 MPa, 1931 ppm NaCl)	1002 kg/m ³
ρ_{CO_2} (16.6 °C, 1.73 MPa)	0.050 kg/m ³
v_p (dry coal)	2480 m/s
ρ (dry coal)	1779 kg/m ³
k_{fr}	8.06 GPa

k_o	9.21 GPa
$k_{sat} (CO_2)$	8.08 GPa
$\rho_{sat} (CO_2)$	1788 kg/m ³
$v_p (CO_2)$	2476 m/s
p-impedance (water saturated)	4.61 x 10 ⁶ kg/m ³ *m/s
p-impedance (CO ₂ saturated)	4.43 x 10 ⁶ kg/m ³ *m/s

6.9 Discussion and Conclusions

Although the 3.9% impedance change predicted with the Gassmann model is not enough to explain the apparent 10% or greater change in the impedance observed in the vicinity of the 102/7-28 well in the inversion result, it is the right order of magnitude and could be argued to be the cause of the impedance anomaly. However, it is not a unique interpretation. Two similar interpretations are that the anomaly could be related to methane in the cleat system or a mixture of methane and CO₂ in the cleat system that would have a similar effect on the impedance. Another possibility is that the CO₂ has reduced the elastic moduli of the coal frame itself, as described in Chapter 2; although this interpretation is more speculative given the dearth of experimental data in this area.

Other geological models are also possible. It has been noted that the Mynheer coal zone is laterally very heterogeneous and that different sub-lithologies of the coal zones have different impedance values. It is possible that the low impedance zone results from an area of greater net pure coal versus shaley coal or coaly shale, or that either of the Mynheer or Silkstone coal zones thickens to the northeast of the 102/7-28 well which causes the low impedance anomaly. Other explanations for the low impedance zone could include reduced rock competency due to fracture stimulation procedures, effects due to the injection of water during the stimulation procedure, effects related to changes in reservoir effective pressure, or subtle tuning effects that are not resolved by the inversion despite an accurate estimation of the embedded wavelet. Differentiating between these possibilities in a conclusive, deterministic manor is not possible with the

given data. Ultimately the only way to conclusively attribute a seismic anomaly to a reservoir change with production activities is to acquire a baseline and monitor seismic survey and analyze the data using time-lapse methods.

However, despite the shortcomings of the available data, attributing the low impedance anomaly to effects due to CO₂ injection remains a realistic explanation that requires few contrived assumptions. Given its proximity to the well, its alignment with the known preferential permeability pathway, its location up-dip of the injection well and its dimensions, interpreting the anomaly as a signature of the CO₂ is reasonable.

Chapter Seven: Conclusions

7.1 Discussion

The principal objective of this work was to use seismic data to characterize the rocks and fluids at Alder Flats after injection of 180 tonnes of CO₂ into the Ardley Coals. Preliminary analysis of the site geology was conducted in order to gain an *a priori* understanding of the project context and modelling was used to understand the ability of seismic data to image the physical attributes of the coal zones. The first two of three seismic data sets acquired at Alder Flats were analyzed in order to further understand the capabilities and limitations of interpreting field data and to provide guidance in designing the 3D survey. The 3D vertical component data set proved to be of high quality and the converted wave data set, although low in fold, proved to be of reasonable quality. Inversion of the 3D vertical component data showed anomalously low acoustic impedance in an area encompassing 1,276 – 1,800 m² area to the northwest of the 102/7-28 injection well. The size of the anomaly and its location up-dip of the injection elevation as well as shape along the expected preferential permeability pathway suggest that it could be related to the CO₂ flood.

Based on this interpretation, several conclusions can be drawn:

- The recorded reflection amplitudes from the Ardley Coals are meaningful representations of the reflectivity of the coal strata; despite the effects of thin-bed tuning, the effects of high reflectivity/low transmissivity, and the complications related to short-path multiple reflections.
- Using the post-stack data, these reflectivity data were inverted to estimate the acoustic impedance of the coal formation. The bandlimited estimates for the Lower Ardley Coal Zone ranged from 4900 – 5400 kg/m³*m/seismic which was very comparable to the acoustic impedance values measured with the 60 Hz high-cut filtered well log. This is remarkable given the challenges related to wavelet estimation in stratigraphy that is highly reflective and cyclically bedded. It is also significant because the inversion algorithms often use approximations that are

deemed to be true if the reflectivity of the stratigraphy is low; which is not the case for coal zones.

- Finally, it is concluded that the imprint of 180 tonnes of CO₂ that was injected as a gaseous phase at a depth of ~0.4 km was detected with seismic reflection techniques. By comparing the acoustic impedance values in the anomalous region to the average value in the rest of the coal zone, the imprint shows an overall decrease in the acoustic impedance of approximately 10% in the coals after an approximately 9 month CO₂ soak period. Using the Gassmann method to model the replacement of formation water with gaseous CO₂, a reduction in acoustic impedance of approximately 4% is predicted. The differential between the Gassmann prediction and the inversion results suggest that *in situ* softening of the solid coal matrix may have been detected.

7.2 Recommendations for Continued Research

This research has highlighted the need to fill two significant knowledge gaps. Firstly, although an imprint of the injected CO₂ has been detected, the mechanism that causes the low acoustic impedance anomaly is not clear. The ambiguity is related to a variety of effects that will likely affect the elastic properties of coals under a gaseous CO₂ flood, including:

- Changes in the fluids and fluid states in the formation macroporosity;
- Changes in the fluid pressure of the macroporosity;
- Molecular species exchange between the macro- and micro-porosity;
- Swelling effects as CO₂ sorbes into the microporosity and the consequent changes in the macroporosity of the formation;
- Possible changes in the elastic moduli of the coal matrix with CO₂ sorption.

Quantitative interpretation of the coal reflectivity requires a deeper understanding of the relationship between these effects which necessitate laboratory measurements.

Secondly, while an imprint of the injected CO₂ was detected in the single 3D survey, the utility of time-lapse analysis to monitor the evolution of a flood remains an open question. To what extent would the amplitudes recorded in a monitor survey be sensitive enough to detect subsurface changes? Could these changes be interpreted in terms of the changes in the formation? What is the minimum threshold for detectability of injected gas in coals? And finally, what would be the minimum threshold for detectability of CO₂ gas, which may dissolve into formation waters, if it were to leak into overlying stratigraphy.

References

Alberta Geological Survey, 2004, Geological appraisal of the Pembina CSEMP project area, Township 26, Range 7W5M, Report to the CSEMP Consortium.

Alberta Research Council, Unconventional Gas Research Group, 2005, Final Report Gas Content Analysis – Pembina-102/07-28-46-07 W5M.

Alberta Research Council, 2007, Development of China's Coalbed Methane Technology/CO₂ Sequestration Project: Final Project Report: Project No. A-030841. Submitted to Canadian International Development Agency by Alberta Research Council, March 31, 2007.

Al Duhailan, M., 2008, Field mapping and seismic analysis of fractures: M.Sc. thesis, University of Calgary.

Arts, R., and P. Winthagen, 2005, Monitoring Options for CO₂ Storage. In Carbon Dioxide Capture for Storage in Deep Geologic Formations, Volume 2. Eds. D.C. Thomas and S.M. Benson. Amsterdam: Elsevier, 2005.p. 1001-1013.

Aster, R.C., Borchers, B., Thurber, C.H., 2005, Parameter estimation and inverse problems: Elsevier Academic Press.

Avseth, P., M. Tapan, Mavko, G., 2005, Quantitative seismic interpretation : applying rock physics tools to reduce interpretation risk, Cambridge University Press.

Batzle, M., Wang, Z., 1992, Seismic properties of pore fluids: Geophysics, v. 57, no. 11, 1396-1408.

Beaton, A., 2003, Coal-bearing formations and coalbed-methane potential in the Alberta Plains and Foothills, CSEG Recorder, n. 11, p. 22-29.

Beaton, A., Pana, C., Chen, D., Wynne, D., Langenberg, C.W., 2002, Coalbed-methane potential of Upper Cretaceous-Tertiary strata, Alberta Plains: Alberta Energy and Utilities Board, EUB/AGS Earth Science Report 2002-06, 76 pages.

Bell, J.S., 2006, In-situ stress and coal bed methane potential in Western Canada, Bulletin of Canadian Petroleum Geology, v. 54, p. 197-220.

Benedictus, T. Vandeweyer, V., Winthagen, P., van Bergen, F., 2008, CO₂-enhanced coalbed methane: the Kaniów demonstration study: First Break, v. 26, p. 59-63.

Benson, S.M., 2005, Overview of Geologic Storage of CO₂. In Carbon Dioxide Capture for Storage in Deep Geologic Formations, Volume 2. Eds. D.C. Thomas and S.M. Benson. Amsterdam: Elsevier, 2005. p. 665-671.

Bustin, R.M., 1997, The importance of fabric and composition on stress sensitivity of permeability in some coals of the northern Sydney Basin, Australia: relevance to coalbed methane exploitation: AAPG Bulletin, v. 81, p. 1894-1908.

Bustin, R. M., 2001, Geology and some engineering aspects of coalbed methane, CBM Solutions Short Course Notes, CBM Solutions, Calgary, Alberta.

Bustin, R.M., Cui, X., Chikatamarla, L., 2008, Impact of volumetric strain on CO₂ sequestration in coals and enhanced CH₄ recovery: AAPG Bulletin, v. 92, p. 15-29.

Calvert, R., 2005, Insights and methods for 4D Reservoir Monitoring and Characterization, 2005 Distinguished Instructor Short Course No. 8, SEG EAGE.

Castagna, J. P., Batzle, M.L., Kan, T.K., 1993, Rock Physics – The link between rock properties and AVO response, from: Offset-dependant reflectivity – theory and practice of AVO analysis, published by the Society of Exploration Geophysicists, edited by Castagna, J, and Backus, M..

Coulombe, C.A., Bird, D.N., 1996, Transmission filter by high-amplitude reflection coefficients: Theory, practice, and processing considerations: *Leading Edge*, Vol. 15, No. 9, 1037-1042.

Cooke, D., Schneider, W., 1983, Generalized inversion of reflection seismic data: *Geophysics*, v. 48, n. 6, p. 665-676.

Day, S., Fry, R., Sakurovs, R., 2007, Swelling of Australian coals in supercritical CO₂: *International Journal of Coal Geology*, 12 pages.

Dawson, F.M., Marchioni, D.L., Anderson, T.C. and McDougall, W.J., 2000, An assessment of coalbed methane exploration projects in Canada: *Geological Survey of Canada, Bulletin 549*, p. 218.

Debye, H.W.J., van Riel, P., 1990, L_p-norm deconvolution: *Geophysical Prospecting*, v. 38, p. 381-403.

Duana, Z., Sun, R., 2003, An improved model calculating CO₂ solubility in pure water and aqueous NaCl solutions from 273 to 533 K and from 0 to 2000 bar: *Chemical Geology*, v. 193, p. 257-271.

Di Federico, G., Camplone, I., Brandini, S., Barker, J., 2006, Coal characterization for carbon dioxide sequestration purposes: *Fluid Transport in Nonoporous Materials*, p. 583-590.

ERCB, 2008, Alberta Energy Resource Conservation Board, http://www.ags.gov.ab.ca/energy/cbm/coal_and_cbm_intro.html

Fertig, J., Müller, G., 1977, Computations of synthetic seismograms for coal seams with the reflectivity method: *Geophysical Prospecting*, 26, 868-883.

Flores, R.M., 1993, Coal-Bed and Related Depositional Environments in Methane Gas-Producing Sequences, in "Hydrocarbons from Coal", edited by B.E. Law and D.D. Rice, AAPG Studies in Geology #38, Chapter 3.

Fogg, A.N., 2001, Short-path seismic multiples in coal cyclic sequences and their impact on p-impedance inversion: SEG Annual Meeting, Expanded Abstracts.

Gale, J., and P. Freund, 2001, Coal-bed methane enhancement with CO₂ sequestration worldwide potential: *Environmental Geosciences*, v. 8, p. 210–217.

Gamson, P., Beamish, B., Johnson, D., 1996, Coal microstructure and secondary mineralization: their effect on methane recovery: *Coalbed Methane and Coal Geology*, Geological Society Special Publication No. 109, p. 165-179.

Gentzis, T., Deisman, N., Chalaturnyk, R., 2006, Geomechanical properties and permeability of coals from the Foothills and Mountain regions of western Canada, *International Journal of Coal Geology*, 12 pages.

Gibson, D.W., 1977, Upper Cretaceous and Tertiary coal-bearing strata in the Drumheller-Ardley region, Red Deer River Valley, Alberta: Geological Survey of Canada, Paper 76-35, 41 pages.

Gochioco, L.M., 1992, Modeling studies of interference reflections in thinlayered media bounded by coal seams: *Geophysics*, v. 57, p. 1209-1216.

Gochioco, L.M., 1991, Tuning effect and interference reflections from thin beds and coal seams: *Geophysics*, v. 57, p. 1209-1216.

Gochioco, L.M., 2002, Recent role of geophysics in U.S. coal and CBM development: *The Leading Edge*, no. 5, p. 452-455.

Gregg, S.J., Sing, K.S.W., 1982, Adsorption surface area and porosity, 2nd Edition, Academic Press, New York, 303 pages.

Gunter, W., Mavor, M., Robinson, J., 2005, CO₂ storage and enhanced methane production: field testing at Fenn-Big Valley, Alberta, Canada, with application: *Greenhouse Gas Control Technologies 7th International Conference, Volume I*.

Hampson Russell Strata Software Theory, 2007, online with Hampson Russell Software, ver. 5.2 CE8R1.2.

Harpalani, S., and Schraufnagel, R.A., 1990, Shrinkage of coal matrix with release of gas and its impact on permeability of coal: *Fuel*, v. 69, 551-556.

Harris, L.A., and Yust, C.S., 1976, Transmission electron microscopy of coal: *Fuel*, V. 55, 233-236.

Hendrick, N., 2006, Converted-wave seismology for coal exploration: *CSEG Recorder*, n. 5, p. 27-31.

Henley, D. C., 1999, Radial trace computational algorithms at CREWES: *CREWES Research Report*, 11.

Hower, T.L., 2003, Coalbed methane reservoir simulation: an evolving science, SPE 84424.

Hsieh, S.T., Duda, J.L., 1987. Probing coal structure with organic vapor sorption: Fuel, v. 66, p.170– 177.

Hughes, J.D., Dawson, F.M., Duggan, J., Hallas, D.F., Khitrova, G., Marchioni, D.L., Richardson, R., Wynne, D., 1999, Regional analysis of the Ardley Coal Zone, Alberta, Canada, for coalbed methane production and CO₂ sequestration: Geological Survey of Canada, Open File 3761.

International Panel on Climate Change, 2005, Carbon Dioxide Capture and Storage, Cambridge University Press, p. 242-252.

Jerzykiewicz, T., 1997, Stratigraphic framework of the uppermost Cretaceous to Paleocene strata of the Alberta Basin: Geological Survey of Canada, Bulletin 510, 121 pages.

Karacan, C.O., 2007, Swelling-induced volumetric strains internal to a stressed coal associated with CO₂ sorption: International Journal of Coal Geology, v. 72, 209-220.

Keary, P., Brooks, M., 1991, An Introduction to Geophysical Exploration, 2nd Ed., Blackwell Science Ltd.

Khan, M.R., Jenkins, R.G., 1985. Thermoplastic properties of coal at elevated pressures: effects of gas atmospheres. Proc. Int. Conf. On Coal Science, Sydney.

Knapp, R.W., 1990, Vertical resolution of thick beds, thin beds, and thin-bed cyclothems: Geophysics, 55, 1183-1190.

- Krebes, E., 2005, Seismic Theory, Geophysics 551 Course Notes, University of Calgary.
- Lamberson, M.N., and Bustin, R.M., 1993, Coalbed methane characteristics of the Gates Formation coals, northeastern British Columbia: effect of maceral composition: AAPG Bulletin, 77, p. 2062-2076.
- Langenberg, C.W., Beaton, A., Berhane, H., 2002, Regional evaluation of the coalbed methane potential of the foothills/mountains of Alberta (2nd edition); Alberta Energy and Utilities Board, EUB/AGS Earth Science Report 2002-05, 125 pages.
- Langenberg, C.W., Berhane, H., Sweet, A.R., Marchioni, D., Heaman, L.M., 2007, Regional Correlations of the Ardley Coal Zone, Alberta: Alberta Energy and Utilities Board, EUB/AGS Earth Science Report 2007-05, 32 pages
- Larsen, J.W., 2004, The effects of dissolved CO₂ on coal structure and properties. International Journal of Coal Geology, v. 57, p. 63–70.
- Latimer, R., Davison, R., van Riel, P., 2000, An interpreter's guide to understanding and working with seismic-derived acoustic impedance data: The Leading Edge, no.3, p. 242-256.
- Levy, J.H., Stewart, J.D., Killingley, K.S., 1997, Methane capacities of Bowen Basin coals related to coal properties: Fuel, V. 76, Issue 9, p. 813-819.
- Levy, S., Fullagar, P., 1981, Reconstruction of a sparse spike train from a portion of its spectrum and application to high-resolution deconvolution: Geophysics, v. 46, n. 9, p. 1235-1243.

Li, H., Shimada, S., Zhang, M., 2004, Anisotropy of gas permeability associated with cleat pattern in coal seam of the Kushiro coalfield in Japan: *Environmental Geology*, v. 47, p. 45-50.

Lindseth, R.O., 1979, Synthetic sonic logs-a process for stratigraphic interpretation: *Geophysics*, v. 44, n. 1, p. 3-26.

Lines, L.R., Newrick, R.T., 2004, Fundamentals of geophysical interpretation: SEG Geophysical Monograph Series No. 13, Society of Exploration Geophysicists.

Margrave, G.F., 2006, Methods of Seismic Data Processing: Geophysics 557/657 Course Notes, University of Calgary.

Margrave, G.F., Lamoureux, M., 2006, Gabor Deconvolution: Recorder, 2006 Special Edition, 30-37.

Margrave, G.F., Stewart, R.R., Larsen, J.,A., 2001, Joint PP and PS seismic inversion: *The Leading Edge*, Sept. 2001, p. 1048-1052.

Mavor, M., Faltinson, J., 2008, Enerplus 102 Pembina 7-28-46-7 W5M, CO₂ Micro-pilot Analysis, Alberta Research Council. Confidential report.

Mazumder,S., Plug, W., Bruining, H., 2003, Capillary Pressure and Wettability Behavior of Coal – Water – Carbon dioxide System, SPE 84339.

McCrank, J., Lu, H., Hall, K., Lawton, D., 2006, Well log study and seismic survey of a coal-bed methane site: Alder Flats, Alberta: CREWES Research Report, 18.

Michael, K., and Bachu, S., 2001, Fluids and pressure distribution in the foreland-basin succession in the west-central part of the Alberta Basin, Canada: evidence for

permeability barriers and hydrocarbon generation and migration: AAPG Bulletin, v. 85, no. 7, p. 1231 – 1252.

Morad, K., Mireault, R., Dean, L., 2008, Reservoir engineering for geologists: coalbed methane fundamentals: Reservoir, v. 35, n. 9, p. 23-26.

Müller, G., 1985, The reflectivity method: a tutorial: Journal of Geophysics, 58, 153-174.

Murray, D.K., 1996, Coalbed methane in the USA: analogues for worldwide development. In: Coalbed Methane and Coal Geology (Edited: R. Gayer and I. Harris), Geological Society Special Publication No. 109, 1-12.

Murray, D.K., 2000, CBM in the United States: World Coal, v. 9, p. 61-64.

Oldenburg, D., Scheuer, T., Levy, S., 1983, Recovery of the acoustic impedance from reflection seismograms: Geophysics, v.48, n. 10, p. 1318-1337.

Ostrander, W.J., 1984, Plane-wave reflection coefficients for gas sands at non-normal angles of incidence: Geophysics, v.49, p. 1637-1648.

Pan, Z., Connell, L.D., 2007, A theoretical model for gas adsorption-induced coal swelling, International Journal of Coal Geology, v. 69, p. 243-252.

Pana, C., 2007, Ardley Coal Zone Characterization and Coal-Sandstone Channels Architecture, Pembina CBM Exploration Block, Alberta, EUB/AGS Earth Sciences Report 2007-04.

Peng, S., Chen, H., Yang, R., Gao, Y., Chen, X., 2006, Factors facilitating or limiting the use of AVO for coal-bed methane: Geophysics, v.71, n.4, p. C49-C56.

Perz, M., 2001, Coals and their confounding effects: Recorder, Vol. 26, No. 10, 34-53.

Ramos, A. Davis, T., 1997, 3D AVO analysis and modeling applied to fracture detection in coalbed methane reservoirs: Geophysics, v. 62, no. 6, p. 1683-1695.

Reeves, S., A. Taillefert, L. Pekot and C. Clarkson, 2003: The Allison Unit CO₂-ECBM Pilot: A Reservoir Modeling Study. DOE Topical Report, February, 2003.

Richardson, S., Lawton, D., 2002, Time-lapse seismic imaging of enhanced coalbed methane production: a numerical modelling study: CREWES Research Report 2002.

Resnick, J., 1993, Seismic data processing for AVO and AVA analysis, from: Offset-dependant reflectivity – theory and practice of AVO analysis, published by the Society of Exploration Geophysicists, edited by Castagna, J, and Backus, M..

Russell, B., Hampson, D., 1991, Comparison of post-stack inversion methods: SEG Expanded Abstracts, SEG Annual Meeting 1991.

Schoenberger, M., Levin, F.K., 1974, Apparent attenuation due to interbed multiples: Geophysics, 39, 278-291.

Schoenberger, M., Levin, F.K., 1978, Apparent attenuation due to interbed multiples, II: Geophysics, 43, 730-737.

Schruafnagel, R.A., 1993, Coalbed Methane Production, in “Hydrocarbons from Coal”, edited by B.E. Law and D.D. Rice, AAPG Studies in Geology #38, Chapter 15.

Shimada, S., Li, H., Oshima, Y., Adachi, K., 2005, Displacement behavior of CH₄ adsorbed on coals by injecting pure CO₂, N₂, and CO₂-N₂ mixture: Environmental Geology, v. 49, p. 44-52.

Shuey, R.T., 1985, A simplification of the Zoeppritz equations: *Geophysics*, v.50, p.609-614.

Skawinski, R., 1999, Considerations referring to coal swelling accompanying the sorption of gases and water. *Archives of Mineral Science*, v. 44, p. 425– 434.

Stewart, R.R., Gaiser, J.E., Brown, R.J., Lawton, D.C., 2002, Tutorial: Converted-wave seismic exploration: *Methods: Geophysics*, v. 67, p. 1348-1363.

Stewart, R.R., Gaiser, J.E., Brown, R.J., Lawton, D.C., 2003, Tutorial: Converted-wave seismic exploration: *Applications: Geophysics*, v. 68, p. 40-57.

Taylor, G.H., Teichmuller, M., Davis, A., Diessel, C.F.K., Littke, R., Robert, R., 1998, *Organic Petrology*, Gebruder Borntraegen, Berlin-Stuttgart, 704 pages.

Thomas, L., 2002, *Coal Geology*, published by John Wiley & Sons Ltd.

Veeken, P., Da Silva, M., 2004, Seismic inversion methods and some of their constraints: *First Break*, v.22, p. 47-70.

Viete, D.R., Ranjith, P.G., 2006, The effect of CO₂ on the geomechanical and permeability behavior of brown coal: implications for coal seam CO₂ sequestration: *International Journal of Coal Geology*, v. 66, no. 3, p. 204–16.

Viete, D.R., Ranjith, P.G., 2007, The mechanical behaviour of coal with respect to CO₂ sequestration in deep coal seams: *Fuel*, v. 86, 2667-2671

Wang, Z.Z., 2001, Fundamentals of seismic rock physics: *Geophysics*, v. 66, p398-412.

White, R.E., 1980, Practical coherence matching of synthetic seismograms with seismic traces: *Geophysical Prospecting*, v. 28, p.333-358.

Widess, M.A., 1973, How thin is a thin bed?: *Geophysics*, 38, 1176-1180.

White, C. M., D. H. Smith, K. L. Jones, A. L. Goodman, S. A. Jikich, R. B. LaCount, S. B. DuBose, E. Ozdemir, B. I. Morsi, and K. T. Schroeder, 2005, Sequestration of carbon dioxide in coal with enhanced coalbedmethane recovery. A review: *Energy and Fuels*, v. 19, p. 659–724.

Wilson, E.J., Johnson, T.L., Keith, D.W., 2003, Regulating the Ultimate Sink: Managing the Risks of Geological CO₂ Storage: *Environmental Science and Technology*, v. 37, n. 16, p. 3476-3483.

Yee, D., Seidle, J.P., Hanson, W.B., 1993, Gas Sorption on Coal and Measurement of Gas Content, in “Hydrocarbons from Coal”, edited by B.E. Law and D.D. Rice, *AAPG Studies in Geology #38*, Chapter 9.

Yilmaz, O., 2001, *Seismic Data Analysis*, Society of Exploration Geophysicists, Investigations in Geophysics No. 10.

Yu, G., Vozoff, K., Durney, D.W., 1993, The influence of confining pressure and water saturation on dynamic elastic properties of some Permian coals: *Geophysics*, v. 58, no. 1, p. 30-38.

Zhu, J., Jessen, K., Kavscek, A., Orr Jr., F., 2003, Analytical theory of coalbed methane recovery by gas injection, *SPE 87338*.